UMCS

UNIWERSYTET MARII CURIE-SKŁODOWOSKIEJ
LUBLIN

Faculty of Mathematics, Physics and
Computer Science

Department of Theoretical Physics

Jie YANG
Supervisor: prof. dr hab. Jerzy Dudek

Systematic Study of Exotic Nuclear Shape Symmetries and Isomers, Including Shape Evolution and Competition in Heavy and Super-Heavy Nuclei

Lublin May 16, 2022

Abstract

We present the nuclear structure theory project focussed on the large-scale, systematic, total energy calculations using a realistic phenomenological mean-field theory approach with newly adjusted parameters with parametric correlations eliminated.

Traditional methods of the mean-field theory are combined with the powerful formal methods of the applications of the group and group representation theories to illustrate symmetry properties of – as it turns out – universal octupole magic number $N = 136$ persisting at all four octupole deformations $\alpha_{3\mu=0,1,2,3}$ simultaneously. The implied shell effects generate exotic symmetry shapes at quadrupole deformation $\alpha_{20} = 0$ and octupole deformations $\alpha_{3\mu} \neq 0$, corresponding to the point groups C_∞, D_{2v}, T_d, and D_{3h}. These effects are predicted to take place in nuclei around Pb for $Z \geq 82$. Experimental identification criteria of these exotic symmetries are formulated and discussed in detail.

In order to study nuclear shape evolution in multidimensional spaces, an often applied description in terms of one-dimensional trajectories is considered. Based on these considerations, the method of the quasi-classical Wentzel-Kramers-Brillouin (WKB) approximation to evaluate the barrier penetration probabilities is employed. To find trajectories of maximum probabilities, the WKB method is combined with the methods of Graph Theory of applied mathematics, in particular the well known Dijkstra algorithm.

Our total potential energy calculations predict the presence of static equilibrium deformations with significant octupole components in many nuclei with proton numbers $Z = 82 - 90$, particularly strong in nuclei around $N = 136$. We estimate the dynamical (most probable) equilibrium deformations by solving the corresponding collective Schrödinger equation; a comparison is presented and discussed.

Our realistic mean-field calculations also address the issue of the coexistence between the quadrupole and octupole shapes and implied symmetries. The comparative calculations including the higher-order multipole deformations $\lambda \geq 4$ are presented and a certain impact of α_{60} is detected in heavy nuclei in the ranges of $Z \approx 98 - 110$ and $N \approx 144 - 160$. We extend our multi-dimensional calculations to the super-heavy nuclei. The predictive power of the new parametrisation of the Hamiltonian is examined and the impact of the octupole deformations is discussed. The tetrahedral (α_{32}) magic number at $N = 196$ is predicted as well as the new geometrical configurations combining quadrupole oblate shapes with octupole-α_{33}; the corresponding results are presented and discussed.

Streszczenie

Prezentowany projekt teori struktury jądra atomowego oparty jest na obliczeniach jądrowych energii potencjalnych w wielowymiarowych przestrzeniach deformacji kształtu. Użyto fenomenologicznej teorii pola średniego z nowo dopasowanymi parametrami Hamiltonianu. Użyte metody dopasowania parametrów pozwalają na wykrycie i usunięcie korelacji parametrycznych, których obecność prowadzi, jak dzisiaj dobrze wiadomo, do destabilizacji przewidywań modelowych.

W prezentowanej pracy połączono tradycyjne metody teorii jądrowego pola średniego z zastosowaniami teorii grup i reprezentacji grup co prowadzi do matematycznie precyzyjnych form opisu właściwości badanych symetrii. Obliczenia pokazują istnienie uniwersalnej magicznej liczby oktupolowej $N = 136$ towarzyszącej wszystkim czterem deformacjom oktupolowym $\alpha_{3\mu=0,1,2,3}$ jednocześnie. Sugerowane efekty powłokowe generują egzotyczne kształty jądrowe przy deformacji kwadrupolowej $\alpha_{20} = 0$ i deformacjach oktupolowych $\alpha_{3\mu} \neq 0$, odpowiadających grupom punktowym C_∞, D_{2v}, T_d, and D_{3h}. Przewiduje się, że efekty te będą miały miejsce w jądrach wokół Pb dla $Z > 82$. Sformułowano i szczegółowo omówiono eksperymentalne kryteria identyfikacji tych egzotycznych symetrii.

Aby badać ewolucję kształtu jądra w przestrzeniach wielowymiarowych, w literaturze rozważany jest często opis w kategoriach trajektorii jednowymiarowych. W tym kontekście wykorzystano metodę quasi-klasycznego przybliżenia Wentzela-Kramersa-Brillouina (WKB) do oceny prawdopodobieństw przenikania przez bariery. Aby wyznaczyć trajektorie maksymalnego prawdopodobieństwa przenikania barier potencjalnych oddzielających minima o znaczeniu fizycznym, metodę WKB połączyliśmy z metodami teorii grafów z matematyki stosowanej, w szczególności ze znanym algorytmem Dijkstry.

Nasze obliczenia całkowitej energii potencjalnej przewidują obecność deformacji równowagi statycznej ze znaczącymi składowymi oktupolowymi w wielu jądrach o liczbach protonów $Z = 82 - 90$, efektów szczególnie silnych w jądrach w okolicach $N = 136$. Obliczyliśmy dynamiczne (najbardziej prawdopodobne) deformacje równowagi, rozwiązując odpowiednie kolektywne równanie Schrödingera. Przedsawiliśmy odpowiednie porównania i dyskusję.

Nasze realistyczne obliczenia pola średniego dotyczą również kwestii współistnienia kształtów o wyższych multipolowościach. Przedstawiono wyniki porównawcze obejmujące deformacje multipolowe wyższych rzędów, $\lambda \geq 4$, oraz omówiono w szczegółach wpływ α_{60} na ciężkie jądra w zakresach $Z \approx 98 - 110$ i $N \approx 144 - 160$. Rozszer-

zono nasze wielowymiarowe obliczenia na obszar super cieężkich jąder. Zbadano moc przewidywawczą nowej parametryzacji i omówiono wpływ deformacji oktupolowych. Przewidziano istnienie nowej tetrahedralnej liczby magicznej $N = 196$ związanej z deformacją α_{32} oraz nowe egzotyczne konfiguracje kształtów spłaszczonych w połączeniu z deformacją oktupolową α_{33}.

Contents

List of Figures

List of Tables

Chapter 1

Introduction

One of the most important issues on the subatomic physics research agenda is the problem of nuclear stability, which turns out to be strongly related to nuclear shapes and their symmetries. In terms of the experimental research these interests translate into important investments (at the level of billions of Euro/Dollars of research budgets) in the studies of exotic, in particular very heavy and super-heavy nuclei, within strongly developing international collaborations.

> *The present PhD research project has been realised following Memorandum of Understanding between the Maria Curie Skłodowska University of Lublin, Poland, and the University of Zhengzhou, China, with one of the important goals being the training of young researchers in our domain of physics. To this end, efforts were undertaken to present in this thesis document several elements of description of the nuclear structure theory methods to facilitate entering into our research field to the new-coming PhD students or post-doctoral fellows who will choose working in our domain.*
>
> *During the last year of the preparation of this thesis, the financing of a new nuclear physics related European Project* Theo4Exp *via* EuroLabs *initiative has been announced. This project consists in preparation of the specialised internet based service allowing to the nuclear experimentalists working in the European accelerator related laboratories to use especially adapted nuclear theory computer programs and theory data bases, in particular related to the nuclear mean field theory. The latter part of the project, referred to as* MeanField4Exp *will be realised in collaboration between the nuclear physics laboratories in Cracow, Strasbourg and Warsaw. Computer programs which will be installed within this European project will contain, among others, the ones employed for the present PhD project. The person in charge of the realisation of the* MeanField4Exp *project will be the supervisor of the present thesis.*

At the modelling side, the nuclear mean-field theory on the one hand, and the nuclear spherical shell model on the other, can be seen as traditional, realistic approaches, employed in quantum mechanical description of nuclei, and this from the beginning of the second half of the previous century onwards. In parallel, the algebraic models have been constructed, usually focussed on a pre-defined class of phenomena such as collective vibrations, collective rotations, etc. The more recent development involves the so-called *ab initio* methods aiming at the fully microscopic description of nuclei, limited rather to the light nuclei at present.

In the present project we will follow a realistic mean-field theory approach. It allows to describe consistently a number of mechanisms and phenomena, which can directly be confronted with experiment. Among these, we may count nuclear and nucleonic binding energies, together with the single particle level energies and the implied excitation spectra. Related to those remain the structures of the so-called K-isomers and yrast-trap isomers. Equally important roles can be attributed to shape isomers and shape evolution with varying proton and neutron numbers, Z and N, respectively, as well as with angular momentum I and nuclear temperature T, allowing to enter the description of nuclear giant resonances but also the associated so-called Jacobi and Poincaré shape transitions. Last but not least, the mean field theory approach with its Hartree-Fock and/or Hartree-Fock-Bogolyubov extensions including adiabaticity and multi-dimensional cranking approximations allows for a successful microscopic description of the nuclear collective rotational bands together with the inherent mechanisms such as multi-quasiparticle excitations, angular momentum alignments, band crossings with the so-called 'back-bending phenomenon' and many others.

Our group has contributed to all these elements of nuclear structure theory evolution in numerous previous projects including Ph-D theses. The present project is focussed on the new symmetry considerations including exotic point group symmetries and the implied transition hindrance mechanisms, which will be used to construct the identification criteria. The traditional methods of the nuclear mean-field theory will be combined with the powerful formal methods originating from mathematics as well as applied mathematics:

• When examining point group symmetries we will apply the applications of the Group and Group Representation Theories.

• In order to perform the Hamiltonian parameter adjustments guaranteeing stable modelling capacities, we will use the Inverse Problem Theory, a subfield of applied mathematics.

• To analyse the properties of the quasi-classical WKB trajectories in the multi-dimensional deformation spaces we will apply Graph Theory, another subfield of applied mathematics.

The concept of elementary space symmetries such as inversion, rotation, reflection, are considered necessary to connect directly the nuclear geometrical properties with their quantum-mechanical description. It turns out that the nuclear shapes are directly related to the properties of the underlying mean-field Hamiltonians, which determine the nucleonic energy spectra. This link implies possibilities of analysing the global properties of nucleonic spectra, such as energy-level degeneracies or fluctuations of the level densities, through the symmetries of the mean-field Hamiltonian. Consequently, our main interest is to focus on the exotic nuclear shapes, which by definition differ from the traditional ellipsoidal prolate, oblate and triaxial shapes. The spectroscopic criteria for experimental identification of exotic configurations corresponding to the exotic shapes are formulated in this project by using group representation theory methods combined with the nuclear mean-field theory ones.

About the Structure of this Document. The presentation of this thesis will be composed of two parts. The first, entitled "General Nuclear Structure Theory Aspects" addresses the description of the theoretical concepts and modelling methods together with specific mathematical tools. The second one, "Results and Discussion", is focussed on the presentation of the new results obtained within this Ph-D thesis. The presentation of this document is subdivided as follows:

Chapter 1
A short introduction presenting this document, the research motivations and the results obtained within the present work.

Chapter 2
Presents the description of our realistic phenomenological nuclear mean-field theory focussing on selected structural elements. We start from the general presentation of nucleon-nucleon interaction to arrive at the concept of the nuclear mean-field, as the leading term of nuclear Hamiltonian. The notion of the mean-field facilitates presentation of the related issues such as nuclear surface and, in particular, the multipole description of nuclear shapes with the help of spherical harmonics. We present the phenomenological central and spin-orbit potentials, and the related specific issues: parametrisation of the Hamiltonian, constant volume condition, elimination of the center of mass motion problem, etc. Finally, we introduce an important and relatively modern issue of parametric uncertainties and parametric correlations in view of the indications originating in the mathematical Inverse Problem Theory.

Chapter 3
We present a description of the numerical solution methods of the Schrödinger equation with our phenomenological mean-field Hamiltonian. We introduce our realisation of the harmonic oscillator basis and the techniques of determining the matrix elements with the help of the Gauss integration theorem. As it turns out, the fact of using real deformation parameters and spherical harmonics to describe the nuclear shapes implies that the mean-field is always invariant under plane reflexion ($+y \rightarrow -y$) referred to as *simplex symmetry*. This, and the *time-reversal symmetry* are the fixed symmetries of our Hamiltonian, and thus can be used for important symmetrisations of the basis, what leads to significant decrease in terms of the c.p.u.-time and computer storage. The corresponding techniques and the structuring of the Hamiltonian matrix are presented.

Chapter 4
The knowledge of the mean-field theory solutions allows taking into account important residual two-body interactions, here taken in the form of pairing. We present briefly the solution to the paring problem within the Bardeen-Cooper-Schrieffer (BCS) approach. We present next the extension of the static pairing approach allowing to describe the collective rotation within the Hartree-Fock Bogolyubov Cranking (HFBC) techniques.

Chapter 5
Since we need in this project several mathematical tools originating from the group-, and group representation theories, the corresponding elements are presented in a very compact manner which allows introducing a minimum knowledge of the leading properties and the underlying notation. We start with the elementary definitions to approach the geometrical symmetry features related to nuclear shapes and thus point group symmetries. Examples of tetrahedral and octahedral symmetries recently discovered by our group are discussed in some detail to illustrate certain general mathematical properties. Group representation theory is employed in predictions of the properties of nuclear collective rotation spectra and the methods of experimental identification of selected exotic point group symmetries: $C_{2\mathrm{v}}$, T_d, D_{4h} and D_{2d} are discussed.

Chapter 6
The final results of the project are presented in the last Chapter. Systematic analysis of exotic shapes in heavy and super-heavy nuclei and their impact on measurable nuclear properties are addressed. We shortly summarise the results of the total energy calculations in the selected multi-dimensional deformation spaces, which lead us to the importance of the octupole magic number $N = 136$, very special in the sense that strong shell gaps are generated at this neutron number for all the four octupole deformations: $\alpha_{30} \neq 0$, $\alpha_{31} \neq 0$, $\alpha_{32} \neq 0$ and $\alpha_{33} \neq 0$. We show which point-group symmetries correspond to these shapes and analyse the corresponding single-nucleon and collective-rotational spectra. We also address the issue of the coexistence between the quadrupole

and octupole shapes and implied symmetries, compare the predictions with the results based on the notion of the dynamical equilibrium deformations as well as the effects of the selected high-multipolarity deformations $\alpha_{\lambda>4,\mu}$. The study of exotic symmetries is extended to the super-heavy nuclei. Our calculations show that octupole components α_{32} and α_{33} play an important role in stabilising the ground-state configurations. The tetrahedral magic number $N = 196$ is predicted, and the importance of the new exotic quadrupole oblate-shapes combined with octupole deformation α_{33} is illustrated in the super-heavy nuclei around $118 \leq Z \leq 130$ and $170 \leq N \leq 186$.

Part I

General Nuclear Structure Theory Aspects

Chapter 2

Nuclear Mean-Field Theory: Our Formulation and Applications

In this chapter we introduce selected general notions related to the description of nuclear interactions often referred to as nucleon-nucleon interactions or, less precisely, as 'nuclear forces' (since the notion of the 'force' makes no sense in quantum mechanics). We will present short summaries related to the fundamental symmetry principles, and the approximate simplifications of the underlying Hamiltonians. They will be helpful for introducing the concepts of the nuclear mean-field approximation addressed next. We are aware of the fact that presented examples are far from bringing the full image of complexity, but more complete reviewing of the subject would bypass the context and the framework of this project.

2.1 Nuclear Interactions: Examples of Complexity

Let us begin by introducing an abbreviated notation, $\hat{x}$, representing nucleonic degrees of freedom: vector operators of position $\hat{r}$, linear momentum $\hat{p}$, spin $\hat{s}$ and isospin $\hat{t}$,

$$\hat{x} = \{\hat{r}, \hat{p}, \hat{s}, \hat{t}\}. \tag{2.1.1}$$

The nucleon-nucleon interaction can be described by two sets of operators, $\hat{x}_1$ and $\hat{x}_2$:

$$\hat{V} = \hat{V}(\hat{x}_1, \hat{x}_2) \to \hat{V}[(\hat{r}_1, \hat{r}_2); (\hat{p}_1, \hat{p}_2); (\hat{s}_1, \hat{s}_2); (\hat{t}_1, \hat{t}_2)]. \tag{2.1.2}$$

We proceed to discussing certain specific features behind the above general expression.

2.1.1 $\hat{V}$: Central, Tensor, Spin-Orbit, Quadratic Spin-Orbit

The general form of the nucleon-nucleon interactions is often expressed as

$$\boxed{\widehat{V}(\hat{x}_1,\hat{x}_2) \equiv \widehat{V}_C(\hat{x}_1,\hat{x}_2) + \widehat{V}_T(\hat{x}_1,\hat{x}_2) + \widehat{V}_{LS}(\hat{x}_1,\hat{x}_2) + \widehat{V}_{LL^2}(\hat{x}_1,\hat{x}_2),} \tag{2.1.3}$$

where the symbols $\widehat{V}_C$, $\widehat{V}_T$, $\widehat{V}_{LS}$ and $\widehat{V}_{LL^2}$ refer to central, tensor, spin-orbit and quadratic spin-orbit interactions, respectively, cf. ref. [5].

Central Interaction. It consists of four terms:

$$\widehat{V}_C(\hat{x}_1,\hat{x}_2) = V_0(r_{12}) + V_s(r_{12})\,[\vec{s}_1\cdot\vec{s}_2\,] + V_t(r_{12})\,[\vec{t}_1\cdot\vec{t}_2\,] + V_{s-t}(r_{12})\,[\vec{s}_1\cdot\vec{s}_2\,]\,[\vec{t}_1\cdot\vec{t}_2\,], \tag{2.1.4}$$

where, as discussed in the following section, the terms $V_0(r_{12})$, $V_s(r_{12})$, $V_t(r_{12})$ and $V_{s-t}(r_{12})$ depend only on the relative distance, r_{12}. For the reasons for this choice see the discussion of the problem of invariance under translations presented below. The second term is proportional to the scalar product of spins $\vec{s}_1$ and $\vec{s}_2$ and it is called spin-spin interaction. Similarly, the third term is proportional to the scalar product of isospins $\vec{t}_1$ and $\vec{t}_2$ and it is therefore called isospin-isospin interaction. The last term is called spin-isospin interaction; it is proportional to the scalar products of spins and isospins.

Tensor Interaction. It has, by definition, the following form:

$$\widehat{V}_T(\hat{x}_1,\hat{x}_2) = [V_{t_0}(r_{12}) + V_{t_1}(r_{12})\,\vec{t}_1\cdot\vec{t}_2\,]\,\vec{S}_{(12)}. \tag{2.1.5}$$

It depends on the so-called tensor term, $\vec{S}_{(12)}$, which is defined by

$$\vec{S}_{(12)} \stackrel{df.}{=} \frac{3\,(\vec{s}_1\cdot\vec{r}_{12}\,)(\vec{s}_2\cdot\vec{r}_{12}\,) - (\vec{s}_1\cdot\vec{s}_2\,)\,r_{12}^2}{r_{12}^2} \quad \text{where} \quad r_{12} \stackrel{df.}{=} |\vec{r}_1 - \vec{r}_2|. \tag{2.1.6}$$

Two-body Spin-Orbit Interaction. It is defined as:

$$\widehat{V}_{LS}(\hat{x}_1,\hat{x}_2\,) = [V_{LS}^{t_0}(r_{12}\,) + V_{LS}^{t_1}(r_{12}\,)\,\vec{t}_1\cdot\vec{t}_2\,](\vec{L}\cdot\vec{S}\,), \tag{2.1.7}$$

where the *relative* orbital angular momentum, $\vec{L}$, and total spin $\vec{S}$, are defined as follows

$$\vec{L} \stackrel{df.}{=} \tfrac{1}{2}(\vec{r}_1 - \vec{r}_2) \wedge (\vec{p}_1 - \vec{p}_2) \quad \text{and} \quad \vec{S} \stackrel{df.}{=} \vec{s}_1 + \vec{s}_2. \tag{2.1.8}$$

Please observe that above we have introduced the relative linear momentum operator, $\vec{p}_1 - \vec{p}_2$, to assure Galilean invariance discussed below in this chapter. The quadratic spin-orbit interaction is defined as

$$\widehat{V}_{LL}(\hat{x}_1,\hat{x}_2) = V_{LL}(r_{12}\,)\{(\vec{s}_1\cdot\vec{s}_2)\,\vec{L}^{\,2} - \frac{1}{2}[(\vec{s}_1\cdot\vec{L}\,)(\vec{s}_2\cdot\vec{L}\,) + (\vec{s}_2\cdot\vec{L}\,)(\vec{s}_1\cdot\vec{L}\,)]\}. \tag{2.1.9}$$

As before, the relative orbital angular momentum of the two particles, $\vec{L}$, is given in eq. (2.1.8).

There exist various specific extensions and variants of the above general scheme, which can be found in the nuclear structure literature. The present research project employs a phenomenological, so-called nuclear mean-field theory approximation. The nuclear mean-field theory uses an effective one-body Hamiltonian. According to this latter scheme, the theoretical description of a rich class of nuclear structure effects is based on the idea of the free motion of a nucleon in the specifically constructed one-body potential, cf. e.g. ref. [6] and references therein. The guide-lines of the construction of the effective one-body potentials profit from the symmetry considerations, which will be discussed next.

2.1.2 Nucleon-Nucleon Interactions: Fundamental Symmetries

In what follows we will consider a number of fundamental symmetry operations, which guarantee that the description of nuclear forces is independent of acceptable arbitrary choices related to the definitions of the Cartesian reference frame Σ rather than its translated image $\Sigma^{'}$, its rotated image $\Sigma^{''}$, or yet another one, moving with respect to the originally chosen one with a constant velocity, $\vec{v}$, the latter independence property referred to as Galilean invariance. Similarly, we will verify that this description does not depend on the sign of the time variable t, referred to as time reversal invariance.

To simplify the notation, we refer to the vector operators by using a single mathematical accent symbol " ˆ " rather than " $\hat{\rightarrow}$ ", e.g. $\hat{r}$ rather than $\hat{\vec{r}}$.

Translational Invariance. Consider a Cartesian system of coordinates $\{x, y, z\} \equiv \vec{r}$, denoted Σ, and another one Σ', which differs from the previous one by an arbitrary translation represented by a constant vector $\vec{a}$:

$$\Sigma \leftrightarrow \vec{r} \text{ and } \Sigma' \leftrightarrow \vec{r}' = \vec{r} + \vec{a}. \tag{2.1.10}$$

Of course, the theoretical description of the nuclear interactions must not depend on the choice of the shift of the Cartesian reference frame, which remains at the physicist's disposal. Applying the above relation to the relative distance between two nucleons, we find

$$\Sigma \xrightarrow{\vec{a}} \Sigma' :\Rightarrow \vec{r}_2 - \vec{r}_1 \rightarrow \vec{r}_2' - \vec{r}_1' = \vec{r}_2 + \vec{a} - (\vec{r}_1 + \vec{a}\,) = \vec{r}_2 - \vec{r}_1. \tag{2.1.11}$$

For this reason, the choice introduced above in eq. (2.1.4), must involve the relative distance associated with the vector $\vec{r}_{12} \equiv \vec{r}_2 - \vec{r}_1$, wherefrom the condition:

$$\hat{V} = \hat{V}(\hat{x}_1, \hat{x}_2\,) \rightarrow \hat{V}[(\hat{r}_1 - \hat{r}_2\,); (\hat{p}_1, \hat{p}_2\,); (\hat{s}_1, \hat{s}_2\,); (\hat{t}_1, \hat{t}_2\,)], \tag{2.1.12}$$

which assures that the nucleon-nucleon interaction is invariant under translation.

Galilean Invariance. Consider a system of coordinates Σ, which we refer to as "initial", together with another one, Σ', moving respect to the initial system with an arbitrary constant velocity $\vec{v}$. The description of velocity of a non-relativistic particle satisfies:

$$\Sigma \leftrightarrow \vec{v}_1 \text{ and } \Sigma' \leftrightarrow \vec{v}_1' = \vec{v}_1 + \vec{v}. \tag{2.1.13}$$

As presented earlier in eq. (2.1.8), the spin-orbit term of the nucleon-nucleon interaction depends on $\vec{p}_1 - \vec{p}_2$. Since linear momenta, $\vec{p}_1 = m\vec{v}_1$ and $\vec{p}_2 = m\vec{v}_2$, it follows that $(\vec{p}_1 - \vec{p}_2) \sim (\vec{v}_1 - \vec{v}_2)$. According to Galilean invariance, interactions expressed in either Σ or Σ' must be exactly the same. It follows from eqs. (2.1.8) and (2.1.13) that the two-body nucleon-nucleon interactions indeed satisfy the condition of Galilean invariance.

Invariance Under Space Reflections. Let us consider transformation of inversion, $\mathcal{I}$, of the reference frame Σ:

$$\Sigma \ni \vec{r} \xrightarrow{\mathcal{I}} -\vec{r} = \vec{r}' \in \Sigma'. \tag{2.1.14}$$

Under this transformation the vector quantities such as position and linear momentum change their signs, $\vec{r} \to -\vec{r}$ and $\vec{p} \to -\vec{p}$, whereas the orbital angular momentum, which is defined as $\vec{\ell} = \vec{r} \wedge \vec{p}$, remains invariant. Similar property holds for the intrinsic spins. It follows that the nucleon-nucleon interactions are invariant under space reflections, since they were constructed using the product of position-, and linear momentum depending operators, cf. eq. (2.1.8). In this way we assure, that the description of nuclear interactions does not depend on the physicist's arbitrary decision about choosing the reference frame: Σ or Σ'.

Time-Reversal Invariance. As can be seen from the above introduction, the Hamiltonian of the nucleon-nucleon interactions has been constructed as not depending on time explicitly, in agreement with the experimental evidence known to us today. Indeed, the nuclear forces seemingly remain the same millions of years ago and now, wherefrom hypothesis of time independence. However, the Hamiltonian of the interactions may depend on time implicitly, since the time-reversal operation influences the linear momentum, angular-momentum, and spins.

Let us denote the time-reversal operator by $\hat{T}$. We have:

$$\boxed{\hat{T}\hat{r}\hat{T} = +\hat{r},\ \hat{T}\hat{p}\hat{T} = -\hat{p},\ \hat{T}\hat{\ell}\hat{T} = -\hat{\ell} \text{ and } \hat{T}\hat{s}\hat{T} = -\hat{s}.} \tag{2.1.15}$$

As shown above, the nucleon-nucleon interactions are proportional to the terms such as $\hat{p}_{12} \cdot (\hat{s}_1 + \hat{s}_2)$ or $(\hat{l}_1 + \hat{l}_2) \cdot (\hat{s}_1 + \hat{s}_2)$, and it follows that these interactions are invariant under time reversal.

2.2 Structure of Nuclear Many Body Hamiltonian

In the previous section we have presented an example of the general form of interactions acting between any two nucleons and the associated fundamental symmetry properties. Atomic nuclei are in fact highly complex in many body-systems and the numbers of strongly-interacting Fermions in nuclei may easily exceed two hundreds. It will be instructive to discuss briefly some general strategies to follow, when examining the possible structure of the Hamiltonians of the subatomic systems in terms of their many-body interactions.

2.2.1 Short-Range Nucleon-Nucleon Interactions

With the help of the compact notation in eq. (2.1.1), one can express the N-body Hamiltonian as depending on all the nucleonic operators $\hat{x}_i$. We may write in full generality:

$$\hat{H} = \hat{H}(\hat{x}_1, \hat{x}_2, ..., \hat{x}_N). \tag{2.2.1}$$

The symbol $\hat{x}$ denotes the position vector $\hat{r}$, linear momentum $\hat{p}$, spin vector $\hat{s}$ and isospin vector $\hat{t}$. Each of these vectors has three components, say $\{x, y, z\}$, and we have 12 operators behind each $\hat{x}$. When considering a system with, e.g., 100 nucleons, $12 \times 100 = 1200$ operators are required. Therefore the above Hamiltonian leads to a very complicated Schrödinger equation with a large number of interaction terms and related operators.

One possibility of simplifying this complicated Hamiltonian is *to take into account the short range of nuclear interactions*. The implied, possible representation of the nuclear short-range interaction Hamiltonian can be introduced as follows:

$$\left.\begin{aligned}
\hat{H}(\hat{x}_{i_1}, \hat{x}_{i_2}, ..., \hat{x}_{i_N}) = &\sum_{i=1}^{N} [\hat{T}_i + \hat{V}_1(\hat{x}_i)] && \leftarrow \text{1 body} \\
&+ \frac{1}{2} \sum_{i_1=1}^{N} \sum_{i_2=1}^{N} \hat{V}_2(\hat{x}_{i_1}, \hat{x}_{i_2}) && \leftarrow \text{2 body} \\
&+ \frac{1}{3!} \sum_{i_1=1}^{N} \sum_{i_2=1}^{N} \sum_{i_3=1}^{N} \hat{V}_3(\hat{x}_{i_1}, \hat{x}_{i_2}, \hat{x}_{i_3}) && \leftarrow \text{3 body} \\
&+ ... \\
&+ \frac{1}{(N-1)!} \underbrace{\sum_{i_1=1}^{N} \sum_{i_2=1}^{A} ... \sum_{i_N-1=1}^{N}}_{(N-1)} \hat{V}_{N-1}(\hat{x}_{i_1}, \hat{x}_{i_2}, ..., \hat{x}_{i_N-1})
\end{aligned}\right\}, \tag{2.2.2}$$

where $\hat{T}_i$ represents the kinetic energy operator of i^{th} particle,

$$\hat{T}_i = \frac{\hbar^2}{2m} \nabla_i^2. \tag{2.2.3}$$

The term $\hat{V}_1(\hat{x}_i)$ represents a one-body interaction, the term $\hat{V}_2(\hat{x}_i, \hat{x}_j)$ two-body interaction, etc. Since the nucleonic mean free-path is relatively long, the probability of interacting between a given nucleon and one of its companions via short range interactions is relatively small. It follows that the probability of activating a simultaneous three-body interaction is even smaller. Under these conditions we may expect that the nuclear Hamiltonian can be represented, within an acceptable approximation, in the form of a sum of one-body and two-body contributions:

$$\boxed{\hat{H} = \sum_{i=1}^{N}[\hat{t}_i + \hat{V}_1(\hat{x}_i)] + \frac{1}{2}\sum_{i,j=1}^{N}\hat{V}_2(\hat{x}_i, \hat{x}_j),} \tag{2.2.4}$$

with the higher order terms neglected. We can consider the first term as an average nuclear interaction between a given nucleon and the remaining $(N-1)$ nucleons, wherefrom the names such as 'mean-field' or 'average field' interaction potentials. The second term can be treated as representing an effective two-body correction term. It represents, what is traditionally called residual interaction term and involves most often pairing, or long range multipole-multipole interactions.

2.2.2 Nuclear Mean-Field: Leading Term of the Hamiltonian

Let us assume that the nuclear interactions can be expressed as a sum of the one-body and two-body terms. We can write the related nuclear Hamiltonian as:

$$\hat{H}_{\text{nuclear}} \approx \hat{H}_{\text{mean-field}} + \hat{H}_{\text{residual}}. \tag{2.2.5}$$

For the nuclear system with n nucleons, the mean-field (also called independent-particle) wave function can be constructed in the so-called product wave function form:

$$\psi_n(x_1, x_2, ..., x_n) = \mathcal{N}_{\alpha_1,\alpha_2,...,\alpha_n}\varphi_{\alpha_1}(x_1)\varphi_{\alpha_2}(x_2)...\varphi_{\alpha_n}(x_n), \tag{2.2.6}$$

in which $\mathcal{N}_{\alpha_1,\alpha_2,...,\alpha_n}$ is the normalisation constant, the symbols $\alpha_1, \alpha_2, ..., \alpha_n$ represent the set of quantum numbers which are used to identify, if possible uniquely, the nucleonic states. The corresponding Schrödinger equation takes the usual form

$$\hat{H}(\hat{x}_1, \hat{x}_2, ..., \hat{x}_n)\psi_n(x_1, x_2, ..., x_n) = E_n\psi_n(x_1, x_2, ..., x_n). \tag{2.2.7}$$

In the case of the mean-field approximation the many-body interaction potential has the form of a sum of individual single-nucleonic potentials

$$\boxed{\hat{V}(\hat{x}_1, \hat{x}_2, ..., \hat{x}_n) = \sum_{i=1}^{n}\hat{V}_1(\hat{x}_i),} \tag{2.2.8}$$

(this is why the solutions take the form of the products of one-particle terms) so that after separating the variables the independent-particle mean-field Schrödinger equation takes the form

$$[\hat{t}_i + \hat{V}_1(\hat{x}_i)]\psi_n(x_i) = e_n\psi_n(x_i), \tag{2.2.9}$$

where $[e_n, \psi_n(x_i)]$ are the single-nucleonic solutions to the mean-field Hamiltonian.

2.3 Nuclear Surface: Existence and Description

Let us come back to the observation that the nucleon-nucleon interactions are of a very short range, comparable with the nucleonic sizes. As the result, the nuclei can be seen as 'tightly packed objects', composed of nucleons which are nearly touching each other. It follows that the density of the nuclear matter, $\rho(x, y, z)$, which – following the picture of the tight packing, is nearly constant at the nuclear interior, falls quickly to zero with the increasing distance from the centre of the system. One usually introduces the notion of the nuclear surface by collecting all the points which satisfy the relation $\rho(x, y, z) = \text{const.}$, in which the constant can be thought of as half of the central density, $\text{const.} = \frac{1}{2}\rho_0$ with $\rho_0 = \rho(0, 0, 0)$. The shape of the so defined surface can be naturally identified with the shape of the nucleus.

Many examples show that the nuclear surface, its shape, and thus the nuclear deformation can be related to experimental information and be used to test the theoretical predictions. Therefore the nuclear surface is definitely an important concept to help us to study the nuclear structure. In nuclear structure theory it is convenient to introduce the nuclear surface as a function, $R(\theta, \varphi)$, with the help of the spherical harmonic basis, $\{Y_{\lambda\mu}\}$, which can be used to represent an arbitrary function:

$$\Sigma: \; R(\theta, \varphi) = c(\{\alpha\}) R_0 \left[1 + \sum_{\lambda} \sum_{\mu=-\lambda}^{\lambda} \alpha_{\lambda\mu} Y_{\lambda\mu}(\theta, \varphi) \right], \tag{2.3.1}$$

where Σ is the short-hand notation for the nuclear surface, and $c(\{\alpha\})$ expresses the constant volume condition; we will give its explicit expression in the following sections. The radius of the equivalent spherical nucleus is denoted as usual by $R_0 = r_0 A^{1/3}$. The expansion coefficients $\{\alpha_{\lambda\mu}\}$ are often called deformation parameters, whereas $Y_{\lambda\mu}(\theta, \varphi)$ are the spherical harmonics, which can be written down as follows, ref. [7]

$$Y_{\lambda\mu}(\theta, \varphi) = \sqrt{\frac{(2\lambda + 1)}{2\pi} \frac{(\lambda - \mu)!}{(\lambda + \mu)!}} P_{\lambda\mu}(\cos\theta) e^{i\mu\varphi}. \tag{2.3.2}$$

Above, $P_{\lambda\mu}(\cos\theta)$ are the standard, well known so-called generalised Legendre functions and λ is referred to as 'rang' or 'multipolarity' index.

2.3.1 The Lowest Multipolarity Sequences

Since the basis of spherical harmonics can be used to describe an arbitrary surface in a three dimensional space, nuclear surfaces can be presented with the help of the expansion into spherical harmonics, a particularly convenient approach, when thinking about nuclear shapes in terms of the deviations from the spherical one. In what follows we just list the explicit expressions of spherical harmonics for the lowest multipolarities, λ, which are used in our project.

Quadrupole deformations:

$$Y_{20}(\theta,\varphi) = +\tfrac{1}{8}\sqrt{\tfrac{5}{\pi}}\,[1+3\cos(2\theta)], \tag{2.3.3}$$

$$Y_{22}(\theta,\varphi) = +\tfrac{1}{8}\sqrt{\tfrac{15}{2\pi}}\,[1-2\cos(2\theta)]\,e^{i\,2\varphi}. \tag{2.3.4}$$

Octupole deformations:

$$Y_{30}(\theta,\varphi) = +\tfrac{1}{16}\sqrt{\tfrac{7}{\pi}}\,[3\cos(\theta)+5\cos(3\theta)], \tag{2.3.5}$$

$$Y_{31}(\theta,\varphi) = -\tfrac{1}{32}\sqrt{\tfrac{21}{\pi}}\,[\sin(\theta)+5\sin(3\theta)]\,e^{i\,\varphi}, \tag{2.3.6}$$

$$Y_{32}(\theta,\varphi) = +\tfrac{1}{16}\sqrt{\tfrac{105}{2\pi}}\,[\sin(\theta)-\cos(3\theta)]\,e^{i\,2\varphi}, \tag{2.3.7}$$

$$Y_{33}(\theta,\varphi) = -\tfrac{1}{32}\sqrt{\tfrac{35}{\pi}}\,[\sin(\theta)-\sin(3\theta)]\,e^{i\,3\varphi}. \tag{2.3.8}$$

Hexadecapole deformations:

$$Y_{40}(\theta,\varphi) = +\tfrac{3}{128}\sqrt{\tfrac{1}{\pi}}\,[9+20\cos(2\theta)+35\cos(4\theta)], \tag{2.3.9}$$

$$Y_{42}(\theta,\varphi) = +\tfrac{3}{64}\sqrt{\tfrac{5}{2\pi}}\,[3+4\cos(2\theta)-7\cos(4\theta)]\,e^{i\,2\varphi}, \tag{2.3.10}$$

$$Y_{44}(\theta,\varphi) = +\tfrac{3}{128}\sqrt{\tfrac{35}{2\pi}}\,[3-4\cos(2\theta)+\cos(4\theta)]\,e^{i\,4\varphi}. \tag{2.3.11}$$

Implied specific geometrical features related to such a description will be discussed next.

2.3.2 Reduced Spherical Harmonics

The reduced spherical harmonics are defined as the following real functions:

$$\tilde{Y}_{\lambda,\mu} = 2Re(Y_{\lambda,\mu}) \quad \text{for} \quad \mu \neq 0 \quad \text{and} \quad \tilde{Y}_{\lambda,0} = Y_{\lambda,0}. \tag{2.3.12}$$

• For quadrupole deformations the corresponding reduced spherical harmonics are:

$$\tilde{Y}_{20}(\theta,\varphi) = +\tfrac{1}{8}\sqrt{\tfrac{5}{\pi}}\,[1+3\cos(2\theta)], \tag{2.3.13}$$

$$\tilde{Y}_{22}(\theta,\varphi) = +\tfrac{1}{4}\sqrt{\tfrac{15}{2\pi}}\,[1-2\cos(2\theta)]\,\cos(2\varphi). \tag{2.3.14}$$

• For octupole deformations the corresponding reduced spherical harmonics take the form:

$$\tilde{Y}_{30}(\theta,\varphi) = +\tfrac{1}{16}\sqrt{\tfrac{7}{\pi}}\,[3\cos(\theta)+5\cos(3\theta)], \tag{2.3.15}$$

$$\tilde{Y}_{31}(\theta,\varphi) = -\tfrac{1}{32}\sqrt{\tfrac{21}{\pi}}\,[\sin(\theta)+5\sin(3\theta)]\,\cos(\varphi), \tag{2.3.16}$$

$$\tilde{Y}_{32}(\theta,\varphi) = +\tfrac{1}{16}\sqrt{\tfrac{105}{2\pi}}\,[\sin(\theta)-\cos(3\theta)]\,\cos(2\varphi), \tag{2.3.17}$$

$$\tilde{Y}_{33}(\theta,\varphi) = -\tfrac{1}{32}\sqrt{\tfrac{35}{\pi}}\,[\sin(\theta)-\sin(3\theta)]\,\cos(3\varphi). \tag{2.3.18}$$

• For hexadecapole deformations the corresponding reduced spherical harmonics satisfy:

$$\tilde{Y}_{40}(\theta,\varphi) = +\tfrac{3}{128}\sqrt{\tfrac{1}{\pi}}\,[9+20\cos(2\theta)+35\cos(4\theta)], \tag{2.3.19}$$

$$\tilde{Y}_{42}(\theta,\varphi) = +\tfrac{3}{64}\sqrt{\tfrac{5}{2\pi}}\,[3+4\cos(2\theta)-7\cos(4\theta)]\,\cos(2\varphi), \tag{2.3.20}$$

$$\tilde{Y}_{44}(\theta,\varphi) = +\tfrac{3}{128}\sqrt{\tfrac{35}{2\pi}}\,[3-4\cos(2\theta)+\cos(4\theta)]\,\cos(4\varphi). \tag{2.3.21}$$

The above relations are particularly useful in numerical applications.

2.3.3 Nuclear Surface as a Real Function of Angular Variables

As shown above, in general the spherical harmonics are complex functions, while the nuclear surface must be presented as a real function. Therefore it follows that we have to impose:

$$R^*(\theta,\varphi) = R(\theta,\varphi) \rightarrow [\sum_{\lambda\mu} \alpha_{\lambda\mu} Y_{\lambda\mu}(\theta,\varphi)]^* = \sum_{\lambda\mu} \alpha_{\lambda\mu} Y_{\lambda\mu}(\theta,\varphi). \tag{2.3.22}$$

It is known that the spherical harmonics satisfy the symmetry relations

$$Y^*_{\lambda\mu}(\theta,\varphi) = (-1)^\mu Y_{\lambda-\mu}(\theta,\varphi). \tag{2.3.23}$$

In order to keep the nuclear surface function real, the following relation is required

$$\alpha^*_{\lambda\mu} = (-1)^\mu \alpha_{\lambda-\mu}. \tag{2.3.24}$$

Indeed, with the above condition imposed we obtain the following property

$$\begin{aligned}[\alpha_{\lambda\mu} Y_{\lambda\mu} + \alpha_{\lambda-\mu} Y_{\lambda-\mu}]^* &= \underbrace{\alpha^*_{\lambda\mu}(-1)^\mu}_{\alpha_{\lambda-\mu}} Y_{\lambda-\mu} + \underbrace{\alpha^*_{\lambda-\mu}(-1)^\mu}_{\alpha_{\lambda\mu}} Y_{\lambda\mu} \\ &= \alpha_{\lambda-\mu} Y_{\lambda-\mu} + \alpha_{\lambda\mu} Y_{\lambda\mu} \leftrightarrow \text{real}.\end{aligned} \tag{2.3.25}$$

Consequently, the symmetry condition for the deformation parameters in eq. (2.3.24) is required, so that the nuclear surfaces satisfy eq. (2.3.22) and remain real functions for an arbitrary expansion in terms of spherical harmonics. It follows that such surfaces must be – what we call – y-simplex symmetric, as discussed in the following sections.

2.3.4 Nuclear Surface as a Scalar

Consider a reference frame Σ and new reference frame Σ', which is obtained from the original one through a rotation, conveniently expressed with the Euler angles. We assume that the nuclear surface is in addition a scalar and invariant under the rotation operations. This implies that the contributions of the individual spherical harmonics remain the same or in the same proportions in the reference frame Σ' as well:

$$\Sigma \ni R(\theta,\varphi) = R'(\theta',\varphi') \in \Sigma'. \tag{2.3.26}$$

This is equivalent to the following expression

$$\Sigma \ni \sum_{\lambda\mu} \alpha^*_{\lambda,\mu} Y_{\lambda,\mu} = \sum_{\lambda\mu} \alpha'^*_{\lambda,\mu} Y'_{\lambda,\mu} \in \Sigma'. \tag{2.3.27}$$

The above condition can be presented with the help of the Clebsch-Gordan coupling coefficients.

According to eq. (2.3.24), we have

$$\begin{aligned}\sum_{\mu}\alpha^{*}_{\lambda\mu}Y_{\lambda\mu} &= \sum_{\mu}(-1)^{\mu}\alpha_{\lambda-\mu}Y_{\lambda\mu}\\ &= (-1)^{\lambda}\sqrt{2\lambda+1}\sum_{\mu}\underbrace{\frac{(-1)^{\lambda-\mu}}{\sqrt{2\lambda+1}}}_{C(\lambda,-\mu;\lambda,\mu|00)}\alpha_{\lambda-\mu}Y_{\lambda\mu}\\ &= (-1)^{\lambda}\sqrt{2\lambda+1}\sum_{\mu\mu'}C(\lambda,\mu;\lambda,\mu'|00)\alpha_{\lambda\mu'}Y_{\lambda\mu}. \end{aligned} \tag{2.3.28}$$

It is known that the Clebsch-Gordan coefficients, $C(j_1, m_1; j_2, m_2|J = 0, M = 0)$, in the particular case of coupling of two spherical tensors with rank λ give a scalar. Therefore the expression in eq. (2.3.28) is indeed a scalar.

2.4 Phenomenological Mean-Field Potentials

The spatial distribution of the nuclear matter can be studied experimentally via e.g., nucleon-nucleon scattering experiments. Experiments show that, in the central zone, the nuclear density is approximately a flat function of the distance from the nuclear centre and falls quickly (exponentially) to zero when the distance increases further. It is this rapid decrease and fast vanishing of the nuclear density, which allows introducing the notion of the nuclear surface, which otherwise would not be justified.

2.4.1 Woods-Saxon Central Potential

One of the most successful phenomenological parameterisations of the nuclear mean-field is obtained with the help of the Woods-Saxon potential. It is negative (attractive) and has a flat bottom but increases fast when approaching the nuclear surface. In the case of spherical symmetry, the Woods-Saxon potential has the form

$$\hat{V}_{\rm WS}(r; V_{\rm c}, r_{\rm c}, a_{\rm c}) = \frac{V_0}{1+\exp[(r-R_{\rm c})/a_{\rm c}]}, \tag{2.4.1}$$

where $R_{\rm c} = r_{\rm c}\,A^{1/3}$, $V_{\rm c}$ and $a_{\rm c}$ are called radius, depth and diffuseness parameters, respectively, and their values can be adjusted to the experimental results. The typical values are: $r_{\rm c} \approx 1.2$ fm, $V_{\rm c} \approx -50$ MeV and $a_{\rm c} \approx 0.7$ fm, respectively. The difference $(r - R_{\rm c})$ is in fact the distance of the point-particle from the nuclear spherical surface. It is often convenient to express the potential depth parameter $V_{\rm c}$ as isospin dependent

$$V_{\rm c} = V_0[1 \pm \kappa(N-Z)/(N+Z)], \tag{2.4.2}$$

where the plus-sign holds for the protons and the minus sign for the neutrons.

Experimental results show that among more than three thousands nuclei only eight are strictly-speaking spherical; these are

$$^{16}_{8}\mathrm{O}_{8},\ ^{40}_{20}\mathrm{Ca}_{20},\ ^{48}_{20}\mathrm{Ca}_{28},\ ^{56}_{28}\mathrm{Ni}_{28},\ ^{90}_{40}\mathrm{Zr}_{50},\ ^{132}_{50}\mathrm{Sn}_{82},\ ^{146}_{64}\mathrm{Gd}_{82},\ ^{208}_{82}\mathrm{Pb}_{126}\ .$$

This implies that in general the nuclear surface is deformed (not spherical). For deformed nuclei, the generalised distance function, $\mathrm{dist}_{\Sigma}(\vec{r}\,)$, is used to represent the distance of a point-particle from an arbitrary deformed surface, where $\vec{r}$ is a position vector of the point particle in space. Consequently the deformed central potential can be written down as

$$\boxed{\hat{V}_{\mathrm{WS}}(\vec{r};V_{\mathrm{c}},r_{\mathrm{c}},a_{\mathrm{c}}) = \frac{V_{\mathrm{c}}}{1+\exp[\mathrm{dist}_{\Sigma}(\vec{r};r_{\mathrm{c}})/a_{\mathrm{c}}\,]}.} \tag{2.4.3}$$

2.4.2 Spin-Orbit Potential

To describe the presence/properties of the intruder orbitals, the central potential must be supplemented with the spin-orbit potential, whose Woods-Saxon form reads:

$$\hat{V}^{SO}_{\mathrm{WS}}(\vec{r};\lambda_{\mathrm{so}},r_{\mathrm{so}},a_{\mathrm{so}}) = -[\vec{\nabla}V_{\mathrm{so}}\wedge\hat{p}\,]\cdot\hat{s}, \tag{2.4.4}$$

with the spin operator $\hat{s}=\frac{1}{2}\hat{\sigma}$, whereas V_{so} by definition satisfies

$$\boxed{V_{\mathrm{so}} = \frac{\lambda_{\mathrm{so}}}{1+\exp[\mathrm{dist}_{\Sigma}(\vec{r},r_{\mathrm{so}})/a_{\mathrm{so}}]},} \tag{2.4.5}$$

where r_{so}, a_{so} and λ_{so} are called spin-orbit radius, spin-orbit diffuseness and spin-orbit strength parameters, respectively. These parameters are adjusted separately for protons and neutrons.

2.4.3 Parameters of the W-S Potentials: Traditional Approach

There are 12 adjustable Woods-Saxon parameters in the potentials introduced above, six for the neutrons and six for the protons:

1. Central potential depth-parameter, V_{c};
2. Central potential radius-parameter, r_{c};
3. Central potential diffuseness-parameter, a_{c};
4. Spin-orbit potential strength-parameter, λ_{so};
5. Spin-orbit potential radius-parameter, r_{so};
6. Spin-orbit potential diffuseness-parameter, a_{so}.

By analysing the properties of the single particle Woods-Saxon potential many authors assume that the diffuseness parameters for both neutrons and protons are equal. In the early literature, realistic sets of parameters were proposed by Blomqvist and Wahlborn[8], Chepurnov[9] and Rost[10]. All of them were obtained by fitting parameters to the contemporarily existing experimental data on spherical nuclei.

In order to find the optimal parametrisation of the Woods-Saxon potential, the systematics of the experimental data was taken into account simultaneously on both spherical and deformed odd-mass nuclei in ref. [11]. The considered optimal parametrisation, which is called "universal", can describe not only the single-particle level sequences but also the equilibrium deformations, cf. ref. [12]. The "universal" parametrisation is often used to describe exotic nuclei.

2.4.4 Deformed Potential and Distance Function $\mathrm{dist}_\Sigma(\vec{r}; r_c)$

In order to define the potential, we need to calculate the distance of an arbitrary point particle between its position $P(x, y, z)$ and the surface. In this section we discuss definition of the distance function, $\mathrm{dist}_\Sigma(\vec{r}; r_c)$.

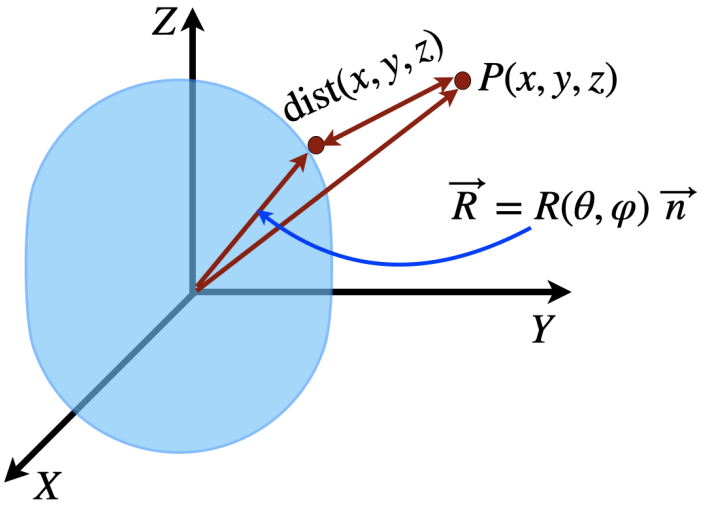

Figure 2.4.1 – *Schematic illustration of the distance function* $dist_\Sigma(x, y, z)$ *between the nuclear surface* $\vec{R}$ *and a given nucleon position* $P(x, y, z)$.

We begin by introducing an auxiliary vector $\vec{d}$:

$$\vec{d} = \vec{r} - \vec{R} \;\leftrightarrow\; \vec{R}(\theta, \varphi) = R(\theta, \varphi)\vec{n}, \tag{2.4.6}$$

where $\vec{n} = \{\cos\varphi \sin\theta, \sin\varphi \sin\theta, \cos\theta\}$, and where $\theta \in [0, \pi]$ and $\varphi \in [0, 2\pi]$. Next, let us introduce an auxiliary function f related to vector $\vec{d}$ as follows

$$f(\theta, \varphi) = [\vec{r} - R(\theta, \varphi)\vec{n}]^2. \tag{2.4.7}$$

2.4.4 Deformed Potential and Distance Function $\mathbf{dist_\Sigma(\vec{r}; r_c)}$

One method of calculating the distance function is to minimise the auxiliary function $f(\theta, \varphi)$ over θ and φ, respectively:

$$\mathrm{dist}_\Sigma(\vec{r}) = \min_{\{\theta,\varphi\}} f(\theta, \varphi). \tag{2.4.8}$$

The problem can be solved by finding the solutions for the system with two nonlinear equations

$$\frac{\partial f(\theta,\varphi)}{\partial \theta} = 0 \quad \text{and} \quad \frac{\partial f(\theta,\varphi)}{\partial \varphi} = 0. \tag{2.4.9}$$

In order to solve the above system of equations we use the Newton method for which we need to calculate the partial derivatives of $f(\theta, \varphi)$:

$$f(\theta,\varphi) = r^2 + R^2(\theta,\varphi) - 2R(\theta,\varphi)\underbrace{[\vec{r}\cdot\vec{n}]}_{N(\theta,\varphi)}, \tag{2.4.10}$$

in which

$$N(\theta,\varphi) = x\sin\theta\cos\varphi + y\sin\theta\sin\varphi + z\cos\theta. \tag{2.4.11}$$

The partial derivatives with respects to θ and φ, N_θ and N_φ, can be obtained as follows

$$\left.\begin{aligned} N_\theta &= \;\; x\cos\theta\cos\varphi + y\cos\theta\sin\varphi - z\sin\theta \\ N_\varphi &= -x\sin\theta\cos\varphi + y\sin\theta\sin\varphi \end{aligned}\right\}, \tag{2.4.12}$$

wherefrom the second order partial derivatives are:

$$\left.\begin{aligned} N_{\theta\theta} &= -x\sin\theta\cos\varphi - y\sin\theta\sin\varphi - z\sin\theta \\ N_{\theta\varphi} &= -x\cos\theta\sin\varphi + y\cos\theta\cos\varphi \\ N_{\varphi\varphi} &= -x\sin\theta\sin\varphi - y\sin\theta\sin\varphi \end{aligned}\right\}. \tag{2.4.13}$$

In order to proceed, we will rewrite eq. (2.4.10) as

$$f(\theta,\varphi) = r^2 + R(\theta,\varphi)[R(\theta,\varphi) - 2N(\theta,\varphi)]. \tag{2.4.14}$$

Based on the above expression, the partial derivatives of $f(\theta, \varphi)$ with respect to θ and φ are:

$$\left.\begin{aligned} f_\theta &= R_\theta[R - 2N] + R[R_\theta - 2N_\theta] \\ f_\varphi &= R_\varphi[R - 2N] + R[R_\varphi - 2N_\varphi] \end{aligned}\right\}, \tag{2.4.15}$$

and the second derivatives are

$$\left.\begin{aligned} f_{\theta\theta} &= R_{\theta\theta}\,[R - 2N] + 2R_\theta[R_\theta - 2N_\theta] + R[R_{\theta\theta} - 2N_{\theta\theta}] \\ f_{\varphi\varphi} &= R_{\varphi\varphi}[R - 2N] + 2R_\varphi[R_\varphi - 2N_\varphi] + R[R_{\varphi\varphi} - 2N_{\varphi\varphi}] \\ f_{\theta\varphi} &= R_{\theta\varphi}[R - 2N] + R_\theta[R_\varphi - 2N_\varphi] + R_\varphi[R_\theta - 2N_\theta] + R[R_{\theta\varphi} - 2N_{\theta\varphi}] \end{aligned}\right\}. \tag{2.4.16}$$

Thus for each point $\vec{r}$ in space needed, e.g., when calculating the matrix elements of the potential, we must calculate the corresponding $\{\theta, \varphi\}$ angles, wherefrom we determine the sought distance.

2.4.5 Constant-Volume Condition

The nuclear volume is considered constant and independent of the actual geometrical form of the nucleus. We assume that the volume of a deformed nucleus is the same as the one of the corresponding spherical one,

$$\frac{4\pi}{3}R_0^3 = \underbrace{\int\int\int}_{\text{Deformed nucleus}} dx\,dy\,dz = V_{\text{def.}}. \tag{2.4.17}$$

It can conveniently be expressed with the help of spherical coordinates:

$$V_{\text{def.}} = \int_0^{\pi}\sin\theta d\theta\int_0^{2\pi}d\varphi\int_0^{R(\theta,\varphi)}r^2dr \equiv \frac{1}{3}\int_0^{\pi}\sin\theta d\theta\int_0^{2\pi}d\varphi R^3(\theta,\varphi). \tag{2.4.18}$$

Let us define an auxiliary function:

$$g(\theta,\varphi) = 1+\sum_{\lambda}\sum_{\mu=-\lambda}^{\lambda}\alpha_{\lambda,\mu}Y_{\lambda,\mu}(\theta,\varphi), \tag{2.4.19}$$

with the help of which we can rewrite the nuclear surface equation in eq. (2.3.1) as

$$R(\theta,\varphi) = c(\{\alpha\})R_0\,g(\theta,\varphi). \tag{2.4.20}$$

According to the volume conservation condition we have:

$$\begin{aligned}\frac{4\pi}{3}R_0^3 &= \frac{1}{3}\int_0^{\pi}\sin\theta d\theta\int_0^{2\pi}d\varphi R^3(\theta,\varphi)\\ &= \frac{1}{3}\int_0^{\pi}\sin\theta d\theta\int_0^{2\pi}d\varphi\,c(\{\alpha\})^3\,R_0^3\,g(\theta,\varphi)^3.\end{aligned} \tag{2.4.21}$$

Consequently the expression for the constant volume condition takes the form

$$\boxed{c(\{\alpha\}) = \left[\frac{4\pi}{\int_0^{2\pi}d\varphi\int_0^{\pi}g^3(\theta,\varphi)\sin\theta d\theta}\right]^{1/3},} \tag{2.4.22}$$

which is recalculated numerically each time a new nuclear deformation is examined.

2.4.6 Center of Mass Problem

In the case of a spherical shape it is clear that the position of the center of mass coincides with the geometrical center of the body. However, for deformed nuclei, it can be demonstrated that in general the centre of mass position varies with deformation for λ-odd. Therefore it is necessary to discuss the problem of the possible unphysical shifts of the central mass.

Let us begin with the usual definition of the centre mass of a system of n material points,

$$\vec{R}_{cm} \equiv \frac{\sum_i m_i\vec{r}_i}{\sum_i m_i}; \qquad \sum_{i=1}^{n}m_i \equiv M, \tag{2.4.23}$$

where the summations extends over the total number of protons and neutrons n. Denoting the total mass of the system by M we can generalise the above expression for the continuous mass distributions,

$$\boxed{\vec{R}_{cm} \equiv \frac{1}{M}\int d^3\vec{r}\rho(\vec{r})\vec{r}, \quad \text{where} \quad \int d^3\vec{r}\rho(\vec{r}) = M.} \tag{2.4.24}$$

• **Case of Axial Symmetry.** We begin with the simplified case of a shape axially symmetric with respect to $\mathcal{O}_z$-axis. The corresponding third component of the centre mass vector can be calculated as follows,

$$\begin{aligned} z_{cm} &= \frac{1}{M}\int_0^{2\pi} d\varphi \int_0^{\pi} \sin\theta d\theta \int_0^{R(\theta,\varphi)} r^2\, z\rho(\vec{r}) dr \\ &= \frac{\rho_0}{M}\int_0^{2\pi} d\varphi \int_0^{\pi} \sin\theta d\theta \int_0^{R(\theta,\varphi)} r^3 \cos\theta\, dr, \end{aligned} \tag{2.4.25}$$

and it follows that

$$z_{cm} = \frac{\rho_0}{4M}\int_0^{2\pi} d\varphi \int_0^{\pi} \sin\theta\cos\theta R^4(\theta,\varphi) d\theta. \tag{2.4.26}$$

If for simplicity we consider a system with uniform mass distribution, the density satisfies

$$\rho_0 = \frac{M}{\frac{4}{3}\pi R_0^3}. \tag{2.4.27}$$

With the help of the above expression and eq. (2.4.20) we may transform eq. (2.4.26) as follows

$$\boxed{z_{cm} = \frac{3R_0}{16\pi}\cdot[c(\{\alpha\})]^4 \int_0^{2\pi} d\varphi \int_0^{\pi} \sin\theta\cos\theta f^4(\theta,\varphi) d\theta.} \tag{2.4.28}$$

• **Two-Component Systems.** Consider a two-component system composed of protons and neutrons. The centre of mass of the two-component system satisfies

$$\boxed{\bar{z}_{cm} \equiv z^{\pi}_{cm} + z^{\nu}_{cm}; \quad \bar{M} \equiv M_{\pi} + M_{\nu},} \tag{2.4.29}$$

where

$$z^{\pi}_{cm} = \frac{\rho^{\pi}_0}{4\bar{M}}\int_0^{2\pi} d\varphi \int_0^{\pi} \sin\theta\cos\theta R^4(\theta,\varphi) d\theta, \tag{2.4.30}$$

and

$$z^{\nu}_{cm} = \frac{\rho^{\nu}_0}{4\bar{M}}\int_0^{2\pi} d\varphi \int_0^{\pi} \sin\theta\cos\theta R^4(\theta,\varphi) d\theta. \tag{2.4.31}$$

Consider the same deformations for protons and neutrons, $\alpha^{\pi}_{\lambda,\mu} = \alpha^{\nu}_{\lambda,\mu}$. It follows that the integral expressions in eqs. (2.4.30) and (2.4.31) are identical. Consequently, we find

$$\bar{z}_{cm} = \frac{\rho^{\pi}_0[R^{\pi}_0]^4 + \rho^{\nu}_0[R^{\nu}_0]^4}{4\bar{M}}\cdot[c(\{\alpha\})]^4 \int_0^{2\pi} d\varphi \int_0^{\pi} \sin\theta\cos\theta f^4(\theta,\varphi) d\theta. \tag{2.4.32}$$

• **Case of Non-Axial Symmetries.** In the case of a non axial symmetry system, with the help of expressions for $x = r\sin\theta\cos\varphi$ and $y = r\sin\theta\sin\varphi$, we can calculate the center of mass positions for the remaining two coordinates,

$$\begin{aligned} x_{cm} &= \frac{1}{M}\int_0^{2\pi} d\varphi \int_0^{\pi} \sin\theta d\theta \int_0^{R(\theta,\varphi)} r^2\, x dr \rho(\vec{r}) \\ &= \frac{\rho_0}{4M}\int_0^{2\pi}\int_0^{\pi} \sin\theta\cos\varphi R^4(\theta,\varphi) d\theta d\varphi \\ &= \frac{\rho_0 R_0^4}{4M}\cdot[c(\{\alpha\})]^4 \int_{4\pi} d\Omega \sin\theta\cos\varphi f^4(\theta,\varphi), \end{aligned} \tag{2.4.33}$$

and similarly

$$\begin{aligned} y_{cm} &= \frac{1}{M}\int_0^{2\pi} d\varphi \int_0^{\pi} \sin\theta d\theta \int_0^{R(\theta,\varphi)} r^2\, y dr \rho(\vec{r}) \\ &= \frac{\rho_0}{4M}\int_0^{2\pi}\int_0^{\pi} \sin\theta\sin\varphi R^4(\theta,\varphi) d\theta\, d\varphi \\ &= \frac{\rho_0 R_0^4}{4M}\cdot[c(\{\alpha\})]^4 \int_{4\pi} d\Omega \sin\theta\sin\varphi f^4(\theta,\varphi). \end{aligned} \tag{2.4.34}$$

Consequently, for the two-component systems, the coordinates of the centre of mass vector can be calculated as follows

$$\bar{x}_{cm} = \frac{\rho_0^{\pi}[R_0^{\pi}]^4 + \rho_0^{\nu}[R_0^{\nu}]^4}{4\bar{M}}\cdot[c(\{\alpha\})]^4 \int_0^{4\pi} d\Omega \sin\theta\cos\varphi f^4(\theta,\varphi) d\theta, \tag{2.4.35}$$

$$\bar{y}_{cm} = \frac{\rho_0^{\pi}[R_0^{\pi}]^4 + \rho_0^{\nu}[R_0^{\nu}]^4}{4\bar{M}}\cdot[c(\{\alpha\})]^4 \int_0^{4\pi} d\Omega \sin\theta\sin\varphi f^4(\theta,\varphi) d\theta, \tag{2.4.36}$$

and

$$\bar{z}_{cm} = \frac{\rho_0^{\pi}[R_0^{\pi}]^4 + \rho_0^{\nu}[R_0^{\nu}]^4}{4\bar{M}}\cdot[c(\{\alpha\})]^4 \int_0^{4\pi} d\Omega \cos\theta f^4(\theta,\varphi) d\theta. \tag{2.4.37}$$

In general, the calculated coordinates of the centre of mass vanish if the deformation considered is inversion symmetric. For that reason, if odd-λ deformation parameters $\alpha_{\lambda\nu}$ do not vanish, the centre of mass in general will move out of the original position and, moreover, there will be induced dipole moments when the centres of mass of protons and neutrons do not coincide as it is the case when $Z \neq N$.

On the other hand, the centre of mass of an isolated system remains at rest with respect to a fixed reference frame. This implies that the shifts of the center of mass due to the deformation of the nucleus should be considered unphysical. A traditional way to remove the undesired consequences of the discussed problem is to shift the reference frame in such a way that the origin of the new reference frame coincides with the actual position of the centre of mass.

2.4.7 Odd-λ Case: Extracting Nuclear Dipole Moments

As one of the most important consequences of the centre of mass considerations we find the possibility of determining the mean-field approximation of the nuclear dipole moments, which allows calculating the reduced electric dipole, $E1$, transition probabilities. To extract this quantity we proceed as follows.

To begin with the classical definition, the electric dipole moment can be expressed as

$$\vec{d} \equiv \int_V \vec{r}\rho_\pi(\vec{r})d^3\vec{r}, \tag{2.4.38}$$

in which $\rho_\pi(\vec{r})$ denotes the nuclear charge distribution. Comparing the above expression with the one in eq. (2.4.24) we find that at first glance the definition of centre of mass coincides with the one of the dipole moment. However, the physical meanings of the density distributions are different, $\rho(\vec{r})$ in the former case denotes the mass distribution, whereas the other one represents the charge distribution. This implies that if the centre of mass position vector is non-null, the dipole moment does not vanish either.

Let us consider nuclear electric multipole moments, which by definition can be calculated as (cf. eq. (1A-116) in ref. [13]):

$$Q_{\lambda,\mu} = \int_V \rho(\vec{r})r^\lambda Y_{\lambda\mu}(\vec{r})d^3\vec{r}. \tag{2.4.39}$$

Consequently, the dipole moment, $\lambda = 1$, is given by

$$Q_{1,\mu} = \int_V \rho(\vec{r})r\, Y_{1,\mu}(\vec{r})d^3\vec{r}, \tag{2.4.40}$$

According to the expressions of spherical harmonics in ref. [7], p. 155, eq. (2), we have

$$Y_{1,+1}(\theta,\varphi) = -\tfrac{1}{2}\sqrt{\tfrac{3}{2\pi}}\cdot\tfrac{(x+iy)}{r}, \tag{2.4.41}$$

$$Y_{1,0}(\theta,\varphi) = +\tfrac{1}{2}\sqrt{\tfrac{3}{\pi}}\cdot\tfrac{z}{r}. \tag{2.4.42}$$

$$Y_{1,-1}(\theta,\varphi) = +\tfrac{1}{2}\sqrt{\tfrac{3}{2\pi}}\cdot\tfrac{(x-iy)}{r}. \tag{2.4.43}$$

Using explicit expressions for spherical harmonics with $\lambda = 1$, we obtain the components of the dipole moment $Q_{1,0}$ in the form

$$Q_{1,0} = \int_V \rho(\vec{r})r\, Y_{1,0}(\vec{r})d^3\vec{r} = \sqrt{\frac{3}{4\pi}}\underbrace{\int_V z\,\rho_\pi(\vec{r})d^3\vec{r}}_{d_z} = \sqrt{\frac{3}{4\pi}}\,d_z, \tag{2.4.44}$$

so that

$$d_z = \sqrt{\frac{4\pi}{3}}\,Q_{1,0}. \tag{2.4.45}$$

Similarly we find that

$$Q_{1,+1} = -\sqrt{\frac{3}{8\pi}}\,d_x - i\sqrt{\frac{3}{8\pi}}\,d_y, \tag{2.4.46}$$

$$Q_{1,-1} = +\sqrt{\frac{3}{8\pi}}\, d_x - i\sqrt{\frac{3}{8\pi}}\, d_y, \tag{2.4.47}$$

or, equivalently

$$d_x = \sqrt{\frac{2\pi}{3}}\,(Q_{1,-1} - Q_{1,+1})\,, \tag{2.4.48}$$

and

$$d_y = \sqrt{\frac{2\pi}{3}}\,(Q_{1,-1} + Q_{1,+1})\,. \tag{2.4.49}$$

The results presented above indicate that the relations between the dipole moments Q_1 and the electric dipole moments $\vec{d}$ differ by multiplicative constants. The explicit expressions of the dipole moments also imply that whenever the position of the centre of mass is non-zero, so is the induced dipole moment.

2.5 Model Uncertainties, Parametric Correlations

Due to the fact that contemporary realistic theoretical modelling methods depend on parameters adjusted to the experimental data and the fact that experimental data are uncertain (with uncertainties characterised by error bars) – it follows that the parameters of the modelling are uncertain and should be regarded as probability distributions rather than sets of numbers. It turns out that various uncertainty sources are contributing to the final uncertainties: These are experimental errors, possible parametric correlations, and incompleteness of the theory employed. We discuss these elements in the following sections.

2.5.1 Inverse Problem Theory of Applied Mathematics

In this section we are going to discuss briefly selected conclusions of the Inverse Problem Theory, which is one of the most dynamically developing sub-fields of *Applied Mathematics*.[1] Inverse Problem Theory addresses, among others, the mathematical conditions for the possibly stable, i.e., non-divergent methods of parameter adjustments of mathematical modelling. The importance of the role of the Inverse Problem Theory stems from the fact that a great majority of methods of mathematical modelling, in particular in theoretical physics, depend on parameters. The parameter adjustment issues within mean-field theory nuclear-structure problems and the relation to the inverse-problem theory methods applied in our projects can be found in articles [14, 15], cf. also references therein.

Let $\hat{\mathcal{M}}$ represent an ensemble of concepts and operations defining a physical model of interest, the latter depending on adjustable parameters $\{p_1, p_2, ..., p_n\} = p$. In applied mathematics, the results obtained by acting with $\hat{\mathcal{M}}$ on the set of known, optimised parameters

[1] The domain of the inverse problem theory which is a sub-field of *Applied Mathematics* is served by specialised journals, such as for instance *Inverse Problems* (IOPP), *Journal of Inverse and Ill-Posed Problems* (De Gruyter), or *Inverse Problems in Science and Engineering* (Taylor & Francis).

$p^{\rm opt}$, are comparable with the experimental data, say e. This process is called *solving a direct problem* and we write:

$$\boxed{\hat{\mathcal{M}}\, p^{\rm opt} = e.} \tag{2.5.1}$$

If the parameters of the model are unknown and the inverse $\hat{\mathcal{M}}^{-1}$ exist, finding the optimal parameters by acting with $\hat{\mathcal{M}}^{-1}$ on the data set e is called formally *solving the inverse problem*:

$$\boxed{\hat{\mathcal{M}}^{-1}\, e = p^{\rm opt}.} \tag{2.5.2}$$

The properties of $\hat{\mathcal{M}}^{-1}$ determine the possible instabilities of a model. If the inverse $\hat{\mathcal{M}}^{-1}$ does not exist, we say that the *inverse problem is ill posed*. The solution to the problem by constructing the inverse of the nuclear physics Hamiltonian, $\hat{H}^{-1}$, in order to find the optimal parameters *via* eq. (2.5.2) is not known in realistic cases. Moreover, we do not know about the existence of formal proofs that such an inverse can even in principle be constructed.

The fact that the inverse operator $\hat{\mathcal{M}}^{-1}$ is unknown or does not exist, implies that alternative methods of improving the parameters of the model must be proposed, such as minimisation of the χ^2-test function. An undesired property in the present context consists in the fact that very often after χ^2-minimisation some parameters of the model turn out to be functions of the others. This mechanism is referred to as "parametric correlations". One can show, cf. e.g. ref. [16], that when this happens, the model predictions become generally unstable, better to say: *divergent, often exponentially*. These and related issues will be discussed in some detail.

Inverse Problem Theory Applied within Nuclear Mean-Field Theory. In what follows we give an example of applying the inverse problem approach to the nuclear mean-field theory. Consider the mean-field potential $\hat{V}(p)$, which depends on the set of adjustable parameters $p = \{p_1, p_2, ..., p_n\}$. The Hamiltonian, written somewhat schematically, has the form

$$\hat{H}(p; x) = \hat{T} + \hat{V}(p; x). \tag{2.5.3}$$

Solving the Schrödinger equation:

$$\hat{H}(p; x)\psi_n(x) = e_n^{th}(p)\psi_n(x), \tag{2.5.4}$$

for each given set of parameters allows one to obtain the solutions as functions of the parameters. We can express this dependence by:

$$e_n^{th}(p) = f_n(p), \tag{2.5.5}$$

in which $f_n(p)$ are considered to be some continuous functions. The parameters of mean-field Hamiltonian in eq. (2.5.3) are adjusted with the help of χ^2 tests based on the experimental single-nucleon level energies, in our case the 8 doubly magic spherical nuclei:

$$^{16}_{8}\mathrm{O}_{8},\ ^{40}_{20}\mathrm{Ca}_{20},\ ^{48}_{20}\mathrm{Ca}_{28},\ ^{56}_{28}\mathrm{Ni}_{28},\ ^{90}_{40}\mathrm{Zr}_{50},\ ^{132}_{50}\mathrm{Sn}_{82},\ ^{146}_{64}\mathrm{Gd}_{82},\ ^{208}_{82}\mathrm{Pb}_{126}\ .$$

In order to find the optimal parameters of the Hamiltonian we need to know the experimental data $d^{\mathrm{exp}} = \{d_1^{\mathrm{exp}}, d_2^{\mathrm{exp}}, ..., d_{n_d}^{\mathrm{exp}}\}$. Typically, χ^2-function is defined by

$$\chi^2(p) = \sum_{i=1}^{n_d} w_i [d_i^{\mathrm{exp}} - f_i(p)]^2, \tag{2.5.6}$$

where w_i are physicist-defined objects called weight factors. Since in this project we are using the experimental data on single-nucleon energies in doubly magic spherical nuclei and thus each of the single-particle levels can be characterised by the angular momentum quantum number j_i, the weight factors can be defined to express spherical degeneracy as follows:

$$w_i = (2\,j_i + 1). \tag{2.5.7}$$

The above form of the weight factor is used in the case of one single nucleus, whereas the summation in eq. (2.5.6) extends over all the nuclei of interest at the same time. It then follows that the weight factors in eq. (2.5.7) for certain nuclei will be over-represented by the ones in other nuclei. For instance, the highest j in ^{16}O is $j = 5/2$, whereas the highest j in ^{208}Pb is $j = 13/2$, thus using the weight factor of eq. (2.5.7) we give more importance to ^{208}Pb as compared to ^{16}O. This is not necessarily what we wish, when optimising the Hamiltonian parameters.

The concept of the universal parametrisation implies that the mean-field parameters are fixed once for all nuclei in the mass table. The reproduction quality of the single-nucleon properties for all the nuclei should be comparable without incidentally favouring certain nuclei over the others. To be able to control this mechanism to an extent, we introduce some extra weight factors, $\tilde{w}_k$, as

$$\tilde{w}_k = \frac{208}{A_k} \quad \text{and} \quad k = 1, 2, ..., 8, \tag{2.5.8}$$

where A_k denotes the mass of any given nucleus, say No. k, and the above weight factor implies that $\tilde{w}_k$ introduces a relative mass dependence of considered nuclei with respect to the mass of ^{208}Pb. Thus we obtain the final expression for χ^2 as follows:

$$\chi^2(p) = \frac{\sum_{k=1}^{N} \tilde{w}_k \sum_{i=1}^{n_k} \{(2_{j_i,k} + 1)[d_i^{\mathrm{exp}} - f_i(p)]^2\}}{\sum_{k=1}^{N} \tilde{w}_k}, \tag{2.5.9}$$

where $N = 8$ is the number of all considered spherical nuclei, n_k are the numbers of the experimental energy levels for each nucleus k, d_i^{exp} and $f_i(p)$ represent the experimental and theoretical single nucleon energy levels, respectively, the latter ones obtained as the solutions of the Schrödinger equation with a mean-field Hamiltonian.

2.5.2 Our Realisation of Monte Carlo Simulations: Remarks

As discussed in ref. [15], there exist correlations between parameters of most of the realistic models implying in particular that among optimal parameters resulting from the fit, some

are functions of the others. This applies in particular for the phenomenological mean-field Hamiltonian with the Woods-Saxon potential of interest for our project, that the parameters are in general not independent as they must be in order to provide stable extrapolations of the use of the modelling. We should expect that, following general features derived within the Inverse Problem Theory, the predictions in terms of these parameters are unstable. This implies that, in particular, a small modification of the input parameters of the χ^2-fitting algorithm, for instance, adding one more experimental point, may lead to large variations in both certain 'optimal' parameter values and the predicted observables. To improve the predictive power of the modelling and to increase the stability of the parametrisation, one of the most important steps is to detect the parametric correlations and eliminate them following the well established rules of *applied mathematics*.

In our parameter fitting, the error bars of the experimental single-nucleon energy levels are taken into account. This implies that strictly speaking our input information has the form of the Gaussian probability distributions centred at the experimental energy values with the distribution widths determined by the error bars. The Monte-Carlo approach consists in employing the numerical random-number generating program which, according to the Gaussian distributions just mentioned, provides the experimental input in the form of single-particle energy-level sets – and this a large number of times [typically $N_{\rm MC} \approx (10^5 - 10^6)$ sets in our case]. The fitting algorithm is repeated $N_{\rm MC}$ number of times producing $N_{\rm MC}$ sets of 'optimal parameters' and these results can be used to produce, e.g., the histograms representing the probability distributions of any given value of the parameters of the studied Hamiltonian. Alternatively, we can produce the 2D projections of the occurrence frequency, say $F_{\rm MC}$, in the form of contour plots which can be used to detect parametric correlations – an approach which will be illustrated below.

In what follows we summarise briefly the application of the Monte Carlo simulations to study the leading features/quality of the parameter adjustments in the nuclear structure context, cf. ref. [17].

Selected Details Concerning the Notation. Let us introduce the Gaussian probability distribution representing the experimental data and the related uncertainties as follows,

$$\mathcal{G}(e; e_i^{exp}, \sigma_i) = \frac{1}{\sqrt{2\pi\sigma_i^2}} \exp\left[-(e - e_i^{exp})^2/2\sigma_i^2\right], \tag{2.5.10}$$

in which e denotes a random variable representing single-nucleon energy and σ_i are the Gaussian widths characterising the experimental uncertainties. The symbol e_i^{exp} represents experimental values of the single-particle energies. For convenience we will introduce a simplified notation and rewrite the single-particle energies as 'data' points

$$\{e_i^{\rm exp}\} \to \{d_1, d_2, ..., d_{n_d}\}, \tag{2.5.11}$$

and the set of the corresponding Gaussian widths as:

$$\{\sigma_1, \sigma_2, ..., \sigma_{n_d}\}, \tag{2.5.12}$$

where n_d represents the number of the experimental data points. Next, according to the principles of the Monte-Carlo method, we employ a random number generator to define a large number of 'pseudo-experimental' input data points in terms of the Gaussian distributions in eq. (2.5.10). After generating these data sets we apply the χ^2-minimisation using the definition in eq. (2.5.9) to obtain the sought information in the form of the probability distributions for each studied parameter. More precisely, we generate a big number, say $\mathcal{N}_{MC} \sim 10^5$, of the experimental data sets according to the mentioned Gaussian distributions, perform $\mathcal{N}_{MC}$ times the χ^2 minimisation, and finally we generate $\mathcal{N}_{MC}$ sets n_p-tuplets, of parameters, i.e.:

$$\{p_1, p_2, ..., p_{n_p}\}_j, \quad \text{for} \quad j = 1, 2, ..., \mathcal{N}_{MC}. \tag{2.5.13}$$

The resulting set of $n_p = 12$ Woods-Saxon mean-field potential parameters appears in 2 sub-sets of six parameters each as presented in section (2.4.3), the one for the protons

$$\{V^{\rm c},\, r^{\rm c},\, a^{\rm c};\, V^{\rm so}\, r^{\rm so},\, a^{\rm so}\}_\pi, \tag{2.5.14}$$

and another one for the neutrons

$$\{V^{\rm c},\, r^{\rm c},\, a^{\rm c};\, V^{\rm so},\, r^{\rm so},\, a^{\rm so}\}_\nu. \tag{2.5.15}$$

A straightforward illustration of the results obtained from Monte-Carlo simulation is provided by two-dimensional 'dot-plots', as in fig. (2.5.1), with two parameters $\{p_i, p_j\}_k$ chosen from the $\mathcal{N}_{MC}$ n_p-tuplets, representing the appearance frequency of these two parameters. As mentioned previously, diagrams of this type can be used to detect possible parametric correlations between the parameters, as shown in figures (2.5.1) and (2.5.2), more detailed explanations in ref. [17].

2.5.3 New Parametrisation with No Parametric Correlations

As mentioned earlier, one of the sources of uncertainties in model-parameter adjustments is the possible existence of parametric correlations. This is why we are interested in detecting, as the first step, the possible correlations between any two parameters, say p_i and p_j. One of the simplest ways of detecting the possible (linear) parametric correlations is by determining the so-called Pearson coefficient:

$$r_{ij} = \frac{\sum\limits_{k=1}^{n} (p_{i,k} - \bar{p}_i)(p_{j,k} - \bar{p}_j)}{\sqrt{\sum\limits_{k=1}^{n} (p_{i,k} - \bar{p}_i)^2}\sqrt{\sum\limits_{k=1}^{n} (p_{j,k} - \bar{p}_j)^2}}, \tag{2.5.16}$$

in which p_i and p_j are two random variables, and $\bar{p}_i$ and $\bar{p}_j$ are the corresponding mean values. This kind of test can be applied to any combination of the Woods-Saxon mean-field parameters, e.g., $p_i \leftrightarrow V^{\rm c}_\pi$ and $p_j \leftrightarrow r^{\rm so}_\pi$. The numerical values for the Pearson coefficients lie in the interval $[-1, 1]$, and in particular, $r_{ij} = \pm 1$ implies the existence of a strong linear correlation between these two parameters, while $r_{i,j} = 0$ indicates that these two parameters are uncorrelated.

Figure (2.5.1) presents the results obtained within our Monte-Carlo simulations based on the χ^2 minimisation, and the Pearson coefficient calculated for the two parameters indicated. It shows an approximately linear correlation between the central potential depth $V_0^{\rm c}$ and

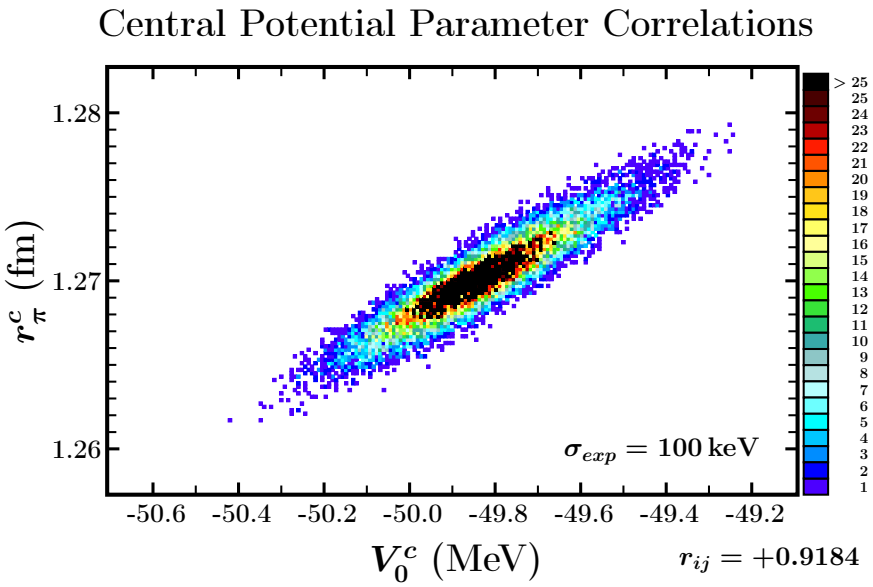

Figure 2.5.1 – *Parametric correlations between the central potential depth $V_0^{\rm c}$ and radius $r_\pi^{\rm c}$ for protons. Pearson coefficient $r_{ij} = 0.9184$ is very close to 1, confirming strong linear correlations between these two parameters visible from the Monte-Carlo 'dot-plot'. Let us emphasise that while the Pearson coefficient can be used to search for the linear correlations, the Monte Carlo 2D plots like the one shown indicate any kind of non-linear and/or multi-valued correlations.*

radius $r_\pi^{\rm c}$ parameters. The corresponding Pearson coefficient is close to 1, which confirms independently the linear correlation between these two parameters seen from the diagram. Similar correlation exists between $V_0^{\rm c}$ and the neutron radius $r_\nu^{\rm c}$. Analogous analysis reveals that there are no correlations between $\{V_0^{\rm c}, a_{\pi,\nu}^{\rm c}\}$ and $\{r_{\pi,\nu}^{\rm c}, a_{\pi,\nu}^{\rm c}\}$. In the past decades, the parameters of the central potential were treated as independent. With the help of the Monte-Carlo simulations we conclude that among the originally introduced three parameters of the central potential – two can be seen as functions of the others.

Figure (2.5.2) shows a similar result for the spin-orbit potential strength $\lambda_0^{\rm so}$ and radius $r_\pi^{\rm so}$ parameters. Note that the distributions in this figure reveal characteristic form of the multi-valued functional relations: the double-valued dependence of the radius parameter $r_\pi^{\rm so}$ as a function of the spin-orbit potential strength $\lambda_0^{\rm so}$. It follows that the Woods-Saxon Hamiltonian leads to two distinct parameterisations. The one with $r_\pi^{\rm so} < 1$ fm is referred to as compact and another one with $r_\pi^{\rm so} > 1$ fm, which can be found in the literature, is called non-compact. From our calculations, we find that the quality of the 'compact' solution is comparable with the quality of the 'non-compact' solution, the former giving slightly better

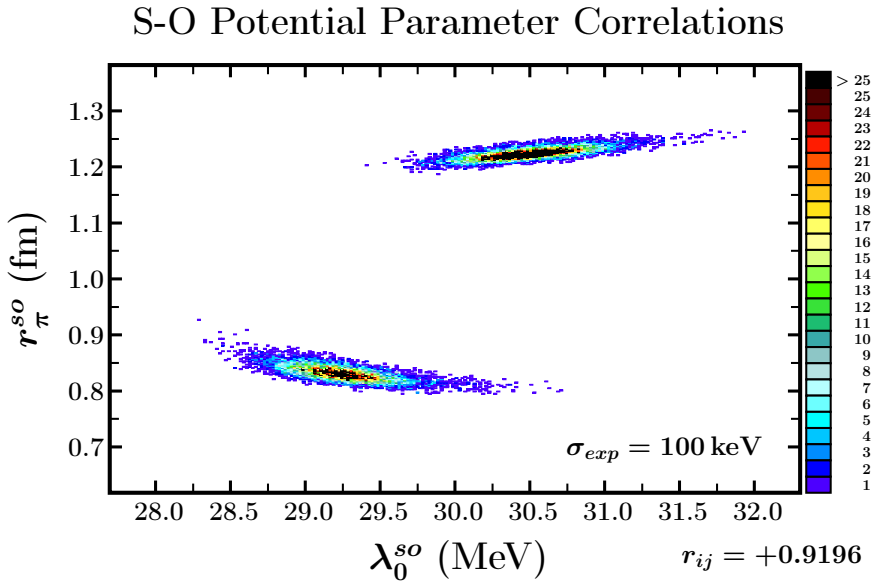

Figure 2.5.2 – *Parametric correlations between the spin-orbit potential strength* $\lambda_0^{\rm so}$ *and radius* $r_\pi^{\rm so}$ *for protons. Two approximately linear dependencies are discovered for these parameters demonstrating a multi-valued pattern.*

description of the rotational properties for many nuclei, refs. [17, 18].

We may conclude that only four parameters among six can be considered independent. We choose the set of parameters $\{V_0^{\rm c}, k^{\rm c}, a_\pi^{\rm c}, a_\nu^{\rm c}\}$ as independent and then the optimal radius $r_{\pi,\nu}^{\rm c}$ value is deduced from the parabolic fit

$$r^c = \alpha (V^c)^2 + \beta V^c + \gamma, \tag{2.5.17}$$

in which the numerical values of the fit coefficients are

$$\text{for protons: } \alpha = 0.003505, \quad \beta = 0.366677 \quad \text{and} \quad \gamma = 10.852558, \tag{2.5.18}$$

and

$$\text{for neutrons: } \alpha = 0.000386, \quad \beta = 0.052687 \quad \text{and} \quad \gamma = 2.935299. \tag{2.5.19}$$

In other words, the parametric correlations shown in Figures (2.5.1) and (2.5.2) indicate that we can reduce the set of originally independent 12 parameters for the protons and neutrons to 8:

$$\{V_0^{\rm c}, k^{\rm c}, a_\pi^{\rm c}, a_\nu^{\rm c}\} \quad \rightarrow \quad \text{for central potential}, \tag{2.5.20}$$

and

$$\{\lambda_0^{\rm so}, k^{\rm so}, a_\pi^{\rm so}, a_\nu^{\rm so}\} \quad \rightarrow \quad \text{for spin} - \text{orbit potential}. \tag{2.5.21}$$

The optimal Woods-Saxon parameters used in our calculations are shown in the following table:

Table 2.5.1 – *Woods-Saxon parameter values fitted to eight doubly magic spherical nuclei. The so-called dependent parameters resulting from the parametric correlations discussed are as follows:* $r_\pi^c = 1.278$ *fm,* $r_\nu^c = 1.265$ *fm,* $r_\pi^{so} = 0.830$ *fm,* $r_\nu^{so} = 0.890$ *fm.*

	V^{c} (MeV)	κ^{c}	$a^{\mathrm{c}}_{\nu,\pi}$ (fm)	λ^{so} (MeV fm$^2/\hbar^2$)	κ^{so}	$a^{\mathrm{so}}_{\nu,\pi}$ (fm)
Protons	-50.225	0.624	0.594	28.998	-0.683	0.700
Neutrons			0.572			0.700

Having briefly summarised the Monte-Carlo approach to the analysis of the parametric correlations resulting from the χ^2-fitting, we change the subject focussing on the standard mean-field potential discrete symmetries.

2.6 Symmetries of the Mean-Field Hamiltonian

Discrete symmetries such as space inversion, time-reversal, signature and simplex, are considered in this project, among others in order to construct the so-called symmetrised (harmonic oscillator) bases used for solving the Schrödinger equation with a mean-field Hamiltonian. In addition to reducing the dimensions of the Hamiltonian matrices, the symmetries help in interpreting the experimental results in particular by allowing one to introduce specific classifications of the nuclear rotational bands, to justify certain hindrance properties and/or allowing one to understand them, etc.

2.6.1 Time-Reversal Symmetry of the Mean-Field

Time-reversal symmetry is one of the most important discrete symmetries in nuclear physics. By definition, time-reversal acts by changing the 'direction' of time, $\hat{T} : t \to t' = -t$. The explicit definition of the time-reversal operator in nuclear physics is given as in, for instance, eq. (1-31) in ref. [13],

$$\hat{T} = i\,\eta\sigma_y\hat{K}, \tag{2.6.1}$$

where $\hat{K}$ stands for the complex-conjugation operator, whereas the phase factor $\eta = \pm 1$ is introduced for convenience and σ_y is the "second" Pauli matrix,

$$\sigma_y = \begin{pmatrix} 0 & -i \\ i & 0 \end{pmatrix}. \tag{2.6.2}$$

• **Time-Dependent vs. Time-Independent Schrödinger Equation.** Let us consider the Schrödinger equation with a hermitian Hamiltonian, $\hat{H}$:

$$i\hbar\frac{\partial\psi_n}{\partial t} = \hat{H}\psi_n. \tag{2.6.3}$$

For each solution ψ_n, a related time reversed solution is obtained as $\bar{\psi}_n = \hat{T}\psi_n$. For the Hamiltonians which do not explicitly depend on time, the case considered here, we find

$$\hat{T}\hat{H}\hat{T}^{-1} = \hat{H} \quad \leftrightarrow \quad [\hat{H},\hat{T}] = 0. \tag{2.6.4}$$

Using the above commutation relation we have

$$\underbrace{\hat{T}(i\hbar\frac{\partial\psi_n}{\partial t})\hat{T}^{-1}}_{i\hbar\frac{\partial}{\partial(-t)}}\underbrace{(\hat{T}\psi_n)}_{\bar{\psi}_n} = \underbrace{\hat{T}\hat{H}\hat{T}^{-1}}_{\hat{H}}\underbrace{(\hat{T}\psi_n)}_{\bar{\psi}_n} \quad \leftrightarrow \quad i\hbar\frac{\partial\bar{\psi}_n}{\partial t'} = \hat{H}\bar{\psi}_n, \tag{2.6.5}$$

with $t' = -t$. We observe that for a given $\psi = \psi(t)$, the solution $\psi(t)$ and its time-reversed image $\bar{\psi}(t) = \psi(-t)$ can be interpreted as a pair of states with opposite time evolutions.

• **Time-Independent Schrödinger Equation and Double (Kramers) Degeneracy.** Let us consider a stationary form of the Schrödinger equation with time independent Hamiltonian. Its solutions satisfy:

$$\hat{H}\Psi_n(\vec{r},t) = E_n\Psi_n(\vec{r},t), \qquad \Psi_n(\vec{r},t) = \psi_n(\vec{r})e^{-iE_nt/\hbar}. \tag{2.6.6}$$

The corresponding time-reversal images are

$$\hat{H}\bar{\Psi}_n(\vec{r},t) = E_n\bar{\Psi}_n(\vec{r},t), \qquad \bar{\Psi}_n(\vec{r},t) = \bar{\psi}_n(\vec{r})e^{+iE_nt/\hbar}. \tag{2.6.7}$$

In general, the nucleonic wave functions are composed of space-, and spin-parts,

$$\psi_n(\vec{r},\vec{s}) = \psi_n(\vec{r})\chi_{m_s}, \tag{2.6.8}$$

with the standard representations for the spin wave functions,

$$\chi_{m_s=\frac{1}{2}} = \begin{pmatrix}1\\0\end{pmatrix}, \qquad \chi_{m_s=-\frac{1}{2}} = \begin{pmatrix}0\\1\end{pmatrix}. \tag{2.6.9}$$

Acting with the time-reversal operator, eq. (2.6.1), on the above representations (consider the convention $\eta = 1$) we find

$$\hat{T}\chi_{m_s=\frac{1}{2}} = i\sigma_yK\begin{pmatrix}1\\0\end{pmatrix} = i\begin{pmatrix}0&-i\\i&0\end{pmatrix}\begin{pmatrix}1\\0\end{pmatrix} = -\begin{pmatrix}0\\1\end{pmatrix} = -\chi_{m_s=-\frac{1}{2}}, \tag{2.6.10}$$

and

$$\hat{T}\chi_{m_s=-\frac{1}{2}} = i\sigma_yK\begin{pmatrix}0\\1\end{pmatrix} = i\begin{pmatrix}0&-i\\i&0\end{pmatrix}\begin{pmatrix}0\\1\end{pmatrix} = +\begin{pmatrix}1\\0\end{pmatrix} = +\chi_{m_s=\frac{1}{2}}. \tag{2.6.11}$$

We rewrite eq. (2.6.10) and eq. (2.6.11) in the general form,

$$\hat{T}\chi_{m_s} = (-1)^{s+m_s}\chi_{-m_s}. \tag{2.6.12}$$

Consequently, the time reversed image of a single-nucleon solution satisfies:

$$\hat{T}[\psi_n(\vec{r})e^{-iE_nt/\hbar}] = \hat{T}[\psi_n(\vec{r})\chi_{m_s}e^{-iE_nt/\hbar}] = (-1)^{s+m_s}\psi_n^*(\vec{r})\chi_{-m_s}e^{+iE_nt/\hbar}. \tag{2.6.13}$$

We arrive at the Kramers degeneracy relations:

> *It follows that $\psi_n(\vec{r})\chi_{m_s}$ and $\psi_n^*(\vec{r})\chi_{-m_s}$ satisfy the Schrödinger equation with the common energy E_n; this degeneracy originating from time-reversal invariance of the Hamiltonian is called Kramers degeneracy.*

Discussion. Suppose for a moment that the time-reversal image of a given wave-function satisfies a direct proportionality to the original wave-function with the proportionality constant c:

$$\bar{\psi}_n = \hat{T}\psi_n = c\psi_n, \tag{2.6.14}$$

Since the twice time-reversed state $\bar{\bar{\psi}}_n$ and ψ_n must represent the same physical state, we find

$$\hat{T}^2\psi_n = \hat{T}(\hat{T}\psi_n) = (c^*c)\,\psi_n = |c|^2\psi_n. \tag{2.6.15}$$

Recall the form of the time-reversal operator, eq. (2.6.1), for a fermion. We have

$$\hat{T}^2 = (i\,\eta\sigma_y\hat{K})^2 = (i\,\eta\sigma_y\hat{K})(i\,\eta\sigma_y\hat{K}) \tag{2.6.16}$$

and since $i^2 = -1$, $\eta^2 = 1$, $\sigma_y^2 = 1$ and $\hat{K}^2 = 1$, it follows that $\hat{T}^2 = -1$. Thus relation (2.6.15) is not satisfied for a Fermion system. This implies that for the fermion wave function $\bar{\psi}_n$ must not be proportional to ψ_n – wherefrom the conclusion that a given fermion wave function and its time-reversed image are linearly independent.

Indeed, according to eqs. (2.6.10) and (2.6.11) we find

$$\langle\bar{\Psi}_n|\Psi_n\rangle = \langle\psi_n|\bar{\psi}_n\rangle^*(-1)^{s+m_s}\langle\chi_{m_s}|\chi_{-m_s}\rangle = 0, \tag{2.6.17}$$

and consequently, $|\psi_n\rangle$ and $\hat{T}|\psi_n\rangle$ must be orthogonal

$$\langle\bar{\Psi}_n|\Psi_n\rangle = 0. \tag{2.6.18}$$

This confirms that $\bar{\psi}_n$ and ψ_n are linearly independent, and thus the basis used must contain both types of wave functions.

2.6.2 Signature Symmetry of the Mean-Field

Another important discrete symmetry in nuclear mean-field theory is the so-called signature, cf. eq. (4-23) in ref. [13] defined in terms of rotation through π about one of the three axes $\mathcal{O}_x$, $\mathcal{O}_y$ or $\mathcal{O}_z$. It is very important, among others, in classification of the nuclear rotational spectra and expressing the related hindrance properties. The signature or the so called y-signature operator, ref. [13], is defined by:

$$\hat{\mathcal{R}}_y(\pi) = e^{i\,\pi\,\hat{J}_y}, \tag{2.6.19}$$

where the nucleon angular momentum operator $\hat{j}_y = \hat{\ell}_y + \hat{s}_y$. It implies rotation through the angle of π around $\mathcal{O}_y$ axis simultaneously in the spatial and spin representations. It follows that

$$\hat{\mathcal{R}}_y(\pi) = e^{i\,\pi\,\hat{j}_y} = e^{i\,\pi\,(\hat{\ell}_y+\hat{s}_y)} = e^{i\,\pi\,\hat{\ell}_y}\cdot e^{i\,\pi\,\hat{s}_y}, \tag{2.6.20}$$

since the orbital angular momentum term, $\hat{\ell}_y$, and the intrinsic-spin term, $\hat{s}_y$, commute. With the help of the auxiliary identity satisfied by spin operator, we find

$$e^{i\,\pi\,\hat{s}_y} = e^{i\,\pi\,\frac{1}{2}\,\sigma_y} = e^{i\,\frac{\pi}{2}\,\sigma_y} = \cos(\pi/2) + i\,\sin(\pi/2)\sigma_y = i\,\sigma_y, \tag{2.6.21}$$

wherefrom we can rewrite eq. (2.6.20) as

$$\hat{\mathcal{R}}_y(\pi) = e^{i\,\pi\,\hat{\ell}_y}\cdot e^{i\,\pi\,\hat{s}_y} = \hat{R}_y(\pi)(i\sigma_y) = i\sigma_y\hat{R}_y. \tag{2.6.22}$$

Observe the difference in notation between $\hat{\mathcal{R}}_y(\pi)$ and $\hat{R}_y(\pi)$, according to which $\hat{R}_y(\pi)$ is the operator of rotation through π about $\mathcal{O}_y$ axis in Cartesian space implying $\{x, y, z\} \to \{-x, y, -z\}$.

Consider a nuclear system with N nucleons. The y-component of the total angular momentum operator, $\hat{J}_y^{(N)} = \sum_{n=1}^{N}\hat{j}_y^{(n)}$. Thus the total signature of the system can be obtained as follows:

$$\hat{\mathcal{R}}_y^{(N)}(\pi) = e^{i\,\pi\,\hat{J}_y} = e^{i\,\pi\,\sum_{n=1}^{N}\hat{j}_y^{(n)}} = \prod_{n=1}^{N} e^{i\,\pi\,\hat{j}_y^{(n)}}. \tag{2.6.23}$$

According to the definition of the signature operator in eq. (2.6.19), applying this operator twice is equivalent to a rotation of the system by 2π. One can demonstrate that applying any rotation of 2π to the system composed of even number of fermions (bosons) leaves the wave function invariant, whereas for the system composed of an odd number of fermions the sign of wave-function changes, cf. ref. [19]. Thus we arrive at the following expression:

$$[\hat{\mathcal{R}}_y^{(N)}(\pi)]^2 = (-1)^N. \tag{2.6.24}$$

Denote eigenvalues of the nucleon signature operator for an even number of Fermions by r,

$$\hat{R}_y|\Psi_n\rangle = r\,|\Psi_n\rangle, \tag{2.6.25}$$

so that

$$r = \pm 1. \tag{2.6.26}$$

One shows, cf. eq. (4-14), in ref. [13], that the total angular momentum of a rotational state, I, for the signature conserving systems satisfies

$$r = (-1)^I. \tag{2.6.27}$$

It follows that the rotation spectra can be classified in terms of signature quantum numbers as shown below:

1. For an even number of nucleons

$$r = +1 \quad \text{and} \quad \mathrm{I} = 0, 2, 4, ... \tag{2.6.28}$$

$$r = -1 \quad \text{and} \quad \mathrm{I} = 1, 3, 5, ... \tag{2.6.29}$$

2. For an odd number of nucleons

$$r = -i \quad \text{and} \quad \mathrm{I} = \tfrac{1}{2}, \tfrac{5}{2}, \tfrac{9}{2}, ... \tag{2.6.30}$$

$$r = +i \quad \text{and} \quad \mathrm{I} = \tfrac{3}{2}, \tfrac{7}{2}, \tfrac{11}{2}, ... \tag{2.6.31}$$

2.6.3 Space Inversion Symmetry of the Mean-Field

Space inversion is defined as a simultaneous inversion of the three axes of the reference frame in a Cartesian 3D space:

$$\hat{\mathcal{I}} : \{x, y, z\} \quad \rightarrow \quad \{-x, -y, -z\}, \tag{2.6.32}$$

where $\hat{\mathcal{I}}$ is the inversion, also called parity operator. Applying parity operator twice we find

$$\{x, y, z\} \ \stackrel{\hat{\mathcal{I}}}{\rightarrow} \ \{-x, -y, -z\} \ \stackrel{\hat{\mathcal{I}}}{\rightarrow} \ \{x, y, z\}, \tag{2.6.33}$$

wherefrom

$$\hat{\mathcal{I}}^2 = 1, \tag{2.6.34}$$

and it follows that the eigenvalues of parity operator $\hat{\mathcal{I}}$ are $\pi = \pm 1$, π referred to as parity. States with $\pi = +1$ are referred to as of positive parity, while the ones with $\pi = -1$ as of negative parity. One can demonstrate that nuclear interactions conserve parity and thus parity operator commutes with the nuclear many-body Hamiltonian, $\hat{\mathcal{H}}$:

$$[\hat{\mathcal{H}}, \hat{\pi}] = 0, \tag{2.6.35}$$

and it follows that $\hat{\mathcal{H}}$ and $\hat{\mathcal{I}}$ have common eigenvalues. In the case of the nuclear mean-field approximation Hamiltonian, $\hat{H}_{\mathrm{mf}}$, certain nuclear shapes may imply a non-commutation, $[\hat{H}_{\mathrm{mf}}, \hat{\mathcal{I}}] \neq 0$; this is the case for the deformation parameters $\alpha_{\lambda\mu}$ with $\lambda = \text{odd}$.

2.6.4 Simplex Symmetry of the Mean-Field

Simplex (also y-simplex) operator, $\hat{\mathcal{S}}_y$, is defined as the combination of inversion and signature:

$$\hat{\mathcal{S}}_y \equiv \hat{\mathcal{I}}\,\hat{\mathcal{R}}_y = \hat{\mathcal{I}}\,\hat{R}_y(i\sigma_y) = \hat{S}_y \times i\sigma_y, \tag{2.6.36}$$

where $\hat{S}_y$ denotes the simplex operator acting on the spatial part, and $\hat{\mathcal{S}}_y$ – the simplex operator acting on the spatial and the spin spaces. Applying the simplex operator within Cartesian space, we find

$$\hat{S}_y \circ \{x, y, z\} = \hat{\pi} \circ \hat{R}_y \circ \{x, y, z\} = \hat{\pi} \circ \{-x, y, -z\} = \{+x, -y, +z\}. \tag{2.6.37}$$

Interpretation. $\hat{S}_y$ symmetry is equivalent to a mirror reflection with respect to π_{xz} plane. Since inversion $\hat{\mathcal{I}}$ and signature $\hat{\mathcal{R}}_y$ satisfy

$$\hat{\mathcal{S}}_y = \hat{\mathcal{I}}\,\hat{\mathcal{R}}_y = \hat{\mathcal{R}}_y\hat{\mathcal{I}}\,, \tag{2.6.38}$$

the definition of the simplex operator does not depend on the order of these two operators. We find

$$\hat{\mathcal{S}}_y^2 = [\hat{\mathcal{I}}\,e^{i\,\pi\,\hat{\ell}_y}\,(i\sigma_y)]^2 = \underbrace{[e^{i\,2\pi\,\hat{\ell}_y}]}_{1}\,\underbrace{[\hat{\mathcal{I}}^2]}_{1}\,\underbrace{[(i\sigma_y)^2]}_{-1} = -1, \tag{2.6.39}$$

and thus $\hat{\mathcal{S}}_y^2$ changes the sign of a spinor wave function. It follows that for the mean-field Hamiltonians obeying to the inversion and signature symmetries we find:

$$\boxed{[\hat{H}, \hat{\mathcal{S}}_y] = 0.} \tag{2.6.40}$$

Let us emphasise that the simplex symmetry of the mean-field Hamiltonian may apply even though *both the inversion and signature symmetries are broken.*

It follows that in the case of the simplex-symmetry of the mean-field Hamiltonian, the common basis for mean-field Hamiltonian and simplex operator can be constructed and we will discuss this issue in the following sections.

Nuclear Surface as an Invariant of the Simplex Operator. Let us recall the expression of the nuclear surface equation with the help the of spherical harmonic expansions in eq. (2.3.22):

$$R^*(\theta,\varphi) = R(\theta,\varphi) \to [\sum_{\lambda\mu}\alpha_{\lambda\mu}Y_{\lambda\mu}(\theta,\varphi)]^* = \sum_{\lambda\mu}\alpha_{\lambda\mu}Y_{\lambda\mu}(\theta,\varphi). \tag{2.6.41}$$

Consider the application of the simplex operation to spherical coordinates $\{r,\theta,\varphi\}$,

$$\hat{S}_y \circ \{x,y,z\} = \{+x,-y,+z\} \leftrightarrow \{r,\theta,2\pi-\varphi\}. \tag{2.6.42}$$

It follows that for the spherical harmonics we have

$$Y_{\lambda\mu}(\theta,2\pi-\varphi) = Y_{\lambda\mu}(\theta,-\varphi) = Y^*_{\lambda\mu}(\theta,\varphi) = (-1)^\mu Y_{\lambda-\mu}(\theta,\varphi). \tag{2.6.43}$$

Recall the condition for deformation parameters in eq. (2.3.24),

$$\alpha^*_{\lambda\mu} = (-1)^\mu\alpha_{\lambda-\mu}. \tag{2.6.44}$$

According to eq. (2.6.39), we consider the surface function as the sum of the terms with $\pm\mu$ separately, wherefrom the contributions with given $|\mu|$ satisfy

$$\begin{aligned}
\alpha_{\lambda\mu}Y_{\lambda\mu}(\theta,+\varphi) + \alpha_{\lambda-\mu}Y_{\lambda-\mu}(\theta,+\varphi) \xrightarrow{\hat{S}_y} & \alpha_{\lambda\mu}\underbrace{Y_{\lambda\mu}(\theta,-\varphi)}_{(-1)^\mu Y_{\lambda-\mu}(\theta,+\varphi)} + \alpha_{\lambda-\mu}\underbrace{Y_{\lambda-\mu}(\theta,-\varphi)}_{(-1)^\mu Y_{\lambda+\mu}(\theta,+\varphi)} \\
= & \underbrace{(-1)^\mu\alpha_{\lambda\mu}}_{\alpha_{\lambda-\mu}}Y_{\lambda-\mu}(\theta,+\varphi) + \underbrace{(-1)^\mu\alpha_{\lambda-\mu}}_{\alpha_{\lambda\mu}}Y_{\lambda+\mu}(\theta,+\varphi) \\
= & \alpha_{\lambda-\mu}Y_{\lambda-\mu}(\theta,+\varphi) + \alpha_{\lambda\mu}Y_{\lambda+\mu}(\theta,+\varphi).
\end{aligned} \tag{2.6.45}$$

The above relation demonstrates that all nuclear surfaces represented in terms of the multipole expansion with real deformation parameters $\{\alpha_{\lambda\mu}\}$ remain invariant under y-simplex operator; this is the case of the multipole deformations used in the literature and in our project.

Chapter 3

Solving the Schrödinger Equation with the Mean-Field Hamiltonian

In the preceding chapter we have introduced the mean-field Hamiltonian, which, in its phenomenological realisation is defined in terms of the so-called deformed Woods-Saxon potential. In this chapter, we are going to present the algorithms allowing for the construction of numerical solutions of the Schrödinger equation together with the corresponding computer programs. The single particle energies and wave functions of the individual nucleons will be obtained by solving the Schrödinger equation numerically employing symmetries and the well known diagonalisation method.

After a short reminder related to the definition of the Hamiltonian we are introducing the standard deformed 3D harmonic oscillator potential with the corresponding solutions in terms of the Hermit polynomials. We formulate next some instructions allowing to construct numerically the matrix elements of the deformed mean-field Hamiltonian.

Our mean field Hamiltonian is time-reversal invariant and obeys the simplex symmetry, the latter invariance guaranteed by the choice of the multipole deformation parameters $\alpha_{\lambda\mu}$ as real numbers. Thanks to the presence of those symmetries we can adopt the harmonic oscillator basis in such a way that the corresponding Hamiltonian matrix splits into two blocks thus decreasing the storage demand and accelerating the computer program execution. Several variants of symmetrisation are discussed and the information necessary to read, understand, and possibly modify the computer programs is provided.

3.1 Method of Solution – Introductory Remarks

The stationary Schrödinger equation has the usual form

$$\hat{H}\psi_n = e_n\psi_n, \tag{3.1.1}$$

where the mean-field Hamiltonian, expressed using the generally deformed Woods-Saxon potential, can be written as

$$\hat{H} = \hat{T} + \hat{V}^{\mathrm{c}}_{\mathrm{WS}}(\vec{r},\alpha) + \hat{V}^{\mathrm{so}}_{\mathrm{WS}}(\vec{r},\alpha) + \hat{V}_{\mathrm{Coul.}}(\vec{r}), \tag{3.1.2}$$

with $\hat{T}$ representing the kinetic energy operator, $\hat{V}^{\mathrm{c}}_{\mathrm{WS}}$ the central Woods-Saxon potential and $\hat{V}^{\mathrm{so}}_{\mathrm{WS}}$ the spin-orbit potential introduced in section (2.4.1). Recall that the central potential has the form:

$$\hat{V}_{\mathrm{WS}}(\vec{r};V^{\mathrm{c}},r^{\mathrm{c}},a^{\mathrm{c}}) = \frac{V^{\mathrm{c}}}{1+\exp[\mathrm{dist}_\Sigma(\vec{r};r^{\mathrm{c}})/a^{\mathrm{c}}]}, \tag{3.1.3}$$

where V^{c} represents the central depth parameter, r^{c} is the central radius and a^{c} the central potential diffuseness parameters. Similarly, the spin-orbital potential has the explicit form:

$$\hat{V}^{so}_{\mathrm{WS}}(\vec{r};\lambda^{\mathrm{so}},r^{\mathrm{so}},a^{\mathrm{so}}) = -[\vec{\nabla}V^{\mathrm{so}}\wedge\hat{p}\,]\cdot\hat{s}, \tag{3.1.4}$$

in which

$$V^{\mathrm{so}} \leftrightarrow V^{\mathrm{so}}(\vec{r};\lambda^{\mathrm{so}},r^{\mathrm{so}},a^{\mathrm{so}}) = \frac{\lambda^{\mathrm{so}}}{1+\exp[\mathrm{dist}_\Sigma(\vec{r};r^{\mathrm{so}})/a^{\mathrm{so}}]}. \tag{3.1.5}$$

Above, λ^{so} represents the dimensionless spin-orbit strength parameter, r^{so} spin-orbit radius parameter, which satisfies $R^{\mathrm{so}} = r^{\mathrm{so}}A^{1/3}$, and a^{so} is the spin-orbit diffusivity parameter. The mean-field Hamiltonian contains the Coulomb potential for the protons, defined as an electrostatic potential generated by the uniform charge distribution $\rho(\vec{r}\,')$ inside the nuclear surface Σ:

$$\hat{V}_{Coul.} = \iiint_\Sigma d^3\vec{r}\,'\frac{\rho(\vec{r}\,')}{|\vec{r}-\vec{r}\,'|}. \tag{3.1.6}$$

The structure of the resulting mean-field Hamiltonian implies that the corresponding Schrödinger equation, eq. (3.1.1), must be solved numerically. For this purpose we introduce a complete orthonormal basis of wave functions $\{\varphi_m\}$ generated by the Cartesian 3D harmonic oscillator Hamiltonian and express for the moment unknown solutions $\{\psi_n\}$ as expansions of the form:

$$|\psi_n\rangle = \sum_m c_{mn}|\varphi_m\rangle, \tag{3.1.7}$$

in which the coefficients c_{mn} will need to be determined. The Schrödinger equation can be rewritten as follows:

$$\hat{H}|\psi_n\rangle = \varepsilon_n|\psi_n\rangle \;\rightarrow\; \hat{H}\sum_m c_{mn}|\varphi_m\rangle = \sum_m c_{mn}\varepsilon_n|\varphi_m\rangle. \tag{3.1.8}$$

Since by construction the basis satisfies orthogonality property

$$\langle\varphi_{m'}|\varphi_m\rangle = \delta_{m'm}, \tag{3.1.9}$$

multiplying both sides of eq. (3.1.8) by $\langle\varphi_{m'}|$ and integrating we find

$$\sum_m c_{mn}\langle\varphi_{m'}|\hat{H}|\varphi_m\rangle = \sum_m c_{mn}\varepsilon_n\delta_{m'm}. \tag{3.1.10}$$

We can rewrite eq. (3.1.10) as follows

$$\sum_m c_{mn}\left(\langle\varphi_{m'}|\hat{H}|\varphi_m\rangle - \varepsilon_n\delta_{m'm}\right) = 0, \tag{3.1.11}$$

and conclude that the non-zero solutions of the above equation are obtained if and only if the determinant constructed out of the above matrix vanishes

$$\det\left(\langle\varphi_{m'}|\hat{H}|\varphi_m\rangle - \varepsilon_n\delta_{m'm}\right) = 0. \tag{3.1.12}$$

It follows that in order to solve eq. (3.1.11) i.e., to find the eigenvalues ε_n and the expansion coefficients c_{mn} for the sought eigenfunctions, we need to diagonalise the matrix of the Hamiltonian $\langle\varphi_{m'}|\hat{H}|\varphi_m\rangle$. As an approximation called basis cut-off, the size of the corresponding basis is assumed finite, say N. In principle the higher the size of the basis, the more accurate the solutions. However, increasing the size of the basis also implies bigger storage space and longer computing time. Optimising the size of the basis cut-off is an important part of the preparations for the numerical solution.

3.2 Cartesian 3D Harmonic-Oscillator Basis

The choice of the basis and its symmetries play an important role in constructing of efficient and numerically stable solutions to the mean-field problem. When selecting the basis we need to address from the beginning the issue of the basis cut off so that the numerical representations of the studied operators are reproduced with maximum precision at minimum computer memory. Secondly, to increase the efficiency of numerical algorithms – if possible – the symmetries of the system are taken care of within the selected basis.

3.2.1 Cartesian Harmonic-Oscillator Wave Functions

In what follows we present the harmonic oscillator Hamiltonian in its Cartesian representation:

$$\hat{H}_{\mathrm{HO}} = -\frac{\hbar^2}{2m_0}\left(\frac{\partial^2}{\partial x^2} + \frac{\partial^2}{\partial y^2} + \frac{\partial^2}{\partial z^2}\right) + \frac{1}{2}m_0\left(\omega_x^2 x^2 + \omega_y^2 y^2 + \omega_z^2 z^2\right), \tag{3.2.1}$$

where m_0 denotes the rest-mass of the nucleon, $\{\omega_x, \omega_y, \omega_z\}$ define the so-called stiffness parameters of the oscillator in the Cartesian space $\{x, y, z\}$, alternatively, harmonic oscillator frequencies. The implied Schrödinger equation has the form:

$$\hat{H}_{\rm HO}\Psi_{n_x,n_y,n_z}(x,y,z) = E_{n_x,n_y,n_z}\Psi_{n_x,n_y,n_z}(x,y,z), \tag{3.2.2}$$

in which the wave-functions and the eigenvalues can be decomposed as follows:

$$\Psi_{n_x,n_y,n_z}(x,y,z) = \psi_{n_x}(x)\psi_{n_y}(y)\psi_{n_z}(z) \quad \text{and} \quad E_{n_x,n_y,n_z} = e_{n_x} + e_{n_y} + e_{n_z}. \tag{3.2.3}$$

In order to solve eq. (3.2.2), we introduce dimensionless variables

$$\xi_\mu = b_\mu x_\mu, \ \{x_\mu, \mu = 1,2,3\} \rightarrow \{x,y,z\}, \tag{3.2.4}$$

where the so-called stretching factors are defined by

$$b_\mu = \sqrt{\frac{m_0\omega_\mu}{\hbar}}, \quad \mu = 1,2,3. \tag{3.2.5}$$

One can demonstrate (here and in the following we are using the mathematical properties of the Hermit polynomials from ref. [20]) that the solutions of eq. (3.2.2) can be expressed with the help of the Hermit polynomials, $H_{n_\mu}(\xi_\mu)$, as

$$\psi_{n_\mu}(x_\mu) = \sqrt{b_\mu}\exp(-\tfrac{\xi_\mu^2}{2})H^{(0)}_{n_\mu}(\xi_\mu), \quad e_{n_\mu} = (n_\mu + \tfrac{1}{2}), \tag{3.2.6}$$

where $n_\mu = 1, 2, ..., \infty$, and where $H^{(0)}_{n_\mu}(\xi_\mu)$ denote the normalised Hermit polynomials, which are defined as follows

$$H^{(0)}_{n_\mu}(\xi_\mu) = \frac{1}{\sqrt{\sqrt{\pi}2^{\,n_\mu}n_\mu!}}H_{n_\mu}(\xi_\mu), \tag{3.2.7}$$

and

$$H_{n_\mu}(\xi_\mu) = (-1)^{n_\mu}\exp(\xi^{\,2})\frac{de^{-\xi^{\,2}}}{d\xi^{n_\mu}}. \tag{3.2.8}$$

The above Hermit polynomials satisfy the following orthogonality relations

$$\int_{-\infty}^{\infty}\exp(-\xi_\mu^2)H^{(0)}_{n_\mu}(\xi_\mu)H^{(0)}_{n'_\mu}(\xi_\mu)d\xi_\mu = \delta_{n_\mu,n'_\mu}. \tag{3.2.9}$$

One demonstrates that the eigenvalues can be expressed as follows

$$E_{n_x,n_y,n_z} = \hbar\omega_x(n_x + \tfrac{1}{2}) + \hbar\omega_y(n_y + \tfrac{1}{2}) + \hbar\omega_z(n_z + \tfrac{1}{2}). \tag{3.2.10}$$

In the particular case of spherical symmetry, we have

$$\omega_x = \omega_y = \omega_z \equiv \omega_0, \tag{3.2.11}$$

and consequently the eigen-energies take the simplified form

$$E_{n_x,n_y,n_z} = \hbar\omega_0 \left(n_x + n_y + n_z + \tfrac{3}{2}\right). \tag{3.2.12}$$

It follows that the above energy levels are degenerate with the energies $E(N)$, and $N \equiv n_x + n_y + n_z$. These degenerate levels form the so-called shells. The shells are separated by the shell-gaps defined as

$$\Delta E_{\text{shell}} = E_{\text{shell}}(N+1) - E_{\text{shell}}(N) = \hbar\omega_0, \tag{3.2.13}$$

whereas the energy difference ΔE_{shell} is sometimes referred to as a gap.

Harmonic Oscillator with Spin. Since nucleons are fermions with spins $s = \frac{1}{2}$, the wave-functions need to be modified as follows

$$\Psi_{n_x,n_y,n_z}(\vec{r},\vec{s}) = \psi_{n_x}(x)\psi_{n_y}(y)\psi_{n_z}(z)\chi_{s,s_z}, \tag{3.2.14}$$

where χ_{s,s_z} are spin wave-functions. It follows from the above expression that the Woods-Saxon solutions $\Psi_{n_x,n_y,n_z}(\vec{r},\vec{s})$, can be represented as linear combination of the harmonic oscillator and the spin components and we can write

$$\Psi_n(\vec{r},\vec{s}) = \sum_{n_x=0}^{N_x}\sum_{n_y=0}^{N_y}\sum_{n_z=0}^{N_z}\sum_{s_z=-\frac{1}{2},\frac{1}{2}} A_n^{n_x n_y n_z, s_z}\psi_{n_x n_y n_z, s_z}(\vec{r},\vec{s}), \tag{3.2.15}$$

where N_x, N_y and N_z are the maximum numbers (the so-called basis cut-off parameters) of the harmonic oscillator basis corresponding to the three Cartesian directions. Using an alternative bra-ket notation, we have

$$|n_x n_y n_z, s_z\rangle \equiv \psi_{n_x n_y n_z, s_z}(\vec{r},\vec{s}). \tag{3.2.16}$$

These basis states can be represented as products in the following way

$$|n_x n_y n_z, s_z\rangle \equiv |\, n_x n_y n_z\rangle \otimes |s_z\rangle, \tag{3.2.17}$$

so that we can calculate the matrix elements in the coordinate space and in the spin space separately.

3.2.2 Matrix Elements within Harmonic Oscillator Basis

As seen from eqs. (3.2.1)-(3.2.2), the matrix elements of the harmonic oscillator Hamiltonian contain terms with the second-order partial derivatives of the wave-function in eq. (3.2.6), and the related terms are:

$$\frac{d}{dx_\mu}\psi_{n_\mu}(x_\mu) = b_\mu^{\frac{3}{2}} e^{-\frac{1}{2}\xi^2} H_{n_\mu}^{(1)}(\xi_\mu), \tag{3.2.18}$$

$$\frac{d^2}{dx_\mu^2}\psi_{n_\mu}(x_\mu) = b_\mu^{\frac{5}{2}} e^{-\frac{1}{2}\xi^2} H_{n_\mu}^{(2)}(\xi_\mu), \tag{3.2.19}$$

where Hermit polynomials $\hat{H}_n^{(1)}(\xi)$ and $\hat{H}_n^{(2)}(\xi)$ satisfy the recurrence relations

$$H_n^{(1)}(\xi) = 2nH_{n-1}^{(0)}(\xi) - \xi\, H^{(0)}(\xi), \tag{3.2.20}$$

$$H_n^{(2)}(\xi) = (\xi^2 - 2n - 1)H^{(0)}(\xi). \tag{3.2.21}$$

It follows that the matrix elements of the differential operators, in particular up to the second order, can be obtained in terms of the recurrence relations involving only $\hat{H}^{(0)}(\xi)$,

$$H_n^{(d)}(\xi)H_{n'}^{(d')}(\xi) = \sum_{k=0}^{m} c_{n\,n'}^{k}(d\,d')H_k^{(0)}(\xi), \tag{3.2.22}$$

where the orders of the polynomials satisfy $0 \leq d + d' \leq 2$ and $m = n + n' + d + d'$. Coefficients $c_{n\,n'}^{k}(d\,d')$ are calculated with the help of the orthogonality relations for Hermit polynomials and the Gauss-Hermit quadratures[1], cf. e.g. ref. [21]. Thus we can write down the matrix elements of an arbitrary operator $\hat{\mathcal{O}}(x, y, z)$ with the help of the expansion:

$$\langle n_x n_y n_z|\hat{\mathcal{O}}(x,y,z)|n_x' n_y' n_z'\rangle = \sum_{k_x} c_{n_x\,n_x'}^{k_x}(00) \sum_{k_y} c_{n_y\,n_x'}^{k_y}(00) \sum_{k_z} c_{n_z\,n_x'}^{k_z}(00)\mathcal{O}_{k_x k_y k_z} \tag{3.2.25}$$

in which

$$\mathcal{O}_{k_x k_y k_z} = \int d\xi_x\, d\xi_y\, d\xi_z \mathcal{O}(\tfrac{\xi_x}{b_x}, \tfrac{\xi_y}{b_y}, \tfrac{\xi_z}{b_z}) H_{k_x}^{(0)}(\xi_x) H_{k_y}^{(0)}(\xi_y) H_{k_z}^{(0)}(\xi_z) e^{-\xi_x^2 - \xi_y^2 - \xi_z^2}. \tag{3.2.26}$$

3.2.3 Matrix Elements of One-Body Hamiltonian

Consider a one-body operator $\hat{F}$ which depends on the coordinates, linear momenta $(\hat{p} = -i\hbar\nabla = -i\hbar[\partial/\partial x, \partial/\partial y, \partial/\partial z) \equiv i\hbar(\partial_x, \partial_y, \partial_z)]$ and spins in the following general manner

$$\hat{F} \leftrightarrow \hat{F}(x, y, z; \partial_x, \partial_y, \partial_z; \sigma_x, \sigma_y, \sigma_z). \tag{3.2.27}$$

[1] According to Gauss quadrature theorem, to integrate a function $f(x)$ numerically one uses the relation:

$$\int_a^b e^{-x^2} f(x)dx \approx \sum_{i=1}^{n} w_i f(x_i), \tag{3.2.23}$$

where the so-called integration nodes are denoted x_i and the weight-factors satisfy

$$w_i = \frac{2^{n-1} n! \sqrt{\pi}}{n^2 [H_{n-1}(x_i)]^2}. \tag{3.2.24}$$

It is known that the integer powers of the Pauli matrices satisfy:

$$\sigma_k^{(2n)} = \mathbb{1}, \quad \text{and} \quad \sigma_k^{(2n+1)} = \sigma_k, \tag{3.2.28}$$

so that the general form of the one-body operator is either spin independent or – at most – linear in terms of Pauli matrices,

$$\hat{F} = \sum_{k=0}^{3} \hat{f}_k(x, y, z; \partial_x, \partial_y, \partial_z)\sigma_k, \quad \text{where} \quad \sigma_0 = \mathbb{1}. \tag{3.2.29}$$

The general form of the spin-dependent wave function can be expressed as

$$|\vec{r}, \alpha; s_z\rangle = |\vec{r}, \alpha\rangle|s_z\rangle. \tag{3.2.30}$$

Consequently, the matrix elements of $\hat{F}$ are composed of two components, one in the coordinate space and one in the spin space:

$$\langle \vec{r}', \alpha'|\hat{f}_k(x, y, z; \partial_x, \partial_y, \partial_z)|\vec{r}, \alpha\rangle, \quad \text{and} \quad \langle s_z'|\sigma_k|s_z\rangle. \tag{3.2.31}$$

One can show that expressions involving Pauli matrices have the following structure:

Matrix Elements Involving $\boldsymbol{\sigma_x}$:

$$\langle s_z|\sigma_x|s_z\rangle = \langle s_z| - s_z\rangle = 0, \tag{3.2.32}$$

$$\begin{aligned}\langle \bar{s}_z|\sigma_x|s_z\rangle &= (-1)^{s+s_z}\langle -s_z| - s_z\rangle \\ &= (-1)^{s+s_z} = -1,\end{aligned} \tag{3.2.33}$$

$$\begin{aligned}\langle s_z|\sigma_x|\bar{s}_z\rangle &= (-1)^{s+s_z}\langle s_z|s_z\rangle \\ &= (-1)^{s+s_z} = -1,\end{aligned} \tag{3.2.34}$$

$$\langle \bar{s}_z|\sigma_x|\bar{s}_z\rangle = \langle -s_z|s_z\rangle = 0. \tag{3.2.35}$$

Matrix Elements Involving $\boldsymbol{\sigma_y}$:

$$\langle s_z|\sigma_y|s_z\rangle = 2is_z\langle s_z| - s_z\rangle = 0, \tag{3.2.36}$$

$$\begin{aligned}\langle \bar{s}_z|\sigma_y|s_z\rangle &= 2is_z(-1)^{s+s_z}\langle -s_z| - s_z\rangle \\ &= 2is_z(-1)^{s+s_z} = -i,\end{aligned} \tag{3.2.37}$$

$$\langle s_z|\sigma_y|\bar{s}_z\rangle = (+i)\langle s_z|s_z\rangle = +i, \tag{3.2.38}$$

$$\langle \bar{s}_z|\sigma_y|\bar{s}_z\rangle = (+i)\langle -s_z|s_z\rangle = 0. \tag{3.2.39}$$

Matrix Elements Involving σ_z:

$$\langle s_z|\sigma_z|s_z\rangle = (2s_z) = +1, \tag{3.2.40}$$

$$\langle \bar{s}_z|\sigma_z|s_z\rangle = 0, \tag{3.2.41}$$

$$\langle s_z|\sigma_z|\bar{s}_z\rangle = 0, \tag{3.2.42}$$

$$\langle \bar{s}_z|\sigma_z|\bar{s}_z\rangle = (-1)^{s+s_z} = -1. \tag{3.2.43}$$

We observe that the matrix elements involving spin are either purely real (x- and z-component) or purely imaginary (y-component). The spin component of the matrix elements usually provides the phase factor, which may depend on the phase conventions introduced in relation to the time-reversal operator.

3.3 Alternative Symmetrised Bases

In order to optimise the matrix representation of the Hamiltonian, we will introduce the so-called symmetrised bases involving harmonic oscillator states and symmetries of the mean-field Hamiltonian. The symmetries of the Hamiltonian such as time-reversal, signature, and simplex are discussed in section (2.6). The symmetrised bases allow expressing relations between certain matrix elements of the mean-field Hamiltonian such that certain convenient block-diagonal structures of the Hamiltonian can be built, often profiting from the recurrence relations between the Hermit polynomials.

3.3.1 B-Basis and Associated Symmetry Relations

The so-called B-basis is defined by multiplying the standard harmonic oscillator wave functions by the phase factor i^{n_y}. Introducing a phase factor does not change the probability density and we always have an equivalent physical solution, however, the appropriate phases may provide useful simplifications. The B-basis is by definition composed of vectors $\{|b_n\rangle, |\bar{b}_n\rangle\}$, the first of which is defined as

$$|b_n\rangle = +i^{n_y}|n_x, n_y, n_z; s_z = +\tfrac{1}{2}\rangle = +i^{n_y}|n; s_z = +\tfrac{1}{2}\rangle. \tag{3.3.1}$$

Recall the definition of the time-reversal operator, eq. (2.6.1),

$$\hat{T} = i\,\sigma_y\hat{K}, \tag{3.3.2}$$

with the help of which we can demonstrate that

$$|\bar{b}_n\rangle \equiv \hat{T}|b_n\rangle = i\sigma_y\hat{K}(+i^{n_y})|n; s_z = +\tfrac{1}{2}\rangle$$
$$= i\sigma_y \underbrace{\hat{K}(+i^{n_y})}_{i^{-n_y}}|n; s_z = +\tfrac{1}{2}\rangle = -i^{n_y}|n; s_z = -\tfrac{1}{2}\rangle, \tag{3.3.3}$$

so that

$$|\bar{b}_n\rangle = -i^{n_y}|n_x, n_y, n_z; s_z = -\tfrac{1}{2}\rangle = -i^{n_y}|n; s_z = -\tfrac{1}{2}\rangle, \tag{3.3.4}$$

where $|\bar{b}_n\rangle$ is time-reversed $|b_n\rangle$. It follows that

$$\hat{T}|\bar{b}_n\rangle = -|b_n\rangle. \tag{3.3.5}$$

Symmetry Relations. Consider an operator $\hat{\mathcal{O}}$. If one of the two following relations is satisfied:

$$\hat{T}^{-1}\hat{\mathcal{O}}\hat{T} = \pm\hat{\mathcal{O}}, \tag{3.3.6}$$

we say that $\hat{\mathcal{O}}$ is time-even when the plus sign applies, otherwise it is called time-odd. Acting with the operator $\hat{\mathcal{O}}$ on the B-basis states we have in particular

$$\langle\bar{b}_n|\hat{\mathcal{O}}|\bar{b}_{n'}\rangle = (\langle b_n|\hat{T})\hat{\mathcal{O}}\hat{T}|b_{n'}\rangle = \langle b_n|\underbrace{\hat{T}^{-1}\hat{\mathcal{O}}\hat{T}}_{\pm\hat{\mathcal{O}}}|b_{n'}\rangle^* = \pm\langle b_n|\hat{\mathcal{O}}|b_{n'}\rangle^*, \tag{3.3.7}$$

and it follows that for

$$\hat{\mathcal{O}}\ \text{time}-\text{even}: \quad \langle\bar{b}_n|\hat{\mathcal{O}}|\bar{b}_{n'}\rangle = +\langle b_n|\hat{\mathcal{O}}|b_{n'}\rangle^*, \tag{3.3.8}$$

$$\hat{\mathcal{O}}\ \text{time}-\text{odd}: \quad \langle\bar{b}_n|\hat{\mathcal{O}}|\bar{b}_{n'}\rangle = -\langle b_n|\hat{\mathcal{O}}|b_{n'}\rangle^*. \tag{3.3.9}$$

Similarly we can demonstrate the following relations

$$\hat{\mathcal{O}}\ \text{time}-\text{even}: \quad \langle\bar{b}_n|\hat{\mathcal{O}}|b_{n'}\rangle = -\langle b_n|\hat{\mathcal{O}}|\bar{b}_{n'}\rangle^*, \tag{3.3.10}$$

$$\hat{\mathcal{O}}\ \text{time}-\text{odd}: \quad \langle\bar{b}_n|\hat{\mathcal{O}}|b_{n'}\rangle = +\langle b_n|\hat{\mathcal{O}}|\bar{b}_{n'}\rangle^*. \tag{3.3.11}$$

The above symmetry relations can be used to adapt expressions of the matrix elements of certain observables to more convenient forms, see below.

3.3.2 T-Basis: Time-Reversal Symmetrised Basis

Time-reversal symmetrised basis (T-basis) is obtained by acting with a simple unitary transformation on the basis $\{|b_1\rangle, ..., |b_n\rangle, |\bar{b}_1\rangle, ..., |\bar{b}_n\rangle\}$ leading to the following alternative form, ref. [22], with

$$|t_n+\rangle = \frac{1}{\sqrt{2}}(i|b_n\rangle - |\bar{b}_n\rangle), \tag{3.3.12}$$

and

$$|t_n-\rangle = \frac{1}{\sqrt{2}}(|b_n\rangle - i|\bar{b}_n\rangle), \tag{3.3.13}$$

in which $|b_n\rangle$ and $|\bar{b}_n\rangle$ are defined in eqs. (3.3.1) to (3.3.4). Applying time-reversal operator on the T-basis states we find

$$\begin{aligned}\hat{T}|t_n+\rangle &= \frac{1}{\sqrt{2}}(-i\underbrace{\hat{T}|b_n\rangle}_{+|\bar{b}_n\rangle} - \underbrace{\hat{T}|\bar{b}_n\rangle}_{-|b_n\rangle}) \\ &= \frac{1}{\sqrt{2}}(|b_n\rangle - i|\bar{b}_n\rangle) = |t_n-\rangle,\end{aligned} \tag{3.3.14}$$

and similarly

$$\begin{aligned}\hat{T}|t_n-\rangle &= \frac{1}{\sqrt{2}}(\underbrace{\hat{T}|b_n\rangle}_{+|\bar{b}_n\rangle} + i\underbrace{\hat{T}|\bar{b}_n\rangle}_{-|b_n\rangle}) \\ &= -\frac{1}{\sqrt{2}}(i|b_n\rangle - |\bar{b}_n\rangle) = -|t_n+\rangle.\end{aligned} \tag{3.3.15}$$

We rewrite the above symmetry relations in a concise form as

$$\hat{T}|t_n+\rangle = +|t_n-\rangle, \tag{3.3.16}$$

$$\hat{T}|t_n-\rangle = -|t_n+\rangle. \tag{3.3.17}$$

After these preliminaries let us proceed with extending the list of properties of the B-Basis.

3.3.3 Basis Symmetry Properties Related to Signature

As discussed in section (2.6.2), the y-signature symmetry operator, denoted $\hat{\mathcal{R}}_y$, is associated with an operation of rotation through the angle of π about $\mathcal{O}_y$-axis. In this section, we are going to verify the symmetry properties when applying $\hat{\mathcal{R}}_y$ on B-basis and T-basis states.

Let us recall the definition

$$\hat{\mathcal{R}}_y(\pi) \equiv e^{i\,\pi\,\hat{\ell}_y} \cdot e^{i\,\pi\,\hat{s}_y} = \hat{R}_y(\pi) \times (i\sigma_y). \tag{3.3.18}$$

It follows that applying y-signature operator in Cartesian space we induce transformation: $\{x, y, z\} \to \{-x, y, -z\}$. Knowing that $H_n(-x) = (-1)^n H(x)$, we find

$$|n_x, n_y, n_z\rangle \xrightarrow{\hat{\mathcal{R}}_y} |-n_x, n_y, -n_z\rangle = (-1)^{n_x+n_z}|n_x, n_y, n_z\rangle. \tag{3.3.19}$$

B-Basis Under $\hat{\mathcal{R}}_y$ Operations. Applying $\hat{\mathcal{R}}_y$-operation to the basis state $|b_n\rangle$ defined in eq. (3.3.1) we find

$$\begin{aligned}
\hat{\mathcal{R}}_y(\pi)|b_n\rangle &= \hat{R}(\pi)(i\sigma_y)(+i^{n_y})|n_x,n_y,n_z;\tfrac{1}{2}\rangle \\
&= (-1)^{n_x+n_z}(-i^{n_y})|n_x,n_y,n_z\rangle\underbrace{(i\,\sigma_y)|\tfrac{1}{2}\rangle}_{-1/2} \\
&= (-1)^{n_x+n_z}\underbrace{(-i^{n_y})|n_x,n_y,n_z;-\tfrac{1}{2}\rangle}_{|\bar{b}_n\rangle} \\
&= (-1)^{n_x+n_z}|\bar{b}_n\rangle. \qquad (3.3.20)
\end{aligned}$$

Similarly,

$$\begin{aligned}
\hat{\mathcal{R}}_y(\pi)|\bar{b}_n\rangle &= \hat{R}(\pi)(i\sigma_y)(-i^{n_y})|n_x,n_y,n_z;-\tfrac{1}{2}\rangle \\
&= (-1)^{n_x+n_z}(-i^{n_y})|n_x,n_y,n_z\rangle\underbrace{(i\sigma_y)|-\tfrac{1}{2}\rangle}_{\frac{1}{2}} \\
&= -(-1)^{n_x+n_z}\underbrace{(+i^{n_y})|n_x,n_y,n_z;\tfrac{1}{2}\rangle}_{|b_n\rangle} \\
&= -(-1)^{n_x+n_z}|b_n\rangle. \qquad (3.3.21)
\end{aligned}$$

We can rewrite the above relations as

$$\hat{\mathcal{R}}_y(\pi)|b_n\rangle = +(-1)^{n_x+n_z}|\bar{b}_n\rangle, \qquad (3.3.22)$$

$$\hat{\mathcal{R}}_y(\pi)|\bar{b}_n\rangle = -(-1)^{n_x+n_z}|b_n\rangle. \qquad (3.3.23)$$

These expressions show that the y-signature operator alternates signs of B-basis states.

T-basis Under $\hat{\mathcal{R}}_y$ Operations. Applying the $\hat{\mathcal{R}}_y$-operation to the basis $|t_n+\rangle$ defined via eq. (2.3.12) we obtain

$$\begin{aligned}
\hat{\mathcal{R}}_y(\pi)|t_n+\rangle &= \frac{1}{\sqrt{2}}\left[\hat{\mathcal{R}}_y(\pi)i|b_n\rangle - \hat{\mathcal{R}}_y(\pi)|\bar{b}_n\rangle\right] \\
&= \frac{1}{\sqrt{2}}\left((-1)^{n_x+n_z}\,i\,|\bar{b}_n\rangle + (-1)^{n_x+n_z}|b_n\rangle\right) \\
&= (-i)(-1)^{n_x+n_z}\underbrace{\frac{1}{\sqrt{2}}\left(i|b_n\rangle - |\bar{b}_n\rangle\right)}_{|t_n+\rangle} \\
&= (-i)(-1)^{n_x+n_z}|t_n+\rangle, \qquad (3.3.24)
\end{aligned}$$

and continuing

$$\hat{\mathcal{R}}_y(\pi)|t_n-\rangle = \frac{1}{\sqrt{2}}\left(\hat{\mathcal{R}}_y(\pi)|b_n\rangle - \hat{\mathcal{R}}_y(\pi)i|\bar{b}_n\rangle\right)$$

$$= \frac{1}{\sqrt{2}}\left[+(-1)^{n_x+n_z}|\bar{b}_n\rangle + (-1)^{n_x+n_z} i|b_n\rangle\right]$$
$$= (+i)(-1)^{n_x+n_z} \underbrace{\frac{1}{\sqrt{2}}\left(|b_n\rangle - i\,|\bar{b}_n\rangle\right)}_{|t_n-\rangle}$$
$$= (+i)(-1)^{n_x+n_z}|t_n-\rangle, \tag{3.3.25}$$

therefore

$$\hat{\mathcal{R}}_y(\pi)|t_n+\rangle = (-i)(-1)^{n_x+n_z}|t_n+\rangle, \tag{3.3.26}$$

$$\hat{\mathcal{R}}_y(\pi)|t_n-\rangle = (+i)(-1)^{n_x+n_z}|t_n-\rangle. \tag{3.3.27}$$

We may conclude that the time-symmetrised states $\{|t_n-\rangle, |t_n+\rangle\}$ are the eigenstates of the y-signature operator, with eigenvalues $\pm i$.

3.3.4 Basis Symmetry Properties Related to Simplex

The y-simplex operation is defined as the reflexion in the y-plane as presented in section (2.6.4). Let us recall the definition of y-simplex symmetry operator:

$$\hat{\mathcal{S}}_y \equiv \hat{\mathcal{I}}\,\hat{\mathcal{R}}_y = \hat{\mathcal{I}}\,\hat{R}_y \times (i\sigma_y). \tag{3.3.28}$$

As seen from the above expression, the y-simplex operator is a product of the y-signature operator $\hat{R}_y \times (i\sigma_y)$ and inversion operator $\hat{\mathcal{I}}$. With the help of symmetry relations shown in eqs. (3.3.22) to (3.3.23) and eqs. (3.3.26) to (3.3.27), it is easy to calculate the symmetry properties for y-simplex operator.

B-Basis Under $\hat{\mathcal{S}}_y$ Operations. Applying the $\hat{\mathcal{S}}_y$-operation to the basis state $|b_n\rangle$ defined in eq. (3.3.1) we find

$$\hat{\mathcal{S}}_y|b_n\rangle = \hat{\mathcal{I}}\,\hat{\mathcal{R}}_y|b_n\rangle = \hat{\mathcal{I}}(-1)^{n_x+n_z}|\bar{b}_n\rangle = +(-1)^{n_y}|\bar{b}_n\rangle, \tag{3.3.29}$$

and

$$\hat{\mathcal{S}}_y|\bar{b}_n\rangle = \hat{\mathcal{I}}\,\hat{\mathcal{R}}_y|\bar{b}_n\rangle = -\hat{\mathcal{I}}(-1)^{n_x+n_z}|b_n\rangle = -(-1)^{n_y}|b_n\rangle. \tag{3.3.30}$$

T-Basis Under $\hat{\mathcal{S}}_y$ Operations. Applying the $\hat{\mathcal{S}}_y$-operation to the basis state $|t_n+\rangle$ defined in eq. (3.3.12) we obtain

$$\hat{\mathcal{S}}_y|t_n+\rangle = \hat{\mathcal{I}}\,\hat{\mathcal{R}}_y|t_n+\rangle = \hat{\mathcal{I}}(-i)(-1)^{n_x+n_z}|t_n+\rangle = (-i)(-1)^{n_y}|t_n+\rangle. \tag{3.3.31}$$

and similarly

$$\hat{\mathcal{S}}_y|t_n-\rangle = \hat{\mathcal{I}}\,\hat{\mathcal{R}}_y|t_n-\rangle = \hat{\mathcal{I}}(+i)(-1)^{n_x+n_z}|t_n-\rangle = (+i)(-1)^{n_y}|t_n-\rangle. \tag{3.3.32}$$

From the above expressions we conclude that the time-symmetrised states $\{|t_n-\rangle, |t_n+\rangle\}$ are the eigenstates of the y-simplex operator with the eigenvalues $\pm i$. This symmetry property allows us to construct the block-diagonal structure of matrices of the mean-field Hamiltonian; some details will be given in the following section.

3.4 Matrix Representations of the Hamiltonian

According to the observation that $\Psi(\vec{r}, s_z)$ and its time-reversal image $\bar{\Psi}(\vec{r}, -s_z)$ are linearly independent (cf. section (2.6.1)), both types of such states must be taken into account when constructing a basis for the mean-field numerical solutions. For instance:

$$\mathbf{B-basis}: \ \{|b_1\rangle, ..., |b_n\rangle; |\bar{b}_1\rangle, ..., |\bar{b}_n\rangle\},$$

and

$$\mathbf{T-basis}: \ \{|t_1+\rangle, ..., |t_n+\rangle; |t_1-\rangle, ..., |t_n\rangle-\}.$$

With the help of so ordered basis vectors, the Hamiltonian matrices take the form of 4 smaller sub-matrices ($N \times N$) rather than the one ($2N \times 2N$). We will verify the consequences of these block-structures in the case of the symmetrised bases.

3.4.1 General Form of Hamiltonian-Matrix Representation

Consider symmetrised B-basis with N states of a given type $\{|b_n\rangle; n = 1, N\}$. The implied representation of the Hamiltonian matrix can be written down using the above ordering of states as:

$$\begin{bmatrix} \langle b_{n'} \mid \hat{H} \mid b_n\rangle & \vdots & \langle b_{n'} \mid \hat{H} \mid \bar{b}_n\rangle \\ \cdots \quad \cdots \quad \cdots & \vdots & \cdots \quad \cdots \quad \cdots \\ \langle \bar{b}_{n'} \mid \hat{H} \mid b_n\rangle & \vdots & \langle \bar{b}_{n'} \mid \hat{H} \mid \bar{b}_n\rangle \end{bmatrix} \tag{3.4.1}$$

The above matrix is composed $2N \times 2N = 4N^2$ matrix elements, which are in general complex numbers, equivalent to $2 * 4N^2 = 8N^2$ real numbers. Since Hamiltonian is hermitian, it follows that

$$\hat{H}^\dagger = \hat{H} \quad \Leftrightarrow \quad h_{ij} = h^*_{ji}, \quad (i, j = 1, 2, ..., 2N) \tag{3.4.2}$$

with

$$\mathcal{R}e(h_{ij}) = \mathcal{R}e(h_{ji}) \quad \text{and} \quad \mathcal{I}m(h_{ij}) = -\mathcal{I}m(h_{ji}). \tag{3.4.3}$$

This symmetric structure implies that the freedom in terms of the *real* numbers can be expressed by

$$\frac{2N * 2N - 2N}{2} + 2N = 2N^2 + N. \tag{3.4.4}$$

Because of $\mathcal{I}m\, h_{ii} = 0$, the freedom of *imaginary* numbers is represented by

$$\frac{2N * 2N - 2N}{2} = 2N^2 - N. \tag{3.4.5}$$

With hermitian Hamiltonians, the freedom in terms of independent real numbers is

$$(2N^2 + N) + (2N^2 - N) = 4N^2. \tag{3.4.6}$$

This is equivalent of the freedom of $2N^2$ complex numbers. It follows that for hermitian matrices, the number of the matrix elements to store by the computer program can be reduced by a factor 2, which for big matrices represents a considerable gain.

Suppose the Hamiltonian is invariant under time-reversal operation, what implies

$$\hat{T}\hat{H}\hat{T}^{-1} = \hat{H}. \tag{3.4.7}$$

According to eqs. (3.3.3) to (3.3.5), we can demonstrate that

$$\langle b_{n'}|\hat{H}|\bar{b}_n\rangle = (\langle b_{n'}|\hat{T}^{-1})\hat{H}\hat{T}|\bar{b}_n\rangle = -\langle \bar{b}_{n'}|\hat{H}|b_n\rangle = \langle b_{n'}|\hat{H}|\bar{b}_n\rangle^*, \tag{3.4.8}$$

and similarly

$$\langle b_{n'}|\hat{H}|b_n\rangle = (\langle b_{n'}|\hat{T}^{-1})\hat{H}\hat{T}|b_n\rangle = +\langle \bar{b}_{n'}|\hat{H}|\bar{b}_n\rangle = \langle b_{n'}|\hat{H}|b_n\rangle^*. \tag{3.4.9}$$

Thus there exist symmetry relations between these 4 sub-block matrices. Consequently we find

$$\left[\begin{array}{ccc|c} \langle b_{n'} \mid \hat{H} \mid b_n\rangle \Rightarrow \hat{\mathcal{H}}_{n',n} & \cdots & & \langle b_{n'} \mid \hat{H} \mid \bar{b}_n\rangle \\ \Rightarrow \hat{\mathcal{H}}_{n',n} & \cdots & & \\ \hline \cdots & \cdots & \cdots & \cdots \\ \hline \langle \bar{b}_{n'} \mid \hat{H} \mid b_n\rangle & \cdots & & \langle \bar{b}_{n'} \mid \hat{H} \mid \bar{b}_n\rangle \\ = -\langle b_{n'} \mid \hat{H} \mid \bar{b}_n\rangle^* & \cdots & & = \langle b_{n'} \mid \hat{H} \mid b_n\rangle^* \\ & \cdots & & \Rightarrow \hat{\mathcal{H}}^*_{n',n} \end{array}\right] \tag{3.4.10}$$

One finds that the storage needed for the block $\hat{\mathcal{H}}_{n',n}$ is totally determined by N^2 real numbers. The 'upper-right' block in general contains $2N^2$ real numbers. Using the symmetry relation in eq. (3.4.8) we can profit from the symmetry properties in that

$$\langle b_{n'}|\hat{H}|\bar{b}_n\rangle = -\langle \bar{b}_{n'}|\hat{H}|b_n\rangle = [\langle b_{n'}|\hat{H}|\bar{b}_n\rangle^*]^T = [\langle b_{n'}|\hat{H}|\bar{b}_n\rangle]^\dagger. \tag{3.4.11}$$

This shows in particular that the 'upper-right' block is itself hermitian and contains N^2 real numbers.

We can conclude that the original freedom of $4N^2$ complex entries is greatly reduced to N^2 complex entries if the Hamiltonian is time-reversal invariant and hermitian.

3.4.2 Hamiltonian Matrix Representation within T-Basis

The block-structure matrices can be obtained in terms of T-basis as well. The general structure of the matrix of interest is

$$\hat{H} = \begin{pmatrix} \langle t_{n'} + |\hat{H}| t_n + \rangle & \langle t_{n'} + |\hat{H}| t_n - \rangle \\ \langle t_{n'} - |\hat{H}| t_n + \rangle & \langle t_{n'} - |\hat{H}| t_n - \rangle \end{pmatrix}. \tag{3.4.12}$$

Let us first calculate the matrix elements within the $\{|t_n+\rangle\}$ fragment of the basis

$$\begin{aligned} \langle t_{n'} + |\hat{H}| t_n + \rangle &= \frac{1}{2}\left(-i\,\langle b_{n'}| - \langle \bar{b}_{n'}|\right)\hat{H}\left(i\,|b_n\rangle - |\bar{b}_n\rangle\right) \\ &= \frac{1}{2}\left[\langle b_{n'}|\hat{H}|b_n\rangle + \langle \bar{b}_{n'}|\hat{H}|\bar{b}_n\rangle\right] + \frac{i}{2}\left[\langle b_{n'}|\hat{H}|\bar{b}_n\rangle - \langle \bar{b}_{n'}|\hat{H}|b_n\rangle\right] \\ &= \frac{1}{2}\underbrace{\left[\langle b_{n'}|\hat{H}|b_n\rangle + \langle b_{n'}|\hat{H}|b_n\rangle^*\right]}_{2\mathcal{R}e(\langle b_{n'}|\hat{H}|b_n\rangle)} + \frac{i}{2}\underbrace{\left[\langle b_{n'}|\hat{H}|\bar{b}_n\rangle + \langle b_{n'}|\hat{H}|\bar{b}_n\rangle^*\right]}_{2\mathcal{R}e(\langle b_{n'}|\hat{H}|\bar{b}_n\rangle)}, \end{aligned} \tag{3.4.13}$$

and it follows that

$$\langle t_{n'} + |\hat{H}| t_n + \rangle = +\mathcal{R}e\langle b_{n'}|\hat{H}|b_n\rangle + i\mathcal{R}e\langle b_{n'}|\hat{H}|\bar{b}_n\rangle. \tag{3.4.14}$$

Similarly we can calculate the matrix elements with for the remaining blocks as follows:

$$\langle t_{n'} - |\hat{H}| t_n - \rangle = +\mathcal{R}e\,\langle b_{n'}|\hat{H}|b_n\rangle - i\,\mathcal{R}e\,\langle b_{n'}|\hat{H}|\bar{b}_n\rangle, \tag{3.4.15}$$

$$\langle t_{n'} + |\hat{H}| t_n - \rangle = +\mathcal{I}m\langle b_{n'}|\hat{H}|b_n\rangle - i\,\mathcal{I}m\langle b_{n'}|\hat{H}|\bar{b}_n\rangle, \tag{3.4.16}$$

and

$$\langle t_{n'} - |\hat{H}| t_n + \rangle = -\mathcal{I}m\langle b_{n'}|\hat{H}|b_n\rangle + i\,\mathcal{I}m\langle b_{n'}|\hat{H}|\bar{b}_n\rangle. \tag{3.4.17}$$

Comparing the matrix elements in eqs. (3.4.13) to (3.4.16), we arrive at the following relations

$$\langle t_{n'} - |\hat{H}| t_n - \rangle = +\langle t_{n'} + |\hat{H}| t_n + \rangle^*, \tag{3.4.18}$$

$$\langle t_{n'} - |\hat{H}| t_n + \rangle = -\langle t_{n'} + |\hat{H}| t_n - \rangle^*. \tag{3.4.19}$$

By using the four identities in eqs. (3.4.14) to (3.4.17) and the related symmetry relations as in eqs. (3.4.18) to (3.4.19), we can reduce the size of the matrix to improve the computer storage and reduce the c.p.u. time. Remark added in passing: The discussed relations in addition demonstrate Kramers double degeneracy of the spectrum of the mean-field Hamiltonian.

Block-Diagonal Structure of the Hamiltonian. We obtained the symmetry relations, eqs. (3.4.9) to (3.4.10), in terms of the B-basis $\{|b_n\rangle; |\bar{b}_n\rangle\}$ for the time-reversal invariant Hamiltonian, which is the case of concern in this project. One can demonstrate that the analogous symmetry relations can be obtained for the simplex-invariant Hamiltonians, i.e., Hamiltonian commuting with $\hat{\mathcal{S}}_y$ operator, and we find:

$$\langle b_{n'}|\hat{H}|\bar{b}_n\rangle = \langle b_{n'}|\hat{H}|\bar{b}_n\rangle^* \quad \text{and} \quad \langle b_{n'}|\hat{H}|b_n\rangle = \langle b_{n'}|\hat{H}|b_n\rangle^*. \tag{3.4.20}$$

The above symmetry relations imply that the matrix elements of the Hamiltonian are all real. Under this condition only the real parts of the matrix elements in eqs. (3.4.14) and (3.4.15) need to be stored and the corresponding matrix in eq. (3.4.12) becomes block-diagonal. Consequently, with the help of the symmetry relation in eq. (3.4.18) we obtain the Hamiltonian matrices as below:

$$\hat{H} = \begin{pmatrix} \langle t_{n'} + |\hat{H}| t_n + \rangle & 0 \\ 0 & \langle t_{n'} + |\hat{H}| t_n + \rangle^* \end{pmatrix}. \tag{3.4.21}$$

Since the Hamiltonian must be hermitian, $\hat{H}^\dagger = \hat{H}$, the corresponding eigenvalues are all real. It follows that eigenvalues of $\langle t_{n'} + |\hat{H}| t_n + \rangle$ and $\langle t_{n'} + |\hat{H}| t_n + \rangle^*$ are identical. Therefore we arrive the conclusion that the spectrum of a hermitian, time-reversal invariant or plane reflection operator within a fermion basis must be at least double degenerate.

Chapter 4

Nuclear Pairing: BCS Theory

Following the results of our introductory discussion of the properties of nuclear interactions in Chapter 2, we can expect that the leading component in the standard, approximate description of nuclear Hamiltonian is represented by mean-field potential. The latter is accompanied by weaker but important, non-negligible, the so called residual-interaction components, among which pairing-interactions play the most important role. The presence of pairing interactions was deduced from the experimental observation that all known nuclei with even proton and even neutron numbers have the ground-state spins equal to 0, with no exception. Moreover, it has been established that there exist energy gaps between the ground-state and the first excited state in the spectra of even-even nuclei, the corresponding energy difference interpreted as an extra binding, coupling nucleons into pairs with equal but anti-parallel angular momenta. Therefore the pairing interaction must be considered in realistic nuclear structure calculations. Below we proceed discussing briefly the main lines of the underlying theory proposed first by Bardeen, Cooper, and Schrieffer, ref. [23], and referred to as BCS theory since.

The role of this chapter is to provide the language of the nuclear BCS theory to allow presenting the results obtained in this project together with the underlying definitions and notation. After brief introduction of the two-body characteristics of nuclear pairing, we present the variational treatment of the corresponding solution arriving at the formulation of the BCS equations. We also discuss an extension to cover the problem of collective rotation in the presence of the pairing interactions.

4.1 Nuclear Pairing: General Aspects

Let us consider a ground-state configuration of an even-even nucleus. The total nuclear spin corresponds to the sum of all nucleonic spins so that we can write:

$$\hat{I} \stackrel{df.}{=} \sum_{n=1}^{A} \hat{\jmath}_n, \quad \text{where} \quad \hat{\jmath} = \hat{l} + \hat{s}, \tag{4.1.1}$$

and where operators $\hat{l}$ and $\hat{s}$ represent nucleonic orbital and intrinsic angular momenta, respectively. Applying the square of the total nuclear angular momentum operator on the ground-state wave function we find

$$\hat{I}^2 |\Psi\rangle_{gs} = I(I+1)|\Psi\rangle_{gs}. \tag{4.1.2}$$

As mentioned above the experimental results for even-even nuclei are compatible only with $I \to I_{gs} = 0$, i.e., the sum of the nucleonic angular momenta equal to zero.

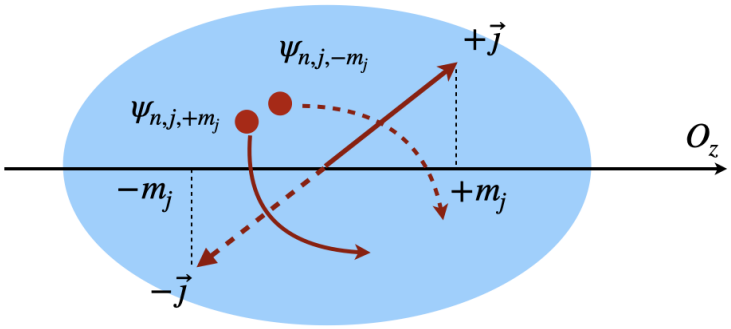

Figure 4.1.1 – *A schematic illustration of a motion of a nucleonic pair in a nucleus. The nucleonic angular momenta of these two nucleons are denoted by* $+\vec{\jmath}$ *and* $-\vec{\jmath}$ *and the related wave-functions are* $\psi_{n,j,+m_j}$ *and* $\psi_{n,j,-m_j}$.

Consider two nucleons moving in a prolate nucleus as shown schematically in figure (4.1.1). The corresponding nucleonic angular momenta, $+\hat{\jmath}$ and $-\hat{\jmath}$, must have opposite directions to assure vanishing of their sum. In what follows we will interpret such two nuclear states as time reversed partners. As discussed in section (2.6.1), the mean-field Hamiltonian leads to doubly degenerate states (Kramers degeneracy) and the solutions are:

$$\{e_n, \psi_n\} \to \{e_{\bar{n}} = e_n, \psi_{\bar{n}} = \hat{T}\psi_n\}, \tag{4.1.3}$$

where $\hat{T}$ is time-reversal operator. The nucleonic mean-field wave function in the so-called spherical representation can be written down as $\psi \leftrightarrow \psi_{n;j,m_j}$, where j and

m_j denote the angular momentum and its projection quantum numbers. One can demonstrate that the time-reversal partner state $\psi_{\bar{n}}$ is obtained by

$$\psi_{\bar{n}} \to \hat{T}\psi_{n;j,m_j} \sim \psi_{n;j,-m_j}. \tag{4.1.4}$$

Consequently, coupling the two angular momenta to zero can be seen as a coupling between $\{\psi_{n;j,m_j}\}$ and its time reversal partner $\{\psi_{n;j,-m_j}\}$.

Another important conclusion from the time-reversal partnership of states $\psi_{n,j,+m_j}$ and $\psi_{n,j,-m_j}$ is that these two states have the same spatial probability distributions. Indeed, since $\hat{T} \propto \hat{K}$ where the latter symbol represents complex conjugation, we find

$$P_n(\vec{r}) = |\psi_n(\vec{r})|^2 = \psi^*\psi \text{ and } P_{\bar{n}}(\vec{r}) = \hat{T}\psi_n^*(\vec{r})\psi_n(\vec{r}) = \psi_n(\vec{r})\psi_n^*(\vec{r}) = |\psi_n(\vec{r})|^2. \tag{4.1.5}$$

Thus the two nucleons in these two states have the biggest chances to be close to each other when moving in a nucleus suggesting that the underlying pairing interaction forcing them to reside in these states is of a short-range.

4.1.1 Nuclear Pairing and Its Interaction Hamiltonian

Employing the concept of the pairing interactions, the experimental results about the total spins of the nuclear ground-states mentioned earlier can be understood. Pairing interactions involve two-body nucleonic configurations, which implies the presence of two-body interactions in the corresponding approximation of the nuclear Hamiltonian:

$$\hat{H} = \sum_{i=1}^{N}[\hat{t}_i + \hat{V}_1(\hat{x}_i)] + \underbrace{\frac{1}{2}\sum_{i,j=1}^{N}\hat{V}_2(\hat{x}_i,\hat{x}_j)}_{\text{pairing interaction}}. \tag{4.1.6}$$

This two-body interaction is considered "weaker" as compared to the leading mean-field effect.

We may expect that the two-body pairing interaction leads to a scattering of fermions within pairs of time-reversed orbitals, the mechanism illustrated schematically in figure (4.1.2). Consequently, each nucleonic level can be considered being partly occupied and partly unoccupied. In order to describe this situation it is instructive to introduce the amplitudes of probability of occupation and un-occupation, denoted v_μ and u_μ respectively, and represent the wave-function of the system as a linear combination of these states,

$$\underbrace{u_\mu|0\rangle}_{\text{unoccupied state}} + \underbrace{v_\mu c_\mu^+ c_{\bar{\mu}}^+|0\rangle}_{\text{occupied state}}, \tag{4.1.7}$$

where c^+ and c represent the creation and annihilation operators, $|0\rangle$ denotes the corresponding vacuum state and $|\bar{\mu}\rangle$ is the time-reversal partner state of $|\mu\rangle$. According

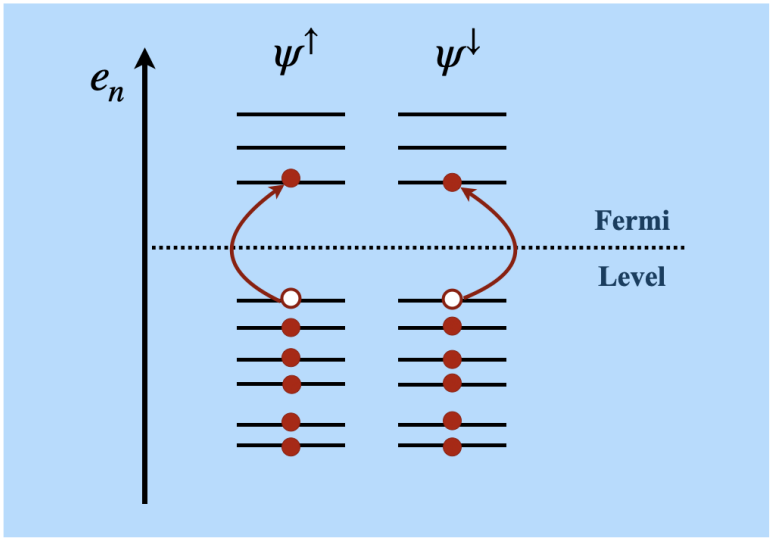

Figure 4.1.2 – *Schematic illustration of the nucleonic excitations with pairing interaction. This two-body interaction leads the scattering of pairs into the originally empty levels above the Fermi level marked as dotted line. Kramers-degenerate states are denoted* $\Psi^{\uparrow}$ *and* $\Psi^{\downarrow}$.

to this way of thinking an approximate wave function of a system takes the form of a product

$$|\Phi\rangle = \prod_{\mu}(u_\mu + v_\mu c_\mu^+ c_{\bar{\mu}}^+)|0\rangle, \tag{4.1.8}$$

with the normalisation condition

$$u_\mu^2 + v_\mu^2 = 1. \tag{4.1.9}$$

Let us recall that the general expression of the two-body Hamiltonian has the form

$$\hat{H} = \frac{1}{2}\sum_{\alpha\beta}\sum_{\gamma\delta}\langle\alpha\beta|\hat{V}|\gamma\delta\rangle c_\alpha^+ c_\beta^+ c_\delta c_\gamma. \tag{4.1.10}$$

Applying this general form to the pairing interaction leads to a reduced form specific for the pairing coupling between the 'spin-up' and the corresponding 'spin-down' states:

$$\hat{H}_p = \frac{1}{2}\sum_{\mu\nu} G_{\mu\nu} c_\mu^+ c_{\bar{\mu}}^+ c_{\bar{\nu}} c_\nu, \quad \text{with} \quad \langle\alpha\beta|\hat{V}|\gamma\delta\rangle \leftrightarrow \langle\mu\bar{\mu}|\hat{V}|\bar{\nu}\nu\rangle \equiv G_{\mu\nu}, \tag{4.1.11}$$

where $G_{\mu\nu}$ are referred to as pairing matrix elements.

4.2 Bardeen, Cooper and Schrieffer Theory

The original pairing theory was introduced for the first time in 1957 in condensed matter physics by Bardeen, Cooper, and Schrieffer (BCS), ref. [23], to explain electron superconductivity. It was extended by Bohr, Mottelson and Pines in ref. [24] in 1958, addressing nuclear systems to explain the energy gap mechanism in excitation spectra of nuclei, today understood with the help of the nuclear pairing interaction.

Basic Ideas. The first step in the BCS approximation is to construct the BCS trial wave-function in its variational form of eq. (4.1.8) with u_ν and v_ν coefficients playing the role of variational parameters. The underlying mathematical form implies that the pairing interaction creates couples composed of the time-reversal partner states with probability of occupation $|v_\nu|^2$ and the probability of un-occupation $|u_\nu|^2$, respectively. In order to find v_ν and u_ν one uses the variational Ansatz and minimises the expectation value of the Hamiltonian of the system using the Lagrange multiplier method to assure an approximate conservation of the particle numbers. Finally one obtains the so-called Bardeen-Cooper-Schrieffer (BCS) equations – for details see below.

4.2.1 Variational Solution of the Pairing Problem

Let us recall the form of the auxiliary function in eq. (4.1.8) as presented above with the unknown amplitudes v_ν and u_ν. This wave function with originally unknown amplitudes is usually called 'trial wave function'. To obtain the solutions, one way to proceed would be to express the expectation value of the Hamiltonian within the trial wave functions and find the parameters by a variational calculus as presented below. In our case we have

$$\langle\Phi|\hat{H}|\Phi\rangle \stackrel{df.}{=} h(\{u_\nu; v_\nu\}) = h(u, v), \tag{4.2.1}$$

where $h(u, v)$ is a known function. The parameters are determined by requiring that the solution corresponds to a minimum of the expected value of the Hamiltonian, knowing that $u_\nu^2 = 1 - v_\nu^2$:

$$\frac{\partial h}{\partial v_1} = 0, \ \frac{\partial h}{\partial v_2} = 0, \ ..., \ \frac{\partial h}{\partial v_n} = 0. \tag{4.2.2}$$

Therefore the minimum condition for the variation of the expectation value of the Hamiltonian takes the form

$$\delta\langle\Phi|\hat{H}|\Phi\rangle = \delta h(u, v) \stackrel{df.}{=} \frac{\partial h}{\partial v_1}\delta v_1 + \frac{\partial h}{\partial v_2}\delta v_2 + ... + \frac{\partial h}{\partial v_n}\delta v_n = 0. \tag{4.2.3}$$

Next, let us introduce the condition that the particle number operator satisfies the 'particle number conservation on the average', namely

$$\langle\Phi|\hat{N}|\Phi\rangle = n = \text{number of nucleons}, \tag{4.2.4}$$

where $\hat{N}$ is the particle number operator either for protons or for neutrons

$$\hat{N} \stackrel{df.}{=} \sum_{\nu}(c_{\nu}^{+}c_{\nu} + c_{\bar{\nu}}^{+}c_{\bar{\nu}}). \tag{4.2.5}$$

Thus in order to find the BCS wave function, the following two conditions must be satisfied at the same time:

$$\left.\begin{aligned}\delta\langle\Phi|\hat{H}|\Phi\rangle = 0\\ \langle\Phi|\hat{N}|\Phi\rangle = n\end{aligned}\right\}. \tag{4.2.6}$$

The above two equations can be solved using the Lagrange multiplier method. The theorem of Lagrange states that looking for a minimum of a function f under a subsidiary condition, $g = \text{const.}$, here expressed with the help of a certain function $g(x, y, ..., z)$:

$$\min\{f(x, y, ..., z)\} =? \quad \text{for} \quad g(x, y, ..., z) = \text{const.}, \tag{4.2.7}$$

is equivalent to a minimisation of a new function

$$F(x, y, ..., z) \stackrel{df.}{=} f(x, y, ..., z) - \lambda g(x, y, ..., z), \tag{4.2.8}$$

where the unknown parameter λ is called the Lagrange multiplier. We can write eq. (4.2.7) as

$$\frac{\partial F}{\partial x} = 0, \quad \frac{\partial F}{\partial y} = 0, \ \ldots, \frac{\partial F}{\partial z} = 0, \quad \text{and} \quad g(x, y, ..., z) = \text{const.} \tag{4.2.9}$$

From the above equations we have

$$\left.\begin{aligned} x_{\min} &= x_{\min}(\lambda)\\ y_{\min} &= y_{\min}(\lambda)\\ &\ldots\\ z_{\min} &= z_{\min}(\lambda)\end{aligned}\right\} \rightarrow g[x_{\min}(\lambda), y_{\min}(\lambda), ..., x_{\min}(\lambda)] = \text{const.}, \tag{4.2.10}$$

where the number of equations is the same as the number of the unknowns. Thus we can calculate the unknown solutions $x_{\min}, y_{\min}, \ldots$ and the unknown Lagrange multiplier by solving the above system of non-linear equations.

Conditional Minimum for the Hamiltonian. As discussed in section (4.1.1) the realistic Hamiltonian of the system is composed of the mean-field part and the pairing part. The latter one does not commute with the particle-number operator $\hat{N}$ with the consequence that the numbers of nucleons (protons and neutrons) remain unspecified in contrast to the physical/experimental situation. To counteract this contradiction we introduce an auxiliary condition requesting that the particle number conservation is at least present in terms of expected values. Following the theorem of Lagrange, we

introduce an auxiliary Hamiltonian, cf. eq. (4.2.8), containing the Lagrange multiplier term λ

$$\hat{H} \stackrel{df.}{=} \hat{H}_{mf} + \hat{H}_p - \lambda\hat{N}. \tag{4.2.11}$$

The variational solution for the "physical" Hamiltonian is equivalent to looking for the minimum of the expected value of the "auxiliary" Hamiltonian

$$\delta\langle\Phi|\hat{H}|\Phi\rangle = 0 \quad \leftrightarrow \quad \min_{\{u_\nu, v_\nu\}}\langle\Phi|\hat{H}|\Phi\rangle = ?, \tag{4.2.12}$$

more precisely,

$$\min_{\{u_\nu, v_\nu\}}\{\langle\Phi|(\hat{H}_{mf} - \lambda\hat{N})|\Phi\rangle + \langle\Phi|\hat{H}_p|\Phi\rangle = ?\}. \tag{4.2.13}$$

We will proceed to present briefly the evaluation of the involved terms.

4.2.2 Expectation Value of $\langle\Phi|(\hat{H}_{mf} - \lambda\hat{N})|\Phi\rangle$

Since the pairing Hamiltonian can be considered as a corrective term with respect to the mean-field Hamiltonian, we assume that the mean-field Hamiltonian has been already diagonalised to determine the core energy contribution so that pairing Hamiltonian will be discussed next using the mean-field solutions treated as a known reference.

The one-body Hamiltonian in the particle-number representation has the form

$$\hat{H}_{mf} = \sum_\mu \sum_\nu \langle\mu|\hat{H}|\nu\rangle c_\mu^+ c_\nu. \tag{4.2.14}$$

We consider diagonalisation of its matrix

$$\langle\mu|\hat{H}|\nu\rangle \to \delta_{\mu\nu} e_\nu, \tag{4.2.15}$$

and obtain the corresponding diagonal form,

$$\hat{H}_{mf} = \sum_\nu e_\nu c_\nu^+ c_\nu. \tag{4.2.16}$$

Consider next the Kramers degenerate states $e_\nu = e_{\bar{\nu}}$, and rewrite the corresponding mean-field Hamiltonian more explicitly as

$$\hat{H}_{mf} = \sum_\nu e_\nu (c_\nu^+ c_\nu + c_{\bar{\nu}}^+ c_{\bar{\nu}}). \tag{4.2.17}$$

Recall the definition for the particle-number operator with the notation adapted to the present case:

$$\hat{N} = \sum_\nu (c_\nu^+ c_\nu + c_{\bar{\nu}}^+ c_{\bar{\nu}}), \tag{4.2.18}$$

and rewrite the sought expectation value, with the operator composed of the mean-field and the particle-number terms

$$\begin{aligned}\langle\Phi|(\hat{H}_{mf}-\lambda\hat{N})|\Phi\rangle &= \langle\Phi|[\sum_{\nu}(e_\nu-\lambda)(c_\nu^+c_\nu+c_{\bar{\nu}}^+c_{\bar{\nu}})]|\Phi\rangle \\ &= \sum_{\nu}(e_\nu-\lambda)\langle\Phi|(c_\nu^+c_\nu+c_{\bar{\nu}}^+c_{\bar{\nu}})|\Phi\rangle. \end{aligned} \tag{4.2.19}$$

Recall the form of an auxiliary function in eq. (4.1.8). We can calculate an auxiliary expression $c_\nu|\Phi\rangle$ needed below,

$$\begin{aligned} c_\nu|\Phi\rangle &= c_\nu\prod_{\mu}(u_\mu+v_\mu c_\mu^+c_{\bar{\mu}}^+)|0\rangle \\ &= c_\nu(u_\nu+v_\nu c_\nu^+c_{\bar{\nu}}^+)\prod_{\mu\neq\nu}(u_\mu+v_\mu c_\mu^+c_{\bar{\mu}}^+)|0\rangle \\ &= [(u_\nu+v_\nu c_\nu^+c_{\bar{\nu}}^+)c_\nu+v_\nu c_{\bar{\nu}}^+]\prod_{\mu\neq\nu}(u_\mu+v_\mu c_\mu^+c_{\bar{\mu}}^+)|0\rangle \\ &= v_\nu c_{\bar{\nu}}^+\prod_{\mu\neq\nu}(u_\mu+v_\mu c_\mu^+c_{\bar{\mu}}^+)|0\rangle. \end{aligned} \tag{4.2.20}$$

Consider the corresponding hermitian conjugate term:

$$\langle\Phi|c_\nu^+ = (\langle\Phi|c_\nu^+)^\dagger = \langle\Phi|c_\nu. \tag{4.2.21}$$

According to eq. (4.2.20) we find

$$\langle\Phi|c_\nu^+ = v_\nu\langle 0|\prod_{\mu\neq\nu}(u_\mu+v_\mu c_\mu c_{\bar{\mu}})c_{\bar{\nu}}. \tag{4.2.22}$$

Using eqs. (4.2.20) and (4.2.22) one can demonstrate that

$$\langle\Phi|c_\nu^+c_\nu|\Phi\rangle = v_\nu^2 \quad\text{and}\quad \langle\Phi|c_{\bar{\nu}}^+c_{\bar{\nu}}|\Phi\rangle = v_{\bar{\nu}}^2 = v_\nu^2. \tag{4.2.23}$$

It follows that the expectation value of the particle number operator is

$$\langle\Phi|\hat{N}|\Phi\rangle = \sum_{\nu}\langle\Phi|(c_\nu^+c_\nu+c_{\bar{\nu}}^+c_{\bar{\nu}})|\Phi\rangle = 2\sum_{\nu}v_\nu^2. \tag{4.2.24}$$

Consequently, we find

$$\langle\Phi|(\hat{H}_{mf}-\lambda\hat{N})|\Phi\rangle = \sum_{\nu}2v_\nu^2(e_\nu-\lambda), \tag{4.2.25}$$

where e_ν represent the single-particle energies obtained by diagonalisation of the mean-field Hamiltonian, the v_ν^2 are the probabilities of occupation of the state e_ν, whereas the Lagrange multiplier λ is still to be determined.

4.2.3 Expectation Value of the Pairing Term $\langle\Phi|\hat{H}_p|\Phi\rangle$

Let us recall the expression of the pairing Hamiltonian,

$$\hat{H}_p = \frac{1}{2}\sum_{\mu\nu} G_{\mu\nu} c_\mu^+ c_{\bar{\mu}}^+ c_{\bar{\nu}} c_\nu. \tag{4.2.26}$$

To simplify the final expressions employed in the computer programming we will work with the so-called monopole paring approximation, which consists in replacing matrix $G_{\mu\nu}$ by a constant G, the latter playing the role of an average matrix element. We have in this case

$$\hat{H}_p = G\sum_{\mu\nu} c_\mu^+ c_{\bar{\mu}}^+ c_{\bar{\nu}} c_\nu. \tag{4.2.27}$$

For the time being we continue working with the more general pairing Hamiltonian to express the expectation value of interest as

$$\langle\Phi|\hat{H}_p|\Psi\rangle = \sum_{\mu\nu} G_{\mu\nu}\langle\Phi|c_\mu^+ c_{\bar{\mu}}^+ c_{\bar{\nu}} c_\nu|\Phi\rangle. \tag{4.2.28}$$

Recall the result in eq. (4.2.20). We have

$$c_\nu|\Phi\rangle = v_\nu c_{\bar{\nu}}^+ \prod_{\rho\neq\nu}(u_\rho + v_\rho c_\rho^+ c_{\bar{\rho}}^+)|0\rangle. \tag{4.2.29}$$

Let us calculate the following expression

$$\begin{aligned} c_{\bar{\nu}} c_\nu|\Phi\rangle &= v_\nu c_{\bar{\nu}} c_{\bar{\nu}}^+ \prod_{\rho\neq\nu}(u_\rho + v_\rho c_\rho^+ c_{\bar{\rho}}^+)|0\rangle \\ &= v_\nu \prod_{\rho\neq\nu}(u_\rho + v_\rho c_\rho^+ c_{\bar{\rho}}^+)\underbrace{c_{\bar{\nu}} c_{\bar{\nu}}^+|0\rangle}_{|0\rangle} \\ &= v_\nu \prod_{\rho\neq\nu}(u_\rho + v_\rho c_\rho^+ c_{\bar{\rho}}^+)|0\rangle, \end{aligned} \tag{4.2.30}$$

and similarly

$$\langle\Phi|c_\mu^+ c_{\bar{\mu}}^+ = \langle 0|v_\mu \prod_{\kappa\neq\mu}(u_\kappa + v_\kappa c_\kappa^+ c_{\bar{\kappa}}^+). \tag{4.2.31}$$

Substituting results from eqs. (4.2.30) and (4.2.31) into eq. (4.2.28), we find the expectation value of the pairing Hamiltonian

$$\begin{aligned} \langle\Phi|\hat{H}_p|\Phi\rangle &= \sum_{\mu\nu} G_{\mu\nu}\langle\Phi|c_\mu^+ c_{\bar{\mu}}^+ c_{\bar{\nu}} c_\nu|\Phi\rangle \\ &= \sum_{\mu\nu} G_{\mu\nu} v_\nu v_\mu \underbrace{\langle 0|\prod_{\kappa\neq\mu}(u_\kappa + v_\kappa c_\kappa^+ c_{\bar{\kappa}}^+)}_{\langle\Phi_\mu|}\underbrace{\prod_{\rho\neq\nu}(u_\rho + v_\rho c_\rho^+ c_{\bar{\rho}}^+)|0\rangle}_{|\Phi_\nu\rangle} \end{aligned}$$

$$= \sum_{\mu\nu} G_{\mu\nu} v_\nu v_\mu \langle \Phi_\mu | \Phi_\nu \rangle, \tag{4.2.32}$$

where we have taken note of the non-orthogonality[1] of the wave-functions in question

$$\langle \Phi_\nu | \Phi_\mu \rangle = u_\nu u_\mu. \tag{4.2.38}$$

The final result for the expected value of the pairing Hamiltonian takes the form

$$\langle \Phi | \hat{H}_p | \Phi \rangle = \sum_{\mu\nu} G_{\mu\nu} v_\nu v_\mu u_\nu u_\mu. \tag{4.2.39}$$

Let us introduce the quantity which will be called from now on the energy gap

$$\Delta_\nu \stackrel{df.}{=} \sum_{\mu} G_{\nu\mu} u_\mu v_\mu. \tag{4.2.40}$$

With the help of this notation, the expectation value of the pairing Hamiltonian can be written down in a simplified form

$$\langle \Phi | \hat{H}_p | \Phi \rangle = \sum_{\nu} \Delta_\nu v_\nu u_\nu. \tag{4.2.41}$$

We proceed now to combine the two contributions discussed so far.

[1] Consider an auxiliary wave function

$$|\Phi_\mu\rangle = \prod_{\rho \neq \mu} (u_\rho + v_\rho c_\rho^+ c_{\bar{\rho}}^+) |0\rangle, \tag{4.2.33}$$

and observe that the $(u_\mu + v_\mu c_\mu^+ c_{\bar{\mu}}^+)$ factor is missing in the above wave function. Thus we introduce a new notation

$$|\Phi_\mu\rangle = (u_\nu + v_\nu c_\nu^+ c_{\bar{\nu}}^+) |\Phi_{\nu\mu}\rangle. \tag{4.2.34}$$

Therefore the overlap of the two auxiliary wave functions reads

$$\begin{aligned} \langle \Phi_\nu | \Phi_\mu \rangle &= \langle \Phi_{\nu\mu} | (u_\mu + v_\mu c_\mu c_{\bar{\mu}}) \cdot (u_\nu + v_\nu c_\nu^+ c_{\bar{\nu}}^+) | \Phi_{\nu\mu} \rangle \\ &= \langle \Phi_{\mu\nu} | (u_\mu u_\nu + u_\mu v_\nu c_\nu^+ c_{\bar{\nu}}^+ + v_\mu u_\nu c_\mu c_{\bar{\mu}} + v_\mu v_\nu c_\mu c_{\bar{\mu}} c_\nu^+ c_{\bar{\nu}}^+) | \Phi_{\nu\mu} \rangle. \end{aligned} \tag{4.2.35}$$

Since $\Phi_{\nu\mu}$ by definition does not contain neither μ nor ν operators, we have

$$c_\mu c_{\bar{\mu}} |\Phi_{\mu\nu}\rangle = 0 \quad \text{and} \quad \langle \Phi_{\mu\nu} | c_\nu^+ c_{\bar{\nu}}^+ = 0. \tag{4.2.36}$$

Consequently, we obtain

$$\langle \Phi_\nu | \Phi_\mu \rangle = u_\mu u_\nu \underbrace{\langle \Phi_{\mu\nu} | \Phi_{\mu\nu} \rangle}_{1} = u_\mu u_\nu. \tag{4.2.37}$$

4.2.4 Variational Procedure

So far we have calculated the expectation values for the one-body Hamiltonian and pairing Hamiltonian in eqs. (4.2.25) and (4.2.41) separately. The total expectation value reads

$$\langle\Phi|\hat{H}_{mf} - \lambda\hat{N} + \hat{H}_p|\Phi\rangle = \sum_\nu 2v_\nu^2(e_\nu - \lambda) + \sum_\nu \Delta_\nu v_\nu u_\nu \stackrel{df.}{=} h(u_\nu, v_\nu). \tag{4.2.42}$$

This implies that the sought expectation value is a function of the coefficients (u_ν, v_ν), which satisfy the normalisation condition $u_\nu^2 + v_\nu^2 = 1$. Therefore the variational condition for the minimum of the expected value of the Hamiltonian in eq. (4.2.13) takes the form

$$\delta\langle\Phi|\hat{H}|\Phi\rangle = \delta h(u_\nu, v_\nu) = 0. \tag{4.2.43}$$

The latter condition implies that

$$\frac{\partial h}{\partial u_\nu} = 0 \quad \text{and} \quad \frac{\partial h}{\partial v_\nu} = 0, \quad \forall\,\nu. \tag{4.2.44}$$

From the normalisation condition

$$u_\nu^2 + v_\nu^2 = 1 \quad \rightarrow \quad 2\frac{\partial u_\nu}{\partial v_\nu}u_\nu + 2v_\nu = 0, \tag{4.2.45}$$

and we find that

$$\frac{\partial u_\nu}{\partial v_\nu} = -\frac{v_\nu}{u_\nu}. \tag{4.2.46}$$

We can calculate the partial derivatives in eq. (4.2.44) in terms of the above relation. We find

$$\frac{\partial h}{\partial v_\nu} = 4v_\nu(e_\nu - \lambda) + 2\Delta_\nu\left(u_\nu - \frac{v_\nu^2}{u_\nu}\right) = 0, \tag{4.2.47}$$

and the new, simplified expression reads

$$2u_\nu v_\nu(e_\nu - \lambda) + \Delta_\nu(u_\nu^2 - v_\nu^2) = 0. \tag{4.2.48}$$

Equation (4.2.48) represents a set of non-linear algebraic equations for the amplitudes (v_ν, u_ν). Taking into account the normalisation relation between these parameters, one can demonstrate that the solutions, eq. (4.2.48), satisfy

$$v_\nu^2 = \frac{1}{2}\left(1 - \frac{e_\nu - \lambda}{E_\nu}\right) \quad \text{and} \quad u_\nu^2 = \frac{1}{2}\left(1 + \frac{e_\nu - \lambda}{E_\nu}\right), \tag{4.2.49}$$

where

$$E_\nu \stackrel{df.}{=} \sqrt{(e_\nu - \lambda)^2 + \Delta_\nu^2}, \tag{4.2.50}$$

and where the last term is usually referred to as “quasi-particle energy”.

4.2.5 Bardeen-Copper-Schrieffer (BCS) Equations

We just found the solutions, cf. eq. (4.2.49), of the variational problem, however, the occupation probabilities contain unknown parameters, the Lagrange multiplier λ and pairing gap parameters Δ_ν. From the relations in eqs. (4.2.49), we find

$$v_\nu^2 u_\nu^2 = \frac{1}{4}\left[1 - \frac{(e_\nu - \lambda)^2}{E_\nu^2}\right] = \frac{1}{4}\frac{\Delta_\nu^2}{(e_\nu - \lambda)^2 + \Delta_\nu^2}, \tag{4.2.51}$$

and thus the term $v_\nu u_\nu$ takes the form

$$v_\nu u_\nu = \frac{1}{2}\frac{\Delta_\nu}{\sqrt{(e_\nu - \lambda)^2 + \Delta_\nu^2}}. \tag{4.2.52}$$

Let us substitute the above into the pairing gap expression, eq. (4.2.40) and the particle number condition repeated below

$$\Delta_\mu = \sum_\nu G_{\mu\nu} v_\nu u_\nu \quad \text{and} \quad N = \sum_\nu 2v_\nu^2, \tag{4.2.53}$$

and obtain in this way the non-linear system of nuclear Bardeen-Cooper-Schrieffer (BCS) equations

$$\Delta_\mu = \frac{1}{2}\sum_\nu G_{\mu\nu}\frac{\Delta_\nu}{\sqrt{(e_\nu - \lambda)^2 + \Delta_\nu^2}}, \tag{4.2.54}$$

$$N = \sum_\nu \left[1 - \frac{e_\nu - \lambda}{\sqrt{(e_\nu - \lambda)^2 + \Delta_\nu^2}}\right]. \tag{4.2.55}$$

Observe in passing that we obtained in this way a system of $(N+1)$ equations for the unknown gap parameters, $\{\Delta_\nu\}$, one per each single nucleonic energy level and the Fermi energy λ.

Simplified Version of the Pairing Hamiltonian: Monopole Pairing. Consider the monopole pairing strength G, cf. eqs. (4.2.25) and (4.2.26). Introducing related simplification into eq. (4.2.39) we find

$$\Delta_\mu \to \Delta = G\sum_\nu v_\nu u_\nu, \tag{4.2.56}$$

from where the simplified system of only two BCS equations follows

$$\frac{2}{G} = \sum_\nu \frac{1}{\sqrt{(e_\nu - \lambda)^2 + \Delta_\nu^2}}, \tag{4.2.57}$$

$$N = \sum_\nu \left[1 - \frac{e_\nu - \lambda}{\sqrt{(e_\nu - \lambda)^2 + \Delta_\nu^2}}\right]. \tag{4.2.58}$$

Now we have only 2 non-linear algebraic equations and two unknown parameters λ and Δ. The above equations are also called gap and particle number equations, respectively.

Critical *G*-value. We notice that $\Delta^2 \geq 0$; this implies

$$\frac{2}{G} = \sum_{\nu}^{n} \frac{1}{\sqrt{(e_\nu - \lambda)^2 + \Delta_\nu^2}} \leq \sum_{\nu}^{n} \frac{1}{|e_\nu - \lambda|}. \tag{4.2.59}$$

It follows that for a given spectrum $\{e_\nu\}$, we have

$$\frac{1}{G} \leq \frac{1}{2} \sum_{\nu}^{n} \frac{1}{|e_\nu - \lambda|} \stackrel{df.}{=} \frac{1}{G_{\text{crit.}}}. \tag{4.2.60}$$

Thus the solution $\Delta > 0$ can be obtained if and only if

$$G \geq G_{\text{crit.}} \tag{4.2.61}$$

This is equivalent to saying that there exists a critical paring strength $G_{\text{crit.}}$: for $G > G_{\text{crit.}}$ we obtain the solution with $\Delta \neq 0$ while for $G \leq G_{\text{crit.}}$ there exists only a trivial solution $\Delta = 0$. Experiments show that among 3000 known nuclei, the great majority of them have $\Delta \neq 0$ in their ground-states and only very few of them have $\Delta = 0$.

4.3 Collective Rotation and Rotating Mean-Field

Because of the very short range of nuclear interactions, the nucleus can be considered as a highly compact object with the density nearly constant in the nuclear interior, quickly dropping down to zero "at the nuclear borders". This allows for introducing the concept of nuclear surface, nuclear shape, and nuclear orientation, the latter concept allowing to introduce the notion of collective nuclear rotation.

Historically, the nuclear rotational motion was introduced to interpret the existence of excitation spectra with very characteristic regularities of the type $E_I \propto I(I+1)$. Rotational mode was a necessary consequence of the existence of non-spherical or even strongly deformed shapes, cf. ref. [13]. Analysing the electromagnetic transition probabilities and in particular the electric quadrupole ($E2$) transitions gave additional evidence for the notion of the collectivity of the underlying effect.

The rotational motion of an object, by definition, implies the change of its orientation in space. One can demonstrate that a quantum object cannot rotate about its symmetry axis, so that the only geometrical configurations allowed are those shown schematically in figure (4.3.1).

Experiments show that the level sequences of the rotational excitations are to a good approximation quadratic in terms of the total angular momenta,

$$E(I) = \alpha(Z,N)R(R+1), \tag{4.3.1}$$

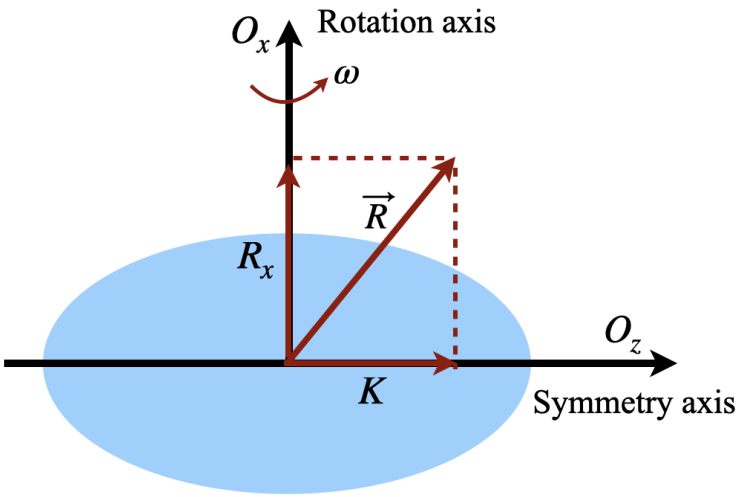

Figure 4.3.1 – *Schematic illustration of the collective nuclear rotation. The symmetry axis is denoted $\mathcal{O}_z$, the rotation axis $\mathcal{O}_x$, the rotational frequency is demoted by $\vec{\omega}$ and K is the projection of the rotational angular momentum $\vec{R}$ onto the symmetry axis.*

where proportionality coefficient, $\alpha(Z,N)$, generally depends on the proton and neutron numbers, R denotes the rotational angular momentum quantum number; it takes integer values for even-even and odd-odd nuclei and half-integer values for odd-even and even-odd nuclei.

In analogy to a rotational motion of a rigid body with the moment of inertia $\mathcal{J}_{\text{class.}}$, and the angular momentum $\vec{L}$ in classical physics,

$$E_{\text{class.}}(\vec{L}) = \frac{\vec{L}^2}{2\mathcal{J}_{\text{class.}}}, \tag{4.3.2}$$

we may introduce the Hamiltonian of the quantum analogue

$$\hat{H}(\hat{R}) = \frac{\hat{R}^2}{2\mathcal{J}} \quad \rightarrow \quad \vec{L} \leftrightarrow \hat{R}. \tag{4.3.3}$$

According to the quantum mechanics, the eigenvalues of the square of the angular momentum $\hat{R}^2$ are given by $R(R+1)$, and thus the energies for the quantum rigid rotor can be written as

$$E_I = \frac{R(R+1)\hbar^2}{2\mathcal{J}}. \tag{4.3.4}$$

Comparing eqs. (4.3.4) and (4.3.1) we find the correspondence between α and the moment of inertia,

$$\alpha(Z,N) = \frac{\hbar^2}{2\mathcal{J}_{\text{nucl.}}}. \tag{4.3.5}$$

Remark: The units of the nuclear moments of inertia are $\hbar^2/MeV$.

4.3.1 Moment of Inertia and Rotational Frequency

The moment of inertia of a rigid body in classical physics is the quantity which determines the nuclear reaction to the acceleration/de-acceleration in terms of the rotational frequency of the rotor. The kinetic energy of a classical rotor can be expressed using the associated frequency of rotation ω, which in classical mechanics satisfies:

$$E_{\text{rotor}}(\omega) = \frac{1}{2}\mathcal{J}_{\text{class.}}\omega^2 \;\text{ in analogy with }\; E_{\text{particle}}(v) = \frac{1}{2}mv^2; \tag{4.3.6}$$

observe analogy in describing the inertia, $\mathcal{J}_{\text{class.}}$ in the case of rotation, and the mass of the particle m in the case particle's translational motion.

Consider the relation between the classical angular momentum L and the velocity of rotation (frequency) ω:

$$L = \mathcal{J}_{\text{class.}}\,\omega \;\rightarrow\; \omega = \frac{L}{\mathcal{J}_{\text{class.}}}, \;\text{ compare with }\; p = mv \rightarrow v = \frac{p}{m}. \tag{4.3.7}$$

Let us substitute the above relation into eq. (4.3.6) obtaining again the previously seen expression

$$E_{\text{class.}}(L) = \frac{L^2}{2\mathcal{J}_{\text{class.}}}. \tag{4.3.8}$$

It follows that

$$\frac{dE_{\text{class.}}}{dL} = \frac{L}{\mathcal{J}_{\text{class.}}} = \omega. \tag{4.3.9}$$

In analogy we may conjecture a similar relation for the quantum rotor as follows,

$$E_R = \frac{R^2}{2\mathcal{J}} \rightarrow \frac{dE_R}{d\,R} = \frac{R}{\mathcal{J}} = \omega. \tag{4.3.10}$$

Comments. The above relation must be taken with a dose of scepticism: The quantum energies are discrete, and not continuous functions of the angular momentum variable R, the latter taking integer or half-integer values so that the derivative expression strictly speaking makes no sense. However, one may defend the idea of using the above analogy with the derivative formula for the particular case of the semi-classical relations with a very regular $E - vs. - R$ dependence, which is indeed the case in nuclear physics. With this extra condition in mind we can write

$$\omega_R \approx \frac{dE_R}{d\,R} \overset{df.}{=} \frac{E_{R+1} - E_{R-1}}{(R+1) - (R-1)}, \tag{4.3.11}$$

where the finite difference expression has been used to approximate the derivative.

Kinematical Moments of Inertia. For a nuclear system with a given rotational frequency ω_R and the related total angular momentum R, in analogy to eq. (4.3.7), the so-called kinematical moment of inertia is defined as

$$\mathcal{J}^{(1)}(R) \overset{df.}{=} \frac{R}{\omega_R}. \tag{4.3.12}$$

The superscript "(1)" has been introduced to emphasise the fact that this quantity depends on the first derivative of the energy vs. angular momentum.

Dynamical Moments. The so-called dynamical moment (observe that we do not use the term moment of "inertia" in this case, since the discussed quantity can become negative) is quite sensitive to the change of the kinematical moments of inertia. This quantity is formally defined in terms of the second derivative of the energy vs. angular momentum R

$$\mathcal{J}^{(2)}(R) \stackrel{df.}{=} \frac{1}{\left(\frac{d^2E}{dR^2}\right)} = \frac{1}{\frac{d}{dR}\left(\frac{dE}{dR}\right)} = \frac{1}{\left(\frac{d\omega_R}{dR}\right)} = \frac{dR}{d\,\omega_R}. \tag{4.3.13}$$

Thus the relation between $\mathcal{J}^{(1)}$ and $\mathcal{J}^{(2)}$ is

$$\mathcal{J}^{(2)} = \frac{dR}{d\,\omega_R} = \frac{d}{d\,\omega_R}(\mathcal{J}^{(1)}\omega_R) = \mathcal{J}^{(1)} + \omega_R \frac{d\,\mathcal{J}^{(1)}}{d\,\omega_R}. \tag{4.3.14}$$

Let us note the use of the superscript "(2)" in this case to emphasise that the just introduced quantity depends on the second order derivative of energy vs. angular momentum.

4.3.2 Individual Nucleons and Collective Rotational Motion

Let us note that the energies of transitions connecting the lowest rotational states observed experimentally, vary typically from dozens of keV in mid-mass nuclei to few keV in heavy nuclei, say $\Delta E_R \sim 10$ keV. A schematic illustration of the observed relations is shown in figure (4.3.2) (left fragment). It follows that, on average, one nucleon contributes of the order of $\delta E_{\text{per nucleon}} = \Delta E_R/A \sim 10^{-1}$-to-$10^{-2}$ keV.

Consider nucleons moving in the mean-field potential with the central potential depth of the order of 50 MeV, as shown schematically in figure (4.3.2) (right). On average one nucleon carries the kinetic energy of the order of $\hbar\omega_\nu \sim 25$ MeV. Therefore we observe that the collective rotational motion can be treated as a small perturbation impacting the nucleonic energies at the level of one-to-two orders of magnitude less.

On the other hand the rotational transition energies are given by $\Delta E_R = \hbar\omega_{\text{rot.}}$ in terms of rotational frequencies, whereas an average energy of the individual nucleonic motion is $e_\nu = \hbar\omega_\nu$, and it follows that $\omega_{\text{rot.}} \ll \omega_\nu$. This allows us to describe the uniform rotational motion of the nucleus as induced by a slow collective rotation in each given rotational state.

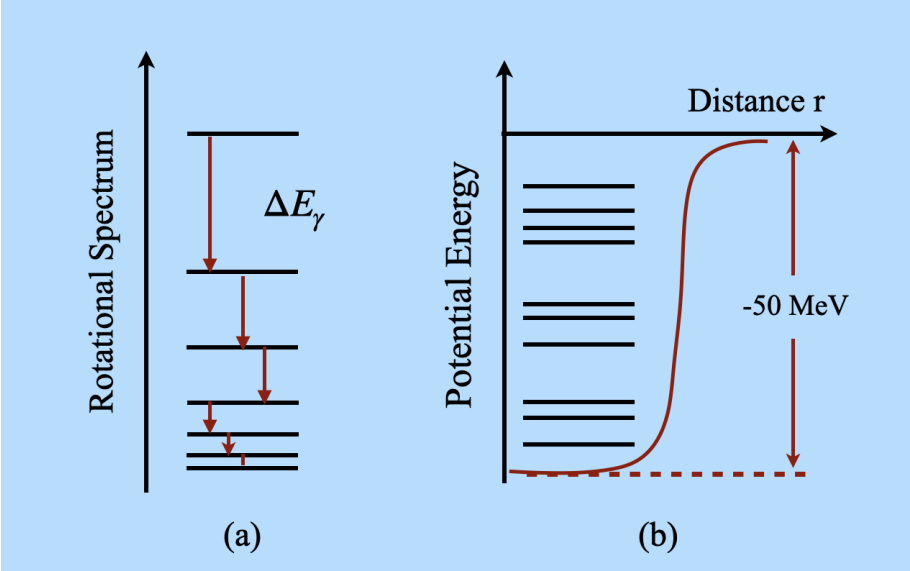

Figure 4.3.2 – *Schematic: (a) Rotational spectrum depending parabolically on the nuclear angular momentum, cf. eq. (4.3.4). Experimental data show that the lowest transition energies are of the order of a dozen of keV for the nuclei with $A > 200$. (b) Schematic illustration of the central potential of nuclear mean-field Hamiltonian. The depth of the potential is about -50 MeV, and it follows that, on average, one nucleon carries the kinetic energy of the order of $\hbar\omega_\nu \sim 25$ MeV.*

To simplify the description of the nuclear collective rotational motion, often the rotating reference frame, also called the body-fixed frame, is considered. This notion allows introducing the concept of the cranking approximation also referred to as the so-called hypothesis of adiabatic enforced rotation, which was suggested originally by Inglis, ref. [25].

4.3.3 Cranking Approximation

The cranking approximation is one of the most powerful theoretical concepts in describing both the collective rotational bands and the high-spin state configurations in nuclei. A direct way to investigating rotating nuclei is to rotate or 'crank' the nucleus with some rotational frequency. The basic idea of the cranking approximation is to treat the rotation of the nucleus as a perturbation to the mean-field potential, whereas the mean-field Hamiltonian rotates with the same rotational frequency as the nucleus. To simplify the theoretical description of a rotating system, the body-fixed frame is considered rotating with the frequency ω with respect to the laboratory frame as shown in figure (4.3.3).

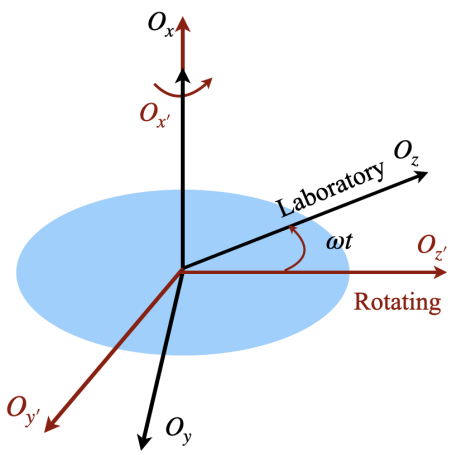

Figure 4.3.3 – *Schematic illustration of a rotating nucleus; the laboratory reference frame,* $\{O_x, O_y, O_z\}$*, and the body-fixed frame,* $\{O_{x'}, O_{y'}, O_{z'}\}$ *are shown.*

Laboratory and Body-Fixed Reference Frames. Let us consider the original time-dependent Schrödinger equation written in the laboratory frame as

$$\Sigma_{\text{lab.}}: \quad i\hbar\frac{\partial\psi_{\text{lab.}}}{\partial t} = \hat{H}_{\text{lab.}}\psi_{\text{lab.}}. \tag{4.3.15}$$

Next, consider a nucleus rotating about O_x-axis. The corresponding rotation operator connecting the two reference frames has the usual form

$$\hat{R}_x = e^{-i\,\omega t\,\hat{j}_x}, \tag{4.3.16}$$

where $\hat{j}_x$ is the x-component of the total angular momentum operator (observe the notation difference: in eqs. (4.3.10) and onwards, $\vec{R}$ denotes the rotational angular momentum of a nucleus, whereas above, $\hat{R}_x$ is an operator of rotation connecting body-fixed and laboratory reference frames). The corresponding relation between the wave-function and Hamiltonian in the laboratory-, and the body-fixed frames, can be expressed as follows

$$\psi_{\text{lab.}} = \hat{R}_x\psi_{\text{rot.}} = e^{-i\omega\,t\hat{j}_x}\psi_{\text{rot.}}, \tag{4.3.17}$$

and

$$\hat{H}_{\text{lab.}} = \hat{R}_x\hat{H}_{\text{rot.}}\hat{R}_x^{-1}. \tag{4.3.18}$$

By inserting eqs. (4.3.17) and (4.3.18) into eq. (4.3.15), we obtain the Schrödinger equation in the body-fixed (rotating) reference frame,

$$\Sigma_{\text{rot.}}: \quad i\hbar\frac{\partial\psi_{\text{rot.}}}{\partial t} = \hat{H}^{\omega}\psi_{\text{rot.}}, \tag{4.3.19}$$

in which

$$\hat{H}^{\omega} \stackrel{df.}{=} \hat{H}_{\text{rot.}} - \hbar\omega\hat{j}_x, \tag{4.3.20}$$

is called cranking Hamiltonian or Routhian and "-$\hbar\omega\hat{j}_x$" is called "cranking term". As mentioned earlier, the basic idea behind the cranking approximation is to follow the fact that the mean-field Hamiltonian in the rotating coordinate frame does not depend on time and thus takes the simplest form when constructing the solutions. This means that we can replace the $\hat{H}_{\text{rot.}}$ by the static, original mean-field Hamiltonian $\hat{H}$, and thus rewrite the above expression as

$$\hat{H}^{\omega} = \hat{H} - \hbar\omega\hat{j}_x. \tag{4.3.21}$$

The Routhian $\hat{H}^{\omega}$ can be seen as the Hamiltonian in the body-fixed reference frame. Since $\hat{H}^{\omega}$ dose not depend on time, the solution of the Schrödinger equation with the above effective Hamiltonian can be obtained by solving the eigenvalue problem of $\hat{H}^{\omega}$ using the standard diagonalisation methods,

$$\hat{H}^{\omega}|\psi_n^{\omega}\rangle = E_n^{\omega}|\psi_n^{\omega}\rangle. \tag{4.3.22}$$

The total Routhian operator $\hat{H}^{\omega}$ is the sum of the single-particle operators

$$\hat{H}^{\omega} = \sum_i \hat{h}_i^{\omega} = \sum_i [\hat{h}_i - \hbar\omega(\hat{j}_x)_i], \tag{4.3.23}$$

where $\hat{j}_x$ is the projection of the nucleonic angular momentum operator on the O_x-axis. Thus we can write the eigenvalue equation of Routhian operator of each single-particle as

$$\hat{h}_i^{\omega}|\psi_i^{\omega}\rangle = e_i^{\omega}|\psi_i^{\omega}\rangle, \tag{4.3.24}$$

where the e_i^{ω} denotes the corresponding single-particle Routhian, i.e., the energy in the rotating coordinate frame. The energies e_i in the laboratory frame are calculated as the expectation values of the Hamiltonian $\hat{h}_i$ with the eigenfunction $|\psi_i^{\omega}\rangle$,

$$\begin{aligned} e_i = \langle\psi_i^{\omega}|\hat{h}_i|\psi_i^{\omega}\rangle &= \langle\psi_i^{\omega}|[\hat{h}_i^{\omega} + \hbar\omega(\hat{j}_x)]|\psi_i^{\omega}\rangle \\ &= e_i^{\omega} + \hbar\omega\langle\psi_i^{\omega}|\hat{j}_x|\psi_i^{\omega}\rangle. \end{aligned} \tag{4.3.25}$$

Within the mean-field approximation (of non-interacting particles) the total energies E_n in the laboratory frame can be expressed as

$$E_n = \sum_{i=1}^{n} e_i^{\omega} + \hbar\omega \sum_{i=1}^{n} \langle\psi_i^{\omega}|\hat{j}_x|\psi_i^{\omega}\rangle. \tag{4.3.26}$$

According to eq. (4.3.25), we can write the single-particle Routhian eigen-value as

$$e_i^{\omega} = e_i - \hbar\omega\langle\psi_i^{\omega}|\hat{j}_x|\psi_i^{\omega}\rangle. \tag{4.3.27}$$

This implies

$$\frac{de_i^{\omega}}{d\omega} = -\hbar\langle\psi_i^{\omega}|\hat{j}_x|\psi_i^{\omega}\rangle, \tag{4.3.28}$$

the relation showing that the slope of the single-particle Routhian is equal to the expectation value of the angular momentum of j_x with reversed sign, and

$$j_x = -\frac{1}{\hbar}\frac{de_i^{\omega}}{d\omega}. \tag{4.3.29}$$

The projection of the total angular momentum I_x along the axis of collective rotation, here O_x, can be obtained by summing up

$$I_x = \sum_{i=1}^{n} j_x^i = \sum_{i=1}^{n}\langle\psi_i^{\omega}|\hat{j}_x|\psi_i^{\omega}\rangle. \tag{4.3.30}$$

The just presented properties apply to the mean-field nuclear description without pairing correlations. The generalisation for the case of pairing will be discussed next.

4.3.4 Cranking Hamiltonian with Pairing Interactions

The Routhian shown in eq. (4.3.22) corresponds to the rotation about O_x-axis. It follows that in the presence of all the three angular momentum components,

$$\hat{H}^{\vec{\omega}} = \hat{H}_{\rm mf} - \hbar\vec{\omega}\cdot\hat{j}, \tag{4.3.31}$$

where

$$\vec{\omega}\cdot\hat{j} = \omega_x\hat{j}_x + \omega_y\hat{j}_y + \omega_z\hat{j}_z, \tag{4.3.32}$$

represents the cranking term in the 3D-space. The scalar product of the rotational frequency vector and the angular momentum represents the projection of the angular momentum onto the axis of rotation. Following eq. (4.3.31), the general form of the nuclear Routhian in the presence of the pairing interactions can be written as follows

$$\hat{H}^{\vec{\omega}} = \hat{H}_{\rm mf} - \hbar\vec{\omega}\cdot\hat{j} + \hat{H}_{\rm pair.} \tag{4.3.33}$$

Routhian $\hat{H}^{\vec{\omega}}$ can be seen as the mean-field Hamiltonian in the body-fixed reference frame, $\hat{H}_{\rm mf}$ represents the phenomenological Woods-Saxon Hamiltonian in the laboratory frame, the cranking term $\vec{\omega}\cdot\hat{j}$ originates from the transforming from the laboratory to the body-fixed reference frame, whereas the pairing Hamiltonian, $\hat{H}_{\rm pair.}$ above, is given by eq. (4.2.26),

$$\hat{H}_p = \sum_{\mu\nu} G_{\mu\nu}c_{\mu}^{+}c_{\bar{\mu}}^{+}c_{\bar{\nu}}c_{\nu}. \tag{4.3.34}$$

Using the particle number representation we can write the Routhian in eq. (4.3.33) as

$$\hat{H}^{\vec{\omega}} = \sum_{\mu\nu}\langle\mu|\hat{H}_{\rm mf}|\nu\rangle c^{+}_{\mu}c_{\nu} - \hbar\sum_{\mu\nu}\langle\mu|\vec{\omega}\cdot\hat{\jmath}|\nu\rangle c^{+}_{\mu}c_{\nu} + \sum_{\mu\nu}G_{\mu\nu}c^{+}_{\mu}c^{+}_{\bar{\mu}}c_{\bar{\nu}}c_{\nu}. \tag{4.3.35}$$

As discussed in section (4.2), within the BCS approximation, the approximate solution for the nuclear Hamiltonian composed of the mean-field and pairing terms can be calculated by minimising the expected value of the sum of them, under the condition of the particle number conservation in eq. (4.2.5), using Lagrange-multiplier method. Consequently, by introducing the Lagrange multiplier λ and the particle number operator $\hat{N}$, the mean-field Hamiltonian in the body-fixed frame is redefined as

$$\hat{H}^{\vec{\omega}} = \hat{H}_{\rm mf} + \hat{H}_{\rm pair.} - \hbar\vec{\omega}\cdot\hat{\jmath} - \lambda\hat{N}, \tag{4.3.36}$$

with the particle number operator

$$\hat{N} = \sum_{\nu=1}^{n} c^{+}_{\nu}c_{\nu}, \quad n = Z\,\text{or}\,\text{N}. \tag{4.3.37}$$

Therefore the Routhian in the second quantisation representation, eq. (4.3.35) can be rewritten as follows

$$\hat{H}^{\vec{\omega}} = \sum_{\mu\nu}[h_{\mu\nu} - \hbar(\vec{\omega}\cdot\hat{\jmath})_{\mu\nu} - \lambda\delta_{\mu\nu}]c^{+}_{\nu}c_{\nu} + \sum_{\mu\nu}G_{\mu\nu}c^{+}_{\mu}c^{+}_{\bar{\mu}}c_{\bar{\nu}}c_{\nu}, \tag{4.3.38}$$

in which $h_{\mu\nu}$ are the matrix elements of the Woods-Saxon mean-field Hamiltonian.

4.4 Hartree-Fock-Bogolyubov Cranking Method

The Hartree-Fock-Bogolyubov theory coupled with the cranking model (HFBC) was applied to describe the high-spin behaviour of atomic nuclei over many years by now. The first step of the HFBC method is to transform the nuclear Routhian in eq. (4.3.38) from the particle representation to the quasi-particle representation with the help of the Bogolyubov transformation.

4.4.1 Bogolyubov Transformation

Quasi-particle operators can conveniently be introduced employing the Bogolyubov transformation. The corresponding new creation and annihilation operators, (α^{+}, α), are defined as linear combinations of the particle creation and annihilation operators $\{c^{+}, c\}$:

$$\alpha^{+}_{i} = \sum_{\nu=1}^{p}(A_{\nu i}c^{+}_{\nu} + B_{\nu i}c_{\nu}), \tag{4.4.1}$$

$$\alpha_j = \sum_{\nu=1}^{p} (B^*_{\nu j} c^+_\nu + A^*_{\nu j} c_\nu), \tag{4.4.2}$$

where the matrices A and B need to be defined later. The quasi-particles are considered as fermions and satisfy the following anti-commutation relations:

$$\{\alpha^+_i, \alpha_j\} = \delta_{ij}, \tag{4.4.3}$$

$$\{\alpha^+_i, \alpha^+_j\} = 0, \tag{4.4.4}$$

$$\{\alpha_i, \alpha_j\} = 0. \tag{4.4.5}$$

Inserting the definitions of the quasi-particle operators, eqs. (4.4.1)-(4.4.2), into anti-commutation relations in eqs. (4.4.3)-(4.4.5), we obtain the following relations for the coefficients in the quasi-particle operators,

$$\sum_{\nu=1}^{p} (A^*_{\nu i} A_{\nu j} + B^*_{\nu i} B_{\nu j}) = \delta_{ij}, \quad i, j = 1, 2, ..., p \tag{4.4.6}$$

$$\sum_{\nu=1}^{p} (A_{\nu i} B_{\nu j} + A_{\nu j} B_{\nu i}) = 0, \quad i, j = 1, 2, ..., p. \tag{4.4.7}$$

It is convenient to write the quasi-particle operators of the Bogolyubov transformation using a matrix representation

$$\begin{pmatrix} \alpha^+ \\ \alpha \end{pmatrix} = \begin{pmatrix} A^T & B^T \\ B^\dagger & A^\dagger \end{pmatrix} \begin{pmatrix} c^+ \\ c \end{pmatrix}. \tag{4.4.8}$$

Let us define a new matrix

$$Z = \begin{pmatrix} A^T & B^T \\ B^\dagger & A^\dagger \end{pmatrix}. \tag{4.4.9}$$

Using eqs. (4.4.6)-(4.4.7), one can demonstrate that matrix Z is unitary, i.e., $ZZ^\dagger = 1$.

The inverse to the Bogolyubov transformation is

$$\begin{pmatrix} c^+ \\ c \end{pmatrix} = \begin{pmatrix} A^* & B \\ B^* & A \end{pmatrix} \begin{pmatrix} \alpha^+ \\ \alpha \end{pmatrix}, \tag{4.4.10}$$

or equivalently

$$c^+_\nu = \sum_{i=1}^{p} (A^*_{\nu i} \alpha^+_i + B_{\nu i} \alpha_i), \tag{4.4.11}$$

$$c_\nu = \sum_{i=1}^{p} (B^*_{\nu j} \alpha^+_j + A_{\nu j} \alpha_j), \tag{4.4.12}$$

showing how to represent the particle operators by the quasi-particle operators.

4.4.2 HFBC Equations in Quasiparticle Representation

With the help of Bogolyubov transformation we transform the particle representation into the quasi-particle representation. We insert the particle operators of eqs. (4.4.11) and (4.4.12) into eq. (4.3.38). Since $\hat{H}^{\omega}$ contains products of $c^{+}_{\nu}c_{\nu}$ and $c^{+}_{\mu}c^{+}_{\bar{\mu}}c_{\bar{\nu}}c_{\nu}$, it will be convenient to group together terms with the same order of α. According to the corresponding new notation, we assume that $\hat{H}_0$ contains the terms without α operators, $\hat{H}_{11}$ contains the terms with two operators of the type $\alpha^{+}\alpha$, $\hat{H}_{20}$ groups the two operators of the type $\alpha^{+}\alpha^{+}$ and $\alpha\alpha$ and $\hat{H}_4$ the terms with four operators in the form $\alpha\alpha\alpha\alpha$, $\alpha\alpha\alpha\alpha^{+}$ and $\alpha\alpha\alpha^{+}\alpha^{+}$. It follows that the transformed Hamiltonian takes the form, ref. [6]:

$$\hat{H}^{\omega} \rightarrow \hat{H}^{\omega} = \hat{H}_0 + \hat{H}_{11} + \hat{H}_{20} + \hat{H}_4, \tag{4.4.13}$$

where the explicit expressions are

$$\hat{H}_0 = \sum_{\alpha\beta}[h_{\alpha\beta}\rho_{\alpha\beta} + \frac{1}{2}\Gamma_{\alpha\beta}\rho_{\alpha\beta} + \Delta_{\alpha\beta}\chi_{\alpha\beta}], \tag{4.4.14}$$

$$\hat{H}_{11} = \sum_{ij,\alpha\beta}[\nu_{\alpha\beta}(A^{*}_{\alpha i}A_{\beta j} - B_{\alpha j}B^{*}_{\beta i}) + \Delta_{\alpha\beta}A^{*}_{\alpha i}B_{\beta j} + \Delta^{*}_{\alpha\beta}B^{*}_{\alpha i}A_{\beta j}]\alpha^{+}_{i}\alpha_{j}, \tag{4.4.15}$$

$$\begin{aligned}\hat{H}_{20} = &\sum_{ij,\alpha\beta}[\nu_{\alpha\beta}A^{*}_{\alpha i}B^{*}_{\beta j} + \frac{1}{2}\Delta_{\alpha\beta}A^{*}_{\alpha i}A^{*}_{\beta j} + \frac{1}{2}\Delta^{*}_{\alpha\beta}B^{*}_{\beta i}B_{\alpha j}]\alpha^{+}_{i}\alpha^{+}_{j} \\ &+ \sum_{ij,\alpha\beta}[\nu_{\alpha\beta}A_{\alpha i}B_{\beta j} + \frac{1}{2}\Delta^{*}_{\alpha\beta}A_{\alpha i}A_{\beta j} + \frac{1}{2}\Delta_{\alpha\beta}B_{\beta i}B^{*}_{\alpha j}]\alpha_{i}\alpha_{j}.\end{aligned} \tag{4.4.16}$$

The definitions of the new objects introduced above, called density-, and pairing density, are

$$\rho_{\alpha\beta} = \sum_{i=1}^{p} B_{\alpha i}B^{*}_{\beta i}, \tag{4.4.17}$$

$$\chi_{\alpha\beta} = \sum_{i=1}^{p} A_{\beta i}B^{*}_{\alpha i}, \tag{4.4.18}$$

whereas the remaining matrices are defined by

$$\Delta_{\alpha\beta} = 2\sum_{\gamma\delta}^{p} v_{\alpha\beta\gamma\delta}\chi_{\gamma\delta}, \tag{4.4.19}$$

$$\Gamma_{\alpha\beta} = 4\sum_{\beta\delta}^{p} v_{\alpha\beta\gamma\delta}\rho_{\beta\delta}, \tag{4.4.20}$$

$$\nu_{\alpha\beta} = \varepsilon_{\alpha\beta} + \Gamma_{\alpha\beta}, \tag{4.4.21}$$

$$\varepsilon_{\alpha\beta} = e_{\alpha\beta} - \lambda_n\delta_{\alpha\beta} - \hbar(\vec{\omega}\cdot\vec{J})_{\alpha\beta}. \tag{4.4.22}$$

One can observe that $\hat{H}_{11}$ and $\hat{H}_{20}$ are determined by the Bogolyubov transformation coefficients A and B. The above Hamiltonian can be simplified by introducing some conditions on A and B. Suppose that the Bogolyubov transformation is chosen in such a way that $\hat{H}_{11}$ in eq. (4.4.15) can be reduced to the so-called "independent quasiparticle representation",

$$\hat{H}_{11} = \sum_{ij} \delta_{ij} E_j^{\omega} \alpha_i^{+} \alpha_j, \tag{4.4.23}$$

analogous to the independent particle representation

$$\hat{H}_{mf} = \sum_{\nu} e_\nu c_\nu^{+} c_\nu, \tag{4.4.24}$$

and let us require that

$$\hat{H}_{20} = 0. \tag{4.4.25}$$

It turns out that the contribution of $\hat{H}_4$, which depends on four quasi-particle operators, is significantly smaller than those of other terms and can be neglected. With the above simplifications, the Hamiltonian can be rewritten as

$$\hat{H}^{\omega} = \hat{H}_0 + \sum_{i=1}^{p} E_i^{\omega}, \tag{4.4.26}$$

where E_i^{ω} are real numbers denoting the quasi-particle energies.

One can demonstrate, cf. ref. [6], that the assumptions in eqs. (4.4.23) and (4.4.24) are equivalent to the following non-linear[2] equations for the transformation coefficients A and B:

$$\sum_{\beta=1}^{p} (\nu_{\alpha\beta} A_{\beta i} + \Delta_{\alpha\beta} B_{\beta i}) = +E_i^{\omega} A_{\alpha i}, \tag{4.4.27}$$

$$\sum_{\beta=1}^{p} (\nu_{\alpha\beta}^{*} B_{\beta i} + \Delta_{\alpha\beta}^{*} A_{\beta i}) = -E_i^{\omega} B_{\alpha i}, \tag{4.4.28}$$

in which $\nu_{\alpha\beta}$ and $\Delta_{\alpha\beta}$ represent the single-particle Routhian and the self-consistent pairing field, respectively. The above non-linear equations depending on the coefficients A and B are called Hartree-Fock-Bogolyubov Cranking (HFBC) equations, their solutions are obtained via numerical iterative procedures based on the conditions of self-consistency.

Comments. The contribution of $\hat{H}_0$ contains summations with no α operator. We expect that this term will describe the ground-state and the rotational band built on top of it; it refers to the so-called zero-quasiparticle configurations. The excitations of

[2] Observe, that ν and Δ depend on ρ and χ – and thus on A and B.

the system are given by $\hat{H}_{11}$, which depends on $\alpha_i^+\alpha_i$, and thus defines two-quasiparticle configurations.

Next we introduce the so called HFB matrix,

$$M = \begin{pmatrix} \nu & \Delta \\ -\Delta^* & -\nu^* \end{pmatrix}. \tag{4.4.29}$$

With this notation we rewrite the HFBC equations in the following compact form

$$M \begin{pmatrix} A_i \\ B_i \end{pmatrix} = E_i^\omega \begin{pmatrix} A_i \\ B_i \end{pmatrix}, \tag{4.4.30}$$

where A_i and B_i denote the i^{th} column of matrices A and B, respectively, and the eigenvalues are denoted $(+E_i^\omega)$ as before. The specific form of the above equation is

$$\begin{pmatrix} e_i - \omega j_i - \lambda & \Delta \\ -\Delta^* & -e_i - \omega j_i + \lambda \end{pmatrix} \begin{pmatrix} A_i \\ B_i \end{pmatrix} = E_i^\omega \begin{pmatrix} A_i \\ B_i \end{pmatrix}, \tag{4.4.31}$$

where e_i is single-particle energy of the mean-field Hamiltonian $\hat{H}_0$ and j_i denotes the component of the angular momentum on the rotational axis.

Chapter 5

Nuclear Geometrical Symmetries Seen Through Group Theory

In the 20th century, the principles of symmetry came to play a fundamental role in physics and became dominating concepts in the exploration and formulation of physical laws. The most important implication of quantum symmetries are the conservation laws. For instance, the momentum of isolated systems is conserved due to the invariance of their Hamiltonians under space-translations, whereas the energy is conserved due to the invariance of the corresponding Hamiltonians under translation in time, etc. In quantum mechanics, the application of group theory is a leading factor in discovering the consequences of various symmetries and establishing conservation laws with the full mathematical exactitude.

Nuclear many-body Hamiltonians are by construction invariant under translations of the reference frame, rotations (thus "spherically symmetric"), space inversion and remain independent (explicitly) of time. On the other hand, it is known that the majority of atomic nuclei are non-spherical. One says that the implied deformations result from spontaneous (spherical) symmetry breaking. It turns out that the nuclear shapes are directly related to the spatial properties of the nuclear *mean-field* Hamiltonians, and impact the nucleonic energy spectra. With the help of the symmetries of the mean-field Hamiltonian one can analyse the implied properties of the nucleonic spectra such as particle-hole excitations, degeneracies of energy levels, variations of their densities, etc.

In this project we follow the rules of the powerful combination of the nuclear mean-field theory and the group theory in searching for stable nuclear configurations, related exotic nuclear geometrical symmetries, and their impact on the spectroscopic properties of nuclei.

Which shapes do we consider being exotic?

> *We refer to a nuclear shape-symmetry as exotic if it does not correspond to the quadrupole prolate, oblate, or triaxial (often called "ellipsoidal") shapes nor axially symmetric pear-shape, the latter already studied for many years.*

In analogy to the spherical magic numbers each symmetry group is expected to generate its own magic gaps in its nucleonic spectra, such as the tetrahedral magic gaps and magic numbers generated by tetrahedral symmetry introduced by our collaboration, c.f. for instance refs. [1, 26].

In this chapter we present briefly the basic concepts of group theory, applied within the context of the nuclear mean-field theory; for more systematic overview cf. for instance refs. [27, 28]. Some selected examples of the high-rank tetrahedral and octahedral symmetries are shown in the following sections as an illustration of the related considerations. This is stimulated by the fact that these two symmetries were recently discovered in subatomic physics by our group, ref. [29].

Let us summarise briefly a number of main ideas and research strategies discussed in this Chapter – which contains occasionally several rather detailed messages. It addresses in particular a number of mathematical subjects which are often not well familiar to the experimental readership.

In this project we address the geometrical symmetries and corresponding symmetry groups. Yet, despite the fact that these particular issues form a relatively limited chapter of group theory, several general mathematical notions need to be recalled. Thus at the beginning of the chapter, section (5.1), we introduce the notion of groups, beginning with the quantum-mechanical background and terminating with the formal definitions. The main focus, however, is on the point groups serving big domains of atomic and molecular physics precisely because of addressing the 3D geometrical properties from the strict mathematical view points. With these goals in mind, we present in some detail the elementary symmetry operations and examples of point groups of special interest for our project.

Presentation of the nuclear geometrical symmetries as described here is based on the notion of a nuclear surface, a real function expressed in terms of expansions involving spherical harmonics, in general complex functions of spherical angles (θ, ϕ). These surfaces are described with the help of the expansion coefficients referred to as deformation parameters which, for practical reasons chosen in the literature, are assumed real. This is a complicating, constraining factor from the mathematical view point, especially for the exotic shape symmetries such as tetrahedral or octahedral ones, but also several others, whose description may require simultaneous combinations of several deformation parameters. The corresponding issues are overviewed in section (5.2).

One of the new elements in this project, with the novelty bypassing just a PhD thesis subject, is the issue of identification of the newly proposed, exotic symmetries. To our knowledge this information is not present in the nuclear physics literature yet. It turns out that in order to construct the corresponding identification criteria we need yet another, rather abstract chapter of mathematics, viz. group representation theory. Of course the related presentation is strongly limited in terms of volume and content. The minimum precision in terms of definitions and a few theorems will be given in section (5.3).

Finally we proceed to brief explanations related to the construction of the symmetry identification criteria via symmetry-implied rotational band structures in section (5.4). These criteria turn out to be unique – a very encouraging element of this part of the discussion because allowing for planning experimental campaigns aiming at well defined goals. On the other hand, the construction of such criteria requires practical applications of the group-representation theorems prepared for this purpose in the preceding section. We focus on the illustration of those applications.

5.1 From Quantum Mechanics to Group Theory

Consider time independent Schrödinger equation with one-body Hamiltonian, $\hat{H}$, written down in a given reference frame Σ:

$$\Sigma: \quad \hat{H}\psi_n = \varepsilon_n \psi_n, \quad \hat{H} = \hat{t} + \hat{V}, \tag{5.1.1}$$

in which

$$\hat{t} = -\frac{\hbar^2}{2m}\nabla^2, \quad \text{and} \quad \hat{V} = \hat{V}(\vec{r}; \{p\}). \tag{5.1.2}$$

Above, symbol $\{p\}$ denotes all the parameters of the interaction potential. Consider a rotation of the frame $\Sigma \xrightarrow{rot.} \Sigma'$ written down with the help of the rotation operator $\hat{R}(\Omega)$ depending on the Euler angles $\{\alpha, \beta, \gamma\} \equiv \Omega$. It follows from eq. (5.1.1) that

$$\hat{R}\hat{H}\psi_n = \varepsilon_n \hat{R}\psi_n, \quad \leftrightarrow \quad \underbrace{[\hat{R}\hat{H}\hat{R}^{-1}]}_{\hat{H}'}\underbrace{\hat{R}\psi_n}_{\psi'_n} = \varepsilon_n \underbrace{\hat{R}\psi_n}_{\psi'_n}. \tag{5.1.3}$$

In this way we obtain the Schrödinger equation in a rotating reference frame, Σ':

$$\Sigma': \quad \hat{H}'\psi'_n = \varepsilon_n \psi'_n. \tag{5.1.4}$$

Invariance of Hamiltonians Resulting from Symmetries. Symmetry transformations imply by definition that the transformed object coincides with the same object

before transformation. Let us first consider the case of the spherical symmetry. In this case the Hamiltonian satisfies equality $\hat{H}' = \hat{H}$, $\forall\ \{\alpha, \beta, \gamma\}$, and therefore

$$\hat{H}' = \hat{R}(\alpha, \beta, \gamma)\hat{H}\hat{R}^{-1}(\alpha, \beta, \gamma) = \hat{H}, \tag{5.1.5}$$

or equivalently

$$[\hat{H}, \hat{R}(\alpha, \beta, \gamma)] = 0,\ \forall\ \{\alpha, \beta, \gamma\}. \tag{5.1.6}$$

The above equations illustrate the fact that a symmetry of a physical system, here under rotations in three dimensions, manifests itself through the invariance of the Hamiltonian. The corresponding mathematical expression is represented by the commutation relation between the Hamiltonian and the underlying transformation operators.

Let us introduce some general transformations of a given Hamiltonian by $\{\hat{\mathcal{D}}\}$, the latter depending on parameters $\{a, b, ...\}$. The invariance of the system against these transformations leads to the following commutation relation

$$\boxed{[\hat{H}, \hat{\mathcal{D}}(a, b, ...)] = 0,\ \forall\ \{a, b, ...\}.} \tag{5.1.7}$$

Consider an eigenstate $|\Psi\rangle$ of $\hat{H}$ and the corresponding eigenvalue ε. It follows from eq. (5.1.7) that

$$\hat{H}\hat{\mathcal{D}}|\Psi\rangle = \hat{\mathcal{D}}\hat{H}|\Psi\rangle = \varepsilon\hat{\mathcal{D}}|\Psi\rangle. \tag{5.1.8}$$

This implies that $\hat{\mathcal{D}}|\Psi\rangle$ and $|\Psi\rangle$ are eigenstates of the Hamiltonian with the common eigenvalue ε.

5.1.1 Group of Rotations: Formal Definition of a Group

We will briefly recall the formal definition of groups in the mathematical sense of the term, first observing the properties of the transformations of rotations. Let us begin by collecting certain elementary properties of the matrices of rotation in a 3-dimensional space.

Rotation Matrices. Consider two rotation matrices, $\mathcal{R}_z(a)$ and $\mathcal{R}_z(b)$, representing rotations about the same axis $\mathcal{O}_z$ through the angles a and b:

$$\mathcal{O}_z: \quad \mathcal{R}_z(a) = \begin{pmatrix} \cos a & \sin a & 0 \\ -\sin a & \cos a & 0 \\ 0 & 0 & 1 \end{pmatrix} \quad \text{and} \quad \mathcal{R}_z(b) = \begin{pmatrix} \cos b & \sin b & 0 \\ -\sin b & \cos b & 0 \\ 0 & 0 & 1 \end{pmatrix}. \tag{5.1.9}$$

1. Multiplying the above rotation matrices gives yet another rotation matrix describing rotations through the angle $a + b$:

$$\mathcal{R}_z(a) \circ \mathcal{R}_z(b) = \begin{pmatrix} \cos a & \sin a & 0 \\ -\sin a & \cos a & 0 \\ 0 & 0 & 1 \end{pmatrix} \begin{pmatrix} \cos b & \sin b & 0 \\ -\sin b & \cos b & 0 \\ 0 & 0 & 1 \end{pmatrix}$$

$$= \begin{pmatrix} \cos a\cos b - \sin a\sin b & \cos a\sin b + \sin a\cos b & 0 \\ -\cos a\sin b - \sin a\cos b & \cos a\cos b - \sin a\sin b & 0 \\ 0 & 0 & 1 \end{pmatrix}$$

$$= \begin{pmatrix} \cos(a+b) & \sin(a+b) & 0 \\ -\sin(a+b) & \cos(a+b) & 0 \\ 0 & 0 & 1 \end{pmatrix}$$

$$= \mathcal{R}_z(a+b). \tag{5.1.10}$$

2. Consider rotation $\mathcal{R}_z(a)$ and a unit matrix e which can be interpreted formally as a matrix of rotation with null-angles. Since combining $\mathcal{R}_z(a)$ with e reproduces the original matrix,

$$\mathcal{R}_z(a)\circ e = \begin{pmatrix} \cos a & \sin a & 0 \\ -\sin a & \cos a & 0 \\ 0 & 0 & 1 \end{pmatrix}\begin{pmatrix} 1 & 0 & 0 \\ 0 & 1 & 0 \\ 0 & 0 & 1 \end{pmatrix} = \begin{pmatrix} \cos a & \sin a & 0 \\ -\sin a & \cos a & 0 \\ 0 & 0 & 1 \end{pmatrix} = \mathcal{R}_z(a), \tag{5.1.11}$$

the above relation shows an existence a "trivial rotation" also called "neutral element" corresponding to the transformation which "changes nothing".

3. To any given rotation through the angle a there exists another one representing rotation in the opposite direction, namely the opposite operation with the angle $-a$, so that:

$$\mathcal{R}_z(a)\circ\mathcal{R}_z(-a) = \begin{pmatrix} 1 & 0 & 0 \\ 0 & 1 & 0 \\ 0 & 0 & 1 \end{pmatrix} = e. \tag{5.1.12}$$

Similarly $\mathcal{R}_z(-a)\circ\mathcal{R}_z(a) = e$, in which case we usually write $\mathcal{R}_z(-a) = \mathcal{R}_z^{-1}(a)$.

4. According to the properties of the matrix multiplication for any three rotation matrices $\mathcal{R}_z(a)$, $\mathcal{R}_z(b)$ and $\mathcal{R}_z(c)$ we have

$$\mathcal{R}_z(a)o\,[\mathcal{R}_z(b)\,o\,\mathcal{R}_z(c)] = [\mathcal{R}_z(a)\,o\,\mathcal{R}_z(b)]\,o\mathcal{R}_z(c). \tag{5.1.13}$$

We can see that rotation matrices always satisfy the 4 characteristic properties listed above. It turns out that this feature can be generalised to any sets of abstract objects by introducing the notion of groups.

Formal Definition of a Group. Consider a set G of elements g_1, g_2, ... and a relation denoted with the symbol "$\circ$", such that the following properties hold:

1. Combination of any two elements with the help of relation $\circ$ gives yet another element $g \in G$:

$$\boxed{\forall\ \boldsymbol{g_1},\ \boldsymbol{g_2} \in \boldsymbol{G}:\quad \boldsymbol{g_1}\circ\boldsymbol{g_2} = \boldsymbol{g} \in \boldsymbol{G}.} \tag{5.1.14}$$

2. For any three elements of G, relation "$\circ$" is associative,

$$\boxed{\forall\ \boldsymbol{g_1, g_2, g_2} \in \boldsymbol{G}: \quad \boldsymbol{(g_1 \circ g_2) \circ g_3 = g_1 \circ (g_2 \circ g_3).}} \tag{5.1.15}$$

3. The set contains an element $e \in G$ called neutral, such that

$$\boxed{\forall\ \boldsymbol{g} \in \boldsymbol{G}: \quad \boldsymbol{e \circ g = g \circ e.}} \tag{5.1.16}$$

4. For each $g \in G$, there exists an element g' called inverse, such that

$$\boxed{\boldsymbol{g \circ g' = e \quad \leftrightarrow \quad g' \circ g = e.}} \tag{5.1.17}$$

One usually writes $g' \stackrel{df.}{=} g^{-1}$.

Generally, transformations of rotations can be treated as abstract operations and the rotation operations as independent of the nature of the rotated object.

5.1.2 Point Groups: Elementary Symmetry Operations

Symmetry point-groups were used to describe the quantum features of, among others, molecular as well as atomic systems for a long time. Such groups are composed of discrete transformations, moreover, all the transformations of the symmetry group of such objects must leave at least one point of the studied object fixed, wherefrom the term 'point-group'. The associated elementary transformations are as follows:

Neutral Element e. It is also called the identity element. Combining it with any other element will just reproduce that element.

Discrete Rotations C_n. They are also called proper rotations defined as rotations about a certain axis through the angle $\alpha = 2\pi/n$ (for n integer). The result of a successive application of such an element ℓ times is denoted by C_n^ℓ. The corresponding axis is referred to as an n-fold rotation axis. For instance $n = 3$ represents the rotation through $2\pi/3 \leftrightarrow 120^o$ which is denoted by C_3. Result of an application of the same rotation twice is denoted C_n^2. It is clear that successive rotations n times through $2\pi/n$ about the same rotational axis return to the initial position and produce the identity transformation

$$(C_n)^n = e. \tag{5.1.18}$$

Generally there will be one axis of the highest order (the biggest n) rotational symmetry; such an axis is traditionally called "vertical' and one writes C_{nv}.

Plane Reflections σ. Plane reflections are also called mirror reflections, for instance plane reflection in $\mathcal{O}_{xz}$-plane: $\{x, y, z\} \xrightarrow{\sigma_y} \{x, -y, z\}$. It is evident that applying such a reflection in the same plane twice will return the object to the initial position,

$$\sigma^2 = e. \tag{5.1.19}$$

Reflection in a plane perpendicular to the principal axis, the latter vertical, is denoted by σ_h (since the corresponding plane is called horizontal) while the reflection in the plane passing through this axis (thus in vertical plane) is denoted σ_v.

Rotary-Reflection S_n. By definition, the rotation-reflection symmetry is defined as the rotation about a certain axis followed by a reflection in a plane perpendicular to that axis

$$S_n \stackrel{df.}{=} C_n \sigma_h. \tag{5.1.20}$$

As illustrated in figure (5.1.1), the two operations, C_n and σ_h commute, and we can write

$$C_n \sigma_h = \sigma_h C_n. \tag{5.1.21}$$

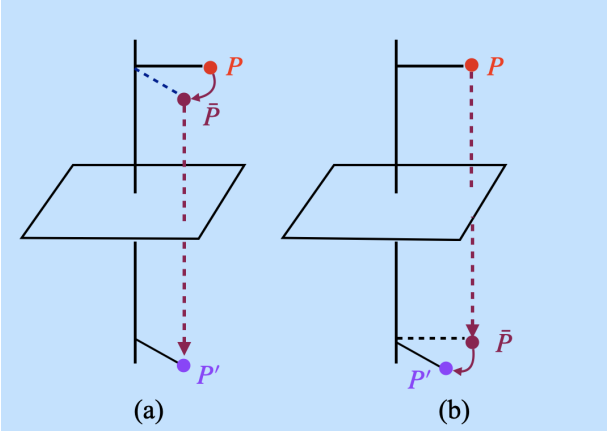

Figure 5.1.1 – *Schematic illustration of the commutativity between C_n and σ_h: (a) the operation of $C_n\sigma_h$ and (b) the operation of $\sigma_h C_n$.*

This transformation is also called improper n-fold rotation and the corresponding axis – 'rotary-reflexion axis'. Similarly successive applying the rotation-reflection symmetry n times we have

$$S_n^n = (C_n \sigma_h)^n = C_n^n \sigma_h^n. \tag{5.1.22}$$

It follows that for even n, $(S_n)^n = e$ and for odd n, $(S_n)^n = \sigma_h$.

Inversion $\mathcal{I}$. The inversion symmetry, as the name indicates, corresponds by definition to inverting directions of all the 3 axes of the reference frame

$$\mathcal{I}: \quad \{x, y, z\} \to \{-x, -y, -z\} \tag{5.1.23}$$

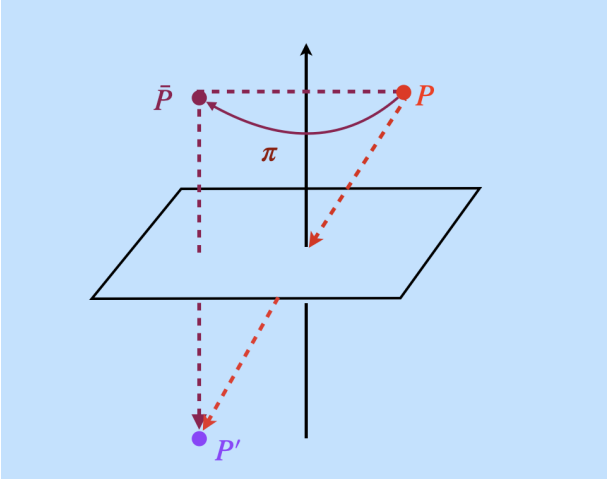

Figure 5.1.2 – *Illustration of the particular case of rotation-reflection transformation of the order $n = 2$, S_2 is equivalent to inversion transformation $\mathcal{I}$.*

It follows that this operation is equivalent to the particular case of S_2, cf. figure (5.1.2):

$$\{x, y, z\} \xrightarrow{C_2} \{-x, y, -z\} \xrightarrow{\sigma_h} \{-x, -y, -z\}, \tag{5.1.24}$$

and thus the following practical identities follow

$$I = S_2 = C_2\sigma_h. \tag{5.1.25}$$

It follows from Eq. (5.1.25) that

$$C_2 = \mathcal{I}\sigma_h, \quad \sigma_h = \mathcal{I}C_2. \tag{5.1.26}$$

As it becomes clear from the relations illustrated in figures (5.1.3)-(5.1.4), the operations $\mathcal{I}$, C_2 and σ commute among themselves.

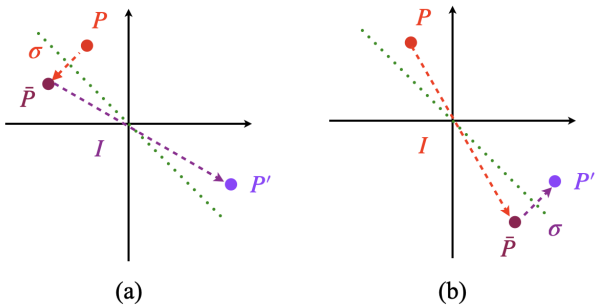

Figure 5.1.3 – *Illustration of the commutation relation $[\sigma, \mathcal{I}] = 0$. The combination $\sigma\mathcal{I}$ in (a) and $\mathcal{I}\sigma$ in (b).*

Let us notice that all the axes of rotation and all planes of reflections must contain at least one common point. We proceed now to presenting a few illustrations of potential interest for the present project.

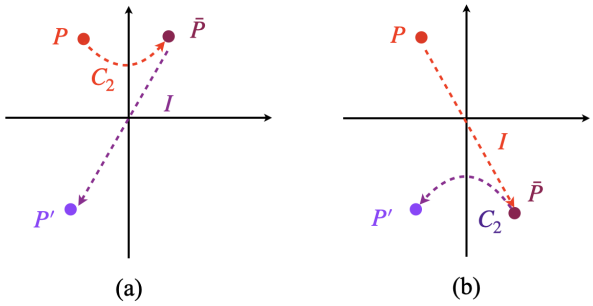

Figure 5.1.4 – *Illustration of the commutation relation* $[C_2, \mathcal{I}] = 0$. *The combination* $C_2\mathcal{I}$ *in (a) and* $\mathcal{I}C_2$ *in (b).*

5.1.3 Point Groups: Selected Possible Nuclear Symmetries

It will be instructive to present explicitly a few definitions of the point groups:

Uni-Axial Groups C_n.

Groups containing rotation axis C_n with $n = 2\pi/n$, for instance for $n = 2$ we find

- C_2: $\{E, C_2\}$;
- D_{2h}: $\{E, C_2, \mathcal{I}, \sigma_h\}$;
- D_{2v}: $\{E, C_2, 2\sigma_v\}$.

Dihedral Groups D_n.

Groups containing an n-fold rotation axis and n perpendicular 2-fold rotation axes; for instance for $n = 3$ we find:

- D_3: $\{E, C_3, 3C_2\}$;
- D_{3h}: $\{E, 2C_3, 3C_2, \sigma_h, 2S_3, 3\sigma_v\}$;
- D_{3v}: $\{E, 2C_3, 3C_2, \mathcal{I}, 2S_6, 3\sigma_d\}$ ("d" for diagonal planes).

As an example for $n = 2$ we find

- D_{2d}: $\{E, 2C_2', C_2, 2\sigma_d, 2S_4\}$;

Family of Tetrahedral-Type Groups, $\boldsymbol{T}$.

- T (Chiral tetrahedral symmetry): $\{E, 3C_2, 4C_3, 4C_3^2\}$;
- T_h (Pyritohedral symmetry): $\{E, 3C_2, 8C_3, \mathcal{I}, 3\sigma_v, 8S_6\}$;
- T_d (Achiral tetrahedral symmetry): $\{E, 3C_2, 8C_3, 6S_4, 6\sigma_d\}$.

Family of Octahedral-Type Groups, $\boldsymbol{O}$.

- O (Chiral octahedral symmetry): $\{E, 3C_2, 6C_2', 6C_4, 8C_3\}$;
- O_h (Full octahedral symmetry): $\{E, 3C_2', 6C_2, 8C_3, 6C_4, \mathcal{I}, 6S_4, 8S_6, 3\sigma_h, 6\sigma_d\}$.

From the above examples we notice that the groups T_d and O_h have the largest number of symmetry operations. We call these groups *high rank* symmetry groups referring to the fact that some nucleonic levels in nuclei with those symmetries are four-fold degenerate (compared to the well-known Kramers two-fold degeneracy applying to any non-spherical nucleus with the 'usual' or 'regular' symmetries). Since the tetrahedral group T_d is a subgroup of the octahedral group O_h, an object which is octahedral symmetric is also tetrahedral symmetric.

Double Point Groups. In nuclear physics applications of the symmetry considerations related to Schrödinger equation we have to take into account that nucleons are Fermions. Let us denote the wave function of a boson by Ψ_B and the one of Fermion by Ψ_F. One demonstrates in quantum mechanics textbooks that applying any rotation of 2π to the Fermion as compared to Boson particles leads to the following difference, cf. ref. [19]:

$$\text{Bosons}: \quad \hat{R}(2\pi)\Psi_B = +\Psi_B, \tag{5.1.27}$$

$$\text{Fermions}: \quad \hat{R}(2\pi)\Psi_F = -\Psi_F. \tag{5.1.28}$$

It follows from eq. (5.1.28) that for Fermions, thus in particular the nucleons, only double application of the operation of the rotation through 2π brings the wave function to itself, namely $\hat{R}^2 = E$. The symmetry point-groups applicable to Fermions are called double point groups and are denoted by G^D.

5.2 Nuclear Shapes and Point-Group Symmetries

In this section we consider the nuclear mean-field Hamiltonian invariant under the symmetry operations of a point group. We address the issue of the symmetry conditions by applying the group theory to the nuclear mean-field theory and to the corresponding solutions of the nuclear Hamiltonian.

5.2.1 Nuclear Surface Invariant under Group G

In the phenomenological nuclear mean-field theory applications we describe nuclear surfaces with the help of the expansions in terms of spherical harmonics. Let us recall the definition of the nuclear surface:

$$\Sigma: \quad R(\theta,\varphi) = c(\{\alpha\})R_0\left[1+\sum_{\lambda}\sum_{\mu=-\lambda}^{\lambda}\alpha_{\lambda\mu}Y_{\lambda\mu}(\theta,\varphi)\right]. \tag{5.2.1}$$

The surface expressed using the expansion coefficients represent a series called *multipole expansion*. Let us recall, cf. section (2.3), that any surface represented with the help of the real multipole expansion coefficients is invariant under the y-simplex symmetry.

Typically, variations of $R(\theta,\varphi)$ as functions of θ and ϕ are stronger and stronger the higher and higher the order λ. In other words, the nuclear surface is getting more and more "wiggly". Since the nuclear macroscopic energy increases quickly with increasing surface of the nucleus, it follows that on average the macroscopic energy will also increase quickly with increasing λ, the corresponding nuclear configurations will lie higher in the energy scale and it will be more and more difficult to produce well defined (i.e. surrounded by significant potential barriers) potential energy minima to possibly observe the underlying configurations experimentally. It then follows that it is often sufficient to apply a rather low cut-off parameter $\lambda_{\max}$, i.e., to consider $\lambda \leq \lambda_{\max}$.

Studying symmetries of the Hamiltonian with the help of the point-group theory, we first examine the symmetry properties of nuclear surfaces. Consider a point group composed of the symmetry elements $\{\hat{\mathcal{O}}_k\}$,

$$G = \{\hat{\mathcal{O}}_1, \hat{\mathcal{O}}_2, ..., \hat{\mathcal{O}}_f\}. \tag{5.2.2}$$

The invariance condition reads

$$\Sigma \xrightarrow{\hat{\mathcal{O}}_k} \Sigma' \equiv \Sigma, \ \forall\, \hat{\mathcal{O}}_k. \tag{5.2.3}$$

It follows from the above condition that $\forall\, k$:

$$\sum_{\lambda=2}^{\lambda_{\max}}\sum_{\mu=-\lambda}^{\lambda}\alpha_{\lambda\mu}[\hat{\mathcal{O}}_k Y_{\lambda\mu}(\theta,\varphi)] = \sum_{\lambda=2}^{\lambda_{\max}}\sum_{\mu=-\lambda}^{\lambda}\alpha_{\lambda\mu}Y_{\lambda\mu}(\theta,\varphi). \tag{5.2.4}$$

The above relation can be considered as a system of linear equations that the unknown $\{\alpha_{\lambda\mu}\}$ satisfying the surface-invariance condition must obey. The elements of the symmetry operations $\mathcal{O}_k \in G$ need to be adapted to the operations acting on the spherical harmonics $Y_{\lambda\mu}(\theta,\varphi)$.

Let us consider rotation operator $\hat{R}(\Omega_k)$ as an example of the symmetry operations, here in the form adapted to our quantum-mechanics considerations

$$\hat{\mathcal{O}}_k \rightarrow \hat{R}(\Omega_k) \equiv \exp(i\alpha_k\hat{j}_z + i\beta_k\hat{j}_y + i\gamma_k\hat{j}_{z'}). \tag{5.2.5}$$

The invariance condition in eq. (5.2.4) can be rewritten as

$$\sum_{\lambda=2}^{\lambda_{\max}} \sum_{\mu=-\lambda}^{\lambda} \alpha_{\lambda\mu}[\hat{\mathcal{O}}_k Y_{\lambda\mu}(\theta,\varphi)] = \sum_{\lambda=2}^{\lambda_{\max}} \sum_{\mu=-\lambda}^{\lambda} \alpha_{\lambda\mu} \sum_{\mu'=-\lambda}^{\lambda} D^{\lambda}_{\mu'\mu}(\Omega_k) Y_{\lambda\mu'}(\theta,\varphi), \tag{5.2.6}$$

where $D^{\lambda}_{\mu'\mu}(\Omega_k)$ are Wigner functions[1]. The above relation is equivalent to what follows

$$\sum_{\lambda=2}^{\lambda_{\max}} \sum_{\mu'=-\lambda}^{\lambda} \left[\sum_{\mu=-\lambda}^{\lambda} \alpha_{\lambda\mu} D^{\lambda}_{\mu'\mu}(\Omega_k) - \alpha_{\lambda\mu'}\delta_{\mu\mu'} \right] Y_{\lambda\mu}(\theta,\varphi) = 0, \ \forall\theta,\varphi, \forall k. \tag{5.2.9}$$

Since the spherical harmonics are linearly independent, it follows from ref. [30] that,

$$\sum_{\mu=-\lambda}^{\lambda} \left[D^{\lambda}_{\mu'\mu}(\Omega_k) - \delta_{\mu\mu'} \right] \alpha_{\lambda\mu} = 0, \ k = 1, 2, ..., f. \tag{5.2.10}$$

In the above equations, Ω_k refers to fixed sets of Euler angles corresponding to the symmetry elements $\mathcal{O}_k$. It follows from the form of eq. (5.2.10) that the discussed invariance conditions can be treated as eigenvalue problems in which the solutions $\bar{\alpha}_{\lambda\mu}$ are eigenvectors of the matrix $D^{\lambda}_{\mu'\mu}(\Omega_k)$ with eigenvalue equal $+1$. In other words, the nuclear surface with the expansion coefficients $\bar{\alpha}_{\lambda\mu}$ will be invariant under the symmetry element $\hat{R}(\Omega_k)$. The above system of linear equations is uniform. Therefore multiplying the solution by a constant will give another solution. This implies that we can set, e.g., $\bar{\alpha}_{\lambda\mu=0}$ as an independent parameter, which fixes other non-zero components in terms of $\bar{\alpha}_{\lambda\mu}$.

5.2.2 Examples: Tetrahedral and Octahedral Symmetries

Evidently, only special combinations of spherical harmonics form the surfaces obeying to tetrahedral and octahedral symmetries. Since the presence of those symmetries in subatomic physics was recently demonstrated by our collaboration, ref. [29], we will concentrate on this particular example for illustrative purposes.

• **Tetrahedral Symmetry.** As demonstrated in ref. [26], the multipole deformation parameters describing tetrahedral symmetry correspond to odd $\lambda \geq 3$, with the exception of $\lambda = 5$ (here we limit ourselves to quoting the 3 lowest solutions):

[1]The symbol D represents a $(2j+1) \times (2j+1)$ matrix, ref. [7]; using the spherical basis it can be expressed as

$$D^{j}_{m'm}(\alpha,\beta,\gamma) = \langle jm'|R(\alpha,\beta,\gamma)|jm\rangle = e^{-im'\alpha} d^{j}_{m'm}(\beta) e^{-im\gamma}, \tag{5.2.7}$$

where

$$d^{j}_{m'm}(\beta) = \langle jm'|e^{-i\beta j_y}|jm\rangle. \tag{5.2.8}$$

$$\lambda = 3: \quad \alpha_{3,\pm 2} \equiv t_1; \tag{5.2.11}$$

$$\lambda = 7: \quad \alpha_{7,\pm 2} \equiv t_2 \quad \text{and} \quad \alpha_{7,\pm 6} \equiv -\sqrt{\tfrac{11}{13}}t_2; \tag{5.2.12}$$

$$\lambda = 9: \quad \alpha_{9,\pm 2} \equiv t_3 \quad \text{and} \quad \alpha_{9,\pm 6} \equiv +\sqrt{\tfrac{28}{198}}t_3. \tag{5.2.13}$$

Examples of the tetrahedral shapes are shown in figure (5.2.1) for illustration.

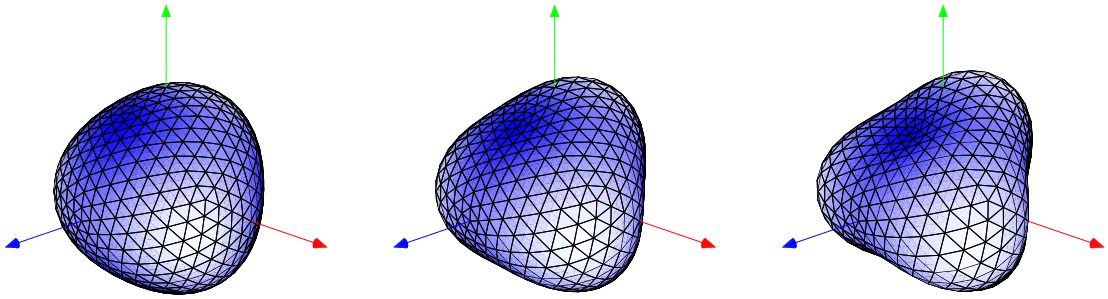

$t_1 = 0.1$ $t_1 = 0.2$ $t_1 = 0.3$

Figure 5.2.1 – *Illustration of the tetrahedral surfaces at* $t_1 = 0.1, 0.2$ and 0.3, *respectively. The shapes of tetrahedral symmetry are sometimes called in jargon 'nuclear pyramids'.*

• **Octahedral Symmetry.** Similarly, the octahedral symmetry conditions can be specified by the special combinations of spherical harmonics with even $\lambda \geq 4$ as shown in ref. [31]:

$$\lambda = 4: \quad \alpha_{4,0} \equiv o_1 \quad \text{and} \quad \alpha_{4,\pm 4} \equiv -\sqrt{\tfrac{5}{14}}o_1; \tag{5.2.14}$$

$$\lambda = 6: \quad \alpha_{6,0} \equiv o_2 \quad \text{and} \quad \alpha_{6,\pm 4} \equiv +\sqrt{\tfrac{7}{2}}o_2; \tag{5.2.15}$$

$$\lambda = 8: \quad \alpha_{8,0} \equiv o_3, \quad \alpha_{8,\pm 4} \equiv -\sqrt{\tfrac{28}{198}}o_3 \quad \text{and} \quad \alpha_{8,\pm 8} \equiv -\sqrt{\tfrac{65}{198}}o_3. \tag{5.2.16}$$

Some illustrations of octahedral shapes are shown in figure (5.2.2).

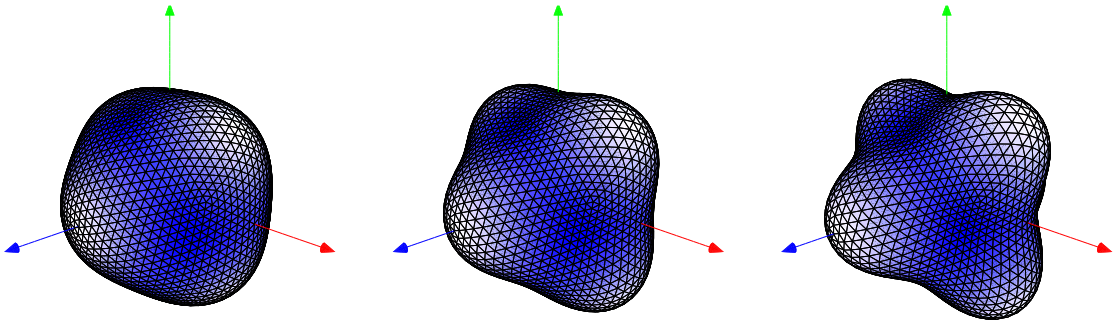

$o_1 = 0.1$ $o_1 = 0.2$ $o_1 = 0.3$

Figure 5.2.2 – *Illustration of octahedral surfaces at* $o_1 = 0.1, 0.2$ and 0.3*, respectively. The shapes of octahedral symmetry are referred to in jargon as 'nuclear diamonds'.*

5.3 Remarks about Group Representation Theory

In the previous sections we have presented selected elementary properties of groups focussing on groups whose elements are symmetry transformations. In order to connect the group theory with the quantum mechanical observables, an intermediate notion of group representations is needed; with the help of the latter it will become possible to express the symmetries and groups of symmetry in terms of matrix representations and numbers.

5.3.1 Group Representations: Elementary Notions

Consider a vector space V over the field F, a group $\{G, \circ\}$ and an ensemble of linear operators D which are functions of $g \in G$ acting in V. Suppose the operations form a group $\{D, \cdot\}$ and there exists a homomorphic mapping between two groups, $G \to D(g)$, satisfying by definition

$$D(g_1 \circ g_2) = D(g_1) \cdot D(g_2), \tag{5.3.1}$$

so that

$$D(g^{-1}) = D^{-1}(g) \to D(g) \cdot D(g^{-1}) = \mathbb{1}. \tag{5.3.2}$$

It follows that for the inverse elements, g^{-1}, we have

$$D(g) \cdot D(g^{-1}) = D(g \circ g^{-1}) = D(e) = \mathbb{1}. \tag{5.3.3}$$

The group composed of operators $\{D(g), \cdot\}$ is called representation of the original group G if the above conditions are satisfied.

Group Representations in Terms of Matrices. Consider a representation $\{D(g), \cdot\}$ of group G acting in vector space V. Assume the dimension of V is n and the basis $u_i \in V$. Acting with the operators $\{D(g), \cdot\}$ on the basis states we have

$$D(g)u_i = u_j D(g)^j_i, \quad 1 \leq i, j \leq n. \tag{5.3.4}$$

For an arbitrary choice of $g_1, g_2 \in G$ we find

$$D(g_1 \circ g_2)u_i = D(g_1) \cdot D(g_2)u_i = D(g_1)[u_j D(g_2)^j_i] = u_k D(g_1)^k_j D(g_2)^j_i. \tag{5.3.5}$$

We conclude that a given representation $\{D(g), \cdot\}$ acting in an n-dimensional vector space V_n with a basis $\{u_i\}$, leads to the matrix $D(g)^j_i$ with dimensions $n \times n$.

Character of a Representation. Given a basis $\{v_i,\, i = 1, 2, \ldots n\} \in V_n$, a group G and its representation $D(g)$. The trace of the matrix $D(g)^j_i$ denoted

$$\chi(g) \stackrel{df.}{=} Tr[D(g)] \stackrel{df.}{=} [D(g)]^i_i, \tag{5.3.6}$$

is called the character of $g \in G$ within representation $D(g)$.

Invariant Subspaces. Suppose there exists a subspace $V_m \subset V_n$, with $m < n$, such that

$$\exists V_m \subset V_n : \forall g \in G \text{ and } \forall\, v \in V_m \to D(g)\, v \in V_m. \tag{5.3.7}$$

When this happens, V_m is called an invariant subspace of V_n with respect to $D(G)$. The subspace is considered trivial if V_n is its own invariant subspace. If the subspace V_m in V_n does not contain any invariant non-trivial subspace V_k with $k < m$, in such a case $V_{k=m}$ is called minimal invariant subspace.

Irreducible Representations. Suppose there exists <u>no</u> invariant sub-space $V_{m<n} \subset V_n$ with respect to $D(G)$. We call such a representation an irreducible representation.

Reducible Representations. Suppose there exists a basis transformation such that in the new basis

$$D(g) = \begin{bmatrix} D_1(g) & A(g) \\ 0 & D_2(g) \end{bmatrix}, \quad \forall g \in G. \tag{5.3.8}$$

We call representation $D(g)$ a reducible representation, the matrix $D_1(g)$ has dimension of $m \times m$ with $m < n$ while matrix $D_1(g)$ has dimension $(n-m) \times (n-m)$. If the representation $D(g)$ has the form

$$D(g) = \begin{bmatrix} D_1(g) & 0 \\ 0 & D_2(g) \end{bmatrix}, \quad \forall g \in G, \tag{5.3.9}$$

we say that $D(g)$ is fully reducible.

5.3.2 Spectral Properties and Group Representations

Let us consider a group $G = \{g_1, g_2, ..., g_f\}$ and assume that G is a symmetry group of the mean-field Hamiltonian, $\hat{H}$. It follows from the commutation relation in eq. (5.1.7) that the representation $D(g)$ of group G satisfies

$$[\hat{H}, \hat{D}(g)] = 0, \quad \forall g \in G. \tag{5.3.10}$$

Suppose that the irreducible representations of G are $\{D_1, D_2, ..., D_r\}$ and the corresponding dimensions are $\{d_1, d_2, ..., d_r\}$. The eigenvalue problem of the mean-field Hamiltonian is

$$\hat{H}\psi_\nu = \varepsilon_\nu \psi_\nu. \tag{5.3.11}$$

According to group representation theory, the eigenvalues ε_ν of the spectrum will split into multiplets ("families") with degeneracies $\{d_1, d_2, ..., d_r\}$, with the degeneracy of each energy level equal to the dimension of the corresponding irreducible representation of the symmetry group.

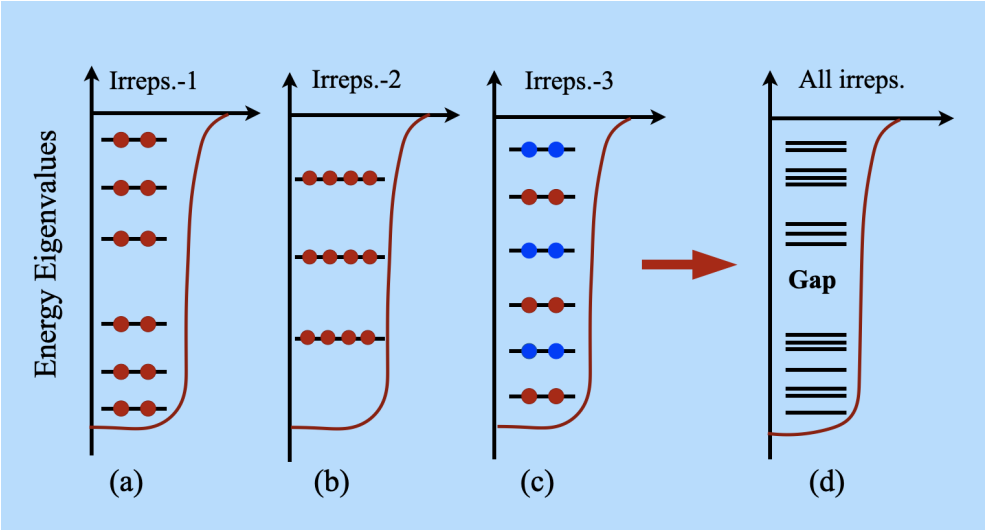

Figure 5.3.1 – *Schematic illustration of inter-spacing (gaps) between the levels resulting from the existence of different irreducible representations.*

It has been suggested in ref. [3] that, generally, the presence of irreducible representations with dimensions larger than 2 (i.e., larger than Kramers degeneracy) implies that the bigger the dimensions of the irreducible representations, the larger (on average) the inter-spacing among the levels. This is because the depth of the nuclear mean field potential, V_0, is approximately constant (of the order of $V_0 = -50$ MeV) and does not vary in any significant manner with varying proton and neutron numbers; thus

the smaller the number of states within the potential depth of V_0-depth, the larger interspacing of the levels. The influence of dimensions of irreducible representations presented in figure (5.3.1) is based on the tests using the realistic mean-field models, cf. e.g. ref.[3]. Let us formulate the following comments in relation to the schematic figure (5.3.1):

A. Plot 'Irreps-1' illustrates schematically a spectrum of the Hamiltonian, whose symmetry group has one 2-dimensional irreducible representation. It follows that there are 2 degenerate energies for each level. Because of the Landau-Zener effect, the energy levels belonging to one irreducible representation can not cross; they effectively "repel each other", and the resulting spectrum tends to fill-in the available energy space in an approximately uniform manner, even though some fluctuations in the inter-level spacings will often be generated.

B. Plot 'Irreps-2' illustrates the case of a hypothetical irreducible 4-dimensional representation so that there are 4-fold degenerate energies each time. If we consider configurations with the same numbers of available nucleonic states as in cases A. and B., the number of the energy levels is smaller in the latter case by a factor of 2 because of the factor of 2 higher degeneracies. It follows that an average inter-spacing between the energy levels is increased by a factor of 2. This increased inter-spacing may contribute, in realistic cases, to an increase of the gaps, thus increasing the stability of the corresponding nuclear configurations and occasionally creation of significant shell-gaps with possibly measurable consequences.

C. Plot 'Irreps-3' illustrates the case of two 2-dimensional irreducible representations. The repulsion mechanism applies for two sets of levels separately, so that the energy levels fill the potential well leading effectively to the increased inter-spacing between the levels for each of the two sets.

D. Plot 'All Irreps.' is an "artist's view" of the full spectrum combining the contributions from some 2D and some 4D irreducible representations. The intention here is to show that even if combining the spectrum out of several contributions, in case of the bigger average spacing in the contributing sets, the chances for having finally a big gap 'here and there in the spectrum' grow. Realistic calculations illustrated in the present project confirm this conjecture very clearly, e.g. fig. (5.3.2).

As it is well known, the presence of big gaps in the single-particle spectra implies an increase in the stability of the concerned nuclear configurations by generating strong negative shell correction energies. We are therefore interested in examining, at least quantitatively, which point-group symmetries have high-dimension irreducible-representations or have relatively many irreducible representations since, as we have argued above, these factors might lead systematically to increasing inter-level spacings. In particular, a nucleus at a given configuration becomes more stable if its lowest

particle-hole excitation energy gets bigger – wherefrom the interests in the search of big gaps in the single-particle spectra.

Table 5.3.1 – *Double point-groups and the corresponding numbers of irreducible representations together with their dimensions. The listed groups are of potential interest in the discussion of stable nuclear shapes, see the text and ref. [3].*

No	Group	Number of irreps	Dimensions
1	O_h^D	6	4 × 2D and 2 × 4D
2	T_d^D	3	2 × 2D and 1 × 4D
3	C_{6h}^D	12	12× 1D(6 × 2D)
4	D_{6h}^D	6	6 × 2D
5	T_h^D	6	6 × 2D
6	C_{4h}^D	8	8 × 1D (4 × 2D)
7	D_{4h}^D	4	4 × 2D
8	D_{3h}^D	3	3 × 2D
9	$C_{6\nu}^D$	3	3 × 2D
10	D_6^D	3	3 × 2D
11	C_6^D	6	6 × 1D(3 × 2D)
12	S_6^D	6	6 × 1D(3 × 2D)
13	C_{3h}^D	6	6 × 1D(3 × 2D)
14	C_{3I}^D	6	6 × 1D(3 × 2D)
15	D_{2h}^D	2	2 × 2D

In table (5.3.1) we present the list of the double point groups which may become of interest in studying the stability of nuclear structures. Notice that only tetrahedral and octahedral double point groups have dimensions of irreducible representation greater than 2, and they are on top of the list of symmetries generating the strongest nuclear shell effects, behind the spherical one. In other words, only these two high rank symmetries, i.e., T_h^D and O_h^D, generate the single-particle energy levels with 4-fold degeneracy. In section (5.2.2) we presented the lowest order of multipole expansions related to tetrahedral and octahedral shapes which are used in our realistic mean-field calculations.

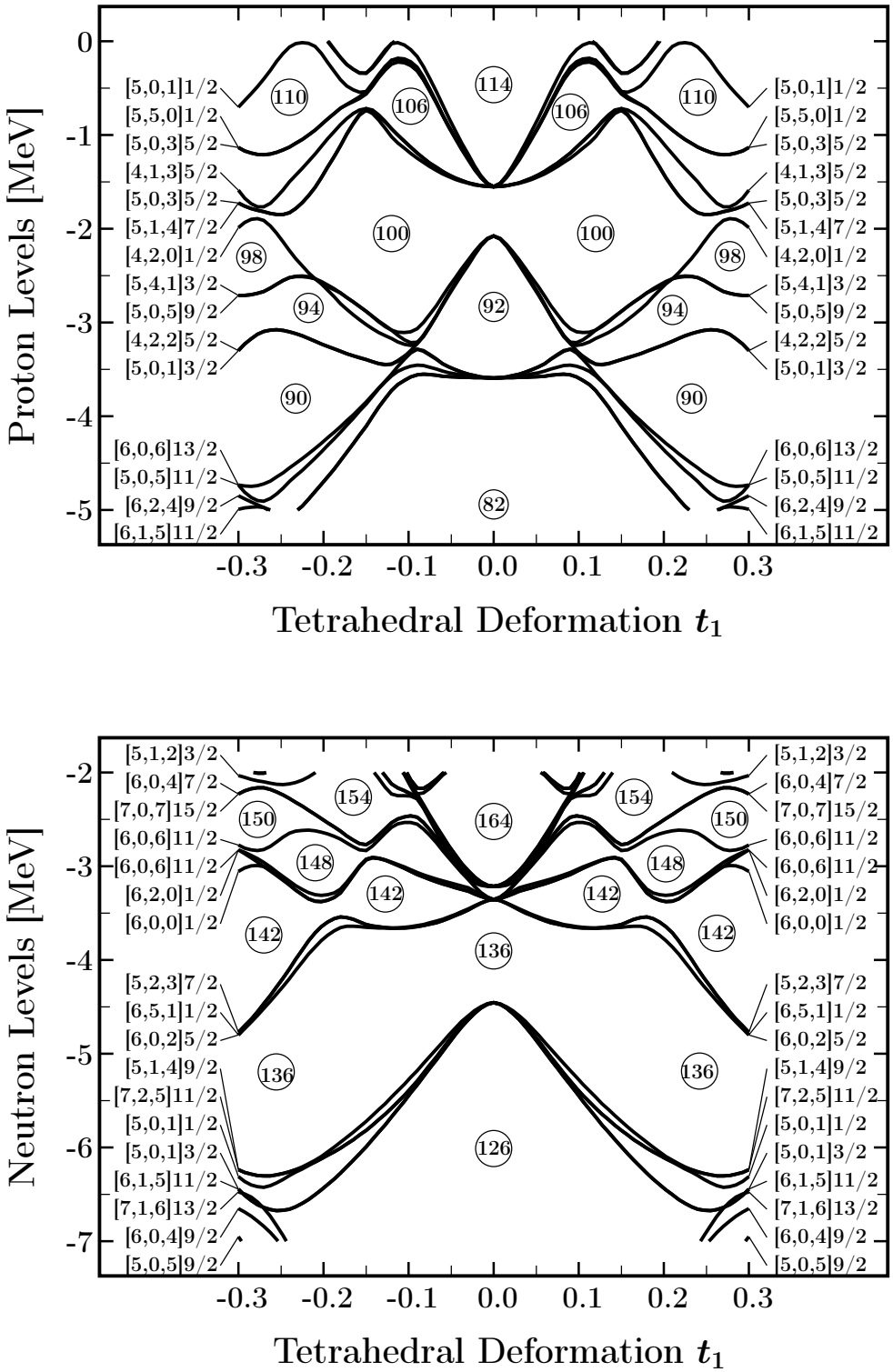

Figure 5.3.2 – *Single-particle proton energies (top) and neutron energies (bottom) as functions of the tetrahedral deformation for nuclei around* $^{226}Th_{136}$. *The full lines represent 4-dimensional irreducible representation, while the dashed lines represent two 2-dimensional irreducible representations. Observe large gaps at non-zero tetrahedral deformations. For more details – see the text.*

5.3.3 Tetrahedral Magic Numbers

Examples of realistic single nucleon spectra with the tetrahedral symmetric nuclear mean-field Hamiltonian are shown in figure (5.3.2), protons - top, and neutrons - bottom. As it can be seen from the figures, the large tetrahedral gaps at proton numbers $Z = 90$ and 100, at neutron numbers $N = 136$ and 142 are dominating. Inspecting many single-particle diagrams similar to the ones in fig. (5.3.2) we conclude that the tetrahedral magic numbers form chains discussed in ref. [32]:

$$\{Z_t, N_t\} = \{32,\ 40,\ 56,\ 64,\ 70,\ 90,\ 136\}. \tag{5.3.12}$$

More precisely, we find that the strongest tetrahedral stability can be expected in doubly-magic tetrahedral nuclei corresponding to the combination of the above magic numbers:

$$^{64}_{32}\mathrm{Ge}_{32},\ ^{72}_{32}\mathrm{Ge}_{40},\ ^{88}_{32}\mathrm{Ge}_{56},\ ^{80}_{40}\mathrm{Zr}_{40},\ ^{96}_{56}\mathrm{Zr}_{40},\ ^{104}_{64}\mathrm{Zr}_{40},\ ^{110}_{40}\mathrm{Zr}_{70},$$
$$^{112}_{56}\mathrm{Ba}_{56},\ ^{126}_{56}\mathrm{Ba}_{70},\ ^{146}_{56}\mathrm{Ba}_{90},\ ^{134}_{64}\mathrm{Gd}_{70},\ ^{154}_{64}\mathrm{Gd}_{90},\ ^{160}_{70}\mathrm{Yb}_{90},\ ^{226}_{90}\mathrm{Th}_{136}.$$

The placement of the above tetrahedral doubly-magic nuclei on the nuclear (Z, N)-plane is shown in fig. (5.3.3). It is worth emphasising that the tetrahedral doubly-magic nuclei are much more numerous than the analogous doubly-magic spherical ones.

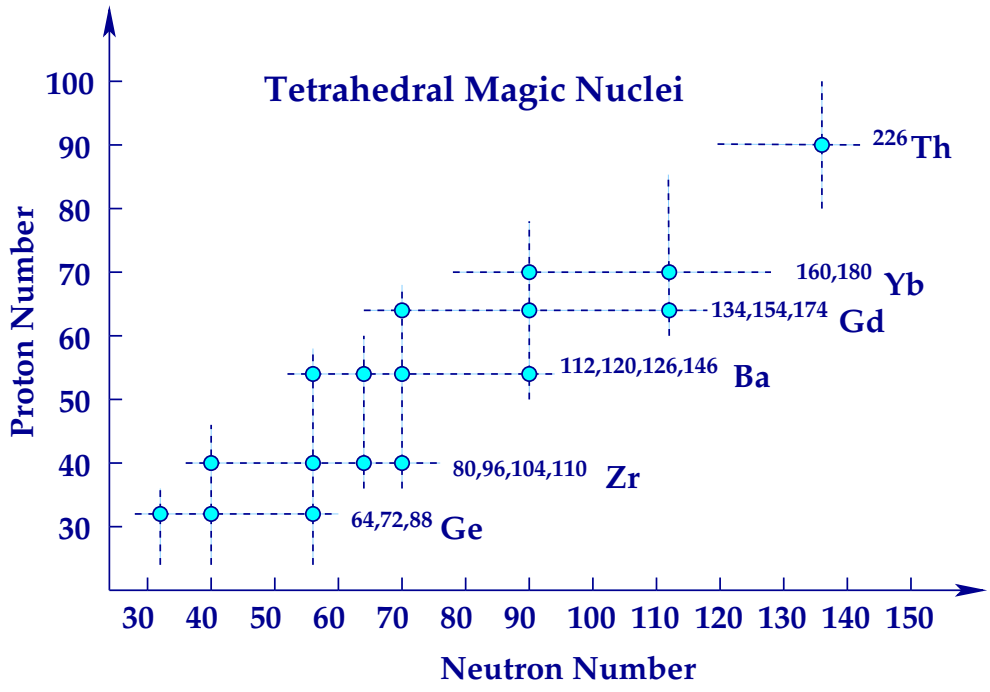

Figure 5.3.3 – *Illustration of the positions of the tetrahedral doubly-magic nuclei on the* (Z, N)*-plane.*

Indeed, we find that only for $Z, N > 30$ there are 17 doubly-magic tetrahedral nuclei, compared, within the same mass range limitation, with ^{100,132}Sn and ^{208}Pb.

5.4 Rotational Bands Induced by Point-Symmetries

Applying group-, and group-representation theories to study symmetries of the nuclear mean-field Hamiltonian allowed us to predict the large single-particle shell gaps and the symmetry-stabilised configurations. In analogy, we would like to find a way of estimating the impact of the point group symmetries on the *collective rotational spectra* and deducing the privileged spin-parity sequences. The specific spectral properties of the quantum rotors obtainable with the help of the point group theory have been studied actively in recent years, cf. e.g., the spectra of the octupole symmetric quantum rotors in ref. [33] and the spectroscopic criteria for tetrahedral symmetry in refs. [29, 34].

5.4.1 Rotational Band Properties Generated by T_d Symmetry

To begin with we will present the rotational band properties generated by nuclei with tetrahedral shape symmetry. Recall two complementary approaches to describe rotating nuclei: The one treating rotating nuclei as structureless quantum rotors, and another one describing the nuclear behaviour via a microscopic (in our case mean-field) theory.

• **Structureless Quantum Rotors.** Up to an approximation, rotating nuclei can be considered as structureless quantum rotors with the Hamiltonian constructed out of nuclear total angular momentum operators, $\hat{I} = \{\hat{I}_x, \hat{I}_y, \hat{I}_z\}$. This approach allows one to calculate directly the energy spectra as well as the reduced electromagnetic transitions. Accordingly, the rotor Hamiltonian adopted in refs. [33, 35] can be expressed as follows:

$$\hat{\mathcal{H}}_{\text{rot}} = \frac{\hat{I}_x^2}{2\mathcal{J}_x} + \frac{\hat{I}_y^2}{2\mathcal{J}_y} + \frac{\hat{I}_z^2}{2\mathcal{J}_z} + \hat{h}(\{p\}; \hat{I}_x, \hat{I}_y, \hat{I}_z), \tag{5.4.1}$$

where the moment of inertia parameters $\mathcal{J}_x$, $\mathcal{J}_y$ and $\mathcal{J}_z$ represent diagonal form of the inertia tensor, and the second term allows for modelling point-group symmetries with the help of the adjustable parameters $\{p\}$. This latter term is expressed using the spherical tensor basis $\{\hat{T}_{\lambda\mu}\}$ as follows

$$\hat{h}(\{p\}; \hat{I}_x, \hat{I}_y, \hat{I}_z) = \sum_{n=3}^{n_{\max}} \hat{h}(n, \lambda), \tag{5.4.2}$$

in which

$$\hat{h}(n, \lambda) = \sum_{\mu=-\lambda}^{\lambda} c_{\lambda\mu}(n) \hat{T}_{\lambda\mu}(n), \tag{5.4.3}$$

where $\hat{T}_{\lambda\mu}(n)$ are by construction uniform polynomials of order n and the coefficients $c_{\lambda\mu}(n)$ are defined with the help of the Clebsch-Gordan coupling theorem.

Consider a more complete collective Hamiltonian including the rotational one, $\hat{\mathcal{H}}_{\rm rot}$, the vibrational one, $\hat{\mathcal{H}}_{\rm vib}$ and the coupling term, $\hat{\mathcal{H}}_{\rm vibrot}$, combined as follows

$$\hat{\mathcal{H}} = \hat{\mathcal{H}}_{\rm rot} + \hat{\mathcal{H}}_{\rm vib} + \hat{\mathcal{H}}_{\rm vibrot}. \tag{5.4.4}$$

What we are interested in, in the present context, is a collective nuclear rotation and therefore, the orientation of the system with respect to a Cartesian reference frame. The corresponding solutions will thus represent the probability of nuclear orientation in the 3D space. The corresponding transformation properties of the solutions of the problem follow the rules of transformation originating from the orthogonal group in 3 dimensions

$$O(3) = C_i \times SO(3), \tag{5.4.5}$$

where C_i denotes the inversion group and $SO(3)$ is the so-called special orthogonal group in 3 dimensions. The formal details applicable to molecular physics have been developed among others in refs. [36, 37].

> *These are the irreducible representations of the rotor Hamiltonian symmetry group which determine the structure of the corresponding matrices, hindrance factors, transition probabilities etc., – the group $O(3)$.*

• **Rotating Nuclei Described within a Microscopic Theory.** A microscopic description of rotational motion is often achieved introducing the concept of external rotation (cranking approximation) on top of a static, non-rotating microscopic Hamiltonian. The problem is then solved employing the well-known cranking and/or Hartree-Fock-Bogolyubov Cranking (HFBC) approaches. One may introduce a self consistent mean-field imposing the geometrical symmetries described with the help of the expectation values of the multipole moment operators treated as constraints

$$\langle\Phi|\hat{Q}_{\lambda\mu}|\Phi\rangle = Q_{\lambda\mu} \quad \leftrightarrow \quad \alpha_{\lambda\mu}. \tag{5.4.6}$$

Thus we arrive at the description of deformations with the help of spherical harmonics. Since the deformed solutions satisfying the conditions in (5.4.6) necessarily break the original symmetries, the quantum numbers characterising the angular momentum and parity will need to be recovered using projection techniques. As discussed in ref. [1] the projection relations can be applied as follows

$$|\Phi\rangle \rightarrow |\Psi^{I_\pm}_{M_k}\rangle = \sum_k g^{I_\pm}_{k,\kappa} \hat{P}^I_{MK} \hat{P}^\pm |\Phi\rangle, \tag{5.4.7}$$

in which $g^{I_\pm}_{k,\kappa}$ represents the expansion coefficients obtained from the Hill-Wheeler equations, and $\hat{P}^I_{MK}$ and $\hat{P}^\pm$ represent the angular momentum and parity projectors, respectively.

Consequently symmetries of the constrained microscopic Hamiltonian are the point-group symmetries of the mean-field and not $O(3)$, the group of symmetry of the quantum rotor. The properties of the physical solutions of the microscopic description are governed by the irreducible representations of the point groups. The relations between the mentioned irreducible representations are governed by the appropriate theorems of group theory which will be addressed next.

5.4.2 Irreducible Representations: Point-Groups vs. $O(3)$

Consider a solution of the rotor problem introduced in eq. (5.4.1), whose wave functions transform as representations of the group $O(3)$, cf. eq. (5.4.5), according to well defined spin and parity (I^π). For a given (I^π) the representations D^{I^π} of the rotor Hamiltonian are $(2I+1) \times (2I+1)$ matrices in the space of rotor wave functions. Let G be a symmetry point-group of our microscopic Hamiltonian and its irreducible representations $\{D_i, i = 1, 2, ..., M\}$. According to one of the fundamental theorems of group representation theory, a representation associated with the rotor Hamiltonian, D^{I^π}, can be decomposed in terms of D_i with the help of the multiplicity factors $a_i^{I^\pi}$ as follows

$$D^{I^\pi} = \sum_{i=1}^{M} a_i^{I^\pi} D_i. \tag{5.4.8}$$

The multiplicity coefficients $a_i^{I^\pi}$ are well known in the literature and the corresponding expressions can be found e.g. in ref. [27]. One finds:

$$a_i^{I^\pi} = \frac{1}{N_G} \sum_{R \in G} \chi_{I\pi}(R)\chi_i(R) = \frac{1}{N_G} \sum_{\alpha=1}^{M} g_\alpha \chi_{I\pi}(R_\alpha)\chi_i(R_\alpha), \tag{5.4.9}$$

where N_G is the order of group G (the number of the elements in the group) whereas $\chi_{I\pi}(R_\alpha)$ and $\chi_i(R_\alpha)$ are the characters of D^{I^π} and D^i, respectively. The shorthand notation "R_α" stands for the point-group elements representing transformations in Cartesian 3D space. The number of group elements in each given class is denoted by g_α; for details, cf. ref. [27].

5.4.3 Point-Groups vs. $O(3)$ – Follow Up: T_d vs. $O(3)$

For quantum rotors of even-even nuclei we will need the 'usual' points groups (in contrast to the double point-groups). The corresponding tetrahedral group has 5 irreducible representations denoted in the literature $\{A_1, A_2, E, F_1, F_2\}$ and the related representative elements $\{E, C_2, C_3, \sigma_d, S_4\}$. The characters $\chi_{I\pi}(R_\alpha)$ for the rotor representations are as follows (see e.g. ref. [1] and references therein):

$$\chi_{I\pi}(E) = 2I + 1, \tag{5.4.10}$$

$$\chi_{I\pi}(C_n) = \sum_{-1}^{1} e^{\frac{2\pi K}{n} i}, \tag{5.4.11}$$

$$\chi_{I\pi}(\sigma_d) = \pi \times \chi_{I\pi}(C_2), \tag{5.4.12}$$

$$\chi_{I\pi}(S_4) = \pi \times \chi_{I\pi}(C_4). \tag{5.4.13}$$

The characters for tetrahedral group are listed in table (5.4.1).

Table 5.4.1 – Character table for tetrahedral group.

T_d |	E	$C_2(3)$	$C_3(8)$	$\sigma_d(2)$	$S_4(6)$
A_1	1	1	1	1	1
A_2	1	1	1	-1	-1
E	2	-1	2	0	0
$F_1(T_1)$	3	0	-1	-1	1
$F_2(T_2)$	3	0	-1	1	-1

From the above relations we find that

$$a_i^{I^\pi} = \frac{1}{N_G} \sum_{\alpha=1}^{M} g_\alpha \chi_{I\pi}(R_\alpha)\chi_i(R_\alpha) \leftrightarrow a_{A_1}^{(I\pm)} = a_{A_2}^{(I\mp)}, a_E^{(I+)} = a_E^{(I-)}, a_{F_1}^{(I\pm)} = a_{F_2}^{(I\mp)}. \tag{5.4.14}$$

Combining the above relations we can calculate the corresponding multiplicities in table (5.4.2) for integer spins of nuclear rotational states; here up to $I = 10$. The states are not allowed if $a_i^{I_\pi} = 0$, whereas if $a_i^{I_\pi} = 2$ the states in question have double degeneracy, $a_i^{I_\pi} = 3$ triple degeneracy etc.

Table 5.4.2 – *The multiplicities $a_i^{I^\pi}$ of states for tetrahedral symmetry for rotors with integer spins. Positive parity - top, negative parity - bottom.*

I^+ |	0^+	1^+	2^+	3^+	4^+	5^+	6^+	7^+	8^+	9^+	10^+
A_1	1	0	0	0	1	0	1	0	1	1	1
A_2	0	0	0	1	0	0	1	1	0	1	1
E	0	0	1	0	1	1	1	1	2	1	2
$F_1(T_1)$	0	1	0	1	1	2	1	2	2	3	2
$F_2(T_2)$	0	0	1	1	1	1	2	2	2	2	3
I^- |	0^-	1^-	2^-	3^-	4^-	5^-	6^-	7^-	8^-	9^-	10^-
A_1	0	0	0	1	0	0	1	1	0	1	1
A_2	1	0	0	0	1	0	1	0	1	1	1
E	0	0	1	0	1	1	1	1	2	1	2
$F_1(T_1)$	0	0	1	1	1	1	2	2	2	2	3
$F_2(T_2)$	0	1	0	1	1	2	1	2	2	3	2

Thus we conclude that the spin-parity sequence for the rotational band of the type A_1 is:

$$A_1: \quad 0^+,\ 3^-,\ 4^+,\ \underbrace{6^+,\ 6^-}_{\text{doublet}},\ 7^-,\ 8^+,\ \underbrace{9^+,\ 9^-}_{\text{doublet}},\ \underbrace{10^+,\ 10^-}_{\text{doublet}},\ 11^-,\ \underbrace{2\times 12^+,\ 12^-}_{\text{triplet}},\cdots \tag{5.4.15}$$

The identification of the bands of this structure in subatomic physics, based on the experimental data, has been published by our collaboration in ref. [29].

> *It has been demonstrated within our collaboration, cf. ref. [1], that the energies of states belonging to the common irreducible representation form a parabolic energy vs. spin dependence, $E_I \propto I(I+1)$, including characteristic parity doublets.*

In what follows we address a particular situation: Spin-parity sequences in the cases of subgroup vs. group dependencies.

5.4.4 Subgroups and Groups: $T_d \subset O_h$ Case

Let us return to the spin-parity relation of eq. (5.4.15) but this time taking explicitly into account that, in view of preparing the same information for comparison with experimental spectra (in which case the energy levels are represented as parabolic $E_I \propto I(I+1)$ sequences called bands) we mark explicitly also the sub-structures of the parabolic relation. The sub-structures are formed by the predicted degeneracies of

certain levels, and in particular the spin-parity sequence based on the 0^+ state from the preceding equation can be displayed in a 'more pedagogical' form as:

$$\underbrace{\mathrm{A}_1: \quad 0^+,\, 3^-,\, 4^+,\, \underbrace{(6^+,\, 6^-)}_{\text{doublet}},\, 7^-,\, 8^+,\, \underbrace{(9^+,\, 9^-)}_{\text{doublet}},\, \underbrace{(10^+,\, 10^-)}_{\text{doublet}},\, 11^-,\, \underbrace{2\times 12^+,\, 12^-}_{\text{triplet}},\cdots}_{\text{Forming a common parabola}} \tag{5.4.16}$$

Recall that the difference between T_d as a subgroup of O_h consists in the fact that inversion is a symmetry element of the latter, but not of the former. Consequently, we may interpret the presence of tetrahedral symmetry as a result of a spontaneous symmetry breaking of the octahedral one, under certain conditions. Which ones? We will attempt to answer this question by reminding the reader that, as it is shown in textbooks, see also more dedicated ref. [29], the sequence displayed in eq. (5.4.16) can be seen as decomposed of two sub-sequences called even (in German: *gerade*, A_{1g}) and odd (in German: *ungerade*, A_{2u}) which take the following forms:

$$\underbrace{\mathrm{A}_{1\mathrm{g}}: \quad 0^+,\, 4^+,\, 6^+,\, 8^+\, 10^+,\cdots,\, I^\pi = I^+}_{\text{Forming a common parabola}} \tag{5.4.17}$$

$$\underbrace{\mathrm{A}_{2\mathrm{u}}: \quad 3^-,\, 6^-,\, 7^-,\, 9^-,\, 10^-,\, 11^-,\cdots,\, I^\pi = I^-}_{\text{Forming a common parabola}} \tag{5.4.18}$$

One can observe that the tetrahedral band in eq. (5.4.16) contains the spin-parity states from the two octahedral bands in eqs. (5.4.17) and (5.4.18).

If the two parabolic sequences above, which correspond to two different irreducible representations, have nevertheless very close curvatures, they can be seen as perturbing the overall curvature of the parabola in eq. (5.4.16) or approximately reproducing the latter. When this happens we may claim that a small difference between the curvatures of parabolas in eqs. (5.4.17) and (5.4.18) is an expression of a small octahedral symmetry breaking by the system or that the dominating octahedral deformation is influenced by a small tetrahedral deformation $\alpha_{32} \neq 0$. We sometimes express this type of relation as O_h symmetry breaking by T_d.

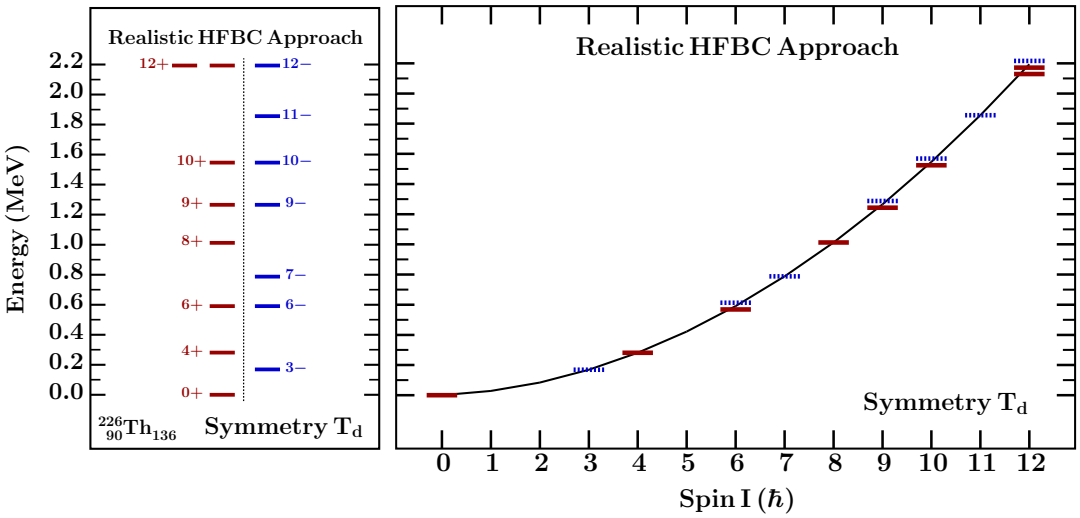

Figure 5.4.1 – *The structure of the lowest energy sequence obtained within the realistic HFBC method together with spin and parity projection techniques, results of* ^{226}Th *adopted from ref. [1]. On the left we present the positive and negative parity states and related degenerate multiplets in the 'ladder' format similar to the one used when presenting the experimental data, while on the right the parabolic dependence of the energies with respect to spin, the negative parity levels are denoted by dotted lines. The doublet or triplet looking structures are strictly degenerate*

In figure (5.4.1) we illustrate the results form ref. [1], obtained within the microscopic projected HFBC calculations for the nucleus ^{226}Th. We limit our discussion to states with $I \leq 12$. As seen from the figure, both even and odd spin states follow a parabolic sequence even though the microscopic calculations involve neither explicit considerations of symmetries nor group theory. Interested readers may compare this diagram with the results in figure 138 of ref. [38] discussing the spectra of tetrahedral symmetry molecules.

Illustration shows the degenerate states, such as spin-parity doublets at $I^\pi = 6^\pm, 9^\pm$ and $10^\pm$ and a triplet-state combined a doublet $I^\pi = 12^+$ and a single state $I^\pi = 12^-$. These degeneracies form the core of experimental identification criteria.

5.4.5 More Examples: D_{4h} and D_{2d} Symmetries

Examples of exotic rotational properties in the case of the tetrahedral and octahedral symmetries are probably among the most important since freshly discovered; however there are many other symmetries which are worth investigating – we discuss 2 more examples following ref. [34].

• **D_{4h} Point-Group Symmetry.** In this case only the combinations of spherical harmonics with even-λ and specific μ can be used to form the D_{4h} point group symmetry.

We limit ourselves to the first four λ-orders:

$$\lambda = 2: \quad \alpha_{20}; \tag{5.4.19}$$

$$\lambda = 4: \quad \alpha_{40},\ \alpha_{4\pm4}; \tag{5.4.20}$$

$$\lambda = 6: \quad \alpha_{60},\ \alpha_{6\pm4}; \tag{5.4.21}$$

$$\lambda = 8: \quad \alpha_{80},\ \alpha_{8\pm4},\ \alpha_{8\pm8}... \tag{5.4.22}$$

One can find in ref. [27] that the elements of D_{4h} point-group symmetry are

$$D_{4h} = \{E, 2C_4, C_2, 2C_2', 2C_2'', 2S_4, \sigma_h, 2\sigma_v, 2\sigma_d\} \tag{5.4.23}$$

An example of the D_{4h} shapes is shown in Figure. (5.4.2).

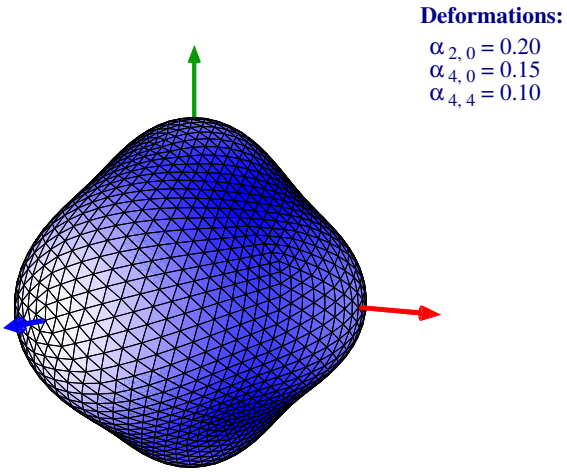

Figure 5.4.2 – *Illustration of a D_{4h}-symmetric surface with deformation parameters selected as $\{\alpha_{20} = 0.20, \alpha_{40} = 0.15,\ \alpha_{44} = 0.10\}$.*

Spin-Parity Sequence for Selected Representations of the D_{4h} Symmetry. Two spin-parity sequences with pure positive parity and negative parity are predicted by D_{4h} symmetry:

$$\mathrm{A_{1g}}: \quad 0^+,\ 2^+,\ \underbrace{2\times4^+}_{\text{doublet}},\ 5^+,\ \underbrace{2\times6^+}_{\text{doublet}},\ 7^+,\ \underbrace{3\times8^+}_{\text{triplet}},\ \underbrace{2\times9^+}_{\text{doublet}},\cdots \tag{5.4.24}$$

$$\mathrm{B_{1u}}: \quad 2^-,\ 3^-,\ 4^-,\ 5^-,\ \underbrace{2\times6^-}_{\text{doublet}},\ \underbrace{2\times7^-}_{\text{doublet}},\ \underbrace{2\times8^-}_{\text{doublet}},\ \underbrace{2\times9^-}_{\text{doublet}},\cdots \tag{5.4.25}$$

D_{2d} Point-Group Symmetry. Some special combinations of the odd- and even-λ form D_{2d} symmetry, a series of possible choices is presented as follows

$$\lambda = 2: \quad \alpha_{20}; \tag{5.4.26}$$

$$\lambda = 3: \quad \alpha_{3\pm2}; \tag{5.4.27}$$

$$\lambda = 4: \quad \alpha_{40},\ \alpha_{4\pm4}; \tag{5.4.28}$$

$$\lambda = 5: \quad \alpha_{5\pm2}; \tag{5.4.29}$$

$$\lambda = 6: \quad \alpha_{60},\ \alpha_{6\pm4}; \tag{5.4.30}$$

$$\lambda = 7: \quad \alpha_{7\pm2},\ \alpha_{7\pm6}; \tag{5.4.31}$$

$$\lambda = 8: \quad \alpha_{80},\ \alpha_{8\pm4},\ \alpha_{8\pm8}\ \ldots \tag{5.4.32}$$

D_{2d} symmetry point group, in addition to the neutral element E, contains one 2-fold rotation axis (the principal axis), two 2-fold rotation axes perpendicular to the principal axis, σ_v plane and S_4 axis:

$$D_{2d} = \{E, C_2, 2C_2', 2\sigma_d, 2S_4\} \tag{5.4.33}$$

An example of the D_{2d}-symmetry shape is shown in figure (5.4.3). Proceeding as

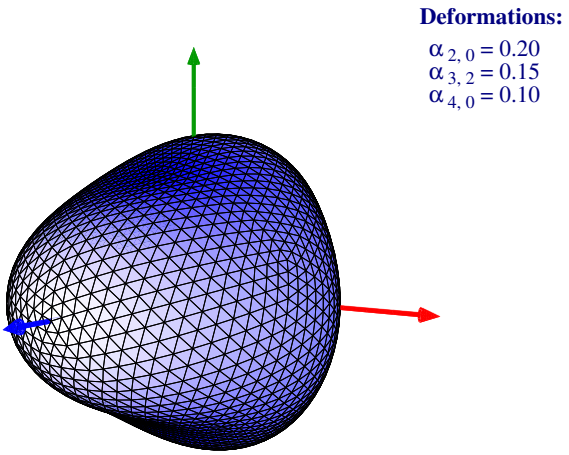

Figure 5.4.3 – *Illustration of a D_{2d}-symmetric surface with the deformation parameters chosen as* $\{\alpha_{20} = 0.20, \alpha_{32} = 0.15,\ \alpha_{40} = 0.10\}$.

before we can determine the spin-parity sequences for the corresponding rotational bands, here for the lowest, so-called D_{2d} ground-state band, whose energies form a parabolic sequence.

• **Spin-Parity Sequence for D_{2d} Symmetry.** The spin-parity sequence based on 0^+ state combines positive and negative parities,

$$\mathrm{A_{1g}}: 0^+,\ 2^+, 2^-,\ 3^-, \underbrace{2\times 4^+}_{\text{doublet}},\ 4^-,\ 5^+,\ 5^-,\ \underbrace{2\times 6^+}_{\text{doublet}},\ \underbrace{2\times 6^-}_{\text{doublet}},\ 7^+,\ \underbrace{2\times 7^-}_{\text{doublet}},\ \underbrace{3\times 8^+}_{\text{triplet}},\ \underbrace{2\times 8^-}_{\text{doublet}},\cdots . \tag{5.4.34}$$

$$\mathrm{B_{1u}}: 1^-,\ 2^+,\ 3^\pm,\ 4^\pm,\ 5^+,\ \underbrace{2\times 5^-}_{\text{doublet}},\ \underbrace{2\times 6^+}_{\text{doublet}},\ 6^-,\ \underbrace{2\times 6^-}_{\text{doublet}},\ \underbrace{2\times 7^+}_{\text{doublet}},\ \underbrace{2\times 7^-}_{\text{doublet}},\ \underbrace{2\times 8^+}_{\text{triplet}},\ \underbrace{2\times 8^-}_{\text{doublet}},\cdots . \tag{5.4.35}$$

Comparing the above spin-parity sequence, eq. (5.4.34), with the ones obtained for D_{4h} seen in eqs. (5.4.24) and (5.4.25), we observe that the spin-parity sequence of D_{2d} ground-state band can be decomposed into two D_{4h}-type bands.

Part II

Results and Discussion

Chapter 6

Exotic Shape Symmetries in Heavy and Super-Heavy Nuclei: Results

In this chapter, we present our analysis of nuclear shape properties in terms of shape evolution and competition together with shape isomers in heavy and super-heavy nuclei. We focus on exotic point-group symmetries which to our knowledge were not discussed yet in the literature, or very rarely. We employ the macroscopic-microscopic method with the classical energy calculated using the so-called Yukawa-folding realisation of the nuclear liquid-drop model and a phenomenological mean-field Hamiltonian of the Woods-Saxon type with the universal parametrisation in which parametric correlations have been eliminated. The nuclear shapes are described employing spherical-harmonic basis, $\{Y_{\lambda\mu}\}$, and including selected combinations of deformation parameters $\{\alpha_{\lambda\mu}\}$ with multipole orders $\lambda \leq 8$. To facilitate the discussion of the nuclear shape evolution and competition the energy minimisation is performed together with the corresponding projections on 2D sub-spaces.

6.1 Short Summary of the Scheme of Calculations

To study the nuclear shapes and symmetries at ground-state configurations we perform the calculations of the total nuclear energy as a function of deformation parameters $\{\alpha_{\lambda\mu}\}$. Calculations are based on the macroscopic-microscopic method presented in Annex A. Let us recall the principal energy expression used within this method:

$$E_{\text{total.}}(Z,N;\alpha) = E_{\text{macro}}(Z,N;\alpha) + E_{\text{micro}}(Z,N;\alpha) \quad \leftrightarrow \quad \alpha \equiv \{\alpha_{\lambda\mu}\}, \qquad (6.1.1)$$

where $E_{\text{macro}}(Z,N;\alpha)$ denotes the macroscopic liquid drop model energy, in our case either the Yukawa-folding realisation, or, alternatively, the Lublin-Strasbourg Drop (LSD) Model, cf. Annex (8.1.3). Comparing these two realisations we found out that

the Yukawa-folding approach gives more realistic results at the vicinities of the nuclear ground-states and thus we have used this model in the majority of the calculations within this project.

The microscopic energy, $E_{\rm micro}(Z,N;\alpha)$, is composed of the Strutinsky-type shell and pairing correction energies, detailed expressions of which are discussed in Annex (8.2):

$$E_{\rm micro}(Z,N;\alpha) = +\delta E_{\rm shell}(Z,N;\alpha) + \delta E_{\rm pair}(Z,N;\alpha). \tag{6.1.2}$$

We proceed to summarising our description of the deformation space used in the calculations.

6.1.1 Multi-Dimensional Deformation Space

The nuclear shapes are parametrised by expressing the equation of the nuclear surface, Σ, with the help of the spherical-harmonic basis, $\{Y_{\lambda\mu}(\theta,\varphi)\}$, as

$$\Sigma: \quad R(\theta,\varphi;\alpha) = c(\alpha)R_0\left[1+\sum_{\lambda}\sum_{\mu=-\lambda}^{\lambda}\alpha_{\lambda\mu}Y_{\lambda\mu}(\theta,\varphi)\right]. \tag{6.1.3}$$

In our analysis of the nuclear shape properties we focus on the deformation parameters with multipole order $\lambda \leq 8$ appearing in various sub-sets:

- Quadrupole deformations: α_{20}, α_{22};
- Octupole deformations: α_{30}, α_{31}, α_{32}, α_{33};
- Hexadecapole deformations: α_{40}, α_{42}, α_{44};
- Higher order deformations: α_{60}, α_{80}.

Let us provide at this point some estimates of the dimensions of the deformation sub-spaces in terms of the numbers of the deformation points in selected 2D-, 3D- and 4D-sets referred to as 2D-, 3D- and 4D-meshes. After systematic comparisons of various geometric properties of nuclei, we selected the typical deformation ranges and deformation steps as follows:

- Quadrupole-axial deformation, $\alpha_{20} \in [-0.9, 0.9]$ with the step 0.025;
- Quadrupole non-axial deformation, $\alpha_{22} \in [-0.3, 0.3]$ with the step 0.025;
- Octupole deformations, $\alpha_{3\mu} \in [-0.3, 0.3]$ with the steps of 0.025 (for $\mu = 0, 1, 2, 3$);

- Hexadecapole deformations, $\alpha_{4\mu} \in [-0.3, 0.3]$ with the steps 0.025 (for $\mu = 0, 2, 4$);
- Deformation $\alpha_{60} \in [-0.3, 0.3]$ with the step 0.025;
- Deformation $\alpha_{80} \in [-0.3, 0.3]$ with the step 0.025.

The total number of deformation points for one 4D-mesh is typically 10^6, with the numerical effort which requires 3 or 4 days of the c.p.u. time with typically 300 processors. The results of the 3D and 4D calculations are presented in the form of the potential energy maps after projecting onto 2D planes and minimising at each point over the remaining deformations.

6.1.2 Defining (Z, N)-Sectors of Nuclei in Nuclear Mass Table

In order to set up the numerical calculations, we split the mass table into the so-called (Z, N)-sectors, each one centred around a selected central nucleus (Z_0, N_0). Given the fact that the mean-field single-particle energies vary very smoothly with proton and neutron numbers it is possible to use the single-particle energies at any given deformation point not only for the central nucleus for which those energies were calculated but also for a number of neighbouring nuclei. However, the calculations become less realistic for Z and N too far away from the central nucleus. For this reason we define the (Z, N)-sectors as follows,

$$Z \in [Z_0 - \Delta Z,\, Z_0 + \Delta Z], \quad \text{and} \quad N \in [N_0 - \Delta N,\, N_0 + \Delta N]. \tag{6.1.4}$$

The choice of the Z and N ranges which provide an acceptable compromise between satisfactory numerical precision of the final results and the c.p.u. computing time is obtained with $\Delta Z \approx \Delta N \approx 8$, employing one spectrum of each central nucleus for the whole sector.

Example of a Total Potential Energy Map. In what follows we present an example of a 3D-mesh calculation results showing a projection on the $(\alpha_{20}, \alpha_{30})$ plane, at each point minimised over hexadecapole deformation α_{40}. By convention we normalise the total energy in such a way that the macroscopic energy of the spherical nucleus is set to zero. Certain numerical details are printed on the right-hand side of the diagram including:

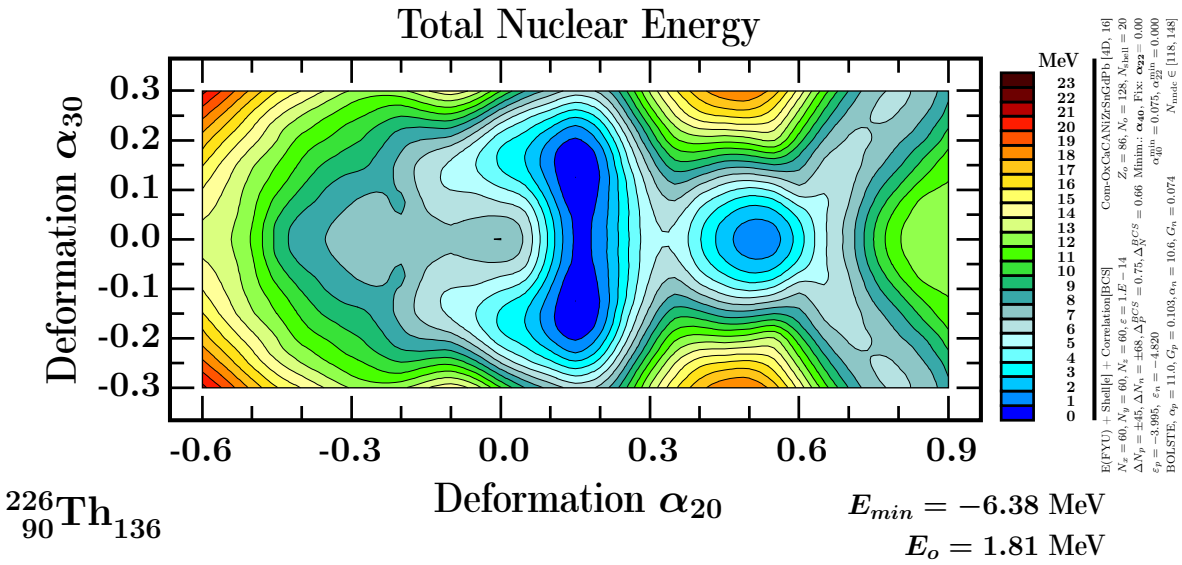

Figure 6.1.1 – *Example of the nuclear potential energy map for* ^{226}Th *nucleus. The 3D mesh energy values are projected on the* $(\alpha_{20}, \alpha_{30})$ *plane and minimised over hexadecapole deformation* α_{40}*. The minimum value of the energy is denoted by* E_{min}*, while* E_0 *represents the shell-correction energy at the spherical shape. The details characterising the used options of the algorithm and certain numerical values of parameters are shown on the right-hand side, see also the text.*

- Nuclear energy variant chosen. The text "E(FYU) + Shell[e] + Correlation[BCS]" signifies that the liquid drop model variant chosen is the Yukawa-folding type. It is accompanied by the Strutinsky shell correction variant denoted "[e]". The latter signifies that the shell energy is calculated using the traditional Strutinsky method, cf. Annex (8.2). An alternative method to calculate shell energy was proposed by Pomorski in ref. [39] in 2004. The rest of the comment-string signifies that the pairing energy contribution was calculated using the BCS correlation (in contrast to correction) energy variant.

- Woods-Saxon parametrisation: The string "Com-OxCaCANiZrSnGdPb", refers to the parameterisation variant of the Woods-Saxon Hamiltonian specified in section (2.5).

- Specification "$N_x = 60, N_y = 60, N_x = 60$", gives the numbers of Gauss-Hermit nodes used in the numerical 3D integrations.

- Central nucleus specification: "$Z_o = 86, N_o = 128$", defines the central nucleus for which the mean-field Hamiltonian has been diagonalised to obtain the single-particle energies used in the calculations for the whole (Z, N)-sector.

- Specification related to the energy minimisation: "Minim: α_{40}, Fix: $\alpha_{22} = 0.0$" signifies that at each point of the 2D projection illustrated the minimisation over α_{40} with $\alpha_{22} = 0.0$ was employed and the minimisation result at the ground state is $\alpha_{40}^{\min} = 0.075$.

- Pairing variant specifications: "BOLSTE, $\alpha_p = 11.0, G_p = 0.103, \alpha_n = 10.6, F_n = 1.00, G_n = 0.074$", means that the paring constant G is defined from eq. (8.3.6) cf. ref. [40] with the optimal α-factor selected for nuclear range $Z \geq 82, N \geq 126$.

- Single-particle energies (in MeV) of the last occupied proton and neutron levels: $\{\varepsilon_p = -3.995, \varepsilon_n = -4.820\}$.

- The extremum values of the neutron numbers of nuclei whose existence has been identified experimentally for $Z = 90$ (after the NNDC database). In the present case these are: $\{N_{\text{NNDC}} \in [118, 148]\}$, the lowest neutron number is 118 and the highest one 148.

6.2 Exotic $\alpha_{3\mu}$-Octupole Magic Number $N = 136$

Studying pear-shape nuclear configurations and the related spectroscopy of negative parity rotational bands has become one of the common interests in nuclear structure physics over the past decades. There exists well recognised regions in the nuclear mass table of nuclei with pronounced octupole deformations corresponding to the particle numbers at 34 ($g_{9/2} \leftrightarrow p_{3/2}$ coupling), 56 ($h_{11/2} \leftrightarrow d_{5/2}$ coupling), 88 ($i_{13/2} \leftrightarrow f_{7/2}$ coupling), and 134 ($j_{15/2} \leftrightarrow g_{9/2}$ coupling), cf. refs. [41][4]. Octupole correlations are also observed in numerous neighbouring nuclei, for instance $N = 136$ was predicted to have the strongest octupole correlations cited e.g. eq. (C1) in ref. [42]. The nuclei with ground-states dominated by octupole correlations often manifest low-lying negative-parity vibrational $I^\pi = 3^-$ states, which in turn become band-heads of the resulting rotational negative-parity bands.

Spherical nuclei can often generate octupole pear-shape vibrations. For instance, the first excited state at 2615 keV of the doubly magic spherical nucleus ^{208}Pb is an $I^\pi = 3^-$ state. The transition strength of the associated $E3$-transition from $I^\pi = 3^-$ to the $I^\pi = 0^+$ ground-state has measured reduced transition probability of $B(E3) = 33.8(6)$ W.u., cf. ref. [43]; one of the strongest ever measured. Similar results are found in certain neighbouring nuclei.

Octupole correlations were investigated at strongly elongated quadrupole deformations in the light Pb and Hg nuclei, cf. e.g. ref. [44] and references therein. Strong octupole effects caused by the octupole deformation components with $\mu = 0$ and $\mu = 2$

at super-deformed minima were predicted in refs. [45, 46]. However, octupole correlations at ground-states in nuclei around Pb have not been analysed in much detail.

To study nuclear octupole shape effects we perform multi-dimensional calculations involving octupole deformation parameters $\{\alpha_{30}, \alpha_{31}, \alpha_{32}, \alpha_{33}\}$ combined with appropriately selected other ones. Recall the expansion of the nuclear surface in terms of the spherical harmonics

$$\Sigma: \quad R(\theta,\varphi) = c(\{\alpha\})R_0\left[1 + \sum_{\lambda}\sum_{\mu=-\lambda}^{\lambda}\alpha_{\lambda\mu}Y_{\lambda\mu}(\theta,\varphi)\right]. \tag{6.2.1}$$

The typical 4D deformation sets (meshes) are defined as:

- Deformation Mesh, set No.1 ($\mathcal{N}_{\rm mesh} = 953\,125 \approx 1\cdot 10^6$ mesh points):
  - $\alpha_{20} \in [-0.6, 0.9]$, step 0.025;
  - $\alpha_{22} \in [-0.3, 0.3]$, step 0.025;
  - $\alpha_{3\mu} \in [-0.3, 0.3]$, step 0.025, for $\mu =$ either 0, or 1, or 2, or 3;
  - $\alpha_{40} \in [-0.3, 0.3]$, step 0.025.
- Deformation Mesh, set No.2 ($\mathcal{N}_{\rm mesh} = 390\,625 \approx 0.39\cdot 10^6$ mesh points):
  - $\alpha_{30} \in [-0.3, 0.3]$, step 0.025;
  - $\alpha_{31} \in [-0.3, 0.3]$, step 0.025;
  - $\alpha_{32} \in [-0.3, 0.3]$, step 0.025;
  - $\alpha_{33} \in [-0.3, 0.3]$, step 0.025.

The total nuclear potential 4D energy meshes lead to 6 different 2D projections; we will illustrate the corresponding results in due course.

6.2.1 Single-Nucleon Shell Effects in Terms of Octupole Shapes

To discuss the presence of deformed shell gaps in the single nucleon spectra we are going to present the corresponding single nucleon energies as functions of $\alpha_{3\mu}$-deformations. To obtain an overview of the shell effects for $N \geq 126$ it will be instructive to compare the diagrams in fig. (6.2.1) showing that the octupole deformation related gaps at the neutron number $N = 136$ play a distinct role. These gaps are caused by a repulsive interaction between the $1j_{15/2}$ intruder orbital from the main shell $N = 7$ and the $2g_{9/2}$ orbital from the main shell $N = 6$.

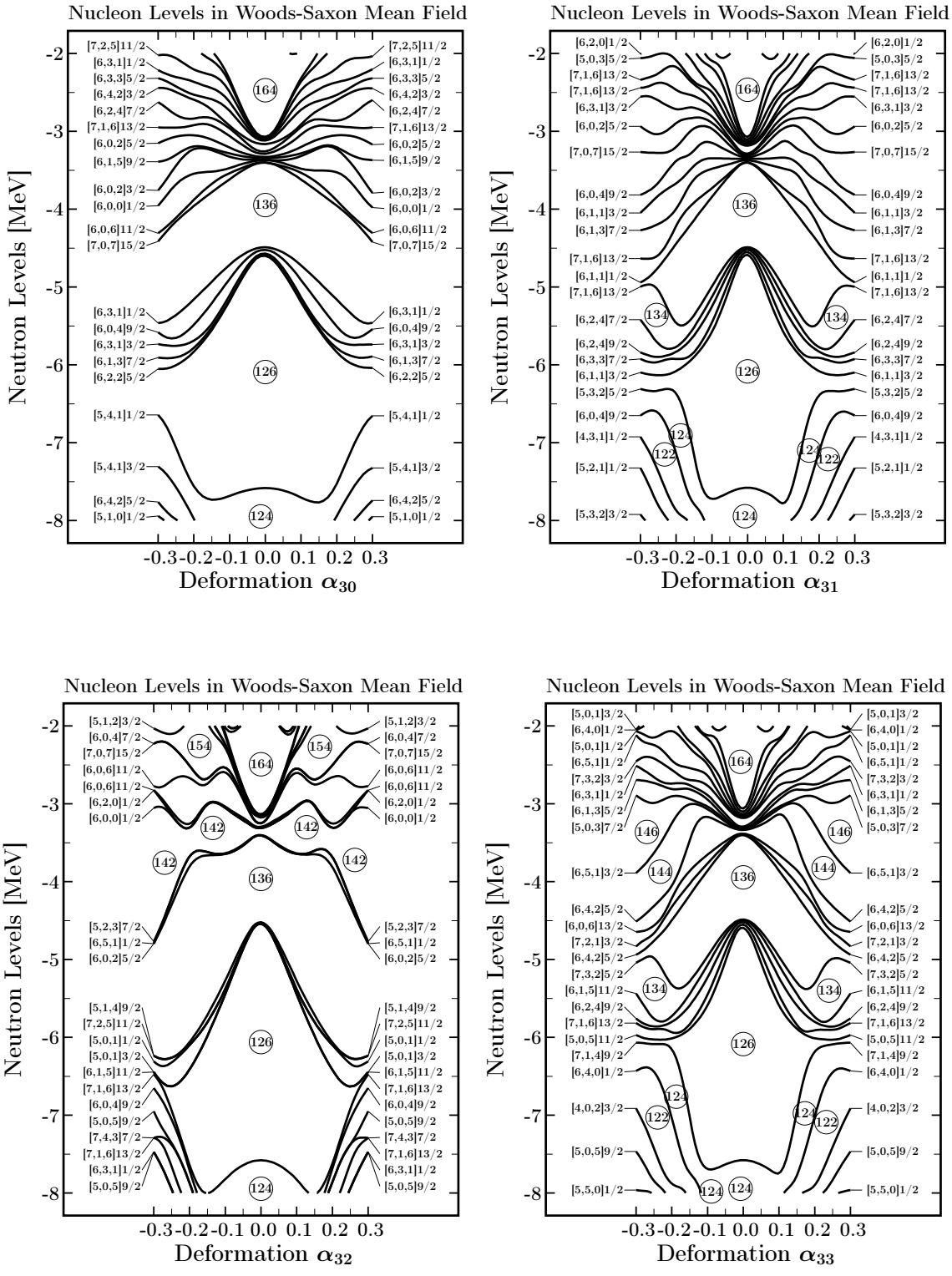

Figure 6.2.1 – *Neutron single-particle energies as functions of the octupole deformations* α_{30}, α_{31}, α_{32} *and* α_{33}. *All other deformation parameters are set to zero.*

Since the corresponding orbital angular momentum quantum numbers differ by $\Delta\ell = 3$ it becomes clear that the octupole-octupole two-body residual interactions are at the microscopic origin of the discussed shell effect, cf. eq. (C1) in refs. [42] and [47]. In the case of α_{32} the nuclear shapes possess tetrahedral symmetry. The energy gap at $N = 136$ is particularly well pronounced in this case with the size of the gap of well over 2 MeV. With growing α_{32} its size is becoming comparable with the size of the spherical gap at $N = 126$ (!). The strong shell effects can be traced back to the particular degree of freedom of the irreducible representations of tetrahedral group T_d^D discussed later.

As presented in chapter 5, section (5.2.2), the double-tetrahedral symmetry group T_d^D applicable to the Fermion mean-field Hamiltonian has one 4-dimensional irreducible representation, which corresponds to 4-fold degeneracy of single particle levels and two 2-dimensional irreducible representations assuring the usual Kramers (double) degeneracy. On average, the 4-fold degeneracy leads to increased single-particle energy spacings. Moreover, a strong tetrahedral symmetry gap opening at large α_{32} for $N = 142$ deserves noticing.

At the same time the presence of the pronounced octupole energy gaps at $N = 136$ for the octupole deformations α_{31} and α_{33}, extending up to deformation ± 0.2 should be emphasised. Comparing the single-particle energies as functions of the four octupole deformations $\alpha_{3\mu=0,1,2,3}$ we may conclude that the neutron number $N = 136$ plays a role of a special, common octupole magic number with respect to all the 4 octupole deformations, with tetrahedral symmetry (α_{32} case) dominating.

With the help of the compared single-particle energy spectra we can learn the global properties of the underlying shell effects qualitatively. However, we cannot use the single-particle energy diagrams to learn about more directly experiment-comparable nuclear properties, such as nuclear equilibrium deformations, shape evolution and the fission barriers. Thus in the following section, we will illustrate the results of these octupole shell effects obtained *via* our large-scale total potential energy calculations.

6.2.2 Octuple Effects in Heavy Pb Isotopes

In order to learn about the impact of the octupole single-particle shell-gaps on the nuclear structure effects which can be identified experimentally, we will present the resulting potential energy maps projected on the $(\alpha_{20}, \alpha_{3\mu=0,1,2,3})$ planes with the energies minimised over α_{22} and/or α_{40} deformations. We will illustrate the evolution of octupole susceptibilities for Pb isotopes with increasing neutron number between $N = 126$ and $N = 136$. Since the magic number $Z = 82$ is known to generate the strongest *spherical proton shell-effects*, by selecting the Pb isotopes we focus mainly

on the *evolution of the octupole effects caused by increasing* N and the implied neutron configurations. We begin by showing representative examples of projection $(\alpha_{20}, \alpha_{30})$ with energies minimised over α_{22} and α_{40} in figs. (6.2.2) and (6.2.3).

Results show the effect of increasing pear-shape deformation susceptibility with increasing neutron numbers. For ^{208}Pb the octupole equilibrium deformation is formally non-zero, $\alpha_{30} \approx \pm 0.05$, even though the energies are flat along α_{30} direction. This result is comparable to the one cited in ref. [48], $\alpha_{30} \approx \pm - 0.0375$, obtained using minimisation-after-projection approach with Hartree-Fock-Bogoliubov self-consistent mean field theory. Comparison of the results in figs. (6.2.2)-(6.2.3) shows an increase in the barriers separating the two symmetric octupole minima, from nearly 0 to over 2 MeV.

Analysing further the shape evolution accompanying an increase of neutron number within the sequence of lead isotopes shown in figs. (6.2.2) and (6.2.3), we find that the equilibrium shapes correspond to vanishing quadrupole deformation, thus $\alpha_{20} = 0$, and this for all examined isotopes and all the 4 octupole deformations. The results for $\alpha_{3\mu=1,2,3}$ are similar to the ones presented for α_{30} and are not shown. Thus we are dealing here with the situation rare in nuclear structure physics:

The lowest multipolarity which breaks the spherical symmetry is not quadrupole.

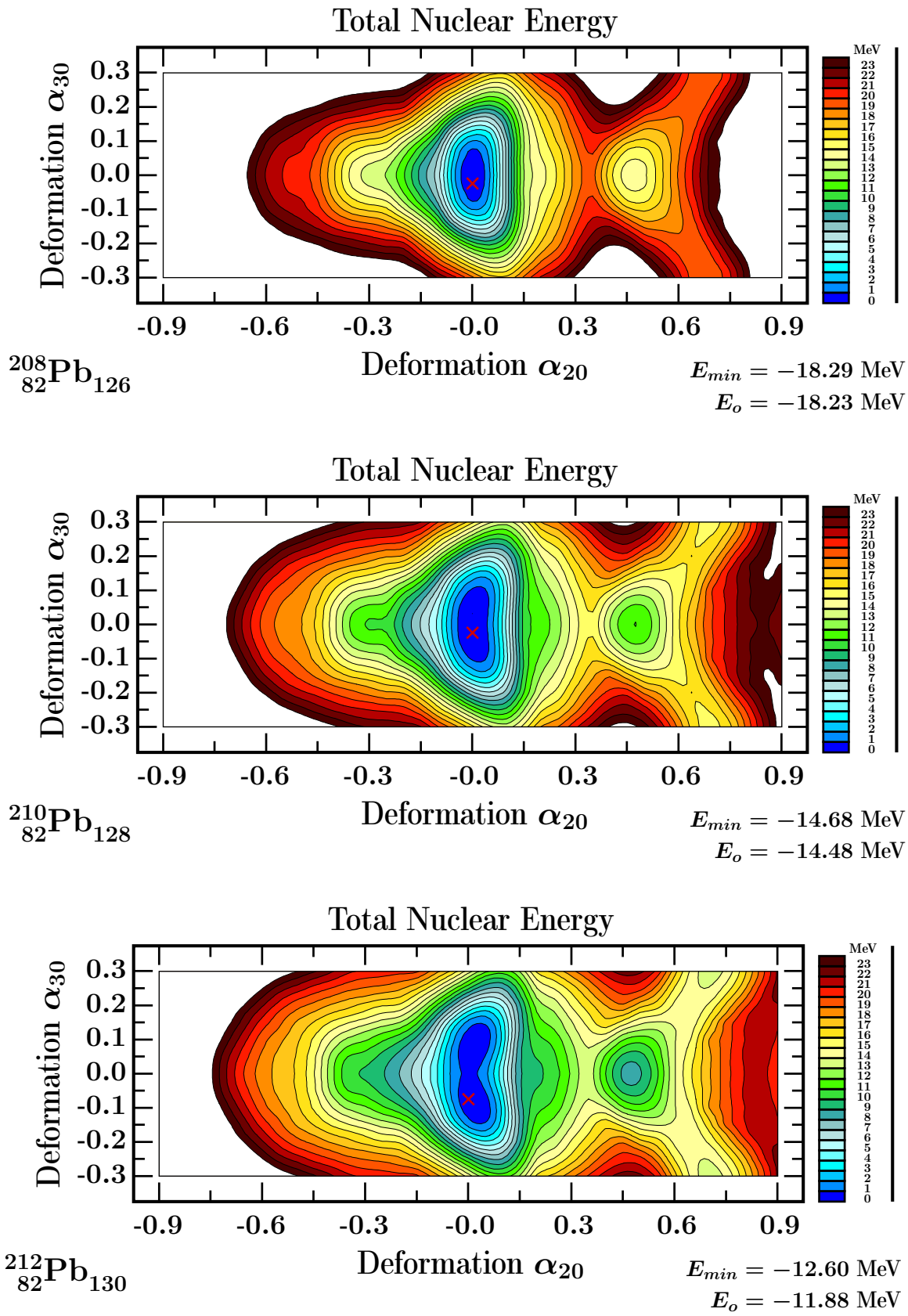

Figure 6.2.2 – *The total nuclear energy projections on the* $(\alpha_{20}, \alpha_{30})$*-plane, minimised over* α_{22} *and* α_{40} *for* $^{208-212}Pb_{126-130}$ *nuclei. Growing octupole susceptibility deserves noticing.*

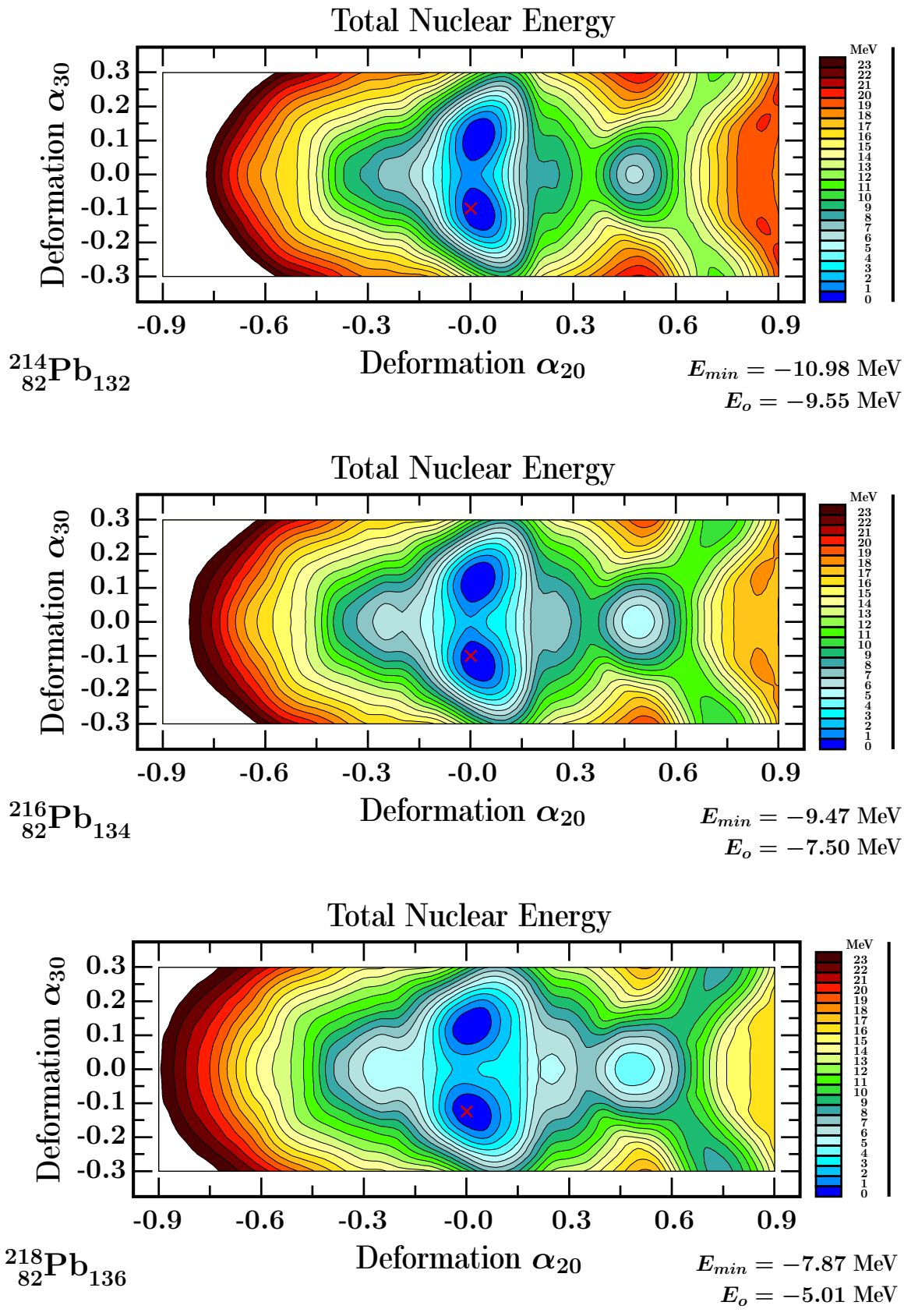

Figure 6.2.3 – *Results similar to the preceding ones but for* $^{214-216}Pb_{132-136}$ *nuclei. Barriers separating* α_{30} *double-minima increase with* N *reaching the height of the order of 2 MeV for* $N = 136$.

Since the most pronounced pear-shape octupole equilibrium deformations appear at $N = 136$, it is instructive to examine the impact of other three octupole components, i.e., α_{31}, α_{32} and α_{33} for this particular neutron number. Figure (6.2.4) shows the octupole equilibrium deformations in the potential energy surfaces projected on $\{\alpha_{20}, \alpha_{3\mu=0,1,2,3}\}$ planes, after minimisation over α_{22} and α_{40}. Comparison shows that all 4 equilibrium deformations are of the similar order of magnitude, $\alpha_{3\mu=0,1,2,3} \approx 0.12$, and all correspond to the vanishing quadrupole deformation: $\alpha_{20} = 0$.

It can be seen from the figure that the energies at the equilibrium configurations are about 1.5 MeV lower in the case of tetrahedral symmetry as compared to the other cases. Comparing the potential energy surfaces in fig. (6.2.4), we find that the barriers separating the double tetrahedral minima are over 3 MeV, while the barrier heights are about 2 MeV in the cases of α_{30}, α_{31} and α_{33}. Recall that the strongest α_{32} octupole (tetrahedral) shell effects result from the properties of the irreducible representations of the T_d^D group.

Studying the tetrahedral point-group symmetry is very important in nuclear structure both for theory and experiment because of its exotic features. In particular, according to the characteristic property of rotational bands based on tetrahedral symmetry ground states, they generate neither the collective $E1$ nor $E2$ transitions. This property leads to the so called *isomeric bands*, the subject discussed in detail in ref. [29]. Other than that, we also observe the pronounced super-prolate minimum at the excitation of the order of 4 MeV above the ground-state.

However, the experimental information about the heavy Pb isotopes is very limited. These nuclei cannot be easily populated and can be considered as increasingly exotic. It is therefore worth extending our discussion to some heavier nuclei with $Z > 82$ which are easier accessible from the experimental view point, and such an extension will be discussed next.

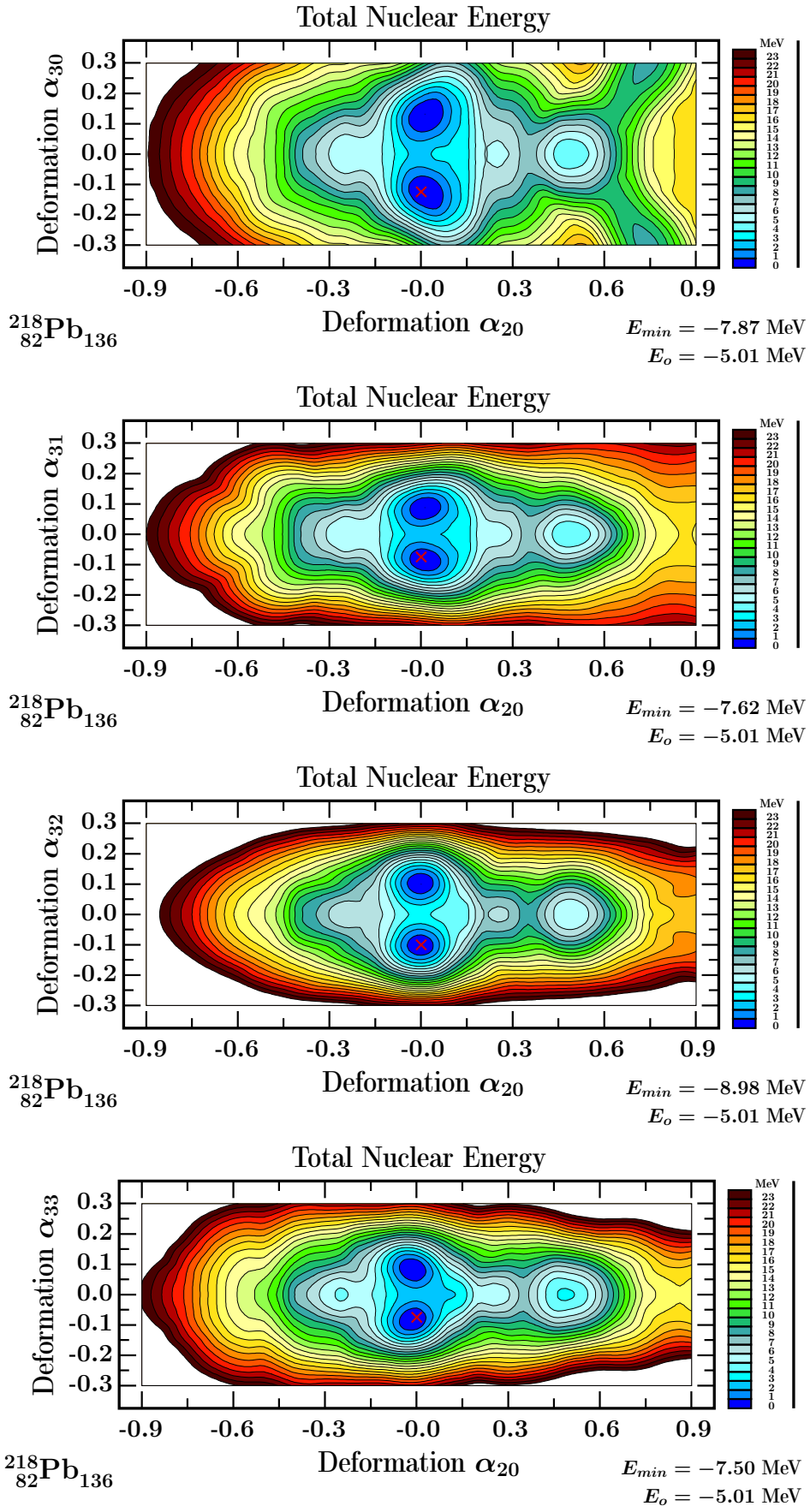

Figure 6.2.4 – *Projections of the potential energies for* $^{218}Pb_{136}$ *on* $(\alpha_{20}, \alpha_{3\mu=0,1,2,3})$ *planes after minimisation over* $\{\alpha_{22}, \alpha_{40}\}$*; illustration of the 4-fold octupole magic gap at* $N = 136$.

6.2.3 Impact of all 4 Octupole Components in Heavy Nuclei

In what follows we will extend our discussion of the symmetries based on the 4 octupole deformations to the heavier nuclei with $Z > 82$. This is motivated by the fact that these nuclei are easier accessible experimentally and thus the newly predicted exotic symmetry effects can be in principle easier identified. According to the results shown so far, the double octupole minima with well pronounced separating barriers correspond to $N \geq 132$. We will focus on Radium isotopes for which there exists relatively rich experimental information in the literature, cf. e.g. refs. [49–52].

We begin with the total energy maps for the sequence of nuclei $\mathrm{Ra}_{132,134,136}$, comparing the projections (α_{20} vs. α_{30}) and (α_{20} vs. α_{32}) in figs. (6.2.5) and (6.2.6), respectively. As seen from the figures there exists a shape competition between the octupole unstable ground-state configurations and the super-prolate minima at $\alpha_{20} \approx 0.5$, together with the less pronounced oblate minima at $\alpha_{20} \approx -0.25$.

Referring to the pear-shape evolution seen from fig. (6.2.5) one notices a steady increase of quadrupole equilibrium deformation starting from $\alpha_{20} \approx 0.10$ in $^{220}\mathrm{Ra}_{132}$ to $\alpha_{20} \approx 0.15$ in $^{224}\mathrm{Ra}_{136}$. In comparison to the $^{214-218}\mathrm{Pb}_{132-136}$ isotopes, the barriers separating the double octupole minima are lower in $\mathrm{Ra}_{132-136}$ nuclei. The calculated equilibrium deformations $\alpha_{20}^{\mathrm{th}} = 0.125$ and 0.150 for $^{222,224}\mathrm{Ra}$ can be compared with experimental ones from ref. [2], $\alpha_{20}^{\mathrm{exp}} = 0.1915(76)$ and 0.179^{+11}_{-8}. These results illustrate the level of predictive power of the newly adjusted universal parametrisation.

It is worth mentioning that the pear-shape octupole deformation commonly discussed in the literature is characterised by the octupole bands or parity-doublet bands, which correspond to the equilibrium shapes with simultaneous nonzero quadrupole and pear-shape octupole combination ($\alpha_{20} \neq 0, \alpha_{30} \neq 0$). A typical experimental evidence of pear-shape octupole configurations referring to the $E1$ transition strengths can be found, e.g., in refs. [49, 50].

From our calculations it follows that the evolution of the α_{31} and α_{33} equilibrium deformations are quite similar to the ones with α_{30}. Because of the similarity of the evolution properties, we present only the selected maps in terms of α_{30} and α_{32} deformations in this section. For more detailed discussion of the effects of α_{31} and α_{33} deformations see the next section.

As seen from comparison of figs. (6.2.5) and (6.2.6), the evolution of the tetrahedral deformation with N is qualitatively different as compared to the one of the pear-shape deformation. The energy barriers increase with increasing neutron numbers, and yet the tetrahedral minima remain at the quadrupole deformation $\alpha_{20} = 0$.

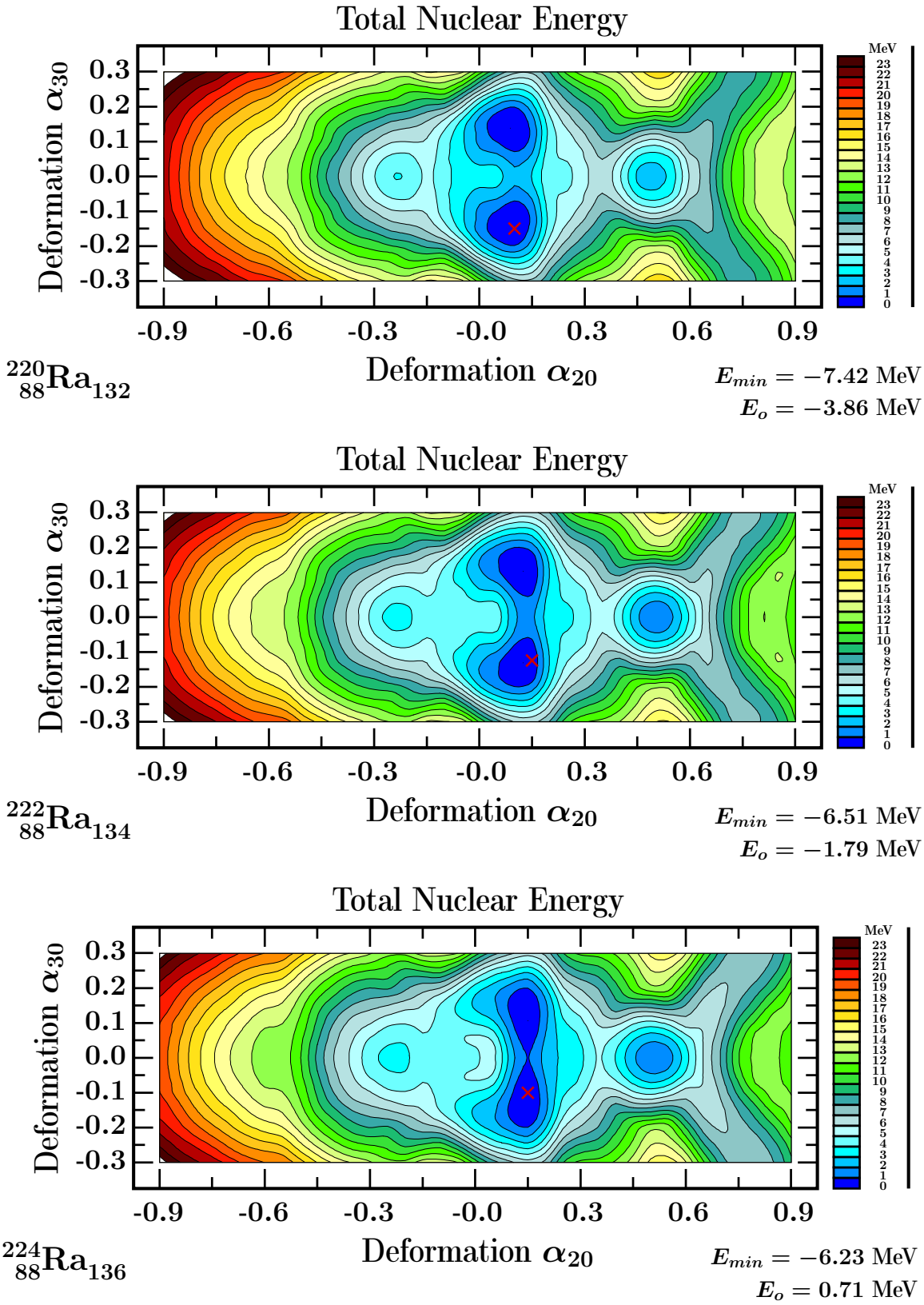

Figure 6.2.5 – *Total energy projections illustrating the pear-shape minimum evolution for* $^{220-224}Ra$*. The calculated equilibrium values are* $\alpha_{20}^{\text{th}} = 0.125$ *and* 0.150 *for* $^{222,224}Ra$ *which can be compared with experimental ones,* $\alpha_{20}^{\text{exp}} = 0.1915(76)$ *and* 0.179^{+11}_{-8}*, from ref. [2].*

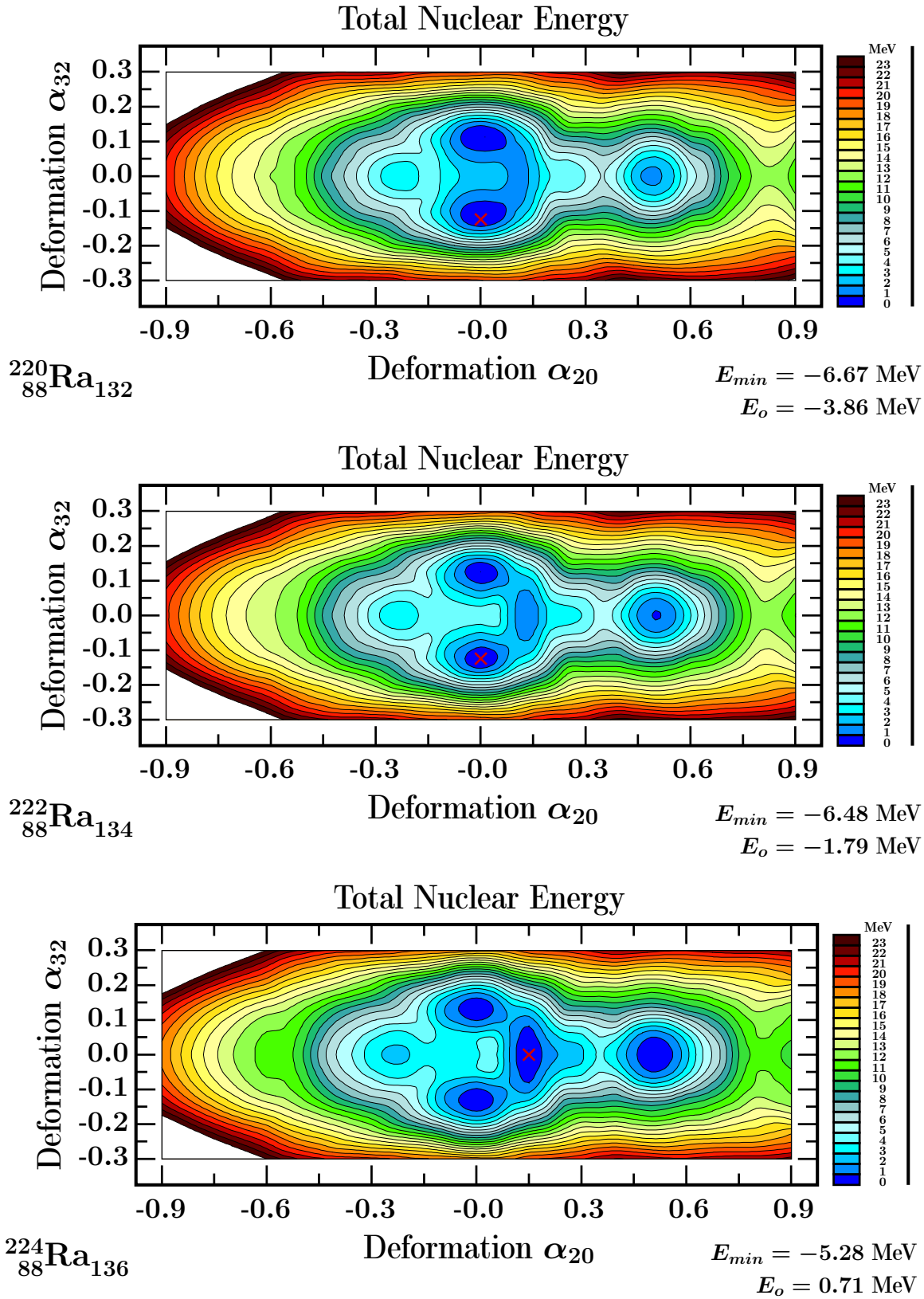

Figure 6.2.6 – *Results similar to those in fig. (6.2.5) but for the projections (α_{32} vs. α_{20}). Ground state configuration with quadrupole shape $\alpha_{20} \approx 0.15$ is most pronounced in ^{224}Ra.*

The barriers between tetrahedral minima and the prolate shape minimum with $\alpha_{20} \approx 0.15$ increase with the neutron number, leading to the prolate ground-state minimum best visible in $^{224}\mathrm{Ra}_{136}$. This implies the shape coexistence of tetrahedral and the prolate shape configurations. It follows the hypothesis of the low energy 'tetrahedral type' α_{32}-oscillatory motion of the quadrupole-deformed configurations in parallel with the tetrahedral rotation at $\alpha_{32} \neq 0$ and $\alpha_{20} = 0$. As it is known from ref. [1], the exact tetrahedral symmetry implied by $(\alpha_{20} = 0, \alpha_{32} \neq 0)$ leads to the special exotic structures with both $E1$ and $E2$ transitions vanishing. Therefore, the symmetry with $\alpha_{32} \neq 0$ and $\alpha_{20} = 0$ are expected to produce a sequence of isomers with increasing spins.

6.2.4 Implications of the Four-Fold Magic Number $N = 136$

As illustrated so far, the strongest octupole shell effects in the form of the large single-particle gaps correspond to $N = 136$ for all the 4 octupole components $\alpha_{3\mu}$. In what follows we compare the total energy maps for Po, Rn, Ra and Th nuclei at fixed neutron number $N = 136$. In analogy to the presentation in figure (6.2.4), we will concentrate on the impact of the four octuple components commenting about the underlying symmetries based on the point group theory.

Begin with some comments about the combinations of octupole and quadrupole deformations. One can demonstrate using the results of the point group theory, that both combinations, $(\alpha_{20} = 0, \alpha_{30} \neq 0)$ and $(\alpha_{20} \neq 0, \alpha_{30} \neq 0)$, lead to the same point group symmetry known as $C_{\infty v}$. Similarly, shapes with $(\alpha_{20} = 0, \alpha_{31} \neq 0)$ and $(\alpha_{20} \neq 0, \alpha_{31} \neq 0)$ lead to the common point group C_{2v}. The situation is different for the combination of α_{20} and α_{32}. Indeed, $(\alpha_{20} = 0, \alpha_{32} \neq 0)$ represents the tetrahedral point group T_d whereas $(\alpha_{20} \neq 0, \alpha_{32} \neq 0)$ generates the point group D_{2d}. Finally, for the case of $(\alpha_{20} = 0, \alpha_{33} \neq 0)$ and $(\alpha_{20} \neq 0, \alpha_{33} \neq 0)$ the underlying symmetry is again common: the point group D_{3h}.

As shown in figure (6.2.7), we find soft pear-shape octupole twin-minima with no clearly separating barriers in Po, Rn, Ra and Th nuclei, whereas the quadrupole deformation increases from $\alpha_{20} = 0.10$ to 0.15 for increasing Z. The flatness of the potential in terms of octupole deformation indicates, from the experimental point of view, that the positioning of the lowest negative parity band members $I^\pi = 1^-$ and 3^- should be close to-, or below the state of 4^+, cf. ref. [4]. Indeed, the experimental energies of the E_{1^-}, E_{3^-} and E_{4^+} for ^{222}Rn, ^{224}Ra and ^{226}Th listed in table (6.3.1) correspond to the experimental excitations discussed in ref. [4].

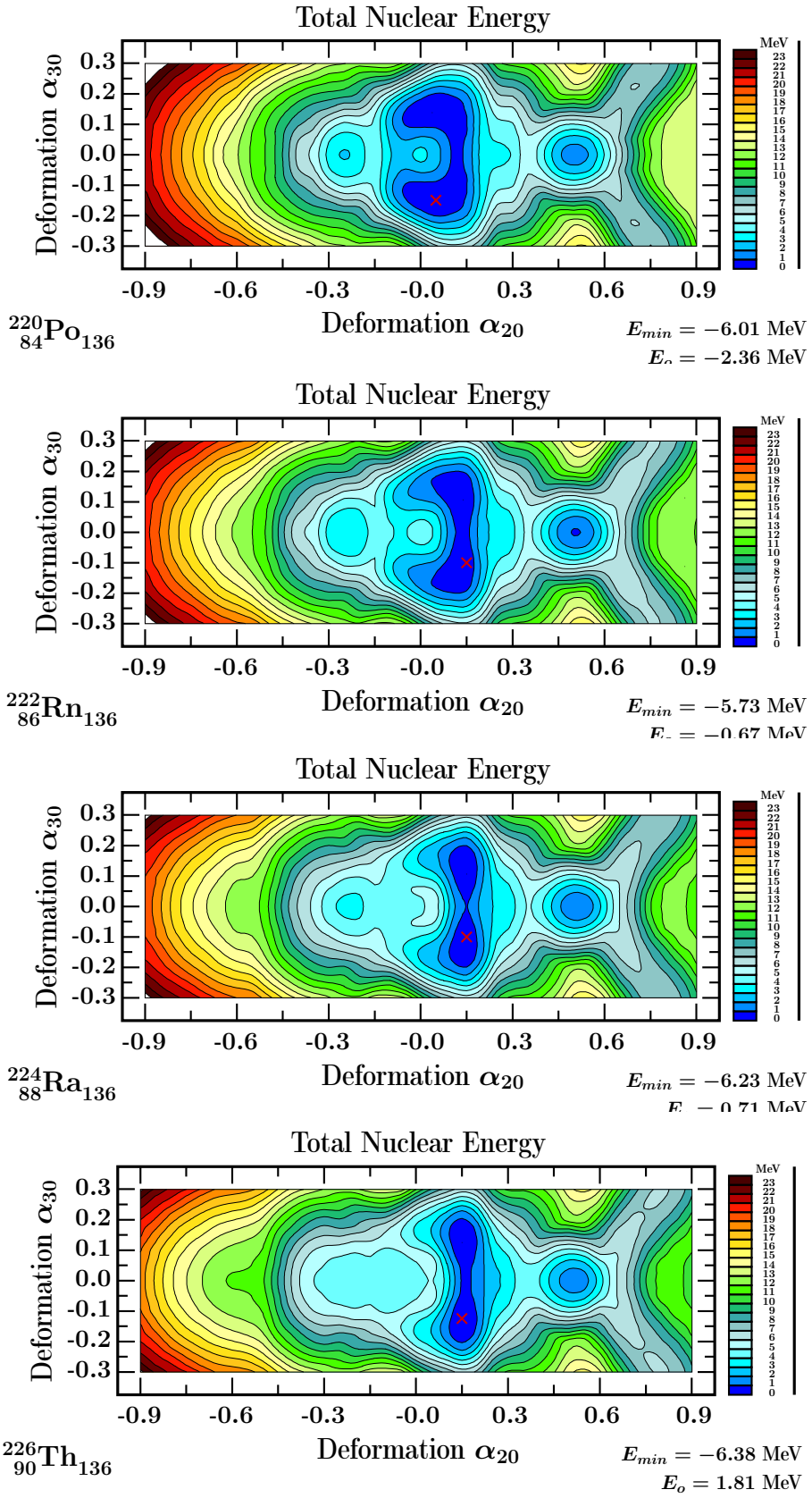

Figure 6.2.7 – *Octupole α_{30} effects at the magic number $N = 136$. Theoretical quadrupole deformations for ^{222}Rn, ^{224}Ra and ^{226}Th are $\alpha_{20}^{\rm th}$ =0.13, 0.15 and 0.16, respectively; the experimental ones from ref. [2] are: $\alpha_{20}^{\rm exp}$ =0.1417(45), 0.179^{+11}_{-8} and 0.2299(19).*

Table 6.2.1 – *Comparing experimental energies of the lowest negative parity E_{1^-} and E_{3^-} and the positive parity E_{4^+} states, whose mutual closeness, according to ref. [4], indicates the flatness of the potential as function of the octupole deformation. The values are taken from National Nuclear Data Center (NNDC) database. There are no experimental results available for ^{220}Po.*

	E_{1^-} (keV)	E_{3^-} (keV)	E_{4^+} (keV)
^{222}Rn	230.4	307.5	226.4
^{224}Ra	216.0	290.4	250.8
^{226}Th	600.7	635.5	448.4

In what follows we compare the evolution of the potential energy surfaces in terms of exotic α_{31}-deformation in fig. (6.2.8). The general properties of those diagrams are similar to the ones seen in fig (6.2.7). The soft octupole α_{31}-deformation combined with nonzero quadrupole deformation increase from 0.10 to 0.15 with increasing proton number, whereas the potential valleys are slightly broader and shorter.

Recall that the point-group symmetry generated by α_{31} deformation in terms of group theory is C_{2v} with or without the contributions from the axial quadrupole deformation. Since the potential energies are steeper in the present case, one may expect that the corresponding vibration energies are higher than the ones generated by α_{30}-deformation. Moreover, the non-axial octupole minima are predicted to be in competition with the super-prolate minima at $\alpha_{20} \approx 0.5$, with only a few hundreds of keV above the ground-state.

We continue comparing the potential energies as functions of tetrahedral deformation α_{32} in fig. (6.2.9). Tetrahedral minima at $\alpha_{32} = \pm 0.15$ are separated by the potential barriers of about 1 to 2 MeV. They are accompanied by vanishing quadrupole $\alpha_{20} = 0$ equilibrium deformation. At the same time, in this particular case, there appear axially symmetric quadrupole minima at $\alpha_{20} \approx 0.15$ in ^{222}Rn, ^{224}Ra and ^{226}Th nuclei. Such quadrupole minima may give rise to the β-, and α_{32}-vibrations, the latter considered as analogues of the γ-vibrations. As mentioned earlier, the formal point groups are different for the α_{32} deformation pure as opposed to the combination of α_{32} with the quadrupole shape components, the former representing T_d-, and the latter D_{2d}-symmetry.

The super-deformed prolate minima at $\alpha_{20} \approx 0.5$, lying about a few hundreds of keV above the ground-state are present in the discussed 2D projections.

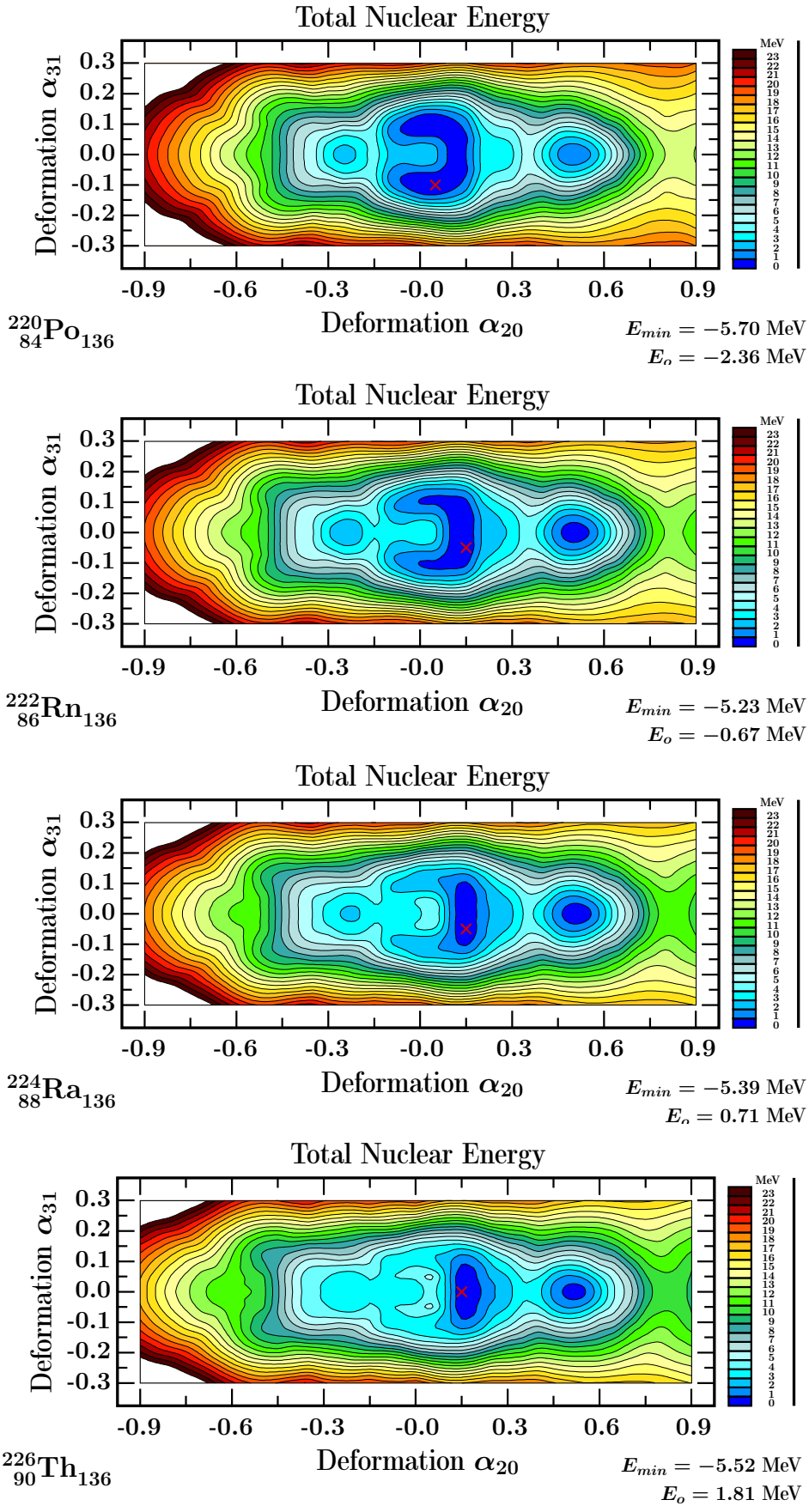

Figure 6.2.8 – *Similar to the preceding figure but for α_{31} deformation.*

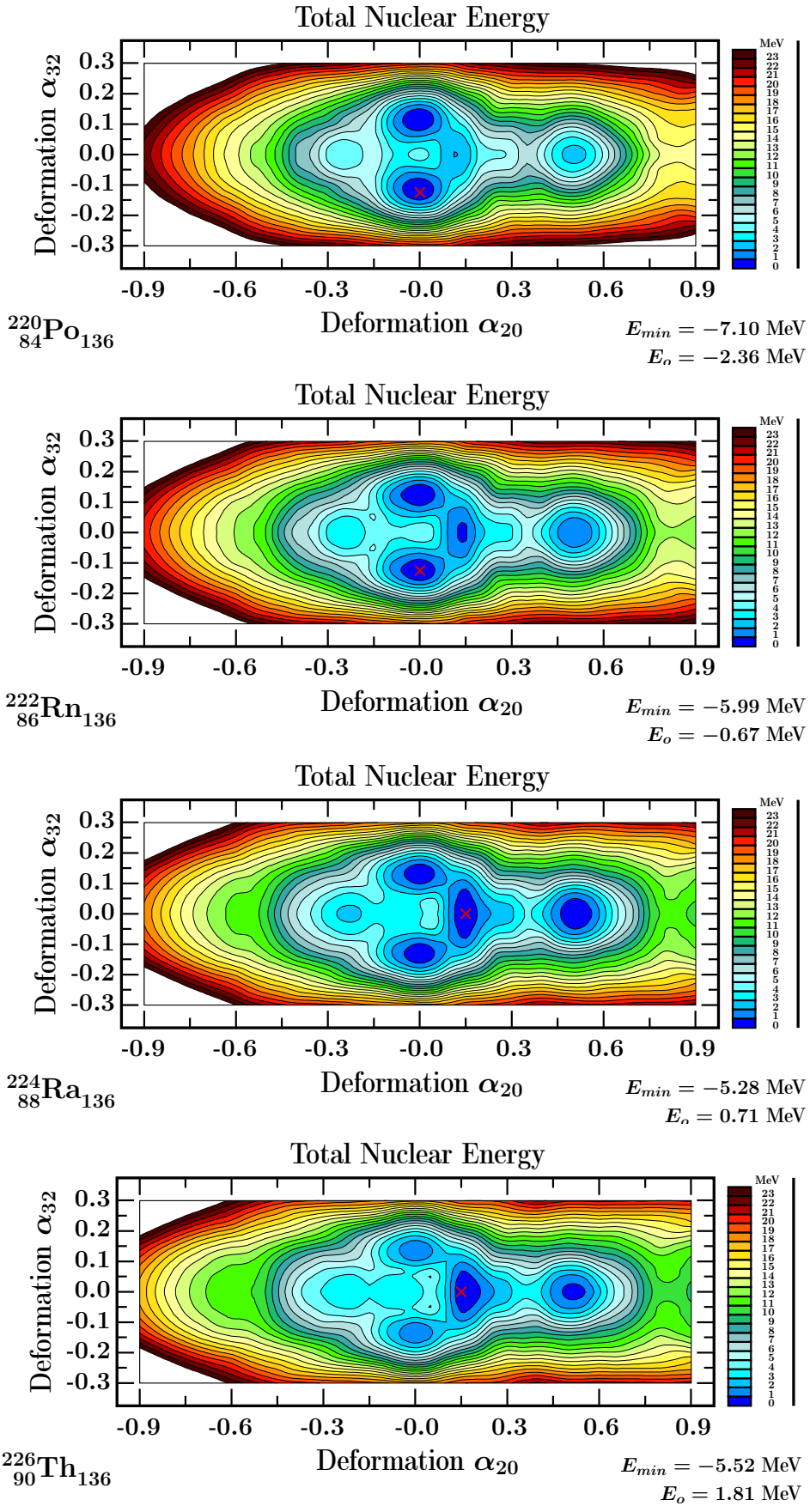

Figure 6.2.9 – *Illustration similar to the preceding ones but for the tetrahedral symmetry generating α_{32}-deformation.*

In figure (6.2.10) we compare analogous potential energy surfaces with α_{32} replaced by α_{33}. Again we note a systematic tendency with the quadrupole minima varying from $\alpha_{20} = 0.05$ to 0.150, whereas the double α_{33} minima are getting less and less pronounced with increasing proton numbers from $Z = 84$ to 90. More precisely, in ^{220}Po and ^{222}Rn, there clearly exist double α_{33} minima, with the separating potential barriers of the order of 1 to 2 MeV. They can be considered sufficiently high to stabilise static D_{3h} configurations. In contrast, in ^{224}Ra and ^{226}Th nuclei, the separating potential barriers are only of the order of a few hundreds of keV, indicating the inclination for the large amplitude oscillations. More precise information concerning such oscillations can be obtained by solving the collective Schrödinger equation, the problem which will be introduced it the next sections. Since the point-group symmetry D_{3h} remains the same with and without quadrupole deformation, we may expect the presence of coexisting D_{3h} -, and quadrupole vibrations.

Results discussed so far illustrate the mechanisms possibly generating the presence of exotic symmetries in the Pb, and in the neighbouring Po, Rn, Ra and Th nuclei. These exotic symmetries are mainly caused by neutron shell effect generated by the octupole-octupole two body residual interactions sandwiched between the neutron $2g_{9/2}$ and $1j_{15/2}$ orbitals, whereas the impact of the proton shell effect can be considered small, and slightly destabilising the exotic symmetries lead by the neutrons.

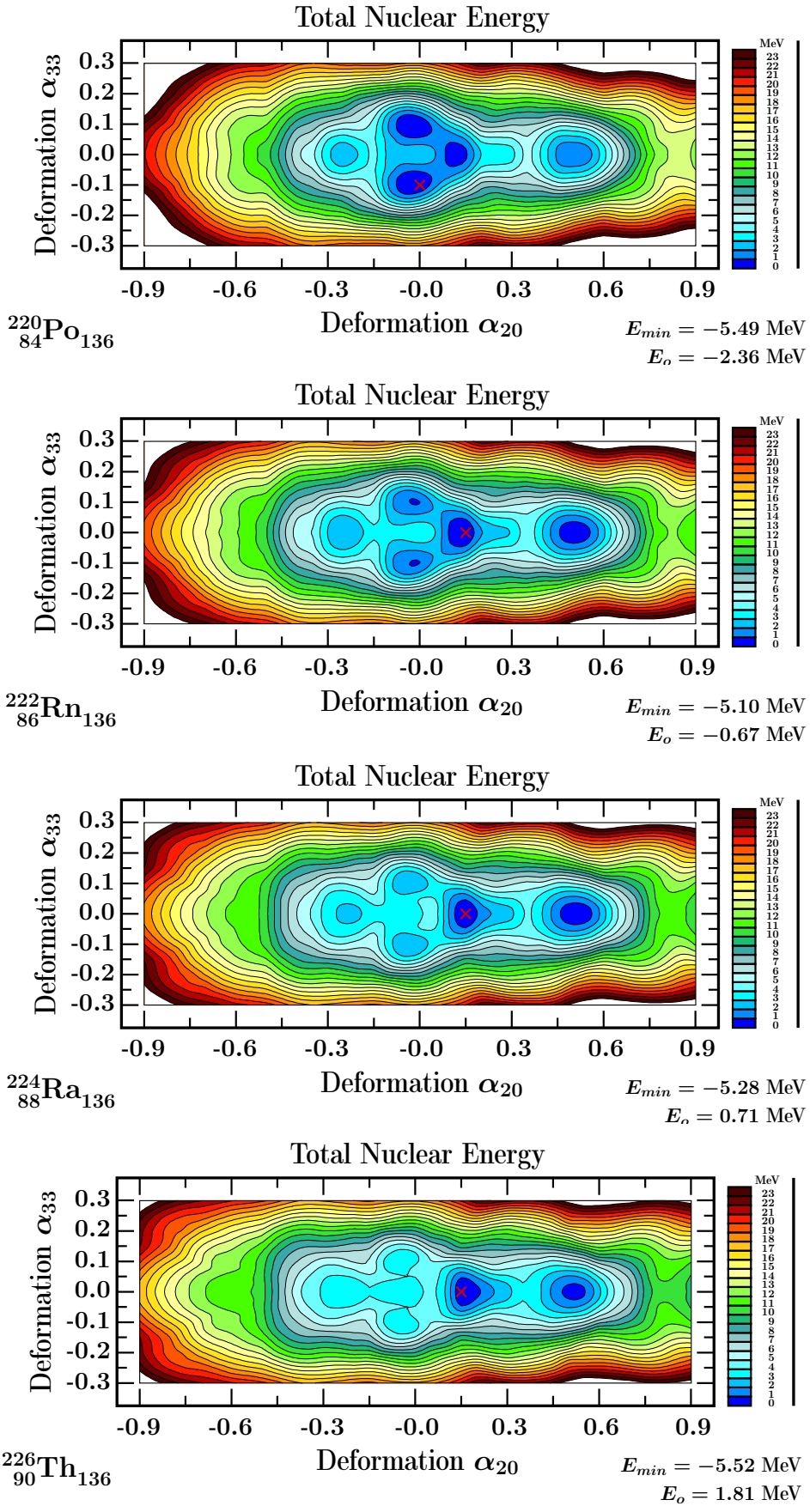

Figure 6.2.10 – *Similar to the preceding ones but for α_{33} deformation.*

6.3 Exotic Symmetries and Their Identification

In the preceding sections we have discussed structural links between the single-particle gaps involving octupole deformations and the repulsion between the neutron $2g_{9/2}$ and $1j_{15/2}$ orbitals. In this section we will examine specific properties of rotational bands implied by exotic symmetries in nuclei. These properties turn out to be unique and, in contrast to the "well known rotational properties", they differ from symmetry to symmetry. Consequently, they provide the criteria for the experimental identification of the underlying symmetries. We will also provide schematic illustrations of the typical properties of those specific rotational bands.

6.3.1 Evolution of the Magic Gaps with Rotational Frequency

Before examining the general quantum properties of the rotational bands generated by the exotic shape geometry, it will be instructive to test the evolution with increasing spin of the underlying exotic shell structures which stabilise such shapes. In order to be able to study the octupole shell evolution with increasing spin (alternatively: rotational frequency) we are going to use the 3D cranking approximation by solving the mean-field cranking problem as summarised in chapter 4, section (4.3.3).

Let us recall the form of the mean-field cranking Hamiltonian

$$\hat{H}_{\rm ws} \rightarrow \hat{H}^{\omega}_{\rm ws} = \hat{H}_{\rm ws} - \vec{\omega} \cdot \hat{\jmath}, \tag{6.3.1}$$

in which the mean-field Woods-Saxon Hamiltonian, $\hat{H}_{\rm ws}$, was defined in eq. (4.3.21). The symbol $\vec{\omega} = \{\omega_x, \omega_y, \omega_z\}$ in eq. (6.3.1) represents the collective rotational frequency vector and $\hat{\jmath}$ the nucleonic angular momentum vector-operator.

Representative illustrations of the single-particle Routhians and their evolution with rotation about $\mathcal{O}_y$-axis as functions of nuclear cranking frequency, here ω_y, are shown in figures (6.3.1)-(6.3.4). Calculations indicate that the total angular momenta (i.e., sums of the proton and neutron contributions) at the maximum frequency presented in the diagrams are of the order of 20 $\hbar$, an approximate estimate valid for all the studied nuclei. This indicates that the discussed exotic shell effects are strong enough to generate rotational bands with exotic quantum properties over sufficiently large spin ranges, possibly allowing for their experimental identifications.

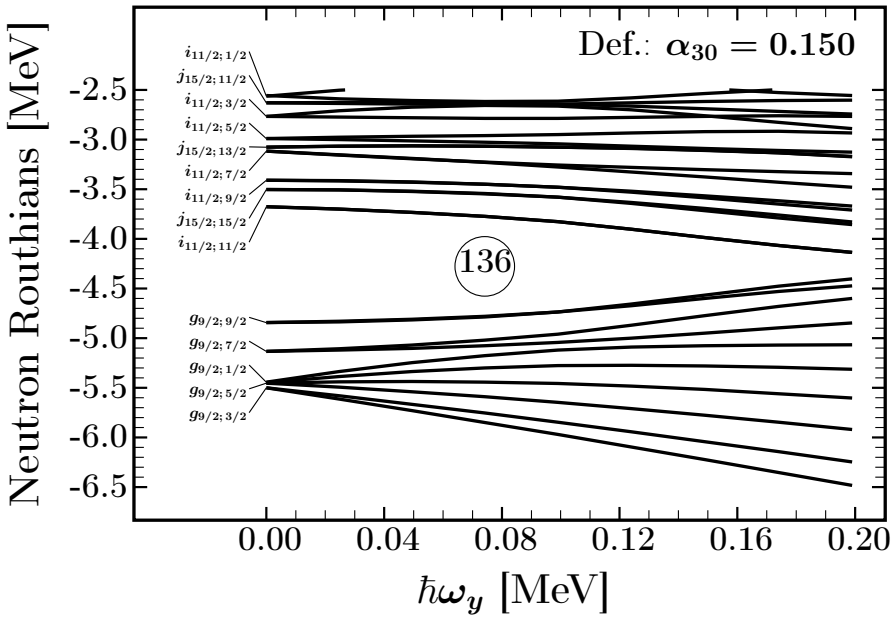

Figure 6.3.1 – *Neutron single-particle Routhians at pear-shape deformation* $\alpha_{30} = 0.15$ *representative for the minima predicted by the potential energy calculations for Pb, Po, Rn, Ra and Th nuclei. The gap appearing at* $\hbar\omega_y = 0$ *is slightly over 1.5 MeV and decreases with cranking frequency.*

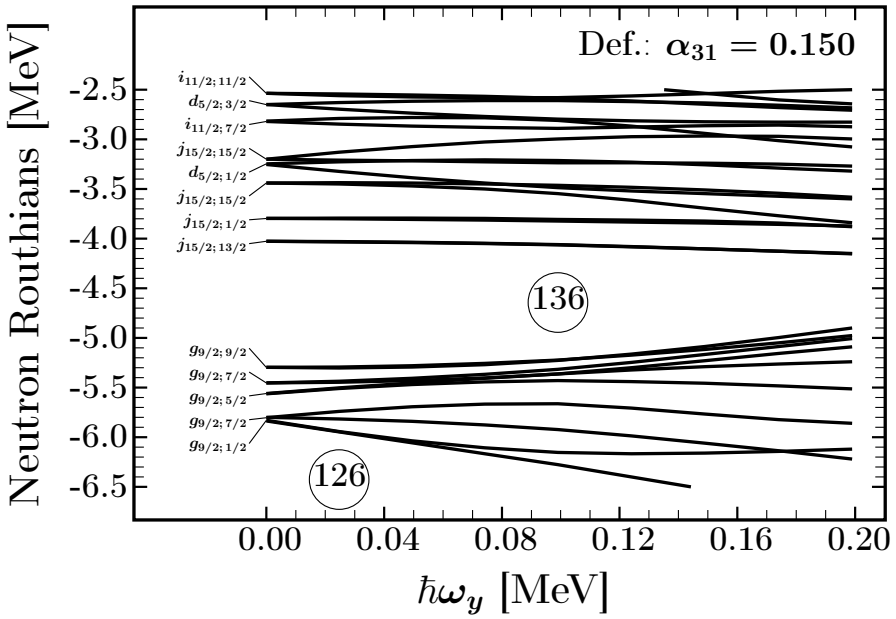

Figure 6.3.2 – *Similar to the preceding one but for the octupole deformation* $\alpha_{31} = 0.15$*. The gap of about 1.5 MeV at* $\hbar\omega_y = 0$ *remains relatively stable over the frequency range up to* $\hbar\omega_y = 0.20$*.*

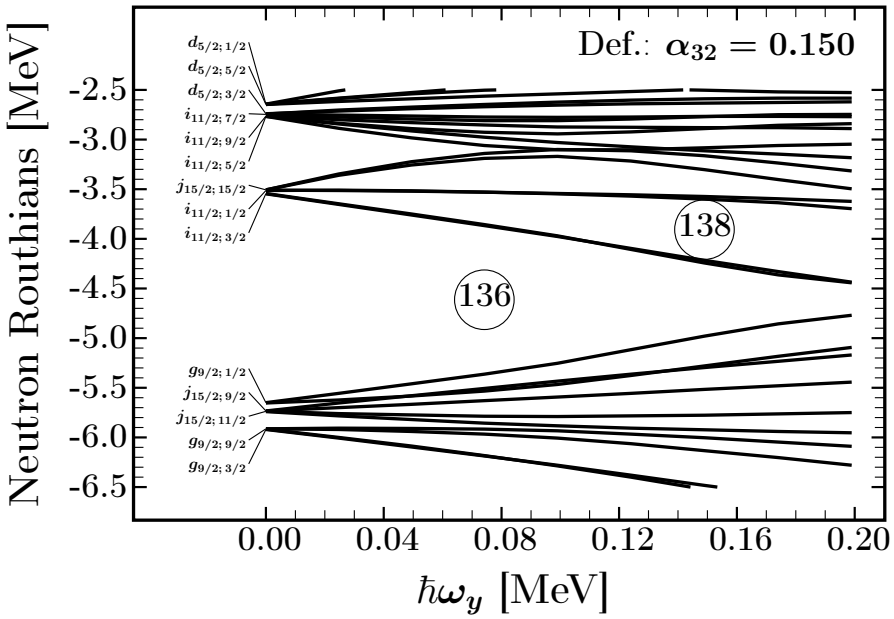

Figure 6.3.3 – *Similar to the preceding ones but for the tetrahedral octupole deformation* $\alpha_{32} = 0.15$ *characteristic for the predicted equilibrium deformations in the studied nuclei.*

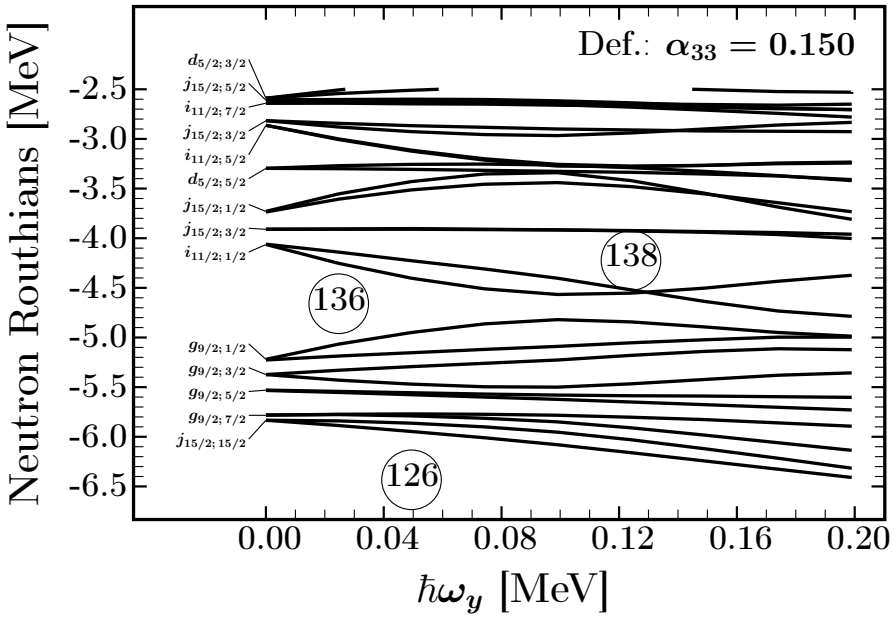

Figure 6.3.4 – *Similar to the preceding ones but for the* α_{33}*-octupole deformation representing the* D_{3h}*-symmetry. Compared to the other octupole deformations, the shell effects in the present case are the weakest and/or their vanishing with rotational frequency the fastest.*

Calculations show that the discussed octupole shell gaps at $N = 136$ decrease with increasing frequency as expected and that the 'speed' of their vanishing depends non-negligibly on the rank $\mu \in \{0, 1, 2, 3\}$ of the octupole deformation. For instance, in the case of α_{31}-deformation, the $N = 136$ energy gap stays almost constant in the tested frequency zone, but the strongest shell effects correspond to the tetrahedral symmetry α_{32}-deformation, due to specific degeneracies of the single-particle spectrum applying in the T_d^D-symmetry case. Comparing the shell effects among all the 4 octupole deformations we find that α_{33}-effect may be considered the weakest and its vanishing with $\hbar\omega_y$ the fastest.

We conclude from the presented mean-field cranking estimates that the octupole shell-gaps at $N = 136$, even though decreasing with increasing spins due to the Coriolis mixing, nevertheless survive within the frequency range large enough to produce rotational bands within the spin range of the order of a dozen of $\hbar$.

6.3.2 Rotational Bands within C_{2v}, D_{3h} and D_{2d} Symmetries

Results presented in the preceding sections encourage us to extend our study to include the symmetries built on the exotic α_{31}-, and α_{33}-octupole deformations which lead to C_{2v} and D_{3h} symmetries, respectively. Furthermore, we wish to include exotic shapes with non-zero quadrupole component, ($\alpha_{20} \neq 0, \alpha_{32} \neq 0$) i.e., D_{2d} point group symmetry.

Symmetry C_{2v}: The Case of ($\alpha_{31} \neq 0$). According to eq. (5.4.9) and with the help of the characters of C_{2v} group we obtain the table of multiplicity factors shown below. The schematic illustration of the structure of rotational band built on the ground-state with $I^\pi = 0^+$ is presented in fig. (6.3.6). It shows in particular that, characteristically, the states $I^\pi = 0^-$ and 1^+ are absent in this 'C_{2v} ground-state' band.

Table 6.3.1 – *Multiplicity factors $a_n^{(I\pi)}$ for C_{2v} group corresponding to 4 irreducible representations denoted A_1, A_2, B_1 and B_2 for integer spins $I \leq 12$ and positive parity are shown. The reader interested in details of the representation theory jargon and notation may consult the Annex* "Groups".

C_{2v} Multiplicity Factors for $D^{(I\pi=+)}$													
I^+	0^+	1^+	2^+	3^+	4^+	5^+	6^+	7^+	8^+	9^+	10^+	11^+	12^+
A_1	1	0	2	1	3	2	4	3	5	4	6	5	7
A_2	0	1	1	2	2	3	3	4	4	5	5	6	6
B_1	0	1	1	2	2	3	3	4	4	5	5	6	6
B_2	0	1	1	2	2	3	3	4	4	5	5	6	6

Table 6.3.2 – *Results similar to those in table (6.3.1) but for negative parity.*

C_{2v} Multiplicity Factors for $D^{(I\pi=-)}$													
I^-	0^-	1^-	2^-	3^-	4^-	5^-	6^-	7^-	8^-	9^-	10^-	11^-	12^-
A_1	0	1	1	2	2	3	3	4	4	5	5	6	6
A_2	1	0	2	1	3	2	4	3	5	4	6	5	7
B_1	0	1	1	2	2	3	3	4	4	5	5	6	6
B_2	0	1	1	2	2	3	3	4	4	5	5	6	6

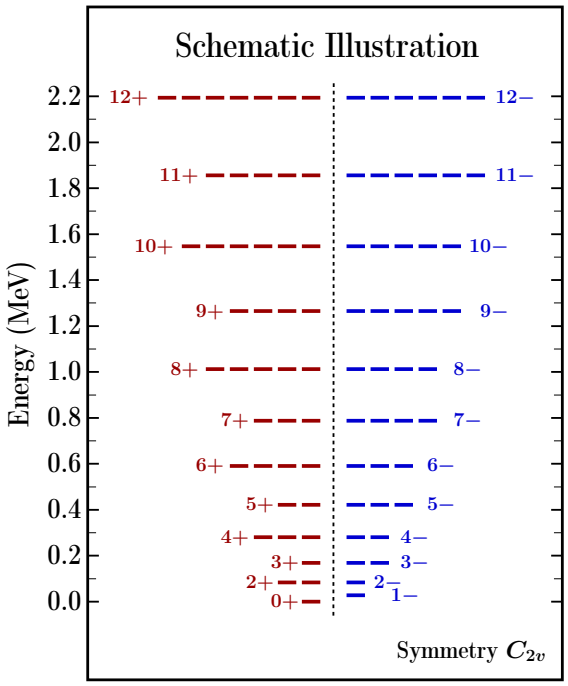

Figure 6.3.5 – *Schematic illustration of the structure of the rotational band based on* $I^\pi = 0^+$ *ground-state for the symmetry* C_{2v}.

As seen from figure (6.3.5), the degeneracies of the multiplets increase with increasing spins, reaching the order 7 at spin 12^+ and the order 6 at spin 12^-.

Symmetry D_{3h}: The Case of $\alpha_{33} \neq 0$. In what follows we will examine rotational properties of nuclei with the octupole deformation $\alpha_{33} \neq 0$ leading to the D_{3h} symmetry. The corresponding point-group contains among other symmetry elements a three-fold symmetry axis. In analogy to the tables of the multiplicity factors for the C_{2v} symmetry, we obtain the following tables based on the irreducible representation of D_{3h} point group.

Schematic illustration of the rotational structure built on the lowest $I^\pi = 0^+$ with intrinsic symmetry D_{3h} state is shown in figure (6.3.6). It shows that the numbers of the degenerate states increase with increasing spins. In particular the negative parity states with spins $I \leq 2$ are absent, similarly the positive parity states with spins $I = 3$ and 5 are missing.

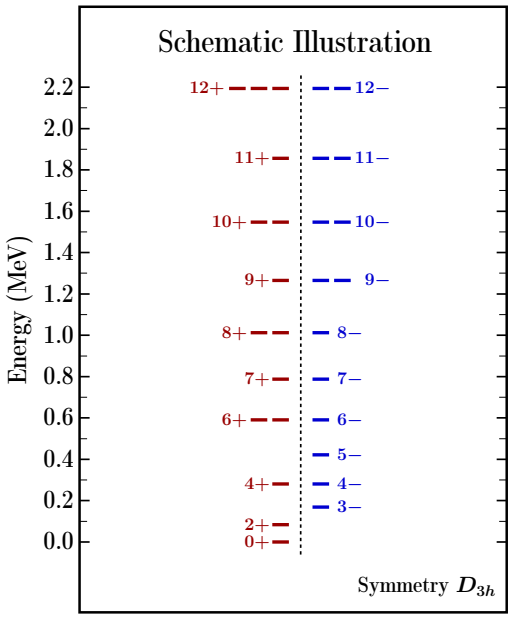

Figure 6.3.6 – *Schematic illustration of the structure of the rotational band built on top of the* $I^\pi = 0^+$ *"*D_{3h} *ground-state".*

Table 6.3.3 – *Results similar to the ones in table (6.3.1) but for octupole symmetry* D_{3h}.

D_{3h} Multiplicity Factors for $D^{(I\pi=+)}$													
I^+	0^+	1^+	2^+	3^+	4^+	5^+	6^+	7^+	8^+	9^+	10^+	11^+	12^+
A_1	1	0	1	0	2	1	2	1	3	2	3	2	4
A_2	0	1	0	1	1	2	1	2	2	3	2	3	3
E	0	1	1	2	2	3	3	4	4	5	5	6	6
B_1	0	0	1	1	1	1	2	2	2	2	3	3	3
B_2	0	0	1	1	1	1	2	2	2	2	3	3	3

Table 6.3.4 – *Results similar to the ones in the preceding table but for the negative parity.*

D_{3h} Multiplicity Factors for $D^{(I\pi=-)}$													
I^-	0^-	1^-	2^-	3^-	4^-	5^-	6^-	7^-	8^-	9^-	10^-	11^-	12^-
A_1	0	0	1	1	1	1	2	2	2	2	3	3	3
A_2	0	0	1	1	1	1	2	2	2	2	3	3	3
E	0	1	1	2	2	3	3	4	4	5	5	6	6
B_1	1	0	1	0	2	1	2	1	3	2	3	2	4
B_2	0	1	0	1	1	2	1	2	2	3	2	3	3

Octupole Symmetry D_{2d}: The case of $\alpha_{20} \neq 0$, $\alpha_{32} \neq 0$. As presented in the preceding sections, equilibrium deformations in some heavy nuclei contain combination of the $\alpha_{20} \neq 0$ and $\alpha_{32} \neq 0$ contributions corresponding to the D_{2d} point group symmetry. Similarly as before we will examine the multiplicity factors implied by the irreducible representations of this group. They are given in tables (6.3.5) and (6.3.6), whereas a schematic illustration of the implied rotational band is presented in fig. (6.3.7). As seen from the figure the states $I^{\pi} = 1^{+}$ and 3^{+} are absent, as well as the negative parity states $I^{\pi} = 0^{-}$ and 1^{-}. Moreover, the spin-parity sequence contains an ample selection of degenerate both positive and negative parity states of both even and odd spins. In contrast to the 'pure $\alpha_{32} \neq 0$' tetrahedral-symmetry states, they all may lead to the combinations of the electromagnetic $E2$ and $E1$ transitions, even if not very strong. This can be seen as a factor encouraging the corresponding experimental identification employing modern γ-detection systems.

Table 6.3.5 – *Similar to the results in table (6.3.4) but for octupole symmetry D_{2d}.*

I^{+}	0^{+}	1^{+}	2^{+}	3^{+}	4^{+}	5^{+}	6^{+}	7^{+}	8^{+}	9^{+}	10^{+}	11^{+}	12^{+}
$A_1^{'}$	1	0	1	0	1	0	2	1	2	1	2	1	3
$A_2^{'}$	0	1	0	1	0	1	1	2	1	2	1	2	2
$E^{'}$	0	0	1	1	2	2	2	2	3	3	4	4	4
$A_1^{''}$	0	0	0	1	1	1	1	1	1	2	2	2	2
$A_2^{''}$	0	0	0	1	1	1	1	1	1	2	2	2	2
$E^{''}$	0	1	1	1	1	2	2	3	3	3	3	4	4

Table 6.3.6 – *Results similar to the ones in table (6.3.5) but for the negative parity states.*

I^{-}	0^{-}	1^{-}	2^{-}	3^{-}	4^{-}	5^{-}	6^{-}	7^{-}	8^{-}	9^{-}	10^{-}	11^{-}	12^{-}
$A_1^{'}$	0	0	0	1	1	1	1	1	1	2	2	2	2
$A_2^{'}$	0	0	0	1	1	1	1	1	1	2	2	2	2
$E^{'}$	0	1	1	1	1	2	2	3	3	3	3	4	4
$A_1^{''}$	1	0	1	0	1	0	2	1	2	1	2	1	3
$A_2^{''}$	0	1	0	1	0	1	1	2	1	2	1	2	2
$E^{''}$	0	0	1	1	2	2	2	2	3	3	4	4	4

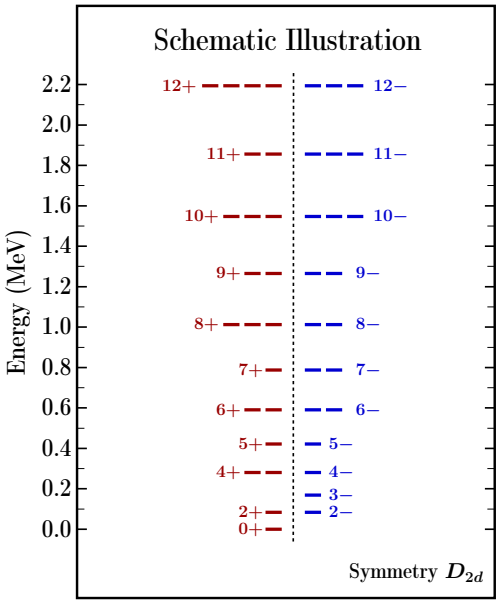

Figure 6.3.7 – *Schematic illustration of the structure of the rotational band based on* $I^\pi = 0^+$ *"ground-state of symmetry* D_{2d}*".*

6.3.3 Identification Schemes of Exotic Symmetries

According to our mean-field theory calculations, potential energy surfaces manifest strong octupole shell effects leading to non-vanishing $\alpha_{3\mu}$ equilibrium deformations. The properties of rotational band structures built on such exotic shapes are derived with the help of the point group and group representation theories and are presented in the preceding sections together with the schematic illustrations. Given the fact that the tetrahedral symmetry, one of the most exotic ones discussed here, has been discovered experimentally in ^{152}Sm nucleus in ref. [29], we believe that the other exotic structures accompanying symmetries C_{2v}, D_{3h} and D_{2d} are worth attention in the future, both from experimental and theory view points. In what follows we will comment on possible experimental identification of the exotic symmetries as they were presented in the preceding sections.

Identification of Exotic Symmetries: Collective-Level Degeneracies. As shown in figures (6.3.5) to (6.3.7), one of the characteristics of the exotic-band structures generated by symmetries C_{2v}, D_{2h} and D_{2d} are the degeneracies of certain levels. Therefore the most evident technique to follow would be to attempt establishing the presence of those degeneracies experimentally. However, such an identification may encounter certain specific difficulties which will be discussed next.

To start, the nuclei which are optimal from the theory view-point usually do not correspond to the potentially most successful experiments, which depend on the optimal

target-projectile combinations as well as on the available detection instrumentation. Therefore the choice leading to the final experimental proposals will be subject to necessary compromises.

Consider next a given spin-parity I^π, d-fold degenerate multiplet. The related wave functions $\Psi^{I_\pi}_{M,\rho}$ for $\rho = 1, 2, ...d$, are mutually orthogonal and therefore representing in general independent, thus different substructures. It follows that the feeding conditions of each of the multiplet members are expected to be generally different. Consequently, some states may not at all be measurably populated within a given reaction, and several alternative reactions and/or experiments may be needed to succeed with the population of all the members of the multiplet of interest.

Despite certain practical difficulties mentioned, there exists a strongly helping factor: All the band levels form parabolic E_I -vs.- I dependence. The latter will be very helpful in eliminating or accepting certain experimental levels as multiple members belonging to the studied band.

Identification of Exotic Symmetries: 4-Fold s.p. Level Degeneracies. Independently of the collective rotational-state degeneracies just discussed, there exists another class of degeneracies implied by the presence of 4-dimensional irreducible representations in the case of T^D_d tetrahedral symmetry. The underlying configurations belong to the non-collective, particle-hole type excitations, first of all of the tetrahedral $I^\pi = 0^+$ lowest-lying states, the same on which the collective, rotational bands just discussed are built.

Let us consider first the 'usual', double (also called Kramers) single-particle degeneracy in some deformed nucleus. Any single particle eigenvalue e_ν is common for both ψ_ν and its time-reversed image $\psi_{\bar\nu} = \hat T \psi_\nu$,

$$\hat H \psi_\nu = e_\nu \psi_\nu \quad \text{and} \quad \hat H \psi_{\bar\nu} = e_{\bar\nu} \psi_{\bar\nu} \quad \text{with} \quad e_\nu = e_{\bar\nu}, \tag{6.3.2}$$

where the solutions ψ_ν and $\psi_{\bar\nu}$ are linearly independent. Next let us consider a particle-hole excitation of an even-even nucleus in which the lower level is originally occupied by two nucleons and the upper level is empty. We have 4 combinations of the 1-particle 1-hole excitations leading to the same energy of the final result as follows:

$$\delta e^*_{\rm 1p-1h} \leftrightarrow e_\mu - e_\nu = e_\mu - e_{\bar\nu} = e_{\bar\mu} - e_\nu = e_{\bar\mu} - e_{\bar\nu}, \tag{6.3.3}$$

where ψ_ν and $\psi_{\bar\nu}$ represent originally occupied states and ψ_μ and $\psi_{\bar\mu}$ originally unoccupied states. There are 4 linearly independent particle-hole configuration wave-functions constructed out of the appropriate combinations involving $\{\psi_\nu \,\text{or}\, \psi_{\bar\nu}\}$ and $\{\psi_\mu \,\text{or}\, \psi_{\bar\mu}\}$.

We conclude that in the case of the 'usual' (i.e., Kramers double degeneracy) with the lower level originally fully occupied by 2 particles and the upper level totally empty,

there are 4 independent wave functions of the 1-particle 1-hole excitations with the excitation energies satisfying a 4-fold degeneracy expressed by a single excitation energy, $\delta e^*_{\mathrm{1p-1h}}$ as in eq. (6.3.3). This provides an experimental (and theoretical) reference structure which will be next compared with the exotic situation of T^D_d single-nucleon 4-fold degeneracies in place of the Kramers double degeneracies.

In the case of 4-fold single nucleon degeneracies, let us consider a configuration with the lower energy states originally fully occupied by 4 particles with their wave functions ψ_{ν_1}, $\psi_{\bar{\nu}_1}$, ψ_{ν_2} and $\psi_{\bar{\nu}_2}$ and the upper ones totally empty with their single-particle solutions ψ_{μ_1}, $\psi_{\bar{\mu}_1}$, ψ_{μ_2} and $\psi_{\bar{\mu}_2}$. Consider next the possible particle-hole excited states which can be constructed in the present situation:

- 1-particle 1-hole excitations leading to 16 linearly independent configurations i.e., with 16 mutually orthogonal wave functions, whose accompanying particle-hole excitation energies are equal $\delta e^*_{\mathrm{1p-1h}}$,
- 2-particle 2-hole excitations leading to 36 linearly independent configurations, with mutually orthogonal wave functions, while the corresponding single excitation energy $\delta e^*_{\mathrm{2p-2h}}$ is given by twice the single-particle energy difference $(2 \times \delta e^*_{\mathrm{1p-1h}})$.

In the case of a slightly broken T^D_d-symmetry – the situation which very likely will be encountered in experiments – each of the 4-fold degenerate multiplets will split into a pair of two very close lying levels e_{ν_1} and e_{ν_2} corresponding to the lower energy and a pair e_{μ_1} and e_{μ_2} corresponding to the higher one, each of them Kramers doubly-degenerate. Using our earlier notation we may write:

$$\text{Exact } \mathrm{T^D_d} : \{\mathrm{e}_{\nu_1,\nu_2} = \mathrm{e}_{\nu_1} = \mathrm{e}_{\nu_2};\ \ \mathrm{e}_{\mu_1,\mu_2} = \mathrm{e}_{\mu_1} = \mathrm{e}_{\mu_2}\} \ \ \leftrightarrow \ \ \{\mathrm{e}_{\nu_1} \approx \mathrm{e}_{\nu_2}; \mathrm{e}_{\mu_1} \approx \mathrm{e}_{\mu_2}\}. \tag{6.3.4}$$

Such configurations with slightly broken symmetry lead to 4 slightly different $\delta e^*_{\mathrm{1p-1h}}$-type excitation energies and 8 slightly different $\delta e^*_{\mathrm{2p-2h}}$-type excitation energies. Thus experimentally we arrive at challenges of identifying the quadruplets of $\delta e^*_{\mathrm{1p-1h}}$-type excited states or octuplets of $\delta e^*_{\mathrm{2p-2h}}$-type excited states with different spins.

More precisely, some information about these spins can be obtained through the mean-field theory employing the angular momentum and parity projection techniques as mentioned above. One may expect numerous weak (single-particle strength) electromagnetic transitions feeding or depopulating those numerous states and the electromagnetic selection rules can exclude certain (forbidden by the spin-parity selection rules) transitions. It is worth mentioning that the most important problem in this part of the discussion is to focus on the evidence for the relatively large number of excited states lying closely. An evidence of even a few of such excitations with their

number exceeding the numbers expected from the usual Kramers-degenerate configurations can be treated as an encouraging step towards the 'full evidence' of the multi-fold degeneracies such as the 4-fold T_d^D degeneracies.

Missing States as Symmetry Identifiers. As shown in figures (6.3.5) to (6.3.7) states with certain spin-parity combinations are simply absent. Let us stress that those absent states can be seen as characteristic signals of the corresponding symmetries. However, we might expect that there exist contaminating transitions originating from levels with the right spin-parity combinations and with energies coinciding with the energies whose absence we try to demonstrate. In what follows we will discuss how to facilitate the elimination of the structural contaminations, which originate from collective and/or non-collective excitations.

> *Observation: Let us emphasise that demonstrating experimentally an absolute absence of certain facts, e.g., the absence of certain levels or transitions, is a very difficult issue. Certain effects may not be measurable with the present day instrumentation and may become observable with future, better devices. It follows that the issue in question must be considered as very important but challenging one.*

Collective rotational signals may originate either from exotic symmetry minima or from the competing prolate-oblate configuration, and possibly super-deformed configurations. Since the latter ones correspond to big moments of inertia, the signals of those configurations should be easy to distinguish. In the former case because of the characteristic parabolic spin-parity sequences, the collective rotational band signals coming from the exotic symmetries can also be recognised with some extra effort. When the possible competition from collective vibrational states is concerned, the later ones are expected in the energy range of the order of 1 MeV, and should not interfere with the low-spin rotational transitions.

Similarly, we need to consider the possible contamination originating from non-collective (particle-hole) excitations either from the competition of prolate-oblate minima or from exotic deformation minima. In the case of axial-symmetry prolate/oblate structures the non-collective excitations will lead to the irregular energy vs. spin excitation patterns, what implies the presence of the so-called K-isomers and yrast-trap energy pockets. Such structures can be interpreted theoretically by employing the well known and well tested so-called 'tilted Fermi surface method', cf. ref. [6] or with the spherical shell-model approach so that this type of contamination can be eliminated (at least to an extent) from the considerations in the present context, in particular with the help of the rather well established theory tools.

The last point to consider is excluding a possible misinterpretation due to the

presence of a state coming from a predefined spin-parity combination in the parabolic energy zone while originating in fact from a particle-hole excited state of the studied exotic symmetry state. However, we believe that in this context incidentally positive signals are not very likely. It is known that the total nuclear spins and parities of such states originate from combinations of the nucleonic spins and parities of the levels near the Fermi level, and one can expect that it is very unlikely that the strict energy and spin conditions would fit incidentally.

6.4 Nuclear Shape Properties in 4D Octupole Space

We will address a number of algorithmic problems, which one encounters studying properties of nuclear shapes and symmetries in 4D deformation spaces. Even though the effects of this kind are expected in many regions of the nuclear mass table, we will focus on the lead nuclei in which a panorama of various complementary scenarios seems very rich.

One of the reasons of a particular interest in this mass region is that the equilibrium deformations in the nuclei of interest are in many cases characterised by ($\alpha_{20} = 0, \alpha_{3\mu} \neq 0$), therefore with no significant contributions from the quadrupole shape components.

> *This element alone is of specific interest in nuclear structure physics, since it allows for examining nuclear properties in which the "usually second rang multipolarity begins playing the first rang roles".*

However, as it turns out, from comparison of the potential energy maps presented in the preceding sections we might expect that there exists a competition between various octupole deformation components and this problem will be addressed next.

6.4.1 Potential Energy Surfaces in the Octupole 4D-Space

In this section we will limit ourselves to discussing the properties of the potential energy surfaces in the 4D octupole deformation space. Ignoring the other shape degrees of freedom is justified in the present case by the fact that the usually leading quadrupole deformation components, $\lambda = 2$, are absent in many non-negligible nuclear ranges of nuclei with the consequence that the leading role is overtaken by the next multipole $\lambda = 3$ with $\mu = 0, 1, 2, 3$, wherefrom the dimension of the considered space equal 4 – rather than 2 for the quadrupole deformations.

We will begin with the usual 2D projections out of the originally 4D space within which our calculations of the potential energies are performed. It follows that for the 4D

octupole space considered we have 6 independent combinations of any two octupole deformations. Consequently, we will deduce the physics information of interest by comparing the corresponding six projections. This will bring us to posing a number of problems encountered in this type of analysis.

Results presented in fig. (6.4.1) show rather rich structures composed of 2 to 4 minima separated by the potential barriers of the order of 1 MeV, whereas the maxima in the centres of the landscapes corresponding to the spherical shapes indicate that the system chooses non-spherical configurations by gaining in this way of the order of 2.5 MeV in the case of the $(\alpha_{30}, \alpha_{31})$ combination and about 3.5 MeV in all other combinations.

In contrast, results presented in fig. (6.4.2) in which the minimisation over the two other available deformations were performed, show essentially flat-bottom potential landscapes contrasting with the preceding figure showing rather rich structures.

It becomes clear that the comparison of the results in figures (6.4.1) and (6.4.2) warns us about significant differences between physical consequences and theory predictions implied by differences between the compared structures. In particular: It is expected that the octupole collective vibration energies are of the order of 1 MeV. The presence of the barriers of the order of 1 MeV separating the discussed minima will result, in terms of the solutions of the collective Schrödinger equation, in the low lying parity-doublet excitation patterns whereas the absence of those barriers will lead more to the vibrator type (harmonic oscillator) excitation patterns. It becomes clear that we will need to address the issue of the 'true physics' behind the two-dimensional reduction to produce the 2D graphical illustrations (maps).

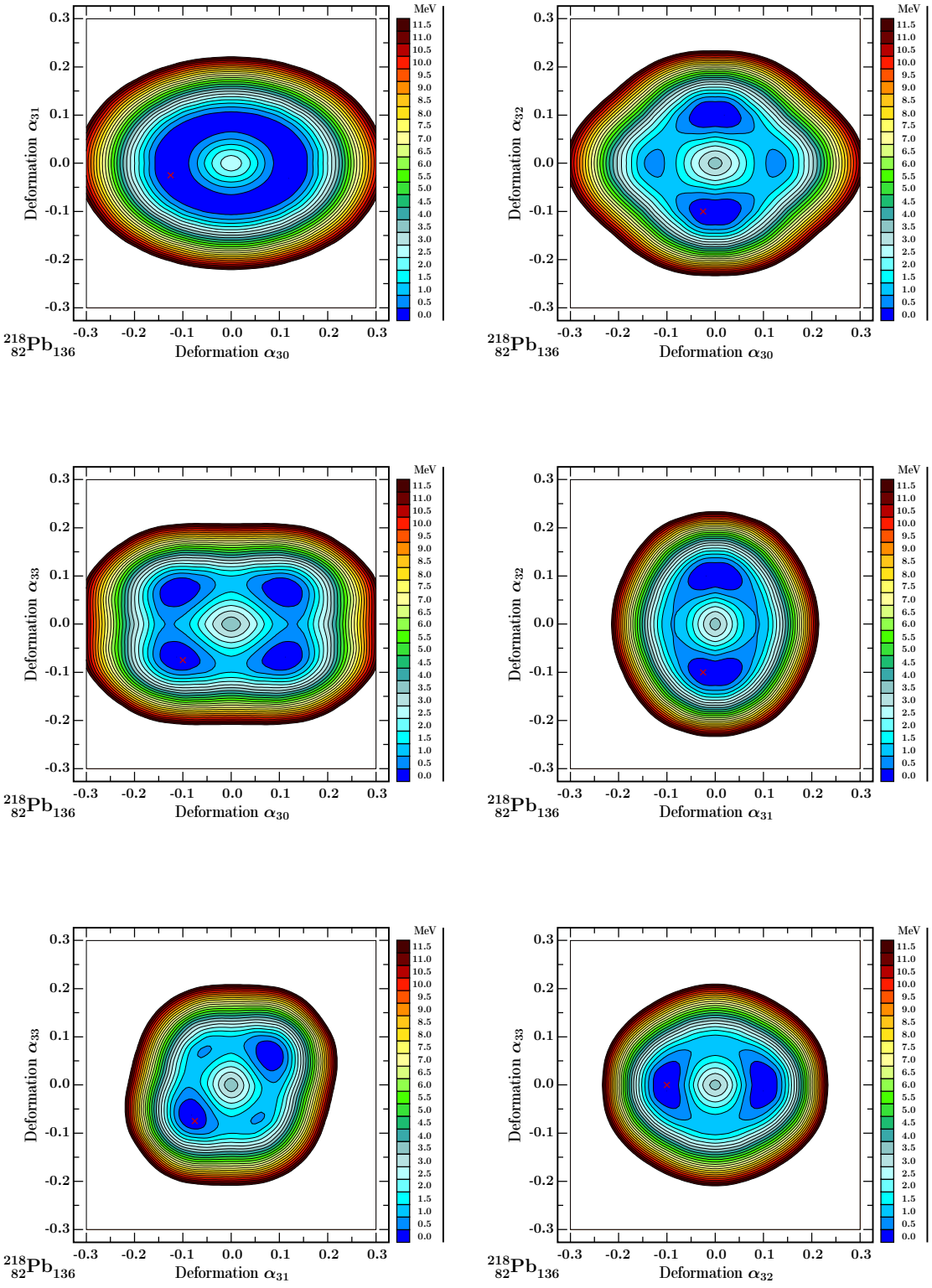

Figure 6.4.1 – *Comparison of the 6 total energy 2D projections with the octupole-octupole* $(\alpha_{3\mu}, \alpha_{3\mu'})$ *combinations for* ^{218}Pb *with octupole magic number* $N = 136$. *At each given 2D-point visible on the plot the remaining two deformations are set to 0.*

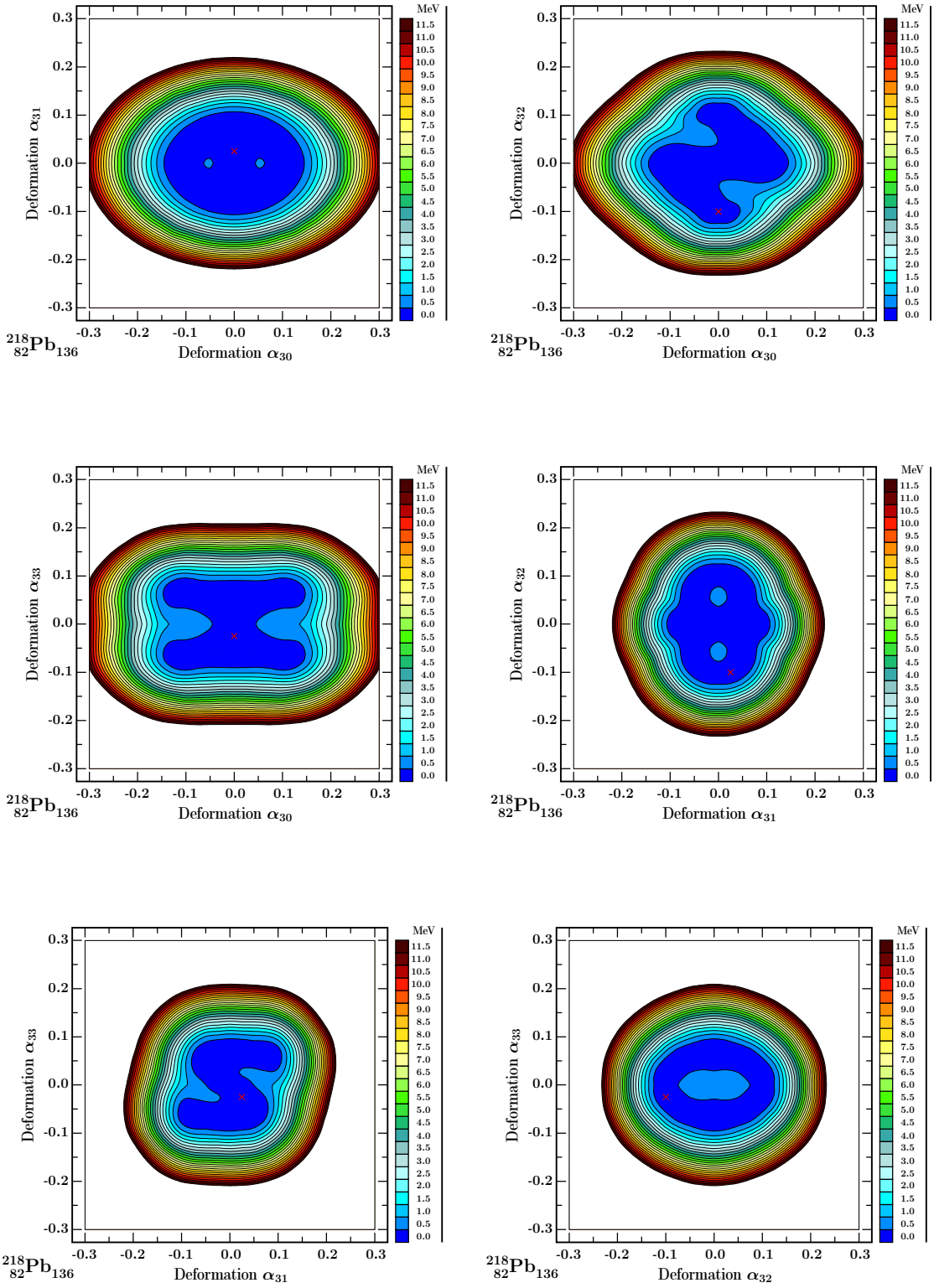

Figure 6.4.2 – *Similar to the preceding one but here at each* $(\alpha_{3\mu}, \alpha_{3\mu'})$ *deformation point the minimisation over the remaining two octupole deformations* $(\alpha_{3\mu''}, \alpha_{3\mu'''})$ *is performed. We conclude from comparison of the shown diagrams that the local minima present on the 2D projections in the preceding figure vanish in the present case.*

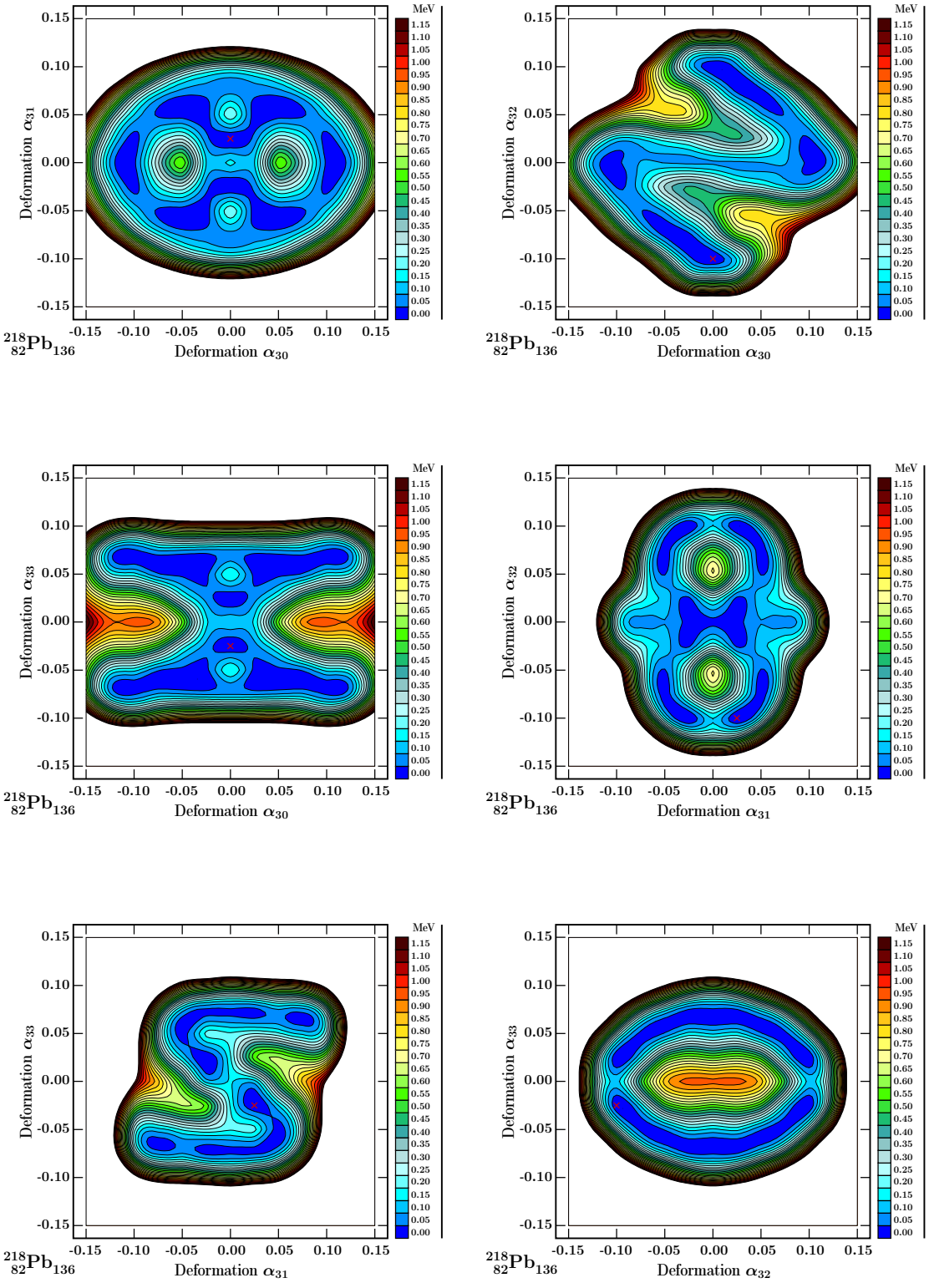

Figure 6.4.3 – *Similar to the preceding ones, but with the energy scale unit decreased by a factor of 10 in order to show the 'fine structures' and the corresponding symmetry patterns of the diagrams. Deformation ranges on the axes are shorter (factor of 2).*

It will be instructive to return to the illustration with the minimisation option but with the 'magnifying glass' in that we multiply the energy scale by a factor of 10. In this way we may address the issue of the effective flatness of the studied potential landscapes, the possible presence of fluctuations and their amplitudes, and, most importantly, trying to deduce the physical interpretation of the obtained final images. Results shown in fig. (6.4.3) show various structures but with the much smaller amplitudes of variation, of the order of a few hundreds of keV, markedly below the expected octupole vibration energies and therefore without direct impact on the solutions which we are interested in.

Inherent Drawbacks of the 'Usual' 2D Minimisation Algorithms. Clearly, the minimisation algorithm, which to our knowledge has been used in the majority of the published articles cannot be accepted as the final solution even if its application can provide some useful *schematic / approximate estimates*. Indeed, according to the discussed algorithm, at each $(\alpha_{3\mu}, \alpha_{3\mu'})$ point we look for the absolute minimum by minimising over the whole plane spanned by the two partner variables $(\alpha_{3\mu''}, \alpha_{3\mu'''})$. This means that we repeat independently for each point $(\alpha_{3\mu}, \alpha_{3\mu'})$ analysis of the full 2D map in variables $(\alpha_{3\mu''}, \alpha_{3\mu'''})$ with all the local minima and other structures varying from one original point $(\alpha_{3\mu}, \alpha_{3\mu'})$ to another. Let us emphasise that by doing so we do not control possibly drastic 'jumps' in the deformation sub-space $(\alpha_{3\mu''}, \alpha_{3\mu'''})$ appearing as a result of smooth moving from one $(\alpha_{3\mu}, \alpha_{3\mu'})$ to its neighbour.

Consequently it may happen, that even if the so obtained final 2D landscapes in terms of $(\alpha_{3\mu}, \alpha_{3\mu'})$ may look smooth, in reality, they will hide uncontrolled deformation jumps (discontinuities) in the $(\alpha_{3\mu''}, \alpha_{3\mu'''})$ subspace, which in any case are unphysical, but occasionally may become unacceptably large.

As it happens, the 2D projections from 4D nuclear potential energies may provide useful qualitative information about the predicted structures, such as global properties of the nuclear path to fission, deducing predictions about mass-asymmetric vs. mass-symmetric fission properties or addressing the large amplitude oscillations influenced by possible deformation-flatness of the potential landscapes.

This brings us to the need of searching for alternative solutions, the subject which will be treated next.

6.4.2 Quasi-Classical Analysis in the Full 4D Octupole Space

One of the central problems we are interested in is not so much a graphical illustration of the 2D projections, but rather constructing the physical paths of the motion in the multidimensional spaces which – starting from a given point selected by a physicist – leads the system to another deformation point in the studied space. In addition, we

will often be interested in estimating quantum-mechanical transitions probabilities.

In classical physics, the Euler-Lagrange approach (cf. e.g. ref. [53]) provides a solution to this kind of a problem by formulating differential equations, which allow one to find an n-dimensional trajectory of the motion in the space of generalised coordinates $\{q_i\}$ and velocities $\{\dot{q}_i\}$ for $i = 1, 2, ..., n$. These differential equations are obtained with the help of the variation/minimisation of the action integral employing trajectories that connect the initial and the final points, Q_{in} and Q_{fin}, respectively. One may say that the physical solution-trajectory is obtained by selecting among the infinity of trajectories passing through the initial and final points – the one minimising the action integral.

In this project we are going to be more interested in a quasi-classical approach to the quantum problem of probability of penetration of multi-dimensional potential barriers known under the name of Wentzel-Kramers-Brillouin (WKB) approximation, cf. for instance refs. [13, 53]. This approach will be applied to the octupole space of interest with dimension $n = 4$ and with the correspondence $q_i \leftrightarrow \alpha_{3\mu}$.

Traditionally the WKB potential barrier penetration problem is formulated for a given energy of the system, E, by specifying the so-called entrance-, and the exit points, here denoted Q_1 and Q_2. The trajectory connecting these two points, $q = q(s)$, *is considered known*; s is a real argument, which can be chosen as the curve length. The probability of the barrier penetration, $P_{1\to 2}(E)$, is then given by

$$P_{1\to 2}(E) = \exp\left\{-2\int_{Q_1}^{Q_2}\sqrt{\frac{2m^*}{\hbar^2}\Big[V[q(s)] - E\Big]}\,ds\right\}, \tag{6.4.1}$$

where m^* represents effective inertia of the system. In principle, this simplified expression is applicable for any given continuous trajectory $q(s)$.

Applying the above generic WKB expression of the barrier transmission probability for a nuclear system requires specifying the two points of interest, Q_1 and Q_2, which in our case will correspond to some potential minima selected by the physicist in the 4-dimensional octupole deformation space, and a known connecting trajectory. Consequently, we will need to have at our disposal an algorithm constructing the multi-dimensional trajectories of interest. In this context, we will apply the so called Dijkstra algorithm, ref. [54], which can be seen as a chapter of the *Graph Theory*, a branch of Applied Mathematics.

6.4.3 A Short Description of the Dijkstra Algorithm

In what follows we will present briefly the Dijkstra algorithm, designed to construct a predefined form of the distance, e.g. the shortest one, d, between two points, Q_1

and Q_2, in an n-dimensional space spanned by variables $\{q^i\}$, corresponding to the deformation parameters $\{q^i\} \leftrightarrow \{\alpha_{\lambda\mu}\}$, to adapt the notation to our problem of nuclear motion.

A *graph* is by definition an ensemble of, say $\mathcal{N}$ points, called *vertices* and of the corresponding *edges* connecting pairs of vertices. Some or all the points are connected by paths that are composed of edges and it is assumed that each edge has attributed a positive number called *length*, alternatively, *weight*. A *tree* is defined as a graph with one and only one path between every vertex. Dijkstra algorithm solves two basic problems:

1) Constructing a tree with minimal total length among $\mathcal{N}$ vertices,
2) Finding a path with minimal total length between two points of interest.

In the present content, the vertices refer to the deformation points defined by 4 coordinates $\{\alpha_{30}, \alpha_{31}, \alpha_{32}, \alpha_{33}\}$, alternatively, deformation mesh. We will be looking for the shortest path problem applying the graph theory algorithm to find the shortest path from one minimum to another, (better: the maximum WKB probability path connecting two given minima), ref. [55]. Our problem of interest belongs to the second class of the above mentioned sequence.

Our geometrical deformation space forms a 4D hyper-cube with the 4 coordinates $\alpha_{3\mu=0,1,2,3} \in [-0.3, 0.3]$ and with the step $\Delta\alpha_{3\mu} = 0.025$. Consequently, the total number of vertices is $\mathcal{N}_v = 390625$ and the graph has $N_e \approx N_v^2 = 152\,587\,500\,000 \approx 1.5 * 10^{11}$ connecting edges. The single 4D-cell related distances of the smallest 4D hyper-cubes in terms of Pythagorean relations are

$$\Delta_1\alpha = 0.025, \tag{6.4.2}$$
$$\Delta_2\alpha = \sqrt{2 \times 0.025^2} = 0.0353, \tag{6.4.3}$$
$$\Delta_3\alpha = \sqrt{3 \times 0.025^2} = 0.0433, \tag{6.4.4}$$
$$\Delta_4\alpha = \sqrt{4 \times 0.025^2} = 0.050, \tag{6.4.5}$$

where $\Delta_1\alpha$ is just a step along any of the 4 axes, $\Delta_2\alpha$ is the length of the diagonal of an elementary square on any of the 2D planes, $\Delta_3\alpha$ is an analogue in the 3D space referring to the elementary (smallest possible) cube and $\Delta_4\alpha$ yet another generalisation to the smallest 4D hyper-cube.

The local minima of the 4D potential energy can be determined numerically from the calculated Strutinsky results. Our goal is to determine, which minima are best stabilised by the surrounding barriers. For this purpose, for any given pair of candidate minima, we determine with the help of the Dijkstra algorithm, the 4D paths with the smallest barrier-penetration between any two minima (the largest transmission probability) as the best estimate of the stability.

In the construction of our computer program, we divide the full trajectory into the smallest steps possible to construct the pre-calculated mesh of octupole deformation points. Consequently, the WKB potential barrier penetration in eq. (6.4.1) will be formed by summing up the contributions to the calculated integral of every pair of vertices, which are treated as the limit points Q_1 and Q_2:

$$\Delta P_{1\to 2} = \int_{Q_1}^{Q_2} \sqrt{\bar{V} - E}\, ds, \tag{6.4.6}$$

in which

$$\bar{V} \stackrel{df.}{=} \frac{1}{2}\left[V(Q_1) + V(Q_2)\right]. \tag{6.4.7}$$

In what follows we will employ the Dijkstra shortest-path search algorithm introduced in ref. [54] to find the maximum WKB probability paths, which connect two local minima. One can find examples of the 2D application of the Dijkstra algorithm in ref. [56], which employed the algorithm to describe the fission process for some heavy nuclei.

6.4.4 Typical Results Obtained Using Dijkstra Algorithm

According to the calculations of the total nuclear potential energy, it is straightforward to find the coordinates of the local minima, which are considered as the starting points in the Dijkstra shortest-path search algorithm.

In order to illustrate the path variation between any two minima, we select two particular minima, one corresponding to the lowest energy state on the energy projection of $(\alpha_{30}, \alpha_{32})$ and another one on the projection $(\alpha_{30}, \alpha_{33})$, cf. figure (6.4.3). Suppose the initial deformation is selected as the one to represent the tetrahedral symmetry $Q_1 = \{\alpha_{30}, \alpha_{31}, \alpha_{32}, \alpha_{33}\} = \{0.0, 0.0, 0.1, 0.0\}$, and the final point of the trajectory is chosen at $Q_2 = \{\alpha_{30}, \alpha_{31}, \alpha_{32}, \alpha_{33}\} = \{-0.10, 0.0, 0.0, 0.075\}$. The illustration of the trajectory with the maximum probability is shown in Figure (6.4.4), where 4 consecutive diagrams illustrate the corresponding projections of the trajectory in terms of 4 octupole deformations. Comparison implies that the trajectory is contained in the 4D hyper-cube defined by $-0.1 \leq \alpha_{3\mu} \leq +0.1$.

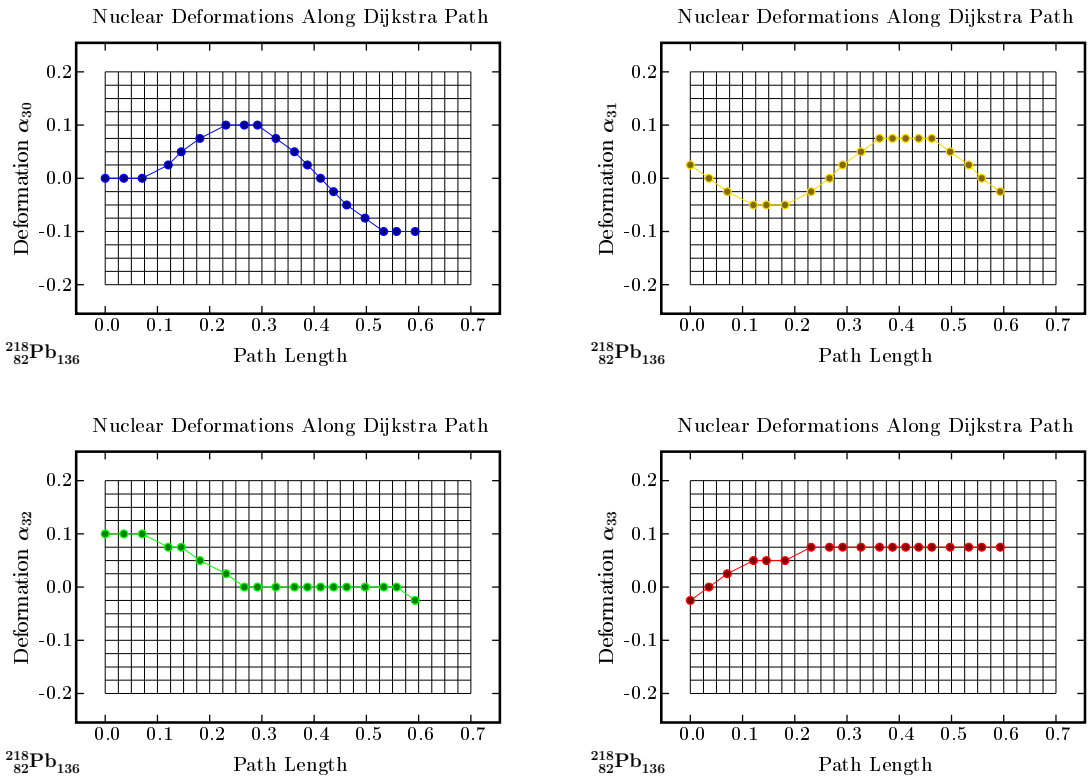

Figure 6.4.4 – *Illustration of the application of the Dijkstra algorithm to find a 4D trajectory connecting two minima. The starting deformation has been selected as* $Q_1 = \{\alpha_{30}, \alpha_{31}, \alpha_{32}, \alpha_{33}\} = \{0.0, 0.0, 0.1, 0.0\}$ *and the final one is* $Q_2 = \{\alpha_{30}, \alpha_{31}, \alpha_{32}, \alpha_{33}\} = \{-0.10, 0.0, 0.0, 0.075\}$*, cf. the lowest energy minimum (red crosses) on the energy projections* $(\alpha_{30}, \alpha_{32})$ *and* $(\alpha_{30}, \alpha_{33})$ *in figure (6.4.3).*

Discussion and Conclusions from the Application of the Dijkstra Algorithm. Figure (6.4.5) illustrates the potential energy along the maximum probability trajectory. The result shows that the variations of the potential energy between the discussed minima do not bypass 100 keV, a result which is comparable to the results with the total energy maps in the figure (6.4.3). The flatness of the effective potential energy is confirmed both within the 2D projection of the potential energy surface with minimisation and with the Dijkstra path algorithm.

Observations related to the two-dimensional projections without minimisation:

- *The discussed projections show rather rich structures with numerous minima separated by the potential barriers of the order of 1 MeV.*
- *The energy barriers at the central zone of the projections are of the order of up to 4 MeV for 5 among 6 projections, suggesting that the spherical symmetry is strongly unfavored.*

In contrast, the 4D behaviour of the nuclear potential represented in terms of six 2D projections with minimisation resembles a 4D flat bottom potential. The results obtained with the Dijkstra approach are qualitatively comparable but quantitatively different. In particular, they *are free from the discontinuity problem* the latter unavoidable when employing the minimisation algorithm.

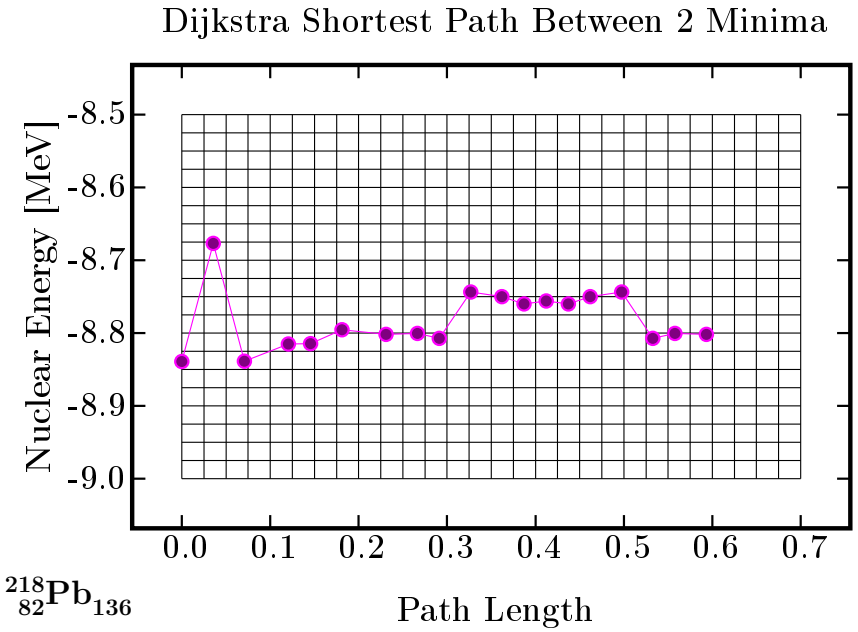

Figure 6.4.5 – Illustration of potential energy along the Dijkstra path.

6.5 Notion of Dynamical Equilibrium Deformations

The method of Strutinsky which, in the light of many publications can be considered a realistic theoretical tool, provides the total energy surfaces with a number of minima separated by the barriers. The behaviour of the potential in the vicinity of the minima may vary from nucleus to nucleus and it becomes clear that the nuclear behaviour is expected to be significantly different when the minima are surrounded by flat energy zones as compared to the minima surrounded by steep potential walls. To advance with quantitative estimates of physical differences generated by various potential energy scenarios we will need to address the quantum description of the collective motion with the specifically adapted Schrödinger equation. Such an adaptation is provided by the so-called collective model of Bohr and we intend to present briefly its principles and results of applications.

6.5.1 A Brief Description of the Collective Model of Bohr

The model of Bohr is based on collective Hamiltonian, which is usually written in the following compact form

$$\hat{H}_{\text{col.}} = \hat{T}_{\text{col.}} + \hat{V}_{\text{col.}}, \tag{6.5.1}$$

in which the collective kinetic energy operator $\hat{T}_{\text{col.}}$ is constructed with the help of the collective inertia tensor discussed below, whereas the collective potential, $\hat{V}_{\text{col.}}$, is obtained in this project employing the macroscopic-microscopic method of Strutinsky, as discussed in details in the preceding sections. The kinetic energy operator is often defined with the help of the Laplacian Δ, written down in the curvilinear space, whose curvature is defined with the help of the inertia tensor $B^{mn}(q)$. To shorten the notation the ensemble of our collective coordinates $\{\alpha_{\lambda\mu}\}$ is represented in a compact manner by the symbol q. Following the Bohr model, with the notation adapted to our applications, cf. e.g. ref. [57], the collective kinetic energy operator can be written down as follows

$$\hat{T}_{\text{col.}} = -\frac{\hbar^2}{2}\Delta \quad \leftrightarrow \quad \Delta \stackrel{df.}{=} \sum_{m,n=1}^{d} \frac{1}{\sqrt{|B(q)|}} \frac{\partial}{\partial q^n}\left(\sqrt{|B(q)|}B^{nm}(q)\frac{\partial}{\partial q^m}\right), \tag{6.5.2}$$

where $|B(q)|$ denotes the determinant of $B^{nm}(q)$ with $m, n = 1, 2, \ldots \mathcal{N}$, and where $\mathcal{N}$ denotes the dimension of the space of the collective variables $\alpha_{\lambda\mu}$ selected for the calculations.

There exist modern methods of calculating the tensor of inertia using the nuclear mean field theory. The interested reader may consult the latest and most advanced study of this subject in ref. [57]. From the mathematical and/or numerical construction view points, we may consider

$$B^{mn} = B^{mn}(q \leftrightarrow \alpha_{\lambda\mu}) \;\text{ for }\; m, n = 1, 2, \ldots \mathcal{N}, \tag{6.5.3}$$

as an ensemble of known functions. Solving the resulting collective Schrödinger equation

$$\hat{H}_{\text{col}}\Psi_{\text{col},\rho}(q) = E_{\text{col},\rho}\Psi_{\text{col},\rho}(q), \;\text{ with }\; \rho = 1, 2, 3, \ldots \tag{6.5.4}$$

will provide the collective eigenvalues $\{E_{\text{col},\rho}\}$ and the corresponding eigenfunctions representing the amplitudes of probability of finding a nuclear system at the deformation $q \leftrightarrow \alpha_{\lambda\mu}$. We will discuss certain simplified solutions of the discussed problem to illustrate the typical conclusions, which can be deduced when the analysis of the static equilibrium deformations deduced from the minima of potential energy surfaces is replaced by the analysis of the most probable deformations, sometimes called dynamical equilibrium deformations.

6.5.2 Solutions of Collective Model of Bohr: Discussion

We are not going to address any multidimensional analysis of the collective model just schematised. Instead we will concentrate on the one-dimensional approximations, which will be sufficient to draw the main physical conclusions of interest for the present project.

An example of the one-dimensional total energy calculations for ^{218}Pb, $N = 136$, is presented in fig. (6.5.1), top, showing the potential energy as a function of octupole pear-shape deformation α_{30}, all other deformations set to zero in this case. The double octupole minima, here at $\alpha_{30} \approx \pm 0.13$, are separated by an energy barrier of the order of 2 MeV. The ground-state and the first excited state energies are obtained by solving the 1D collective Schrödinger equation assuming for simplicity a constant mass parameter, $B^{mn}(q) \to B_{mass} = 200\hbar^2\,\mathrm{MeV}^{-1}$, according to the notation adopted in our graphical illustrations.

The corresponding probability density functions are shown in fig. (6.5.1), bottom. The probability density functions of the ground-state solution with energy E_0 and the first excited state solution, E_1, show characteristic asymmetry of the solutions. It is worth mentioning that the energies of E_0 and E_1 are nearly degenerate. The so-called 'root-mean-square' estimate, $\alpha^{\mathrm{eq}}_{rms}$, the latter taken as the measure of the most probable equilibrium deformation is defined as

$$\alpha^{\mathrm{eq}}_{rms} = \sqrt{\langle \alpha^2 \rangle} \stackrel{df.}{=} \int \Psi^*(\alpha)\alpha^2\Psi(\alpha)\,d\alpha. \tag{6.5.5}$$

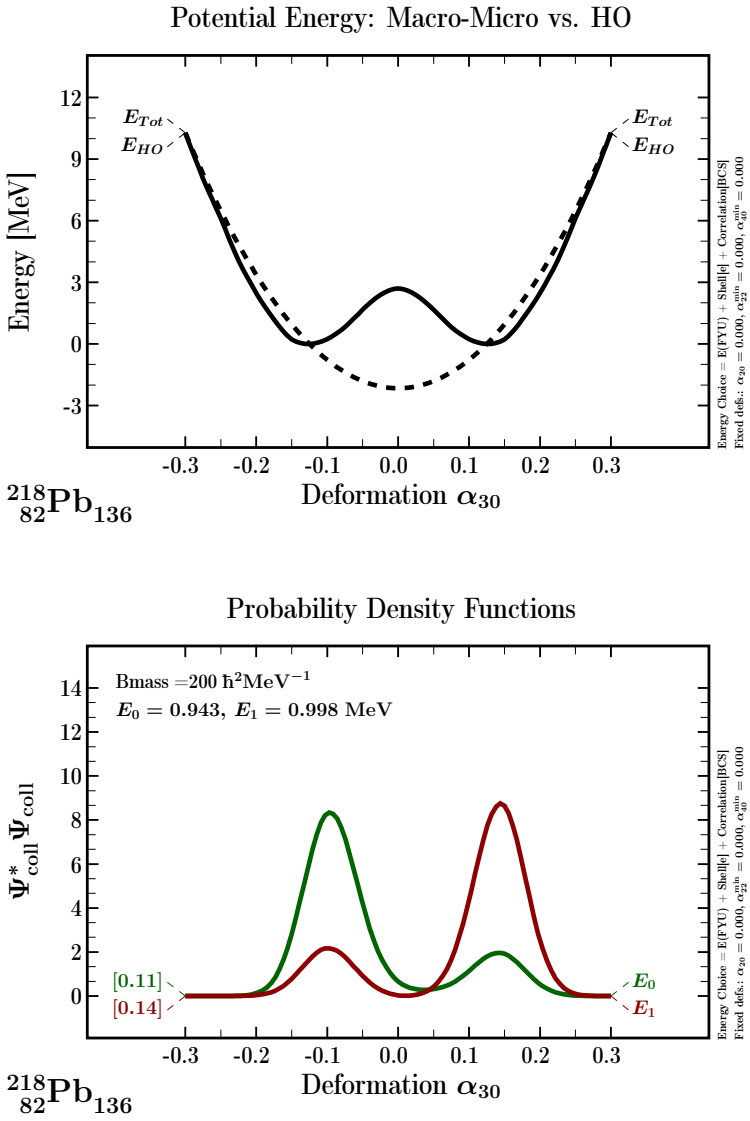

Figure 6.5.1 – *Top: Illustration of the potential energy for* ^{218}Pb *as a function of octupole deformation* α_{30}*,* $E_{\rm Tot}$ *(solid line). For comparison, the harmonic oscillator potential* $E_{\rm HO}$*, dashed line, serving as the basis generating potential is shown. Bottom: Resulting probability density functions for the ground-state, denoted* E_0 *and the first excited state, denoted* E_1*. The labels in square brackets give* $\alpha^{\rm eq}_{rms}$ *representing the most probable (dynamical) equilibrium deformation, cf. eq. (6.5.5).*

It follows from the information at the bottom of figure (6.5.1) that the dynamical equilibrium deformations, $\alpha^{\rm eq}_{rms} = 0.11$ and 0.14 for the ground-state and the first excited state, respectively, are relatively close to the static equilibrium deformations $\alpha_{30} \approx 0.13$ in the discussed case.

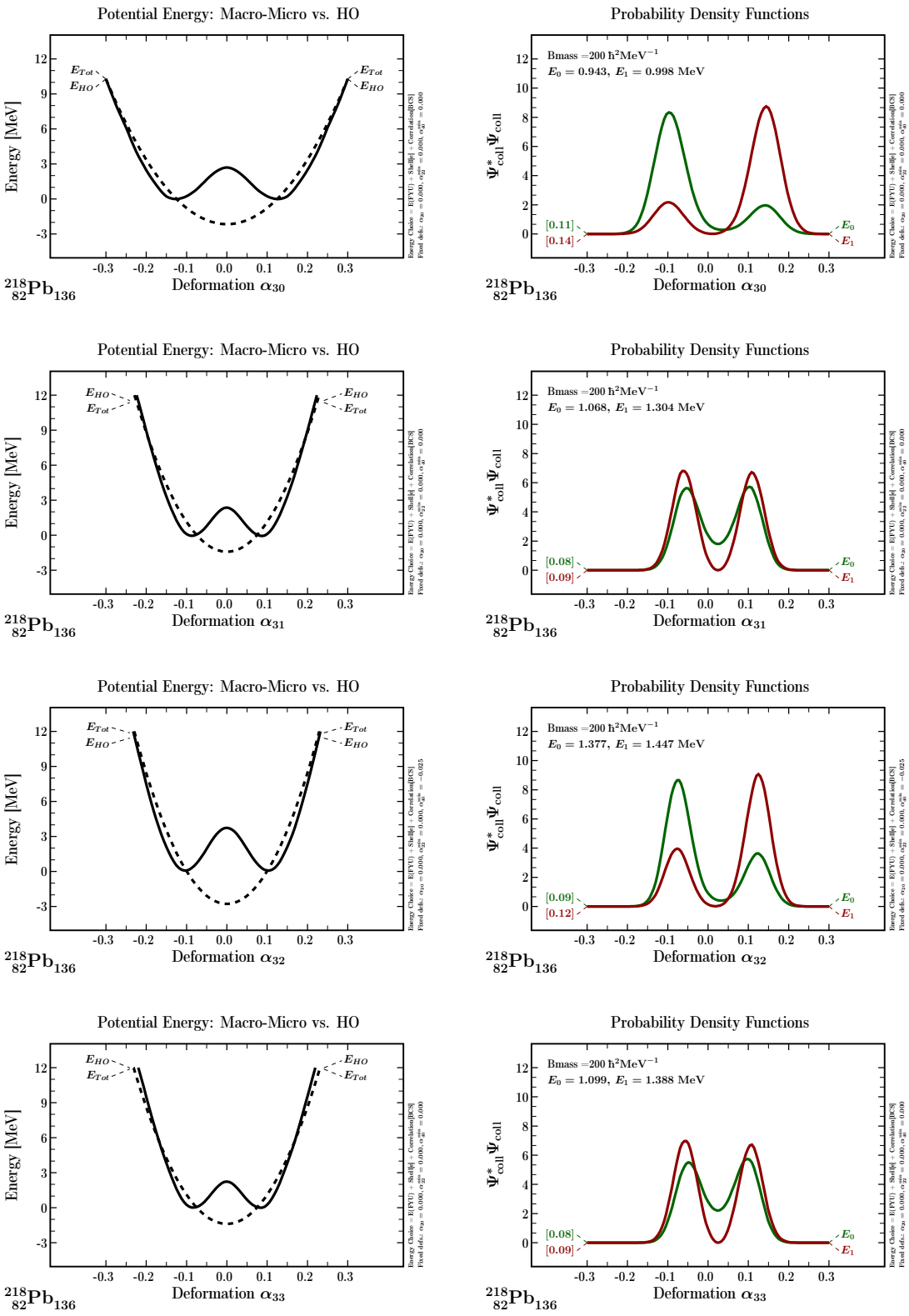

Figure 6.5.2 – *Illustration of the potential energies, $E_{\rm Tot}$ (solid lines), resulting from the macroscopic-microscopic method as functions of octupole deformations $\alpha_{3\mu,\mu=0,1,2,3}$, in the left column. The corresponding probability density functions for ground-, and first excited states are presented in the right column.*

Figure (6.5.2) illustrates comparison of potential energies, $E_{\rm Tot}$, as functions of the octupole deformations $\alpha_{3\mu=0,1,2,3}$, left column, and the related probability density functions, right column. The energy barriers separating double minima happen to be comparable in the α_{30} and α_{32} cases, nearly 3 MeV each, and similarly for the α_{31} and α_{33} cases, comparable, nearly equal 2 MeV each. The probability density functions show similarities pairwise: in the α_{30} compared to α_{32} case, and analogously in the other two cases. However, the dynamical equilibrium deformations remain close both for the ground-, and the first excited states and close to the respective static equilibrium deformations. Let us notice that the calculated energies of the collective solutions happen to be significantly lower than the barriers separating the two minima of about 3 MeV in the α_{30} and α_{32} cases and remain pairwise nearly degenerate: $E_0 = 0.943$ and $E_1 = 0.998$ for α_{30} and $E_0 = 1.377$ and $E_1 = 1.447$ for α_{32} deformations.

It follows from the discussed illustrations that variations of the barrier heights, even if seemingly not very significant, may lead to systematic differences in terms of the level degeneracies and behaviour of the wave functions (the latter may imply differences in predictions of the reduced transition probabilities which, however, are not our subject in the present project). To examine closer the impact of the variation in the separating barrier heights we are going to compare the effects of this mechanism by artificially setting the barrier heights at the levels of approximately 5, 2 and nearly 0 MeV, as illustrated in fig. (6.5.3), left column, compared to the resulting solutions, right column.

When decreasing the barrier heights from 5 MeV to 2 MeV, dynamical equilibrium deformations do not change in any significant manner. Comparing the analogous change in the case of 5 MeV vs. 0 MeV, shows that the dynamical equilibrium deformation decreases by about 30% in the case of the ground-state configurations and by about 40% in the case of the 1-phonon solutions. Let us notice that an approximate degeneracy of the two solutions remains as along as the barriers separating the two minima are significantly higher than the energies E_0 and E_1. At the vanishing barriers, the degeneracy between the two compared energies vanishes totally. We arrive at the following conclusions:

1) The dynamical equilibrium deformations decrease with decreasing heights of the barriers separating the doublet-minima. Importantly, even for totally vanishing barriers (flat bottom potentials) the dynamical equilibrium deformations remain at the level of 60-to-70% of the original ones calculated with the very high barrier separations.

2) These are the dynamical equilibrium deformations corresponding to the quantum solutions of the collective motion problem which should be taken into further consideration.

3) Importantly, in the case of the flat potential wells the dynamical equilibrium deformations might be quite far from the mathematical minimum points.

4) Most importantly: The exotic symmetries will be manifested in subatomic physics even in the case of flat potential landscapes extending into the exotic $\alpha_{\lambda\mu}$-zones.

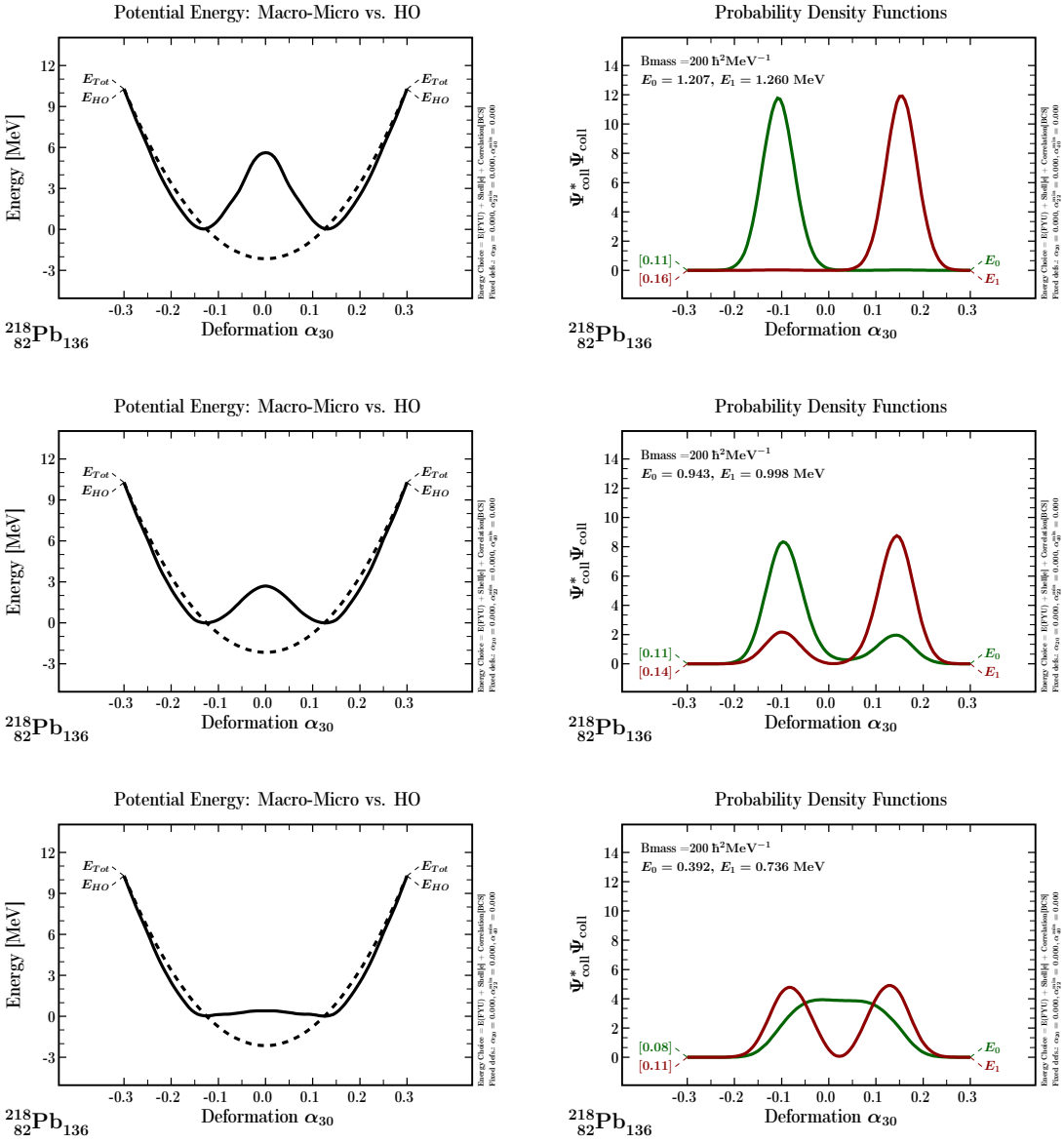

Figure 6.5.3 – *Illustration of the potential energy of E_{Tot} (solid lines, left column) with energy barriers of the order 5 MeV (top), 2 MeV (middle) and 0 MeV (bottom), and the corresponding probability density functions for the ground-state and the first excited states presented in the right column.*

6.6 Coexisting Octupole Shape Symmetries

In the light Actinide region, the ground-state equilibrium deformations contributed by both quadrupole and octuple degrees of freedom have been discussed in the literature both from the experimental and theoretical view points. To cite some examples, stable octupole shapes have been observed experimentally in the Actinides in ^{220}Rn, and furthermore in ^{222,224,228}Ra [49][50], as well as in ^{228}Th [58]. These properties have been studied employing numerous theoretical approaches, i.e., macroscopic-microscopic model [59], Hartree-Fock-Bogoliubov (HFB) method with Gogny density functional [52, 60, 61], but also within the covariant density functional theory [62], with the relativistic energy density functional [63], using the algebraic methods such as interacting boson approximation (IBA) [51] and references therein as well as with the geometrical collective models [64, 65].

The possible presence of the high-rank symmetries, tetrahedral and octahedral ones, has been predicted in a series of articles using the realistic phenomenological mean-field calculations, cf. refs. [26, 29, 33, 35]. According to ref. [26] tetrahedral (octupole deformation α_{32}) magic numbers are predicted at the proton and neutron numbers 34, 40, 56, 64, 70, 90, 112 and 136, suggesting the presence of strong shell effects in the Zirconium, Rare-Earth and Actinide regions. Nuclei with exact tetrahedral symmetry have all deformations equal to zero except for the tetrahedral degrees of freedom. From the results presented in the preceding sections of this document it follows that the tetrahedral and octahedral symmetry minima could be accompanied by the presence of competing octupole shape exotic deformations and we could expect the coexistence of the specific rotational bands generated by these special symmetries.

In this section, we intend to review the properties of the ground-state equilibrium deformations obtained with the help of the phenomenological mean-field Hamiltonian with the optimal universal parametrisation as discussed in the first chapter. We will focus on the nuclei in which the pear-shape and tetrahedral symmetries have been predicted in the past, i.e., those with neutron numbers close to the magic number $N = 136$ and proton numbers centred around $Z = 90$.

We begin with the illustration of the single nucleon shell effects impacted by the corresponding octupole deformations. Characteristic results are presented in the diagrams in fig. (6.4.1) for the protons, top, and the neutrons, bottom. As one can see from the figure, the proton single-particle energy spectra are dominated by the gaps at $Z = 90$, together with $Z = 100$ and $Z = 110$ in the case of the tetrahedral-symmetry deformation, the corresponding sizes of the gaps are about 1.5 and 2 MeV, respectively. The analogous shell effects are significantly weaker in the case of the pear-shaped deformations, with main gaps localised at $Z = 92$ and $Z = 100$.

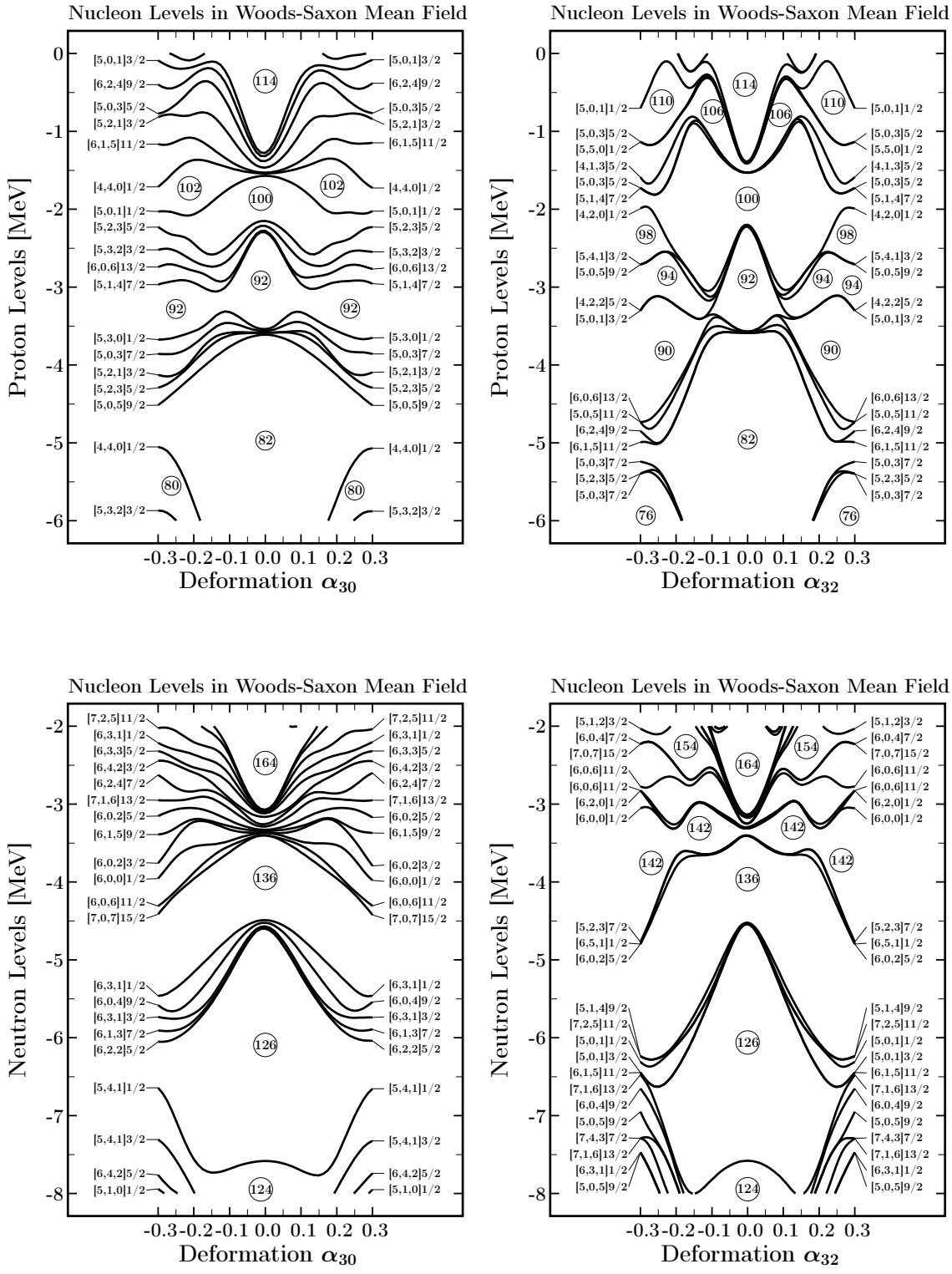

Figure 6.6.1 – *Proton single-particle energies (top) and neutron single-particle energies (bottom) as functions of the octupole deformations α_{30} and α_{32}. All other deformation parameters are set to zero. For interpretation see the text.*

Compared with those, the neutron gaps presented in the figure are significantly bigger, approaching about 3 MeV at $N = 136$, which confirms the neutron domination in the octupole deformations effects on the nuclei in this region.

As discussed in refs. [51, 52] and references cited therein, in light actinide nuclei around Radium and Thorium, some well deformed quadrupole shapes are expected. In the following figures (6.6.2) to (6.6.7), we compare the potential energy surfaces for $N = 136$ isotones with proton numbers varying between $Z = 82$ and 92 by using the $\alpha_{3\mu=0,2}$ vs. α_{20} representation. The underlying potential energies were obtained by the corresponding projections from the 4-dimensional mesh with $\{\alpha_{20}, \alpha_{30}, \alpha_{32}, \alpha_{40}\}$ deformations. The series of illustrations is constructed in such a way that we first compare the landscapes characterising the competition between α_{30} and α_{32} deformations using 2D $(\alpha_{30}, \alpha_{20})$ and $(\alpha_{32}, \alpha_{20})$ representations, top and middle diagrams, followed by the projections $(\alpha_{32}, \alpha_{30})$ demonstrating in such a way a direct competition between these two octupole degrees of freedom.

With increasing proton number, typical landscapes combining vanishing quadrupole deformation with the non-zero octupole components evolve into a combination of non-vanishing both quadrupole and octupole components. In particular, a flatness of the potential energy in terms of the pear-shape deformation around quadrupole deformation $\alpha_{20} \approx 0.0$ is visible from figures (6.6.5) to (6.6.7). However, in view of the preceding discussion we may conclude that measurable effects will be compatible with the presence of the corresponding deformations due to the just demonstrated properties of the dynamical equilibrium shapes.

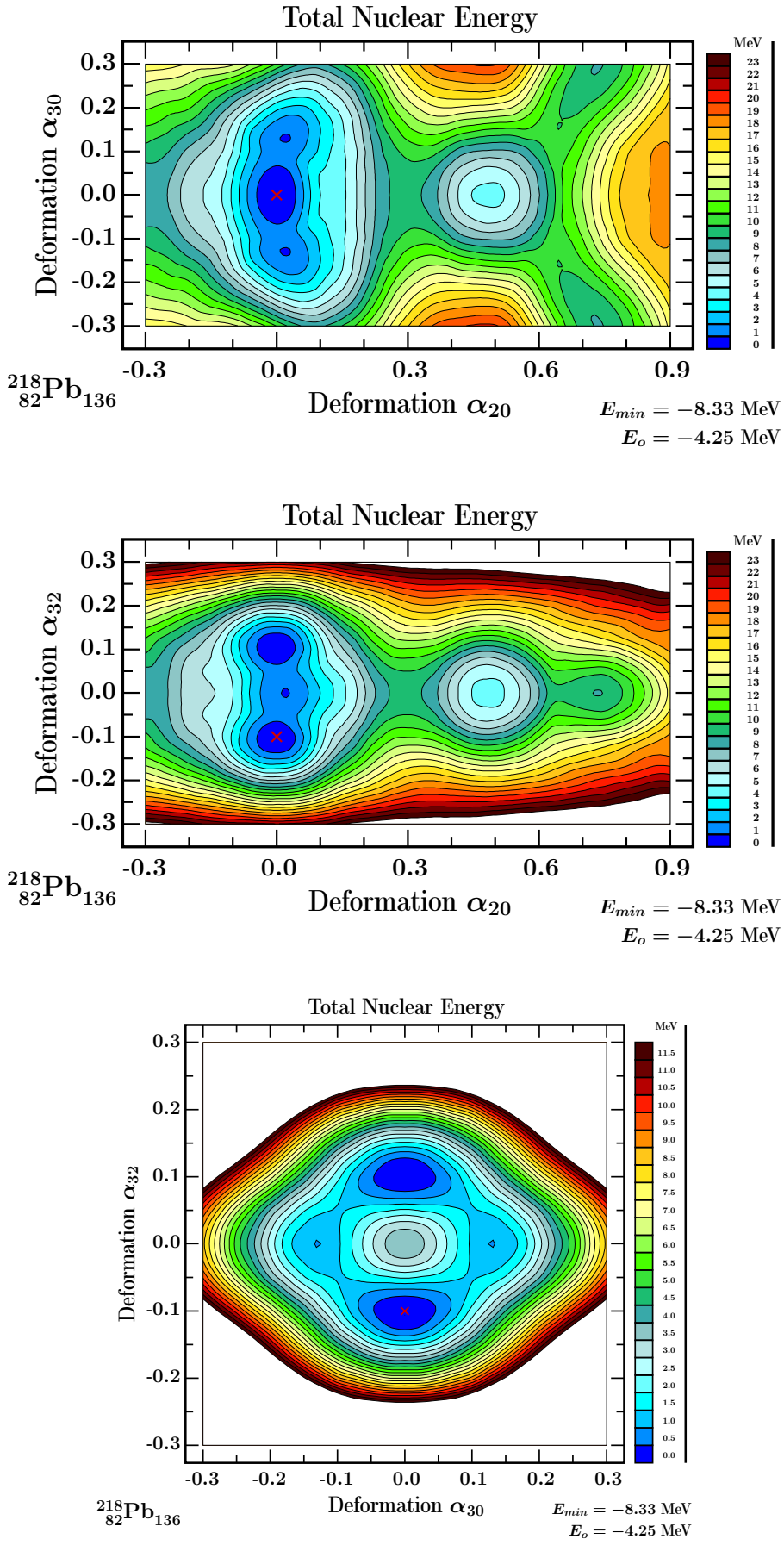

Figure 6.6.2 – *2D projections of the potential energies on the deformation planes displayed, obtained for* ^{218}Pb *from the 4D mesh involving* $\{\alpha_{20}, \alpha_{30}, \alpha_{32}, \alpha_{40}\}$.

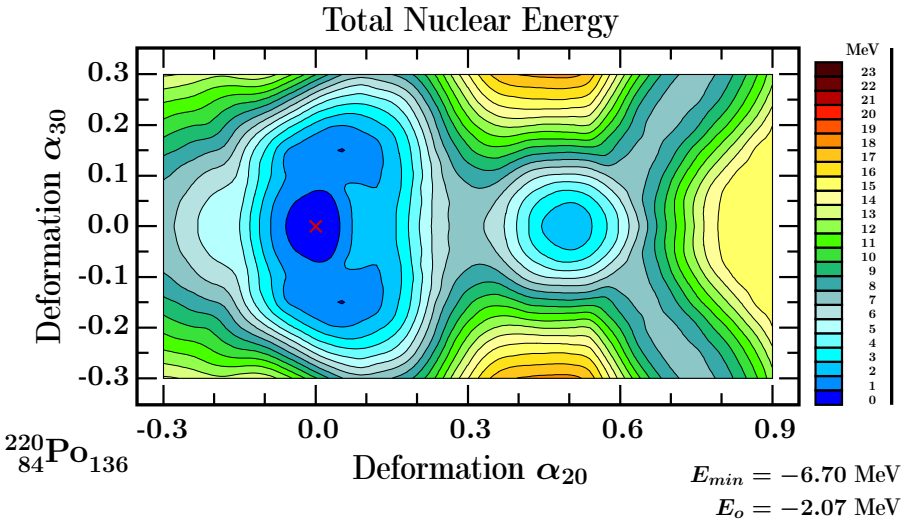

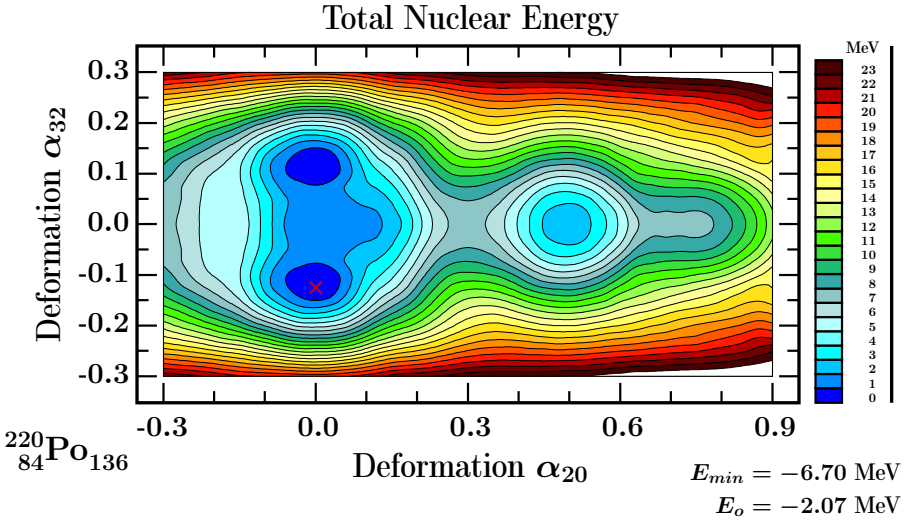

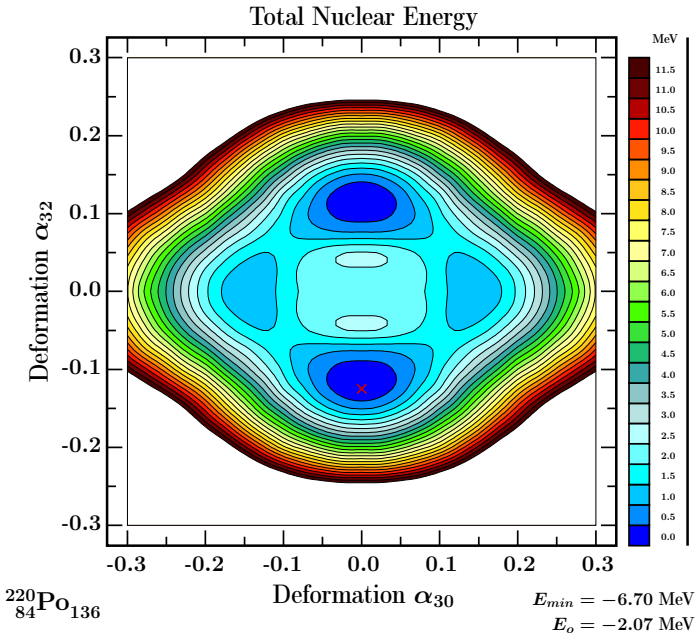

Figure 6.6.3 – *Similar to the preceding one but for* ^{220}*Po nucleus.*

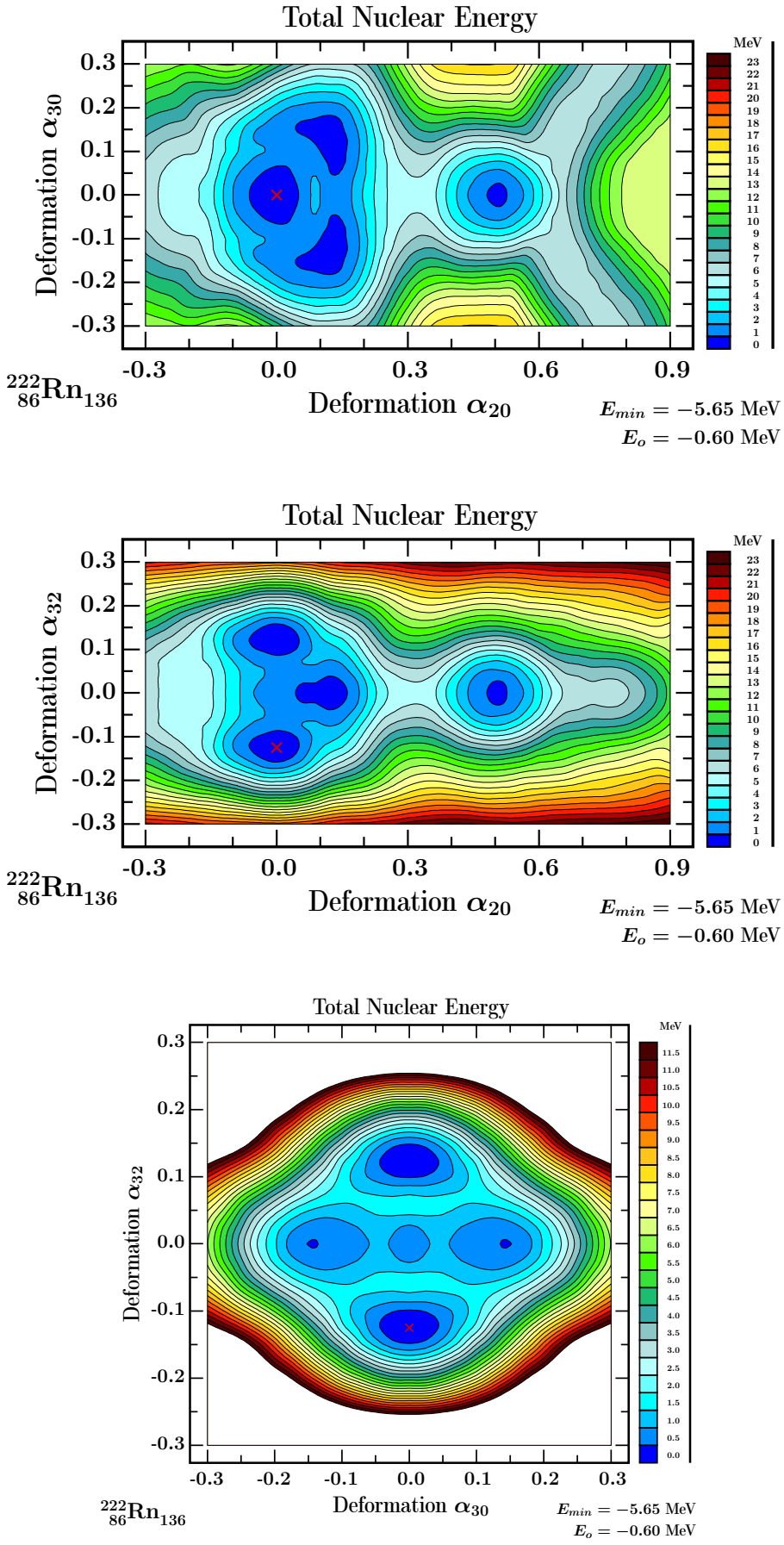

Figure 6.6.4 – *Similar to the preceding one but for* ^{222}*Rn nucleus.*

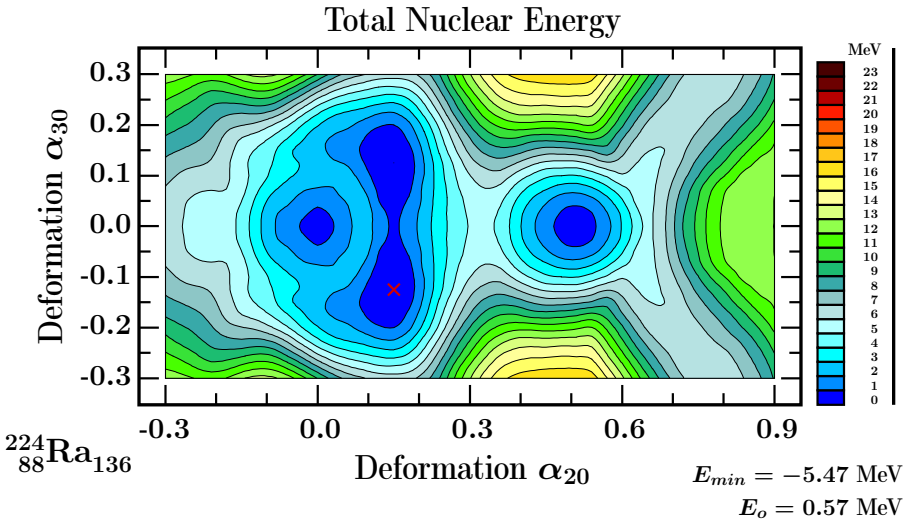

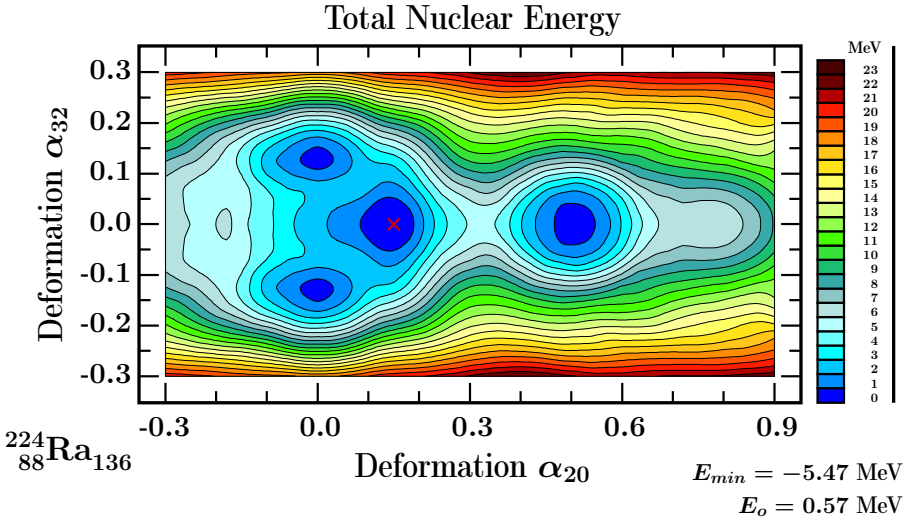

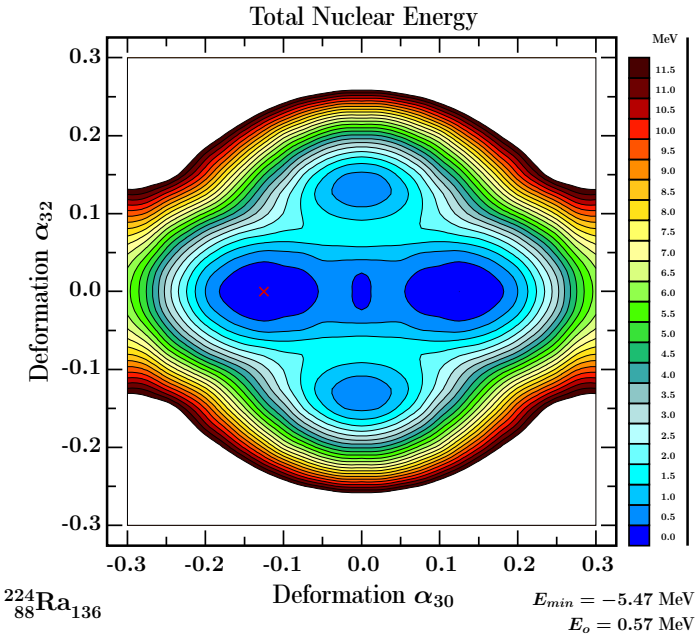

Figure 6.6.5 – *Similar to the preceding one but for* ^{224}*Ra nucleus.*

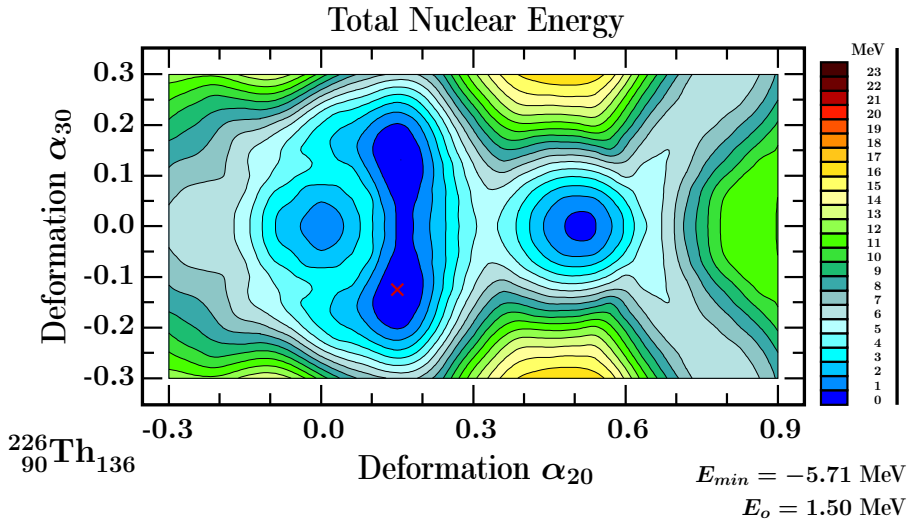

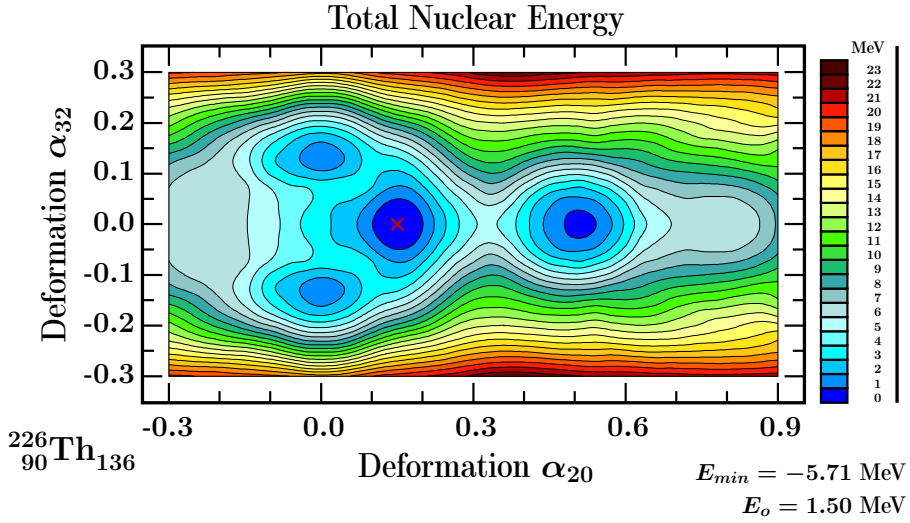

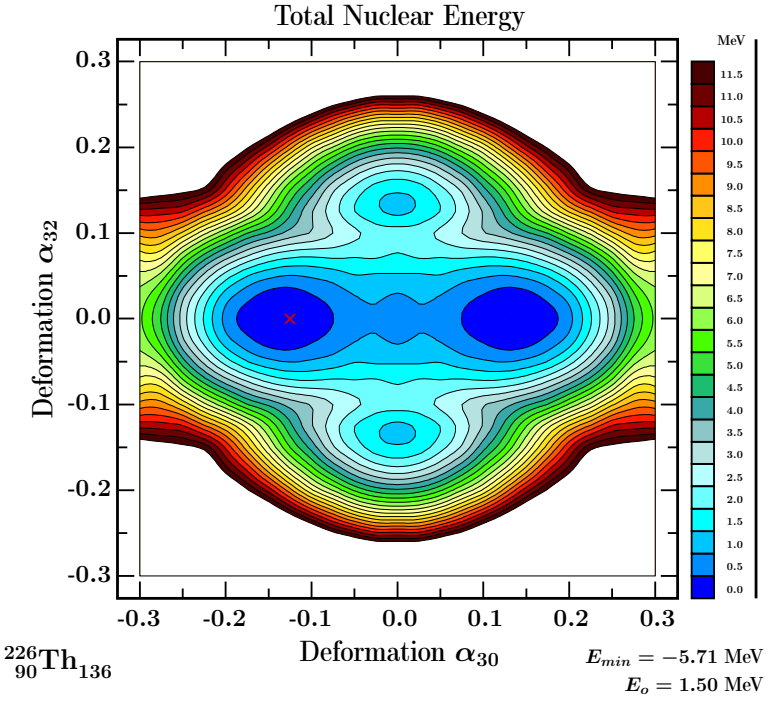

Figure 6.6.6 – *Similar to the preceding one but for* ^{226}*Th nucleus.*

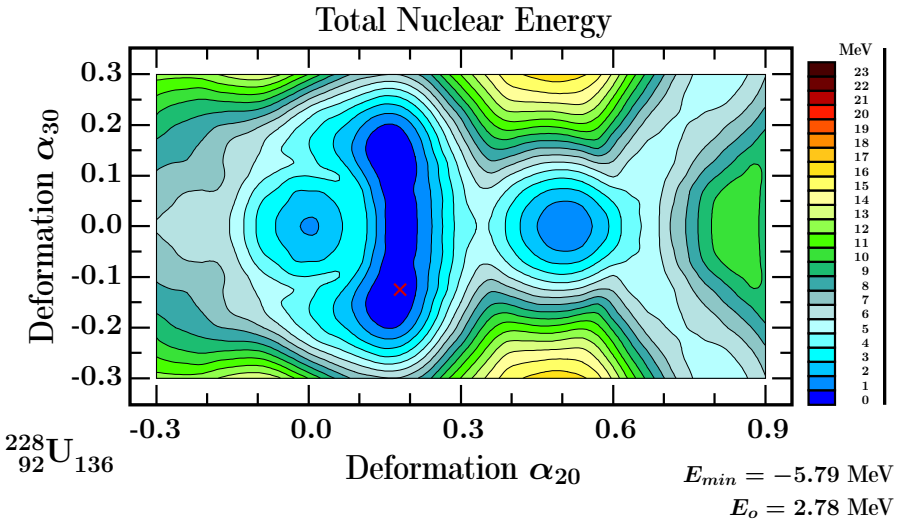

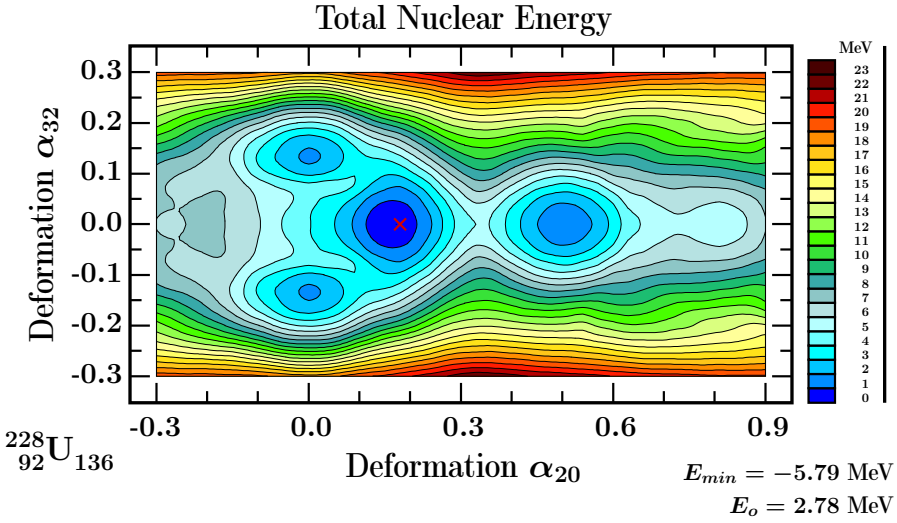

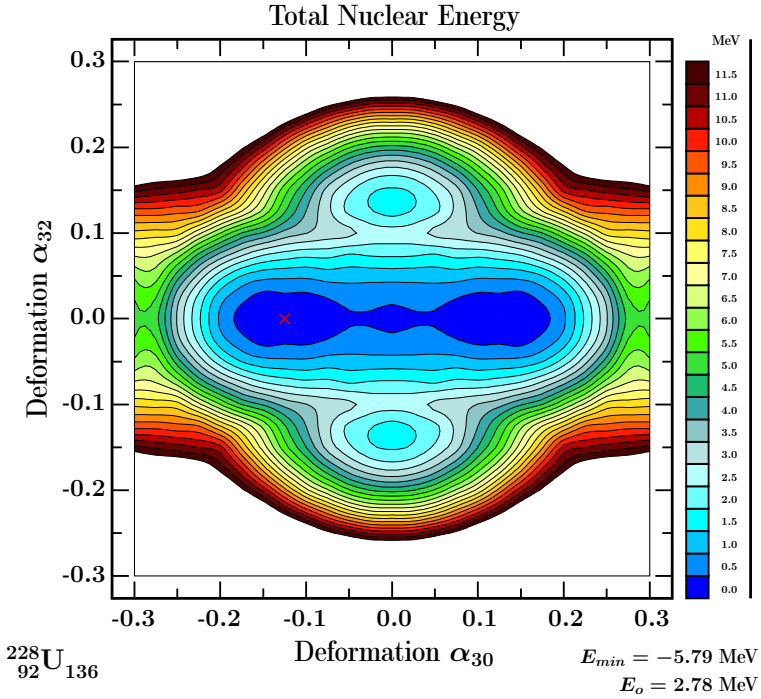

Figure 6.6.7 – *Similar to the preceding one but for* ^{228}U *nucleus.*

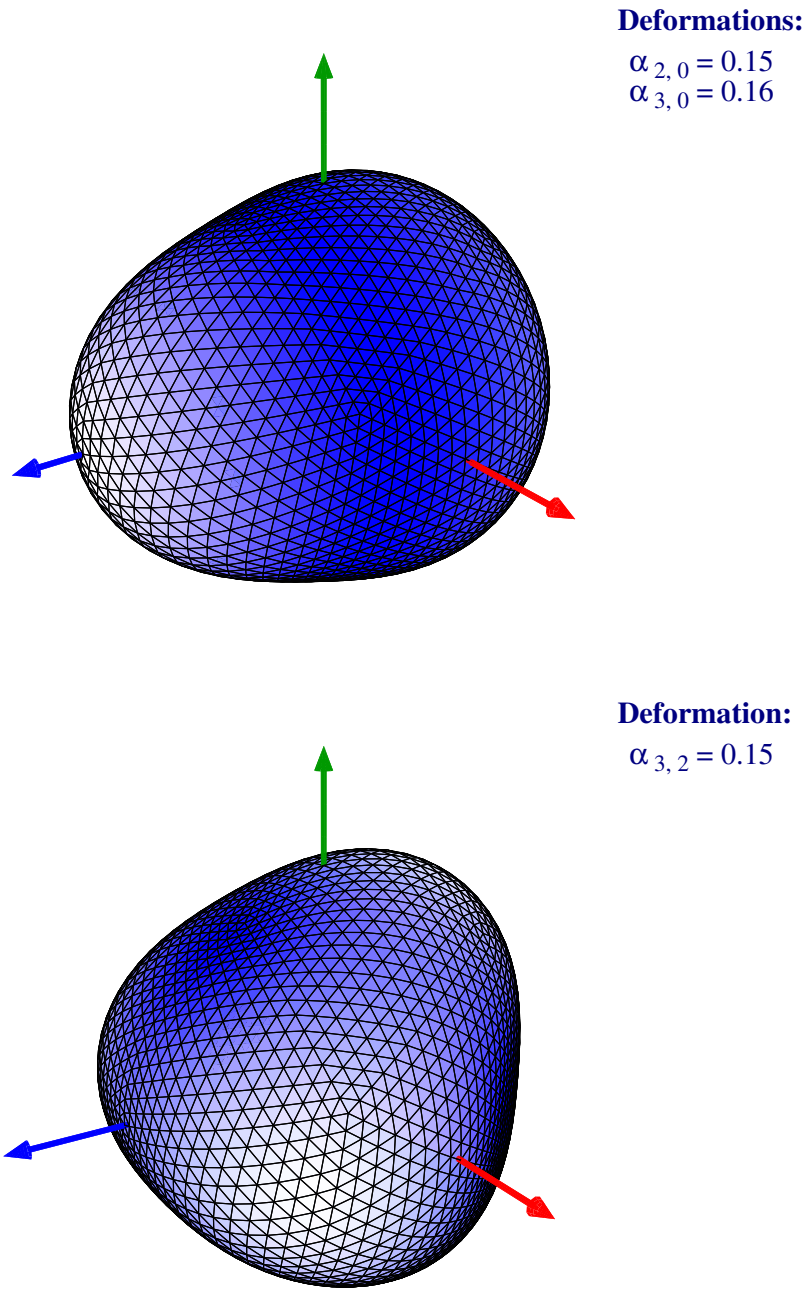

Figure 6.6.8 – *Illustrations of the nuclear surfaces corresponding to the typical equilibrium deformations discussed. Top: for* ($\alpha_{20} \approx 0.15, \alpha_{30} \approx 0.16$)*. Bottom: for* ($\alpha_{20} = 0.0, \alpha_{32} \approx 0.15$)*.*

6.7 Effects of $\lambda > 2$ Deformations in Heavy Nuclei

It is well known that among 3000 nuclei known experimentally, a great majority are deformed. One of the important questions in studying the fission process and other properties of the ground-state is how many various multipole deformations should be employed in order to obtain a realistic description. Since the shell structures are generally sensitive to deformation, various deformation degrees of freedom should be treated as accurately as possible in describing the nuclear structure. For example, selected higher-order deformations, including β_6 were discussed in refs. [66][67], and the authors stressed that still higher-order deformations could have a certain impact on studying heavy nuclei.

The nuclear shapes are described with the help of the spherical harmonics and the related multipole deformation parameters. To study the stability and the symmetry properties of the heavy nuclei we take into account the multipole orders with $\lambda \leq 8$. Using the macroscopic-microscopic approach with the phenomenological mean-field Woods-Saxon Hamiltonian and the universal parameters adjusted for 8 doubly magic nuclei, we review the effects of higher-order deformations in the nuclear range $Z \in [92, 112]$ and $N \in [148, 168]$.

6.7.1 4D Deformation Spaces: Particular Test-Selections

In this section, we are going to present a series of 'pedagogical' illustrations of 2D potential energy surfaces for selected combinations of variables obtained by projections from the original sets of results calculated in 4D spaces. Examples of 4D sub-spaces will be constructed by selecting the quadrupole set $\{\alpha_{20}, \alpha_{22}\}$ as the standard reference supplemented with selections of extra sub-sets of multipole deformations $\lambda \leq 8$.

Let us begin by recalling the standard conventions used to describe the quadrupole deformations $\{\alpha_{20}, \alpha_{22}\}$, which are often presented with the help of relations involving alternative variables $\{\beta, \gamma\}$ and/or $\{x, y\}$:

$$\alpha_{20} = \beta \cos(\gamma), \tag{6.7.1}$$

and

$$\alpha_{22} = \frac{1}{\sqrt{2}} \beta \sin(\gamma), \tag{6.7.2}$$

cf. for instance, ref. [68], where β is referred to as elongation parameter and angular variable γ as a measure of quadrupole triaxiality. In our project we use the equivalent Cartesian coordinates $\{x, y\}$, which are defined as follows

$$x = \beta \cos(\gamma + 30^o), \tag{6.7.3}$$

and

$$y = \beta \sin(\gamma + 30^o). \tag{6.7.4}$$

To study the impact of selected multipole deformations with $\lambda \in [3, 8]$ we have chosen to present the 2D projections on the $\{x, y\}$-plane each time changing the extra 2 deformations over which the minimisations are performed. This choice offers some possibilities for comparing the effects of the extra degrees of freedom considered as complementary with respect to the leading, quadrupole ones.

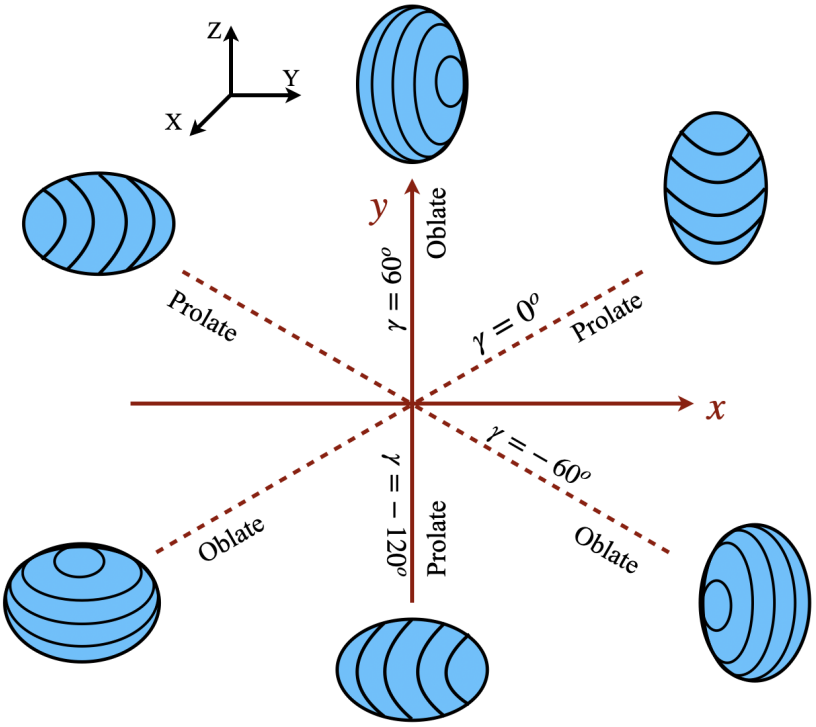

Figure 6.7.1 – *Illustration of the nuclear shapes expressed with the help the coordinates* $\{x = \beta\cos(\gamma{+}30^o), y = \beta\sin(\gamma{+}30^o)\}$. *Nuclear prolate and oblate shapes are defined by appropriately specifying* γ*:* $\gamma = 0^o, 120^o$ *and* -120^o *represent axially-symmetric prolate shapes with different orientations with respect to a fixed Cartesian reference frame. By specifying* $\gamma = \pm 60^o$ *and* -180^o *one obtains a series of axially-symmetric oblate shapes with varying roles of the three reference axes.*

At each of those $\{x, y\}$ points, the energies are minimised over the remaining two deformations. The 4D spaces are chosen (we define below the ranges of each deformation and the corresponding deformation steps) as follows:

- Deformation Mesh No.1:
  - $x \in [0.0, 0.8]$, $\Delta x = 0.025$;
  - $y \in [-0.4, 0.4]$, $\Delta y = 0.025$;
  - $\alpha_{30} \in [-0.3, 0.3]$, $\Delta\alpha_{30} = 0.025$;
  - $\alpha_{40} \in [-0.3, 0.3]$, $\Delta\alpha_{40} = 0.025$.
- Deformation Mesh No.2:
  - $x \in [0.0, 0.8]$, $\Delta x = 0.025$;
  - $y \in [-0.4, 0.4]$, $\Delta y = 0.025$;
  - $\alpha_{40} \in [-0.3, 0.3]$, $\Delta\alpha_{40} = 0.025$;
  - $\alpha_{42} \in [-0.3, 0.3]$, $\Delta\alpha_{42} = 0.025$.
- Deformation Mesh No.3:
  - $x \in [0.0, 0.8]$, $\Delta x = 0.025$;
  - $y \in [-0.4, 0.4]$, $\Delta y = 0.025$;
  - $\alpha_{40} \in [-0.3, 0.3]$, $\Delta\alpha_{40} = 0.025$;
  - $\alpha_{44} \in [-0.3, 0.3]$, $\Delta\alpha_{44} = 0.025$.
- Deformation Mesh No.4:
  - $x \in [0.0, 0.8]$, $\Delta x = 0.025$;
  - $y \in [-0.4, 0.4]$, $\Delta y = 0.025$;
  - $\alpha_{40} \in [-0.3, 0.3]$, $\Delta\alpha_{40} = 0.025$;
  - $\alpha_{60} \in [-0.3, 0.3]$, $\Delta\alpha_{60} = 0.025$.
- Deformation Mesh No.5:
  - $x \in [0.0, 0.8]$, $\Delta x = 0.025$;
  - $y \in [-0.4, 0.4]$, $\Delta y = 0.025$;
  - $\alpha_{40} \in [-0.3, 0.3]$, $\Delta\alpha_{40} = 0.025$;
  - $\alpha_{80} \in [-0.3, 0.3]$, $\Delta\alpha_{80} = 0.025$.

Our limited selection of deformation parameters used for comparisons may seem arbitrary, but it summarises a richer choice checked within the project and illustrates, even if to some limited extent, the roles of shape components with increasing rang λ and/or with varying the kind of triaxiality in the shape parametrisation.

6.7.2 Results of Multi-Dimensional Mesh Calculations

We begin by showing in figure (6.7.2) an example of the total nuclear potential energy for ^{248}Cf nucleus projected on (x, y) plane and minimised over $\{\alpha_{30}, \alpha_{40}\}$ deformations. For convenience the nuclear shape variation within the same deformation space is shown on top of the diagram. By combining the two, fig. (6.7.2) illustrates direct interpretation in terms of the nuclear geometry of the contour plots defined within the $\{x, y\}$ coordinate frame. Still in reference to fig. (6.7.2), top, the up-sloping dashed straight line represents a collection of the axial prolate shapes ($\gamma = 0^o$), whereas the down-sloping one represents a collection of oblate shapes ($\gamma = -60^o$). Similarly, the prolate ($\gamma = -120^o$) and oblate ($\gamma = +60^o$) axes represent the axial symmetry shapes as indicated.

Let us remind the reader that for pure quadrupole deformations, presenting the 2D projections in the full $x > 0$ half-plane may seem superfluous since as one can easily demonstrate, the three γ-sectors limited by the dashed straight lines contain repetitions of the same information. Indeed, the $\Delta\gamma = 60^o$ sectors separated by the lines $\gamma = 0^o$ and $\gamma = -60^o$ are mutually symmetric and the related energies in the sectors remain in one-to-one correspondence. However, when an extra deformation is introduced (here we introduce each time 2 deformations with respect to which the energies are minimised) the symmetry just mentioned is broken.

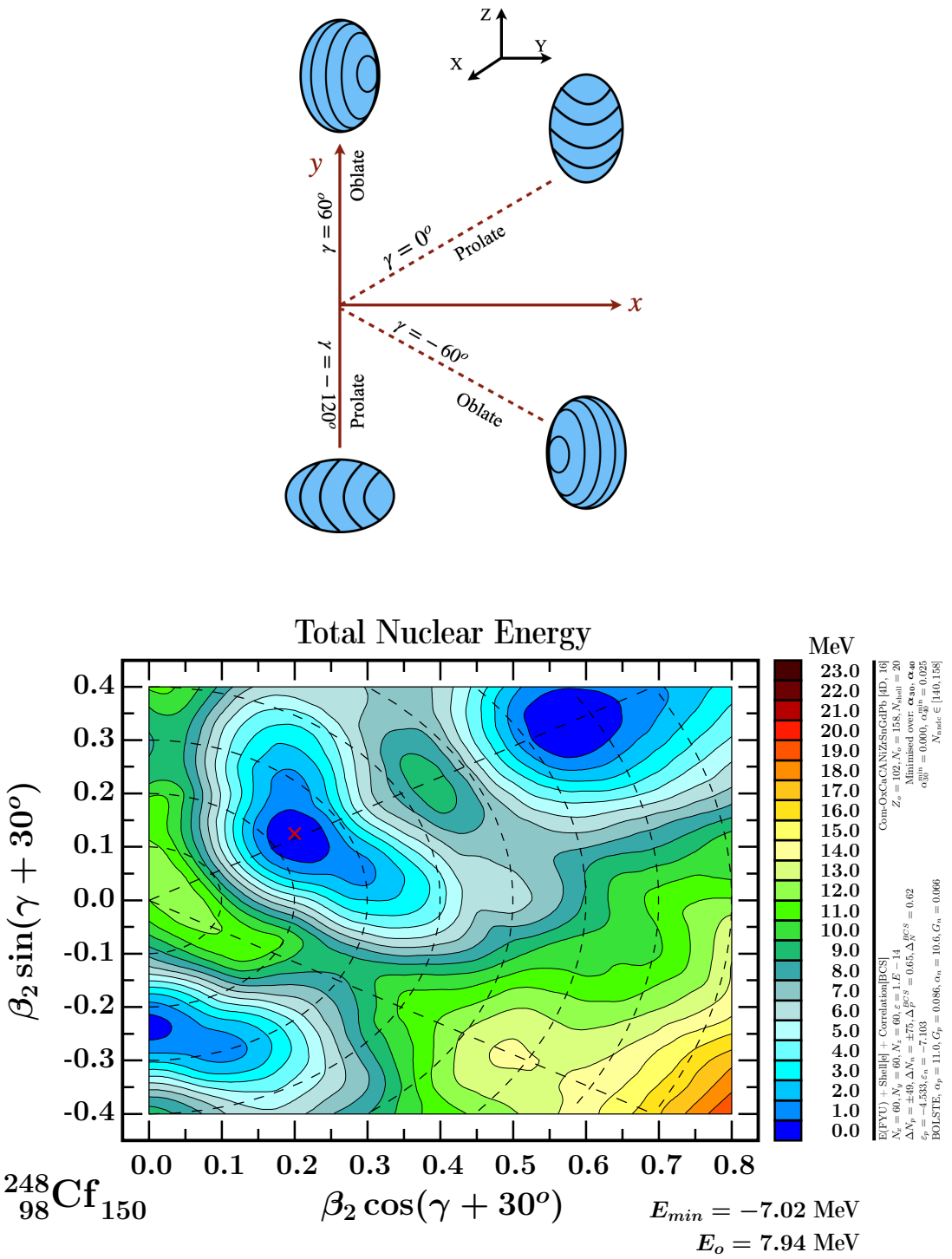

Figure 6.7.2 – *Illustration of the nuclear shapes within Cartesian deformation coordinates* $\{x = \beta\cos(\gamma + 30^o), y = \beta\sin(\gamma + 30^o)\}$ *(top). The nuclear potential energy surface for* ^{248}Cf *projected on the* $\{x, y\}$ *plane and minimised over* $\{\alpha_{30}, \alpha_{40}\}$*, mesh No.1 (bottom). Straight dashed lines represent the shapes with axial symmetry, while the dashed circles refer to increasing quadrupole deformation* β*.*

In figure (6.7.3) we present a comparison of the total nuclear potential calculations for ^{248}Cf nucleus selected as an example. The potential energy surfaces are projected on the $\{\beta, \gamma\} \leftrightarrow \{x, y\}$ plane and minimised over the deformations: (a) $\{\alpha_{30}, \alpha_{40}\}$, (b) $\{\alpha_{40}, \alpha_{42}\}$, (c) $\{\alpha_{40}, \alpha_{44}\}$, (d) $\{\alpha_{40}, \alpha_{60}\}$ and (e) $\{\alpha_{40}, \alpha_{80}\}$.

We notice that the deformation of the ground-state equilibrium remains the same in all the plots. The equilibrium deformation marked with the red cross, $\beta^{\rm th} = 0.267$ at $\gamma^{\rm th} = 0^o$, is in a very good agreement with the experimental value $\beta^{\rm exp} = 0.285(74)$ from ref. [2]. Remark in passing: The experimental quadrupole deformation β can be obtained from the measured electric quadrupole reduced transition probabilities, $B(E2)$, between the ground-state and the first excited 2^+ state using known empirical expressions, cf. e.g. ref. [69]

$$\beta = \frac{4\pi}{3ZR_0^2}\left[\frac{B(E2)}{e^2}\right]; \tag{6.7.5}$$

Z is the atomic number, $R_0 = 1.2A^{1/3}$ the nuclear radius and e is the electric charge unit.

Comparing the energy minima at the potential energy surfaces shown in fig. (6.7.3), we observe that in the case (d) the minimum energy (marked at each diagram at the bottom, right), $E_{\rm min} = -8.70$ MeV, is lower by 1.7 MeV as compared to the reference value $E^{\rm ref}_{\rm min} = -7.02$ MeV (the latter visible in the preceding 3 diagrams), when deformations α_{40} and α_{60} were used for the minimisation. The resulting equilibrium values are $\alpha^{\rm min}_{40} = 0.05$ and $\alpha^{\rm min}_{60} = -0.05$. Let us notice that in the case of the minimisation over α_{40} and α_{80}, case (e), the ground-state minimum is also lower (by approximately 300 keV) than the original reference value $E^{\rm ref}_{min} = -7.02$ MeV, indicating that α_{80}-minimisation has some impact on the ground-state energy. At the ground-state, the octupole deformation $\alpha^{\rm min}_{30} = 0$, and the components of hexadecapole deformations $\alpha^{\rm min}_{42} = 0$ and $\alpha^{\rm min}_{44} = 0$, which indicates that these deformations do not influence the stability of the ground-state for this particular nucleus. Overall, these observations confirm that the higher-rank deformations α_{60} and α_{80} may have a certain importance for modeling of the nuclear ground-states in the discussed heavy nuclei.

Let us also notice the presence of a secondary minimum which appears at $\gamma = -120^o$ axis, at the point which corresponds to another axial-prolate configuration with different orientation with respect to the reference frame and different contributions of the non-quadrupole deformation components. Another secondary minimum corresponds to a very large elongation, $\beta \approx 0.65$, referred to as super-deformed. Both of these secondary minima change only very little from one projection to another visible in the figure.

The contour maps shown in the figure can be considered characteristic for several nuclei in this mass range as shown in the diagram (6.7.3).

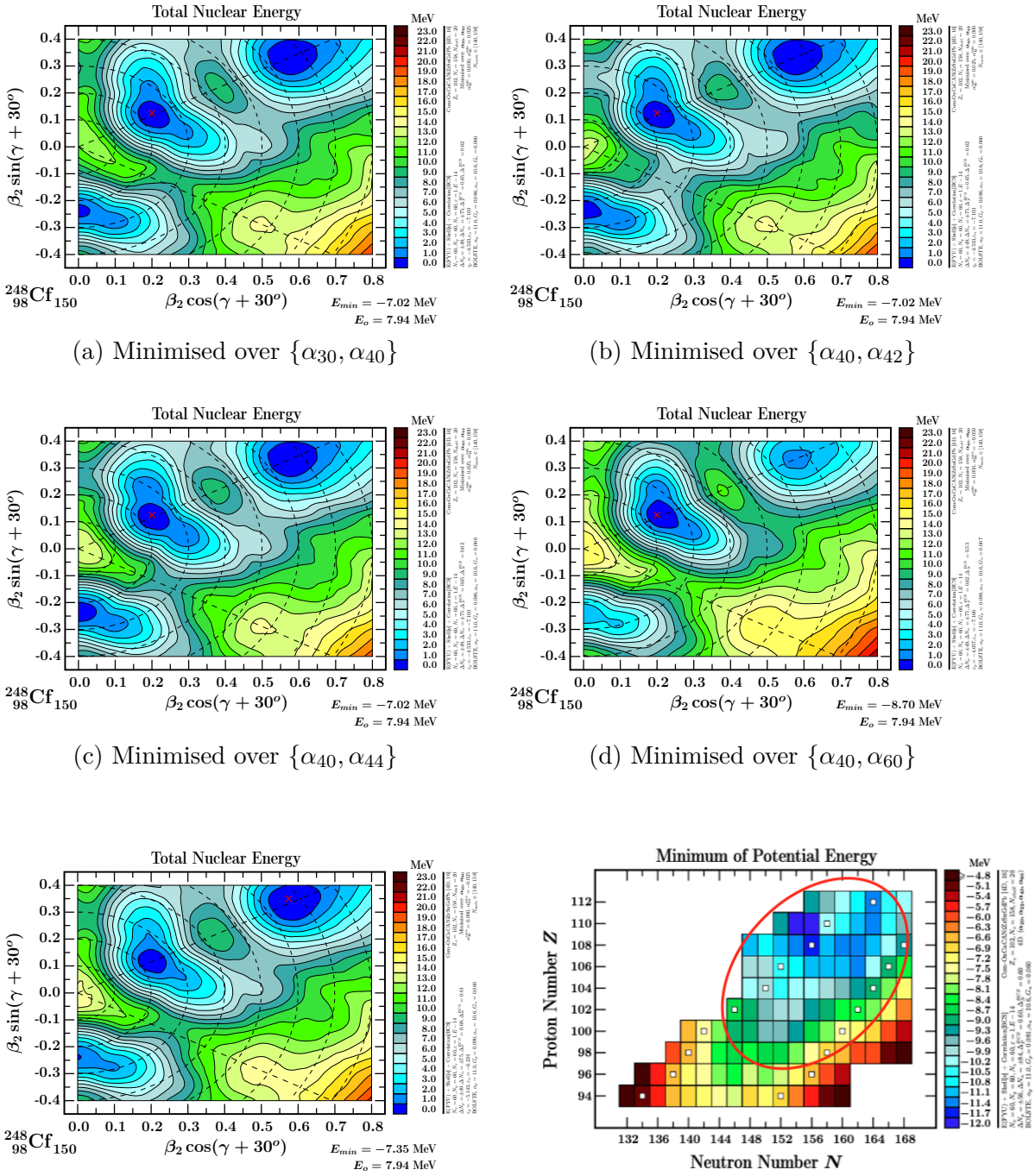

(a) Minimised over $\{\alpha_{30}, \alpha_{40}\}$

(b) Minimised over $\{\alpha_{40}, \alpha_{42}\}$

(c) Minimised over $\{\alpha_{40}, \alpha_{44}\}$

(d) Minimised over $\{\alpha_{40}, \alpha_{60}\}$

(e) Minimised over $\{\alpha_{40}, \alpha_{80}\}$

(f) Behaviour characteristic for (Z,N) shown

Figure 6.7.3 – *Total energy projected on the quadrupole deformation plane represented by $\{x, y\}$ coordinates, for $^{248}_{98}Cf$. At each point the minimisation over: (a) $\{\alpha_{30}, \alpha_{40}\}$, (b) $\{\alpha_{40}, \alpha_{42}\}$, (c) $\{\alpha_{40}, \alpha_{42}\}$, (d) $\{\alpha_{40}, \alpha_{60}\}$ and (e) $\{\alpha_{40}, \alpha_{80}\}$ has been peformed. The ground state minimum is predicted at $\alpha_{20}^{\text{th}} = 0.267$ which is comparable with the experimental result $\alpha_{20}^{\text{exp}} = 0.285(74)$ from ref. [2]. The energy maps shown can be considered characteristic for the nuclei encircled in the diagram (f).*

To compare in a more direct manner the effect of the axial deformations of rank $\lambda > 2$ in the nuclei of interest, we illustrate the one-dimensional cuts in the form of the energy curves as functions of quadrupole deformation $\alpha_{20} = \beta_2 = \beta$, shown in fig. (6.7.4). These energy curves were extracted fixing $\gamma = 0^o$ in the potential maps in fig. (6.7.3) taking the projections (a), (b), (d) and (e) with minimisation over $\{\alpha_{30}, \alpha_{40}\}$, $\{\alpha_{40}, \alpha_{42}\}$, $\{\alpha_{40}, \alpha_{60}\}$ and $\{\alpha_{40}, \alpha_{80}\}$, respectively.

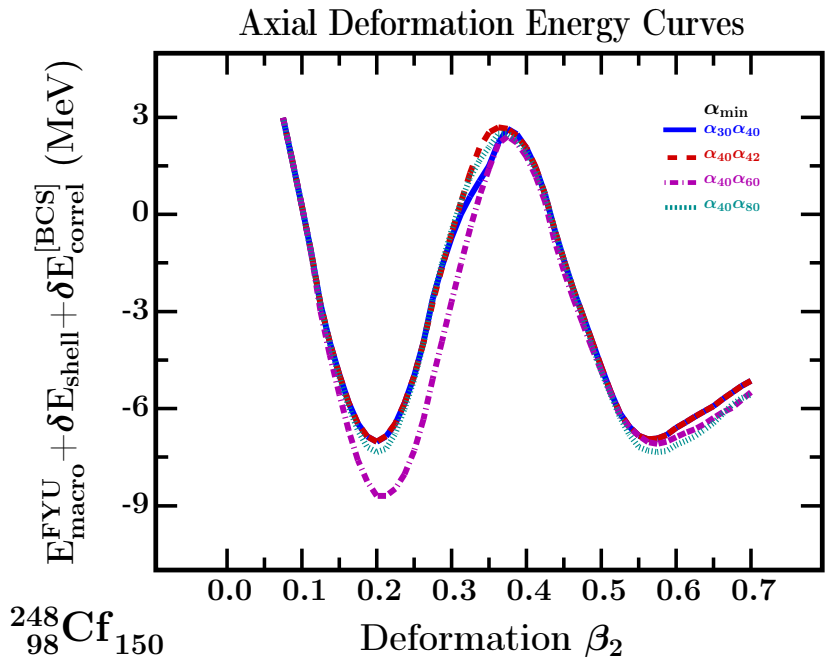

Figure 6.7.4 – *Illustration of the deformation energy cuts at $\gamma = 0^o$. These curves are extracted from the total potential energy maps in figure (6.7.3) including minimisations over $\{\alpha_{30}, \alpha_{40}\}$, $\{\alpha_{40}, \alpha_{42}\}$, $\{\alpha_{40}, \alpha_{60}\}$ and $\{\alpha_{40}, \alpha_{80}\}$, respectively.*

The comparison shows that the energy curve including α_{60} minimisation generates significantly deeper ground-state energy. To extend the comparison, we show similar one-dimensional projection curves for a few isotopes of Cf nucleus ($Z = 98$) in figure (6.7.5) and for $N = 150$ isotones in figure (6.7.6), respectively. Results for $Z = 98$ isotopes show that the effect of α_{60} decreases with increasing neutron number; the effect is most pronounced at neutron numbers $N = 150$ and 152 and disappears around $N = 160$. Similarly, the effect of α_{60} deformation for $N = 150$ isotones in figure (6.7.6) shown for proton numbers $Z \in [94, 106]$ is the most pronounced for $Z = 102$ and the nearest neighbours.

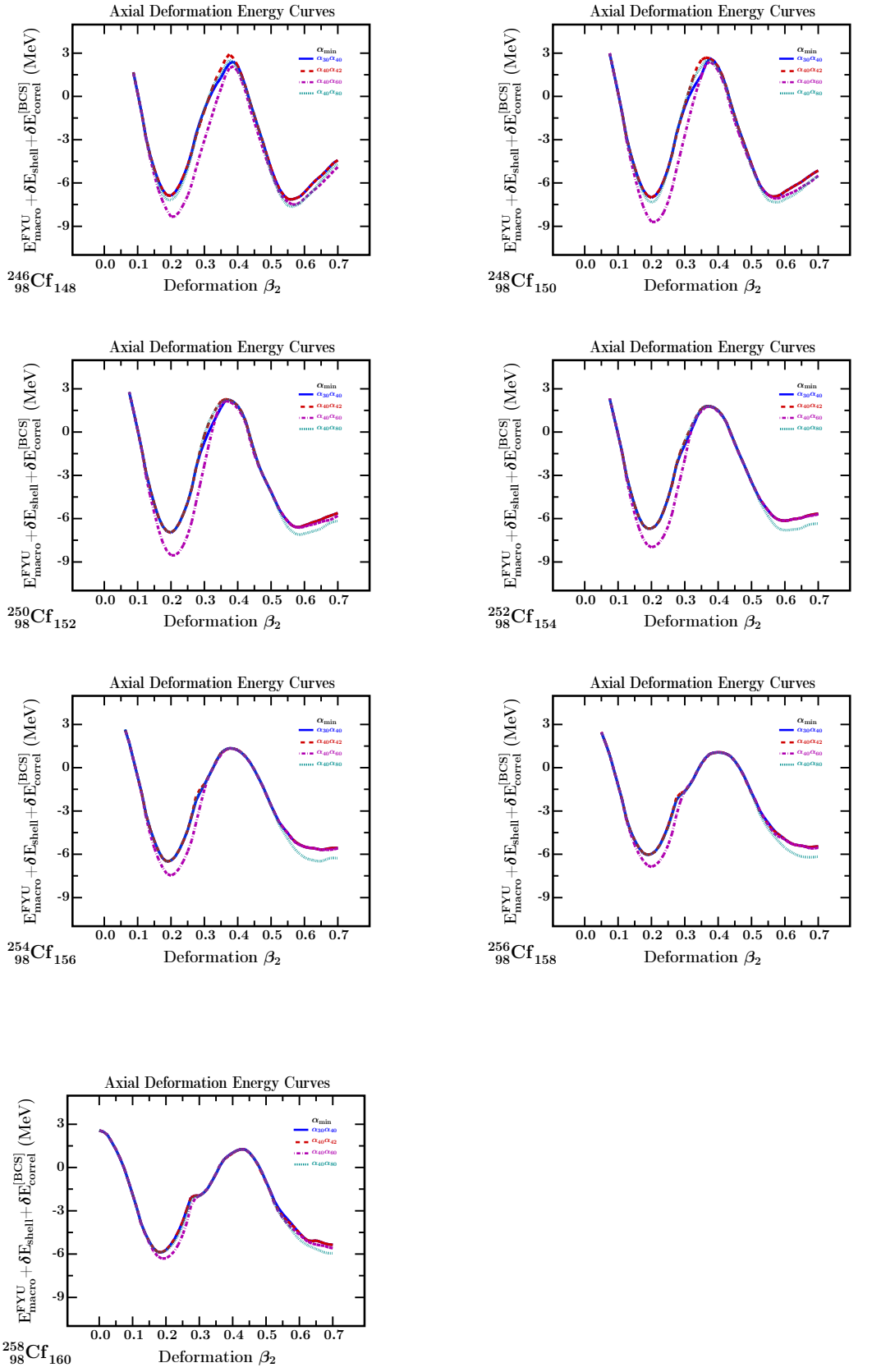

Figure 6.7.5 – *Similar to the preceding one but for a series of isotopes of the Cf nucleus, as indicated.*

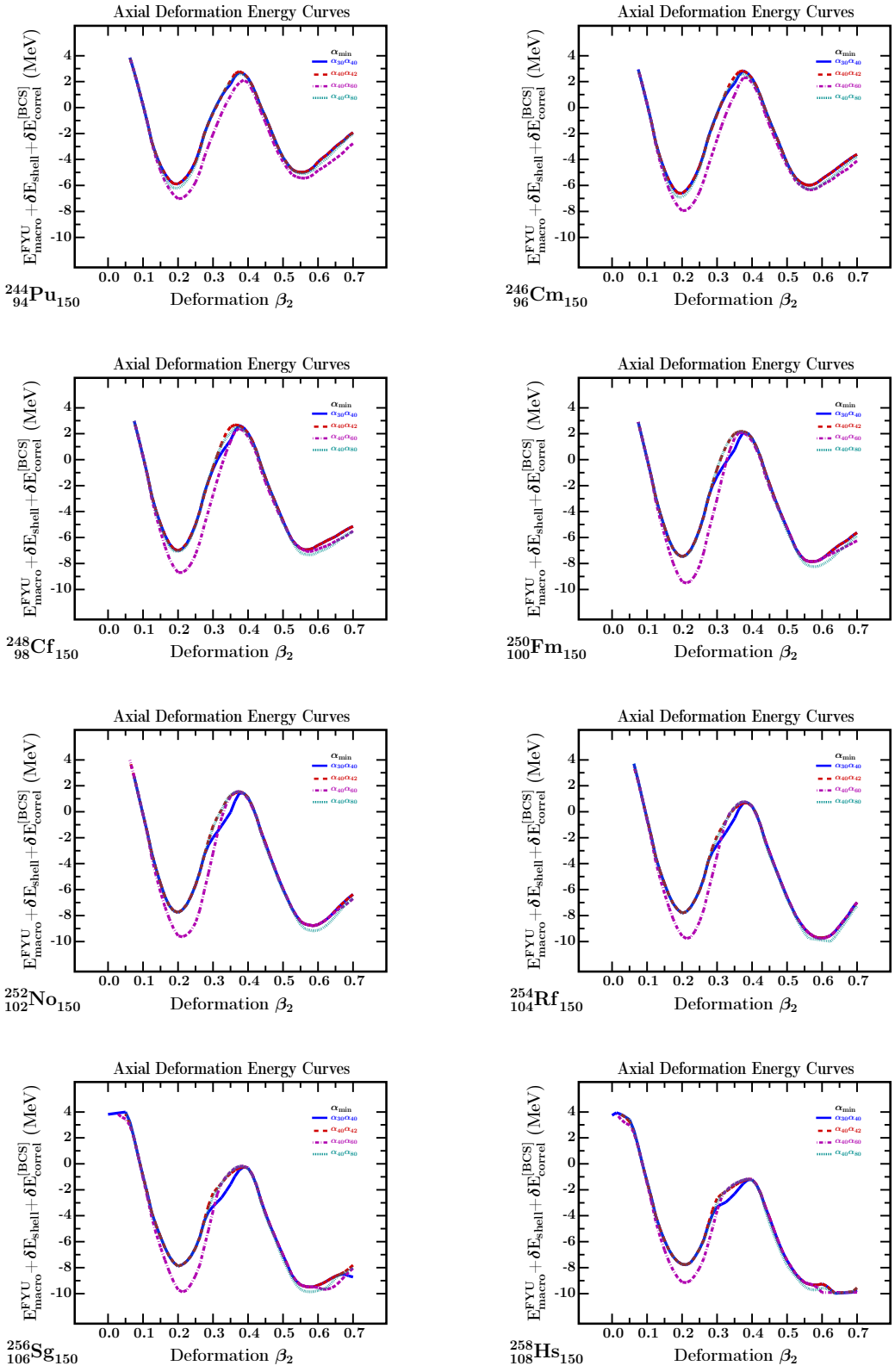

Figure 6.7.6 – *Similar to the preceding one but for a series of* $N = 150$ *isotones, as indicated.*

We may conclude that among the axial multipole deformations with $\lambda > 2$ the impact of α_{60} on the ground-state energy minima is the strongest in heavy and super-heavy nuclei discussed in our project.

6.7.3 Selected Ground-State Properties – Concluding Remarks

The energy values at the ground-states were obtained via total potential surface calculations combining various multipole deformations. It turns out that in the test accomplished the axial symmetry deformations α_{60} and α_{80} have the most significant impact on the ground-state minimum energies.

To give a general picture of the properties of the ground-state energies, in figure (6.7.7) we summarise the equilibrium energy values using (Z, N) representation. For the heavy and super-heavy nuclei with $94 \leq Z \leq 112$, we present here the energy values obtained from the 3D-dimensional calculations (top) with the potential energies projected on (β, γ) plane and minimised over (α_{40}), and from the 4D-dimensional calculation (bottom) where the minimisation deformations are $\{\alpha_{40}, \alpha_{60}\}$.

Figure (6.7.7) shows that the energy minima obtained minimising over α_{60} are by 1-2 MeV lower for the nuclei around $Z \approx 98 - 110$ and $N \approx 144 - 160$. It follows that the higher-order, α_{80}, allows to gain still a few hundreds of keV.

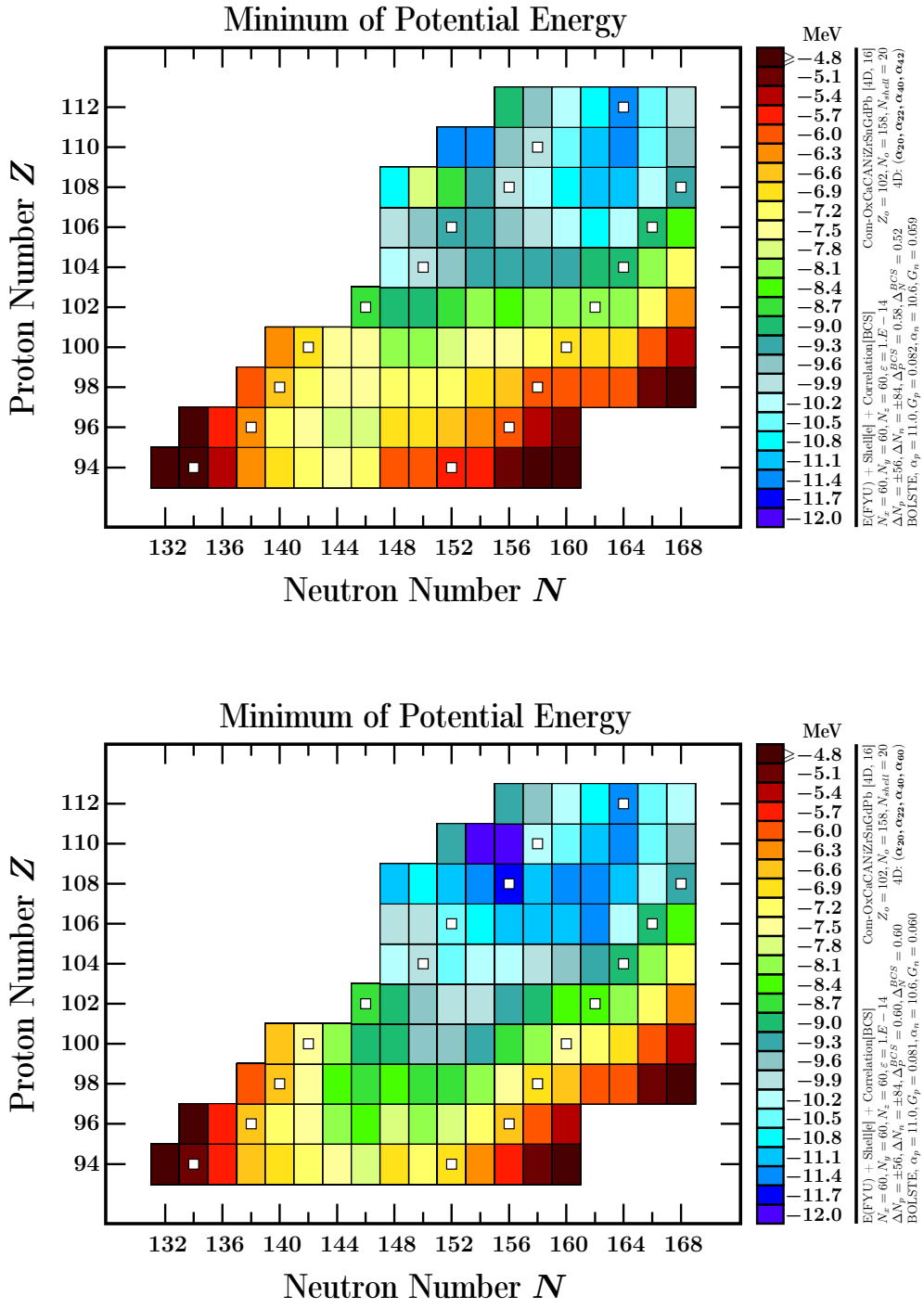

Figure 6.7.7 – *Ground-state energy minima calculated from 3D mesh projected on the (β, γ) plane and minimised over α_{40} deformation (top), and the ones from 4D mesh projected on the (β, γ) plane and minimised over α_{40} and α_{60} deformations (bottom). White squares denote the experimentally confirmed existence limits (from NNDC database).*

6.8 Exotic Symmetries in Super-Heavy Nuclei

Only 278 nuclei among about 3000 experimentally known today can be found in nature. Scientific attempts to synthesise new elements beyond uranium were undertaken since the early 1930's. One of the fundamental questions about the existence of nuclear systems, which intrigues nuclear physicists, concerns the limits of the existence of nuclei, which can be found in nature or produced in the laboratory. In particular: What are the biggest proton and neutron numbers leading to existing nuclear objects? One of the limitations is caused by the nucleon binding: As soon as the neutron or proton separation energies bypasses zero, $B_{n/p} = 0$, the existence of the corresponding system becomes impossible. Another one is related to the balance between the Coulomb repulsion and the nuclear binding determining the heights of the nuclear fission barriers. Vanishing of those barriers, $B_f = 0$, leads to vanishing of the nuclear stability and thus existence as well. In other words: With the fission barriers tending to zero, the nucleus losses its stability and can fission in very short times of $T \approx 10^{-19}$s, whereas the limit of the existence of the chemical elements defined by the spontaneous fission model is about $T \approx 10^{-14}$s, cf. e.g. ref. [70].

In 1955, J. A. Wheeler [71] attempted for the first time to search for the limitations of existing nuclei with the mass values twice heavier than the element ${}^{256}_{100}\mathrm{Fm}_{156}$, which was the heaviest element known at that time. The properties of these nuclei were discussed in detail in 1958, cf. ref. [72]. The concept 'super-heavy nuclei' was used for the first time at the conference on the Peaceful Uses of Atomic Energy, in Geneva, in 1955, ref. [73]. Nowadays, super-heavy nuclei are referred to as elements beyond Rutherfordium, $Z = 104$.

In the experimental research, the new generation of facilities such as GANIL[1], FRIB[2], RIKEN[3], HILAC[4], SHIP[5], and EXCYT[6] etc., have served for many years to explore the limits of stability of super-heavy nuclei. Between 1981 and 1992, the super-heavy elements $Z = 107 - 112$ were discovered and identified at the GSI[7] laboratory, see ref. [74] and the references therein, where $Z = 107$ was the first new synthesised element. Synthesis of the element $Z = 113$ was produced in RIKEN laboratory, cf. ref. [75]. The recent experiments in Dubna have discovered the super-heavy nu-

[1]Grand Accelerateur National d'Ions Lourds, Accelerator Laboratory in Caen, France.
[2]The Facility for Rare Isotope Beams (FRIB), at Michigan State University.
[3]Institute of Physical and Chemical Research in Saitama near Tokyo, Japan.
[4]Heavy Ion Linear Accelerator at LBNL in Berkeley, California, later updated to the SuperHILAC.
[5]Separator for Heavy Ion reaction Products, velocity filter for fusion reaction products at GSI, Darmstadt, Germany.
[6]Exotics with Cyclotron and Tandem is the development of a facility for producing and accelerating exotic beams up to 8 MeV/amu. The laboratory is located in Catania, Italy.
[7]Gesellschaft für Schwer-Ionen-Forschung, Accelerator laboratory in Darmstadt, Germany.

clei $Z = 114 - 118$ and confirmed through hot fusion processes refs. [76–79]. Other attempts to produce or synthesise the new elements with $Z > 120$ were discussed in refs. [80–82].

On the theoretical side, although many collective properties can be reproduced by the charged liquid drop model, the shell structures such as the spherical energy gaps with proton and neutron numbers, 2, 8, 20, 28, 50, 82, and neutron number 126 can only be explained by microscopic description more explicitly nucleon-nucleon interactions, cf. early attempts e.g. in ref. [83]. In ref [84], the proton number $Z = 114$ and neutron number $N = 184$ were predicted as the next spherical shell closures. In 1967, Strutinsky introduced his macroscopic-microscopic method to calculate the binding energies of nuclei and to discuss several problems, e.g., nuclear deformations, shell effects in deformed nuclei and nuclear fission, etc., ref. [85]. In particular, the binding energy as a function of deformation for heavy fissioning nuclei was used to determine the fission barriers, which provide important information about nuclear stability. One of the most important results of the calculation of fission barriers was discovering the fission isomers resulting from the secondary minima at large deformations, ref. [86].

As an alternative to the macroscopic-microscopic approach, purely microscopic self-consistent approaches such as self-consistent Skyrme-Hartree-Fock-Bogolyubov approximation within the effective density functional formalism have been used to predict the spherical magic numbers at $Z = 126$ and $N = 184$ in super-heavy region cf. ref. [87, 88]. On the other hand, a systematic study using spherical relativistic and non-relativistic mean-field calculations showed that the spherical shell gaps appeared at $Z = 114, N = 184$ or $Z = 120$, $N = 172$ or $Z = 126$, $N = 184$ depending on parameterisations, ref. [89], while the deformed relativistic mean-field calculation predicted the possible magic numbers at $Z = 120$ and $N = 184$, cf. refs. [90, 91] and references therein. More recently, the predictions of the existence and shell stabilisation of super-heavy nuclei using the non-relativistic Skyrme-Hartree-Fock approach were extended to hyper-heavy nuclei regions around $N = 258$ and 308, where the nuclei with $Z > 126$ are referred to as hyper-heavy, cf. ref. [92]. Three regions of the spherical hyper-heavy nuclei: $(Z \approx 138, N \approx 230)$, $(Z \approx 156, N \approx 310)$, and $(Z \approx 174, N \approx 410)$ are predicted within the framework of the relativistic Hartree-Bogolyubov approximation, ref. [93]. The heaviest elements in the mass table are predicted at $Z = 173$ based on the relativistic multi-configuration Dirac-Fock calculations [94].

Theoretical studies of the properties of the super-heavy nuclei were fast developing in nuclear physics over the past 70 years. The analysis of different theoretical models has been presented in a number of review articles [70, 95–99].

It is worth mentioning that in the studies of super-heavy nuclei not only the predictions of the closed spherical shells, but also the existence of exotic nuclear geometry has

been considered. The possible existence of strongly deformed spheroidal nuclei and the spherical bubble nuclei were discussed already in 1967 ref. [100]. The stability of these exotic structures was studied in detail by Wong in 1973, cf. ref. [101]. He investigated nuclei around the β-stability line, and found that around certain nuclei, e.g. $^{200}_{80}\mathrm{Hg}_{120}$ and $^{138}_{58}\mathrm{Ce}_{80}$, the spherical bubble-structure configurations are more stable, whereas in some others the toroidal shapes may gain additional stability. Later, with the help of the generalised rotating liquid drop model, Wong also discussed the nuclear toroidal shapes appearing at high angular momentum, ref. [102]. Recent publications [93, 103–105] showed that the spherical bubble nuclei may exist in the superheavy region with $A \approx 450$. The evolution of toroidal configuration is dominated by hyper-heavy nuclei with $Z > 130$ and the flattest toroidal nuclei are placed in the $Z \approx 136$ and $N \approx 206$.

The physical origin of these particular shapes is the rapidly increasing repulsion between the protons and attractive interactions of all other nucleons. In other words, since the repulsive Coulomb interaction increases with increasing proton number, forming extended exotic shapes such as bubbles or toroidal forms, may lead to a reduction of the electrostatic energy of the nucleus, ref. [104].

In our project, we extend the multi-dimensional deformation mesh calculations to super-heavy nuclei with $Z \in [110, 130]$, to study possible exotic symmetries. The discussion will be presented in the following sections.

6.8.1 Octupole Magic Numbers in Super-heavy Nuclei

As discussed so far, the exotic shapes in the form of spherically symmetric bubbles and toroidal forms were discussed in several publications. Besides that, calculations of the pear-shape octupole deformation effects in neutron-rich actinides and super-heavy nuclei were carried out over the last decades as well.

The axial reflection-asymmetric Hartree-Fock-Bogolyubov approach showed that many neutron-rich actinide nuclei, in particular with $184 < N < 206$ are pear-shaped in their ground-states, cf. fig. 4 in ref. [106] and the references therein. Within the relativistic Hartree-Fock-Bogolyubov theory, a region of octupole deformation in heavy nuclei around $Z \sim 98, N \sim 196$ was predicted, whereas the octupole effects were predicted not to appear in these super-heavy nuclei according to refs. [62, 107, 108]. In contrast, the existence of octupole deformed nuclei in the super-heavy region of $Z \approx 120, N \approx 190$ was predicted by the macroscopic-microscopic model of ref. [109] and the Hartree-Fock-Bogolyubov approach with density-dependent Gogny interactions, ref. [110]. Moreover, recent macroscopic-microscopic calculations in refs. [111, 112] have shown that the tetrahedral-octupole deformation appears in $Z \approx 98, N \approx 192$ and $Z \approx 126, N \approx 192$. More generally, it follows from these articles that octupole

deformation in super-heavy nuclei occurs at the neutron numbers around $N \approx 190$.

Since the octupole effects are expected as the results of the strong gaps in the single-particle spectra, we examine first the proton and neutron single-particle spectra as functions of the octupole deformations $\alpha_{3\mu=0,1,2,3}$ in figs (6.8.1-6.8.2), respectively. The spherical shell gap of the order of 2 MeV at $N = 114$ is clearly visible. It is caused by a repulsive spin-orbit interaction between $2f_{7/2}$ and $2f_{5/2}$ orbitals shown in fig. (6.8.3). The strongest proton shell effects appear at tetrahedral deformation α_{32}, but the overall octupole proton gaps are not visibly strong.

As shown in fig. (6.8.2), a strong spherical shell gap is found at $N = 184$, of the order 1.5 MeV, while the octupole gap at $N = 196$ is predicted at all four octupole deformations. The size of the tetrahedral gap is comparable with the spherical gap, both with an energy of about 2 MeV. This strong octuple gap is presented by the interaction between the orbitals $1k_{17/2}$ and $2h_{11/2}$. Comparing the single-particle energy spectra for all four octuple deformations we may conclude that the neutron number $N = 196$ can be considered as a four-fold octupole magic number similar to $N = 136$.

In order to study the octupole effects, we focused on the ${}^{310}_{114}\mathrm{Fl}_{196}$ nucleus whose quadrupole deformation vanishes, similarly to the ${}^{218}_{82}\mathrm{Pb}_{136}$ case. In fig. (6.8.4) we represent the potential energy surfaces projected on $\{\alpha_{20}, \alpha_{3\mu=0,1,2,3}\}$ planes and minimised over α_{40} deformation. Comparison shows that all equilibrium deformations are of the similar order of $\alpha_{3\mu} = 0.15$ with vanishing quadrupole deformation, similarly to the nuclei with $N = 136$ in fig. (6.2.4). The highest barrier separating two octupole minima is found for tetrahedral deformation with the barrier heights of the order of 3-to-4 MeV. The fission barrier in the case of the (α_{32}-vs.-α_{20})-plane reaches the energy order of 3-to-4 MeV as well. The remaining octupole deformations produce the barrier heights of the order of 1.5-to-2 MeV.

As discussed in section (6.2.4) the point group symmetries $C_{\infty v}$, C_{2v}, T_d and D_{3h} are related to the deformations $(\alpha_{20} = 0, \alpha_{30} \neq 0)$, $(\alpha_{20} = 0, \alpha_{31} \neq 0)$, $(\alpha_{20} = 0, \alpha_{32} \neq 0)$ and $(\alpha_{20} = 0, \alpha_{33} \neq 0)$, respectively. The structures of the rotational bands for the above symmetries can be found in fig. (6.3.5), fig. (5.4.1) and in fig. (6.3.6).

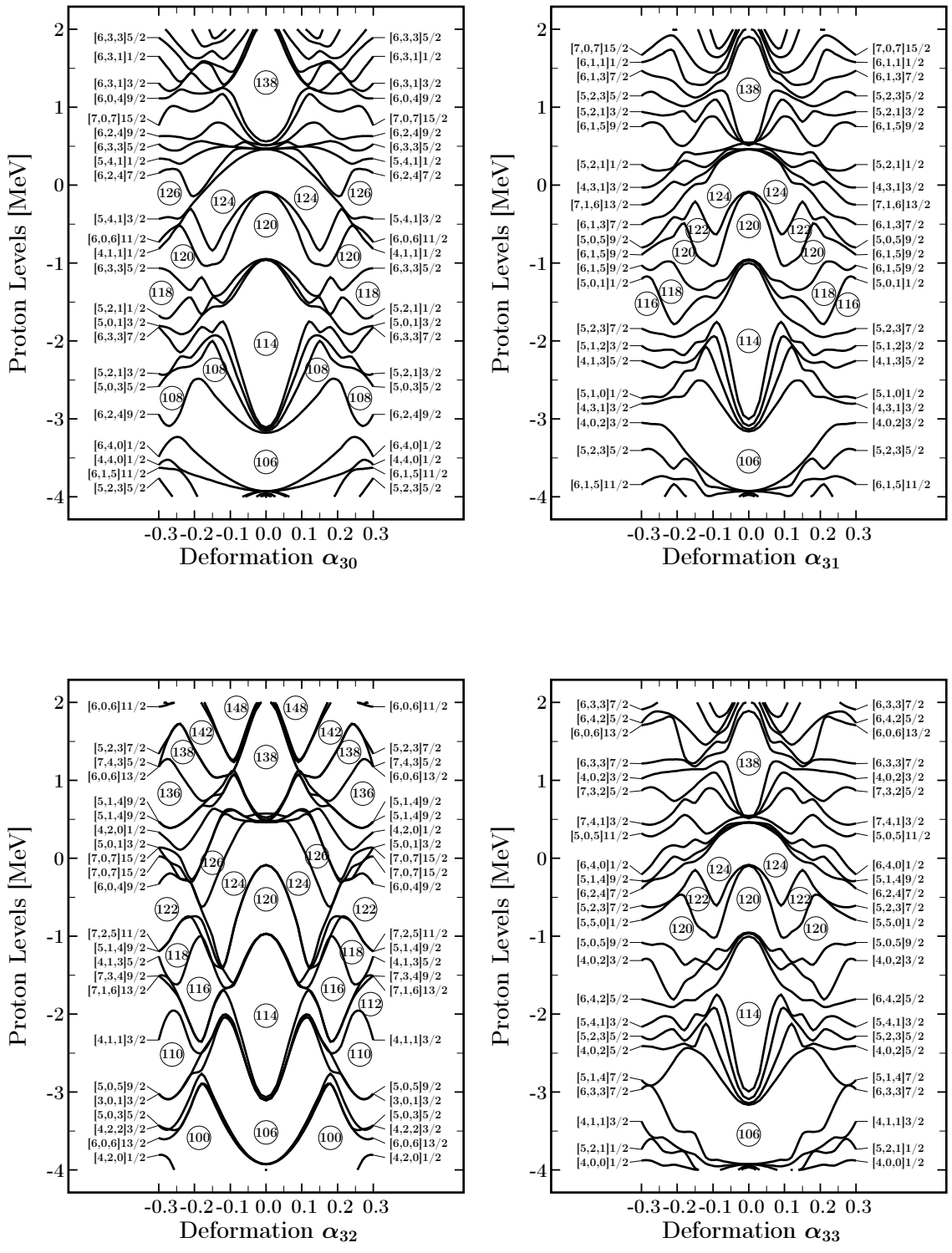

Figure 6.8.1 – *Proton single-particle energies as functions of the octupole deformations* $\alpha_{3\mu=0,1,2,3}$ *in super-heavy regions. All other deformation parameters are set to zero. Except for* $Z = 106$ *there are no strong octupole shell effects favoured by the protons;* $(Z_0 = 122, N_0 = 186)$.

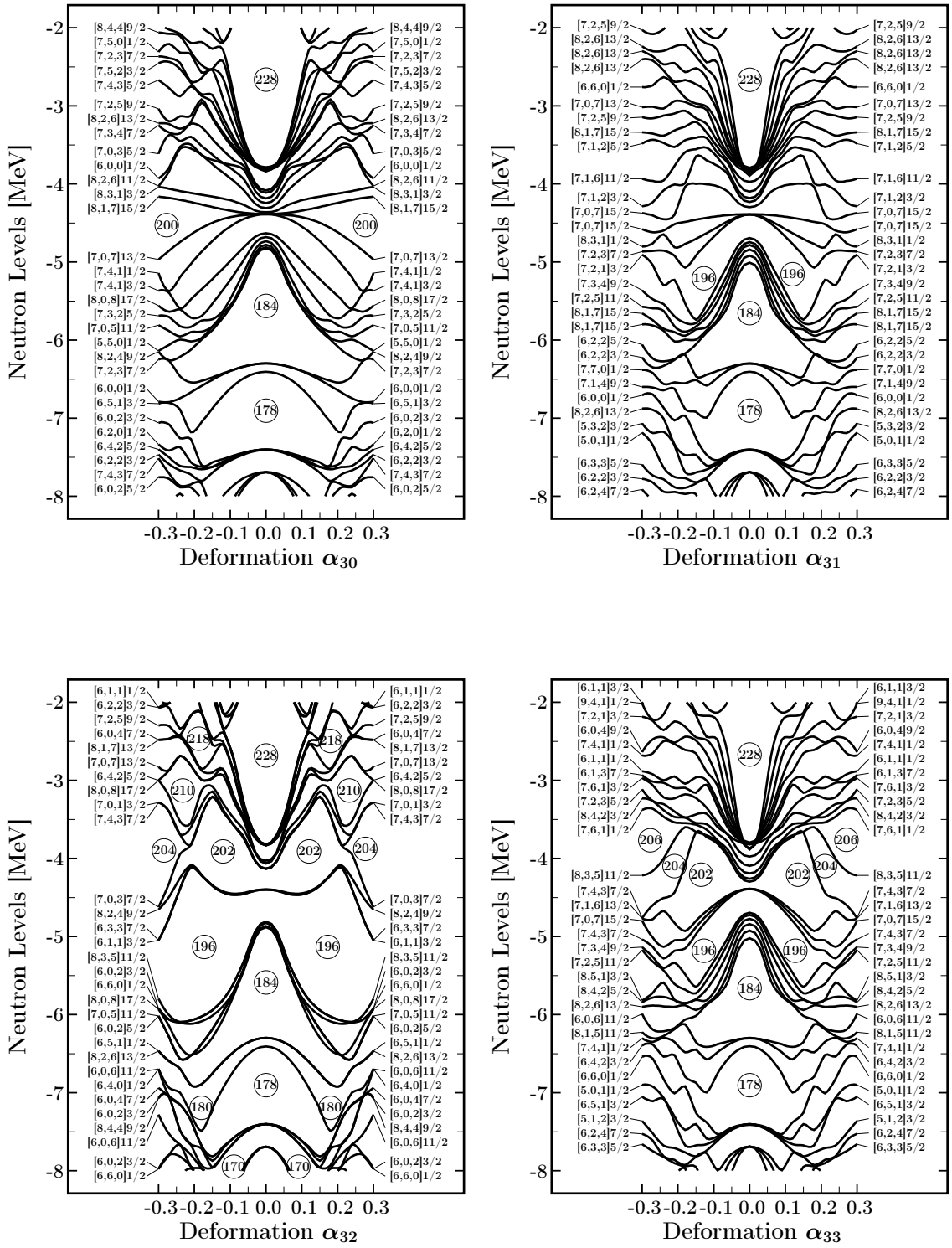

Figure 6.8.2 – *Neutron single-particle energies as functions of the octupole deformations* $\alpha_{3\mu=0,1,2,3}$ *in super-heavy regions. The strongest octupole shell effects are predicted at* $N = 196$*, caused by tetrahedral symmetry* α_{32} *deformation;* $(Z_0 = 122, N_0 = 186)$.

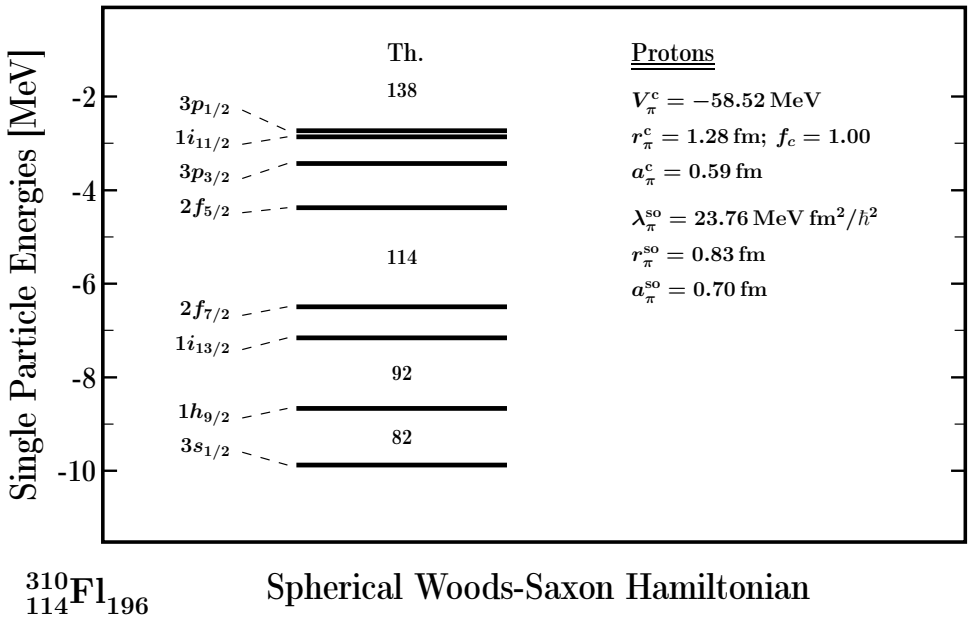

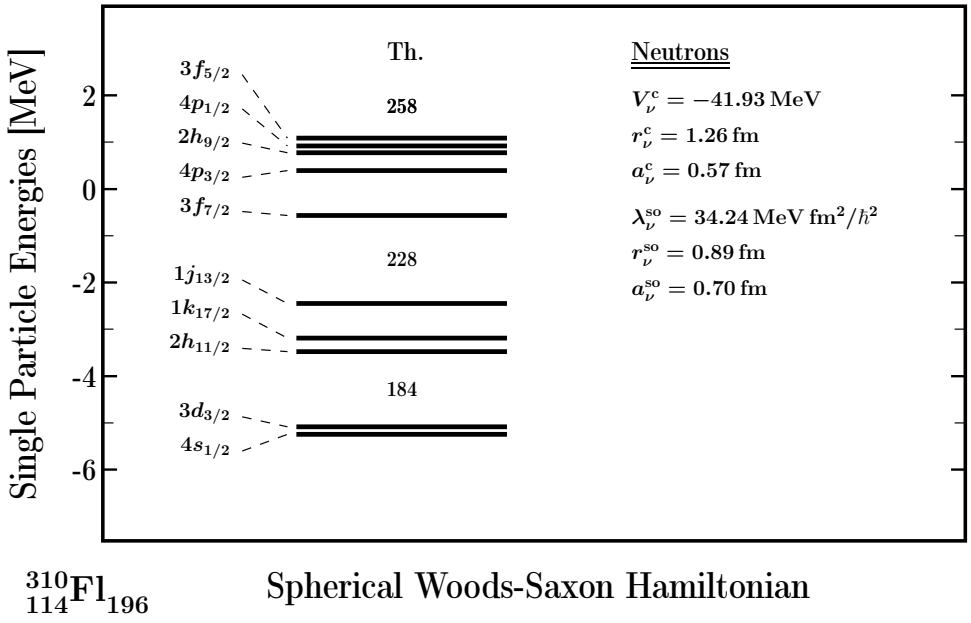

Figure 6.8.3 – *Proton (top) and neutron (bottom) single-particle energies showing the single particle spherical orbitals and the induced strongest shell gaps; parameters of the Woods-Saxon Hamiltonian are displayed in the figures.*

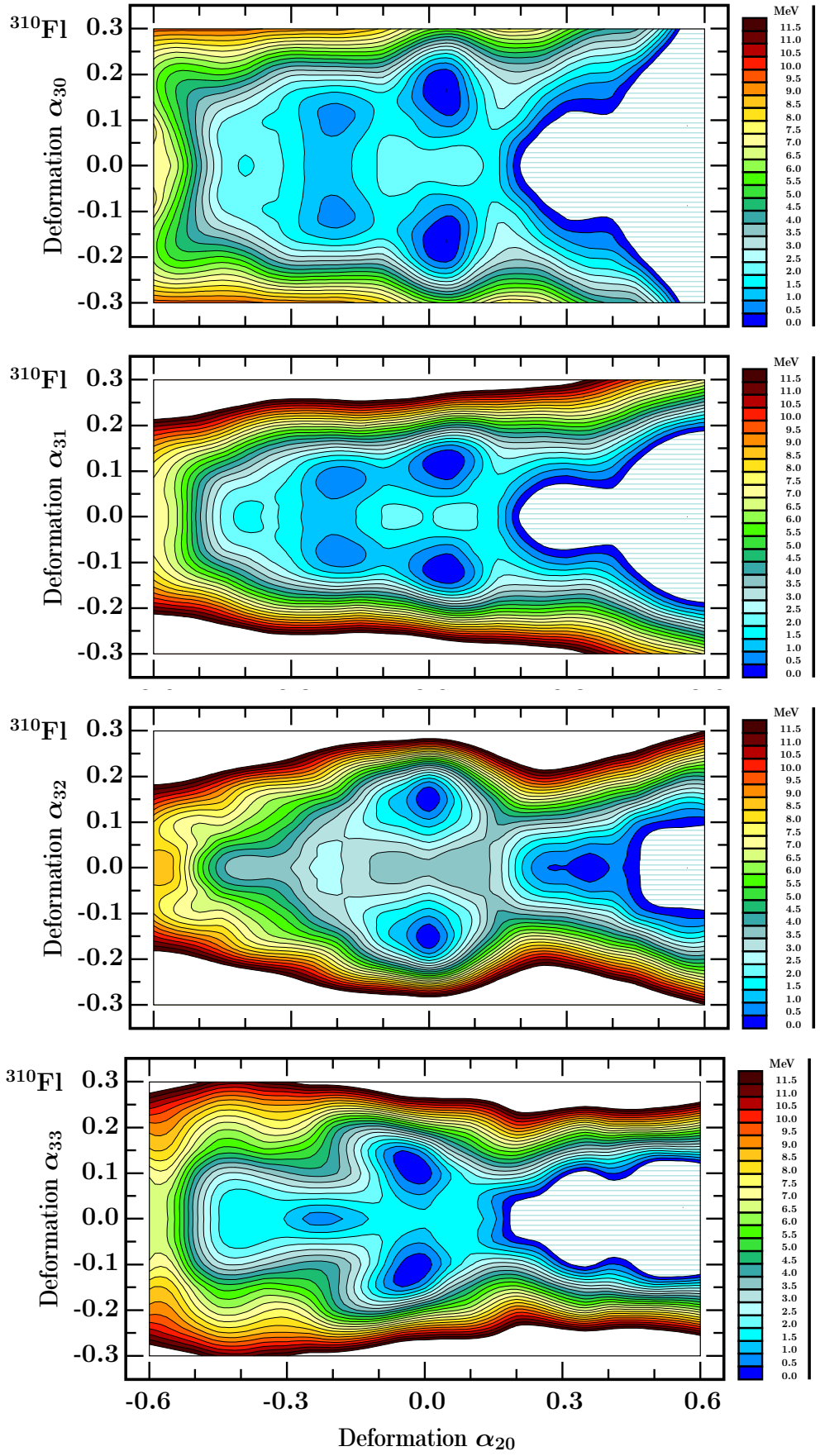

Figure 6.8.4 – *Projections of the total energy on* $(\alpha_{20}, \alpha_{3\mu=0,1,2,3})$ *planes, minimised at each deformation point over axial hexadecapole deformation* α_{40} *for the* $^{310}_{114}Fl_{196}$ *nucleus.*

6.8.2 Oblate-octupole(α_{33}) Symmetry in Super-heavy Nuclei

The presence of super-deformed oblate ground-state in many super-heavy nuclei with $108 < Z < 128$ has been studied in systematic macroscopic-microscopic calculation ref. [113] and confirmed by the Hartree-Fock calculation by Jachimowicz ref. [114]. One year later the calculations of the ground state energies of the super-heavy nuclei were extended to the area of $Z = 120 - 124$ and $N = 160 - 168$ using the Hartree-Fock-Bogolyubov approach; they confirmed the predictions of the super-oblate states of ref. [115]. In particular, the macroscopic-microscopic approach of refs. [111, 112, 116] showed that the ground states of the nuclei with $Z = 119 - 126$ and $N = 173 - 188$ combined the oblate quadrupole deformation with the octupole component α_{33}. It is worth mentioning that the oblate quadrupole deformation combined with α_{33} shown in the above articles was induced by the combination of the oblate minimum combined with two octupole deformations α_{30} and α_{32} in proportion $\alpha_{32}/\alpha_{30} \approx \sqrt{3/5}$, which is equivalent to α_{33} deformation.

In contrast to the method mentioned above, in our actual project, we employ the multi-dimensional mesh calculations including quadrupole α_{20} deformation, all four octupole deformations $\{\alpha_{30}, \alpha_{31}, \alpha_{32}, \alpha_{33}\}$, and the hexadecapole deformation α_{40}, which is considered for the minimisation. One of the advantages is that the equilibrium deformation can be read directly from the potential energy surfaces, which are projected on the $\{\alpha_{20}, \alpha_{3\mu}\}$ planes.

In figs. (6.8.1-6.8.2) we have shown variations of the proton and neutron single-particle energy spectra with respect to the pure octupole deformations $\alpha_{3\mu}$ with all other deformations set to zero. To study the impact of the oblate vs. octupole α_{33} combination, in fig. (6.8.5) we compare of the proton single-particle energy spectra in terms of the pure octupole-α_{33} deformation with the ones obtained by combining oblate quadrupole deformation $\alpha_{20} = -0.15$ with variable α_{33}. This particular value of the oblate deformation is obtained from our systematic calculations. It shows that the new shell gaps at $Z = 112, 116, 118, 120$ are opening when the oblate quadrupole deformation is considered.

A similar comparison for neutrons is illustrated in fig. (6.8.6) and it follows that the new gaps at $N = 174, 176, 182, 184$ are opening. As presented in the preceding section, the neutron number $N = 184$ is predicted as the spherical magic number, whereas it losses its stability by introducing an oblate quadrupole deformation; here it enters a new competition.

The nucleus ^{118}Og is the heaviest element known experimentally today. Basing on the shell effects just discussed, in fig. (6.8.7) we compare to potential energy surfaces for Og nuclei: $^{290}\mathrm{Og}_{172}$, $^{294}\mathrm{Og}_{176}$, $^{298}\mathrm{Og}_{180}$, and $^{302}\mathrm{Og}_{184}$ to illustrate the evolution of

the combination of the quadrupole-oblate and α_{33} deformations. It follows that the equilibrium deformations with $\alpha_{33} \approx 0.1$ are accompanied by the oblate deformation $\alpha_{20} = -0.15$. The effect of α_{33} increases with increasing neutron numbers leading to up to about 2.5 MeV separations between the double minima.

It is instructive to verify the impact of the other octupole components in the nucleus ${}^{302}_{118}\mathrm{Og}_{184}$ showing strongly developed α_{33} minima. The results in fig. (6.8.8) show that the oblate minima at $\alpha_{20} = -0.15$ remain with no octupole-α_{30}, -α_{31} and -α_{32} effects. The effect of the octupole-α_{33} deformation lowers the energy of the oblate minimum at $\alpha_{20} \approx -0.15$ by about 1-to-1.5 MeV.

In fig. (6.8.9) we present the evolution of the oblate-octupole minimum in $N = 184$ isotones with proton numbers $Z = 114, 118, 122, 126$. We can conclude from the figure that the pronounced oblate-octupole type minima are produced in the super-heavy nuclei with proton number $Z \geq 118$ and neutron numbers around $N = 184$.

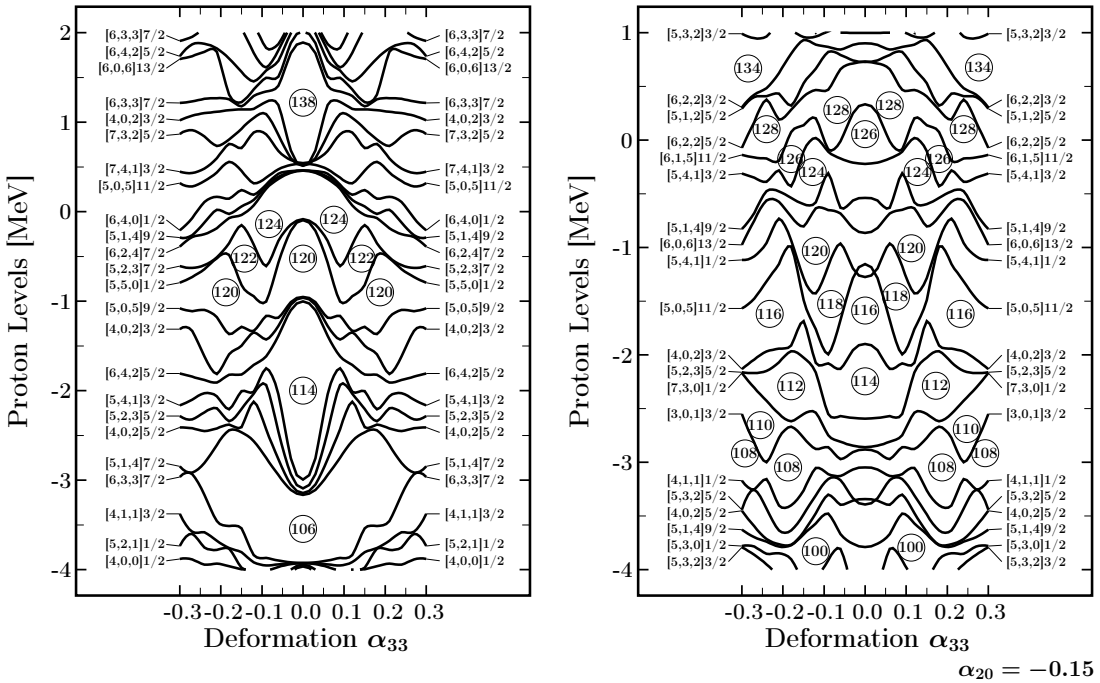

Figure 6.8.5 – *Comapring the proton single-particle enrgies as function of octupole-α_{33} at quadrupole deformation $\alpha_{20} = 0$ (left) with the ones at $\alpha_{20} = -0.15$ (right).*

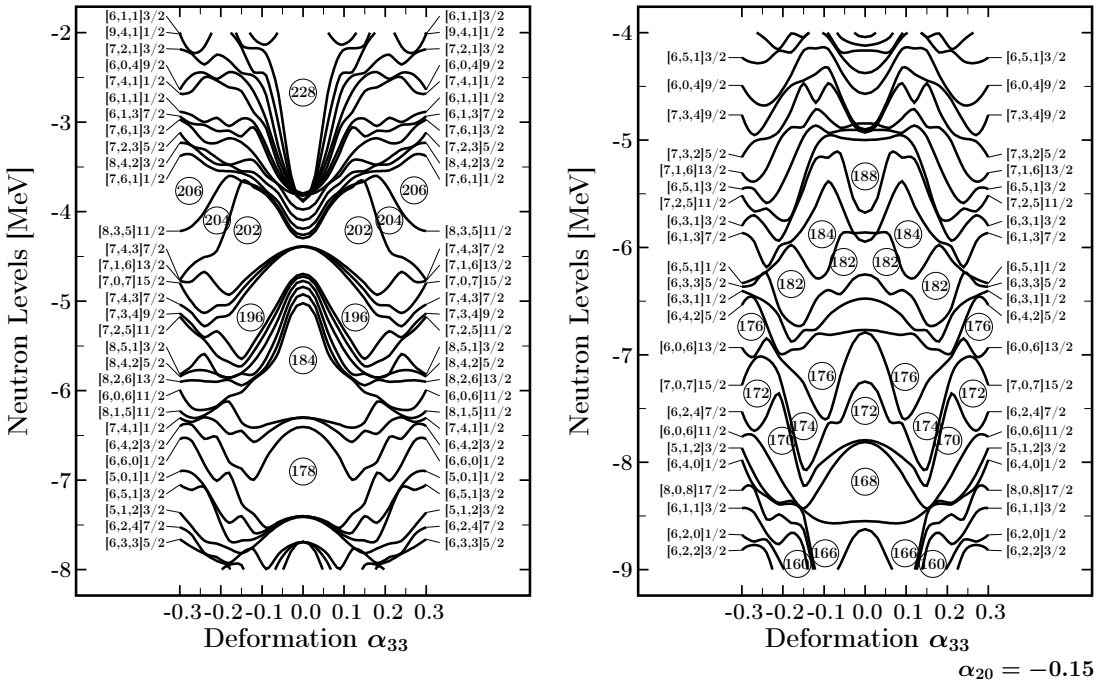

Figure 6.8.6 – *Similar to fig. (6.8.5) but for neutrons.*

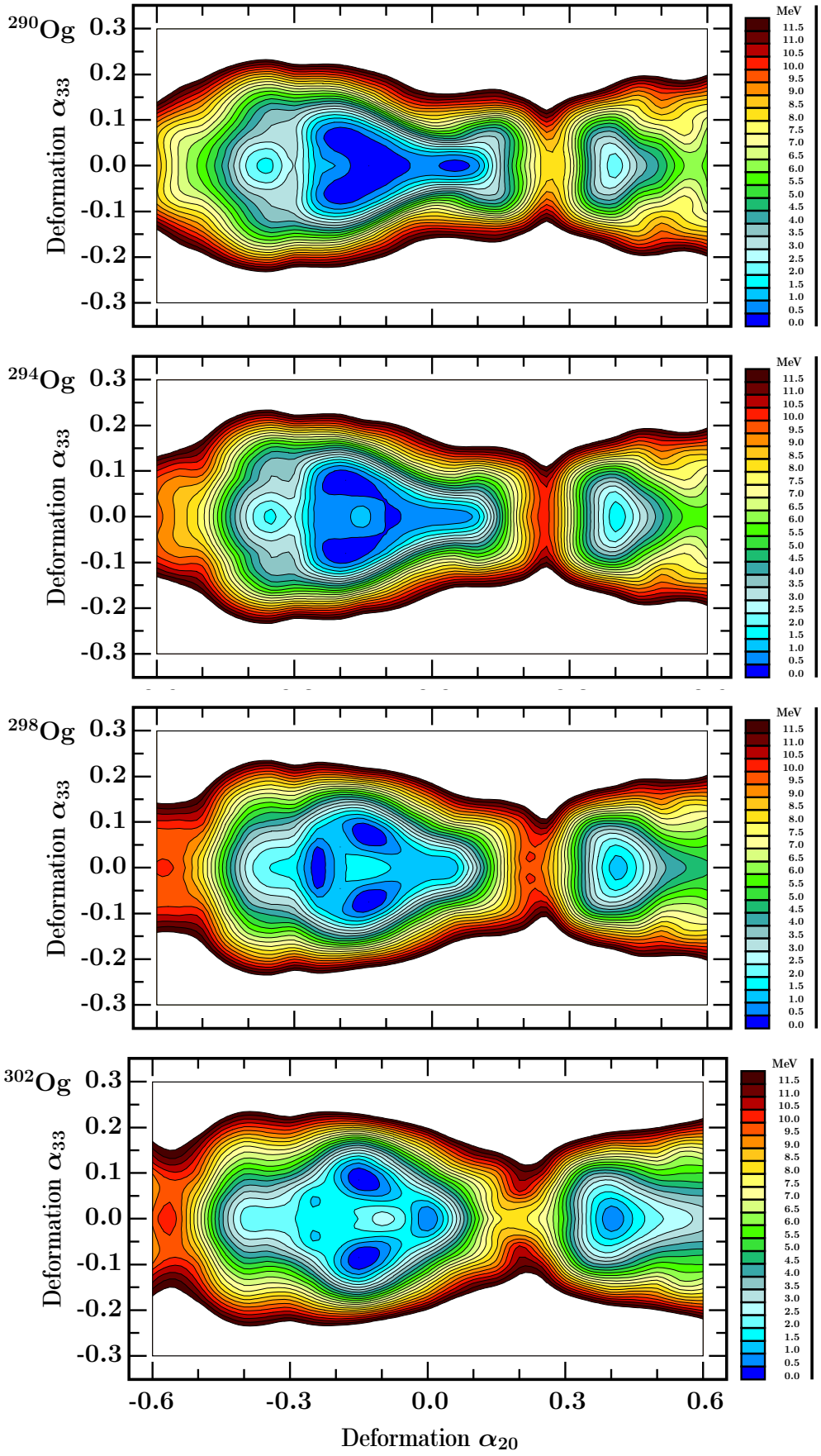

Figure 6.8.7 – *Projections of the total energy on $(\alpha_{20}, \alpha_{33})$ plane and minimised at each deformation point over axial hexadecapole deformation α_{40} for $^{290-302}Og$ $(Z = 118)$ isotopes with neutron numbers $N = 172, 176, 180, 184$.*

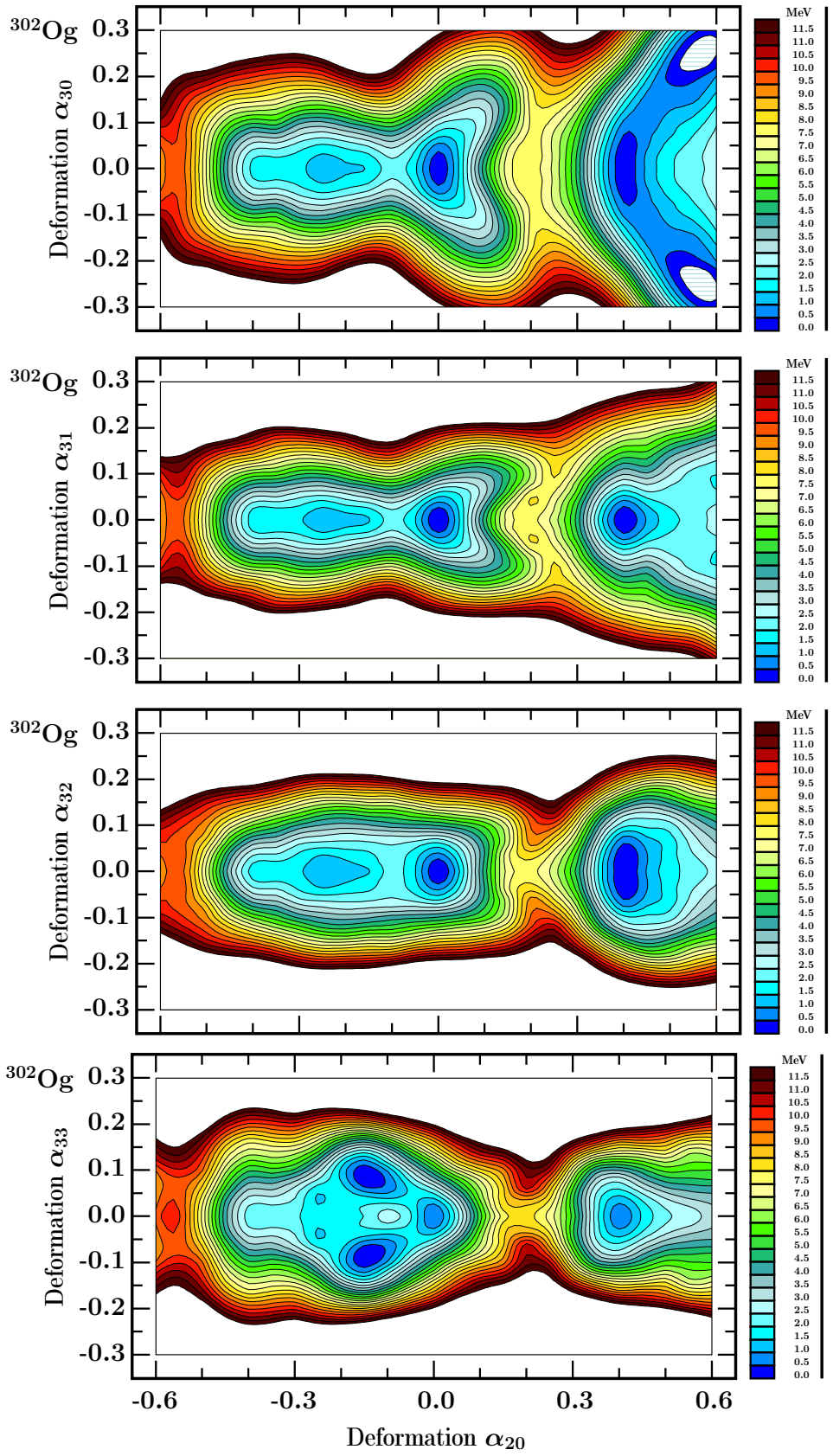

Figure 6.8.8 – *Projections of the total energy on* $(\alpha_{20}, \alpha_{3\mu=0,1,2,3})$ *plane and minimised at each deformation point over axial hexadecapole deformation* α_{40} *for the* $^{302}_{118}Og_{184}$ *nucleus.*

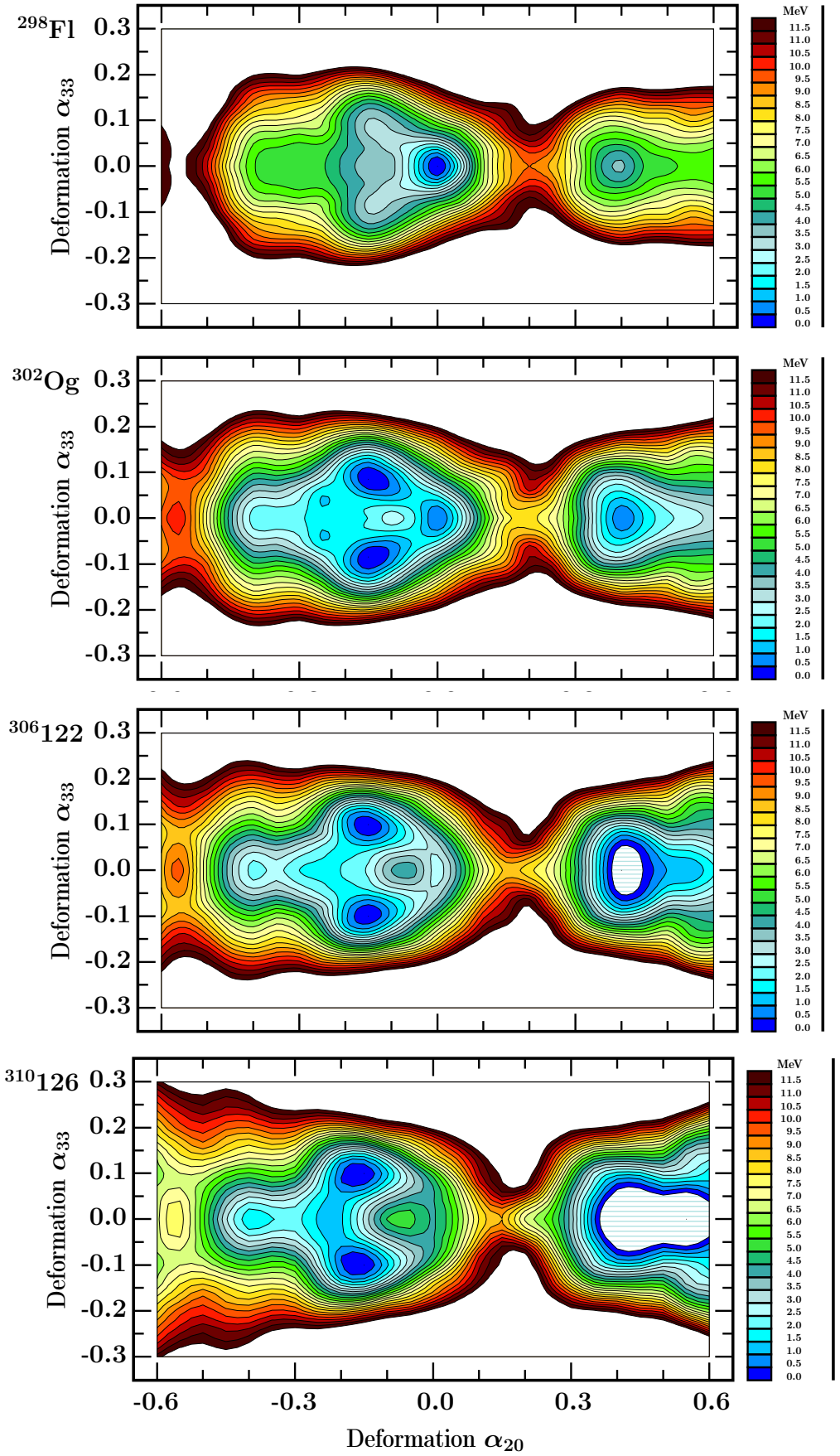

Figure 6.8.9 – *Projections of the total energy on* $(\alpha_{20}, \alpha_{33})$ *plane and minimised at each deformation point over axial hexadecapole deformation* α_{40} *for the* $N = 184$ *isotones with proton numbers* $Z = 114, 118, 122, 126$.

6.8.3 Results on Super-heavy Nuclei: Concluding Remarks

As an extensive study of exotic symmetries, we presented the multi-dimensional mesh calculations including all four octupole deformations in super-heavy nuclei with $112 \leq Z \leq 130$ and $166 \leq N \leq 206$.

One of the most visible conclusions is that the adjusted new parametrisation applied in our calculations gives reliable results, e.g., the prediction of the spherical magic numbers at $Z = 114$ and $N = 184$ and the properties of the ground-states, which can be comparable with our theoretical models, although the shell effects in super-heavy nuclei are strongly model dependent. The quadrupole deformations at the ground-states are summarised in fig. (6.8.10), which reveals that the majority of super-heavy nuclei have oblate deformations.

Exotic symmetries, in particular, the octupole components α_{32} and α_{33} are important in stabilising the ground-state configurations, as seen in fig. (6.8.11). The highest fission barriers are found for tetrahedral deformation ($\alpha_{32} \approx \pm 0.15$) in super-heavy nuclei around $N = 196$, which is predicted as the tetrahedral magic number next to $N = 136$. Figure (6.8.11) (bottom) shows the impact of the octupole-α_{33} the latter leading to a new exotic oblate-quadrupole vs. octupole (α_{33}) shapes, with energies lower than in the case of the pure oblate configurations by about 1.0-1.5 MeV – in the super-heavy nuclei around $118 \leq Z \leq 130$ and $170 \leq N \leq 186$.

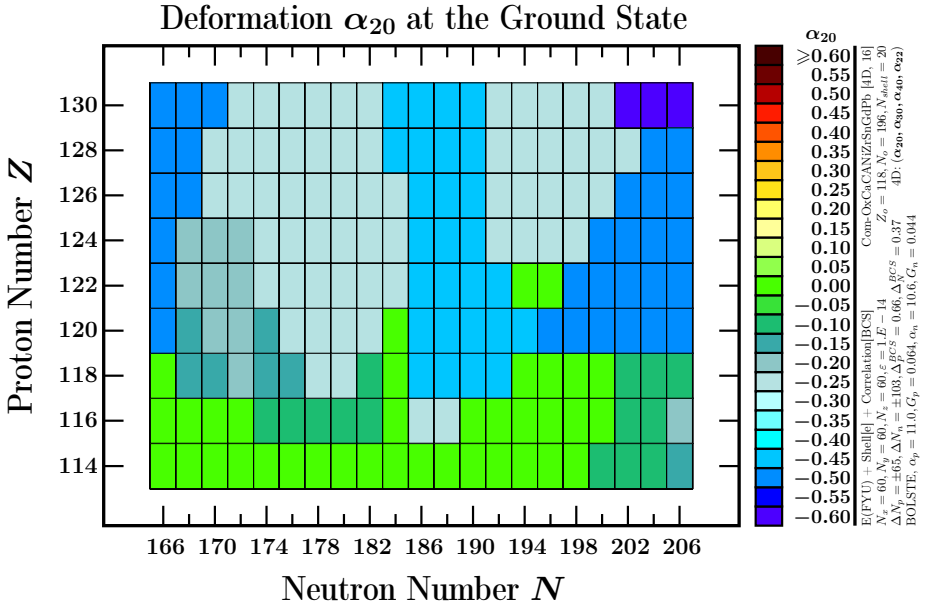

Figure 6.8.10 – *Ground-state deformation α_{20} calculated from 3D mesh projected on the $(\alpha_{20}, \alpha_{30})$ plane and minimised over α_{40} deformation.*

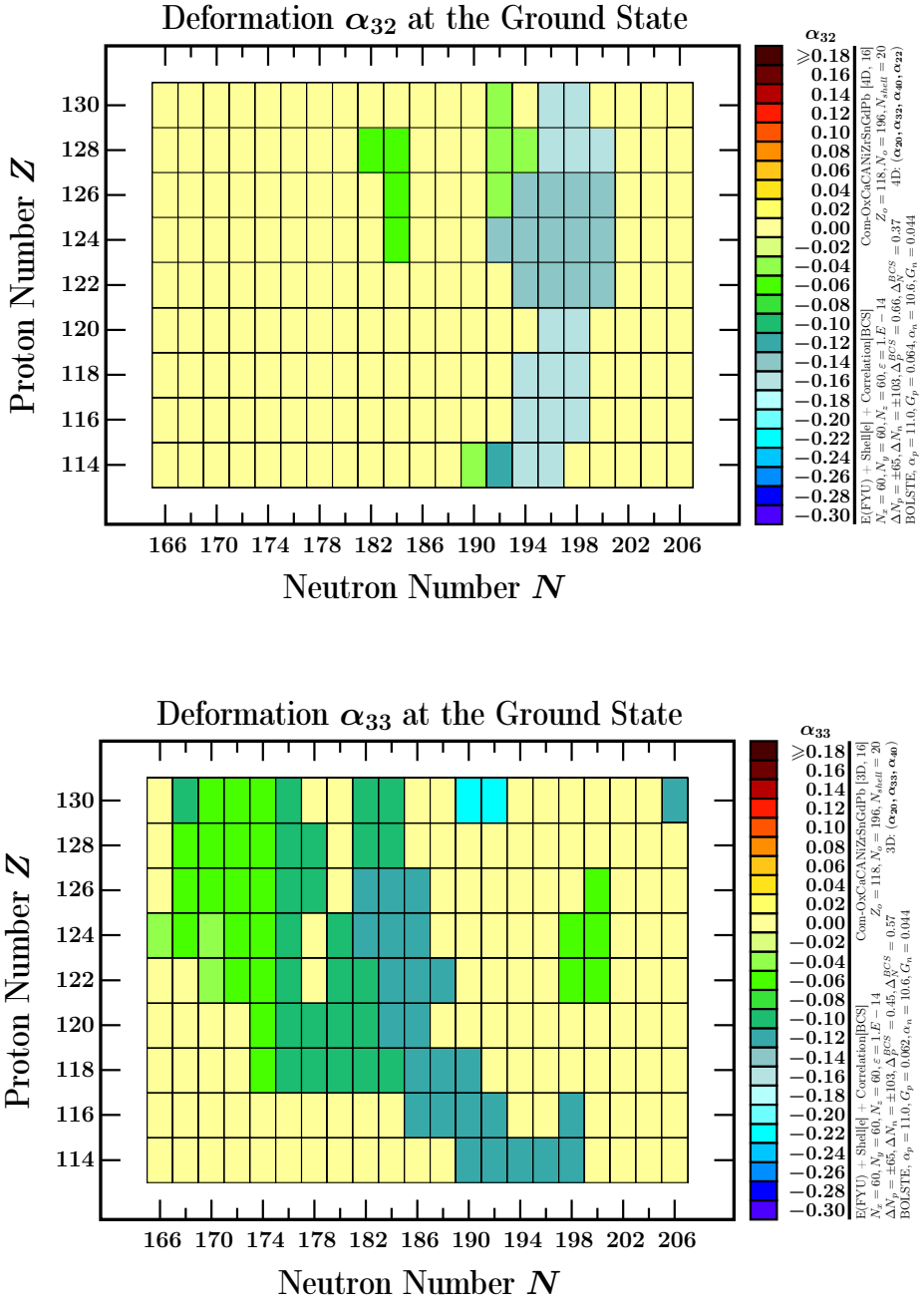

Figure 6.8.11 – *Ground-state deformation α_{32} (top) and α_{33} (bottom) calculated from 3D mesh projected on the $(\alpha_{20}, \alpha_{30})$ plane and minimised over α_{40} deformation. Note that the signs of the octupole deformations are irrelevant due to the elementary symmetry properties.*

Chapter 7

Conclusions and Perspectives

In order too be able to describe nuclear symmetry properties using the realistic methods of theoretical modelling we combined four among the most powerful tools of the nuclear structure theory: The nuclear mean-field-theory, the group and group representation theories and the inverse problem theory.

The present PhD research project has been realised following Memorandum of Understanding between the Maria Curie Skłodowska University of Lublin, Poland, and the University of Zhengzhou, China, with one of the important goals being the training of young researchers in our domain of physics. To this end, efforts were undertaken to present in this thesis document several elements of description of the nuclear structure theory methods to facilitate entering into our research field to the new-coming PhD students or post-doctoral fellows who will choose working in our domain.

During the last year of the preparation of this thesis, the financing of a new nuclear physics related European Project Theo4Exp *via* EuroLabs *initiative has been announced. This project consists in the preparation of the specialised internet based service allowing to the nuclear experimentalists working in the European accelerator related laboratories to use especially adapted nuclear theory computer programs and theory data bases, in particular related to the nuclear mean field theory. The latter part of the project, referred to as* MeanField4Exp *will be realised in collaboration between the nuclear physics laboratories in Cracow, Strasbourg and Warsaw. Computer programs which will be installed within this European project will contain, among others, the ones employed for the present PhD project. The person in charge of the realisation of the* MeanField4Exp *project will be the supervisor of the present thesis.*

In this PhD project we have studied systematically exotic shape symmetries and implied shape isomers, as well as shape evolution and competition in heavy nuclei. We used realistic mean-field theory and its phenomenological Woods-Saxon Hamiltonian. Parameters of the Hamiltonian were adjusted eliminating the parametric correlations with the help of the Monte-Carlo simulations. Point group and group representation theories were used to examine the underlying mathematical features. In particular, rotational properties of nuclei with exotic symmetries and the implied spectral properties were derived to construct the experimental symmetry identification criteria. We focussed our analysis on nuclear realisations of symmetries: T_d, O_h, C_{2v}, D_{2d} and D_{3h}.

Concerning the phenomenological realisation of the Woods-Saxon Hamiltonian, in the past, a parametrisation involving 12 parameters, 6 for protons and 6 for neutrons was used. These Woods-Saxon parameters were reviewed by our group in recent years and with the help of the Monte-Carlo approach the parametric correlations were detected and eliminated. The new parameters were fitted to single particle levels of eight doubly magic spherical nuclei. We have shown that among 12 parameters only 8 are independent; they were used for the systematic calculations within this project. Predictive power of our model with the new parametrisation was analysed and it was shown that our modelling provides a very good agreement with experimental results, among others, on the nuclear equilibrium deformations.

We have used spherical harmonic expansion to describe nuclear surfaces and shapes. Our deformation space involved deformation parameters $\alpha_{\lambda\mu}$ of the following orders: $\lambda = 2$ (quadrupole), $\lambda = 3$ (octupole), $\lambda = 4$ (hexadecapole) and selected orders $\lambda > 4$. The lowest order multipolarities, $\{\alpha_{20}, \alpha_{22}\}$, are found most often in the literature. The latter leads to the simplest, ellipsoidal symmetries. We have focussed on the exotic symmetries just listed involving various combinations of $\{\alpha_{30}, \alpha_{31}, \alpha_{32}, \alpha_{33}\}$ octupole degrees of freedom together with specific combinations involving higher multipolarities.

To set up the numerical calculations for the present project and to save c.p.u. time, we split the mass table into the so called (Z, N)-sectors. Each sector is defined by a central nucleus, say (Z_0, N_0), together with the ΔZ and ΔN intervals: The nuclei belonging to the sector are those with proton numbers $Z \in [Z_0 - \Delta Z, Z_0 + \Delta Z]$ and with the neutron numbers $N \in [N_0 - \Delta N, N_0 + \Delta N]$. The calculations of the single nucleon energies are performed by solving the mean-field Schrödinger equation for the central nucleus only. These were used to calculate the total nuclear energies of all the nuclei in the sector employing the well known macroscopic-microscopic method of Strutinsky. Such an approximation was found very practical thanks to the fact that the dependence of the single particle energies on the Z and N numbers is very regular; we have used the selection $\Delta Z \sim 8$ and $\Delta N \sim 10$.

The calculations for the selected deformation spaces were run on the multiprocessor

systems involving, in our case, typically several hundreds of processors. We have introduced various deformation sub-sets forming 2D-, 3D-, and 4D-deformation meshes. In order to analyse and illustrate the results for 3D and 4D deformation spaces, projections on 2D sub-spaces were introduced and the minimisation of the nuclear potential energies over the extra deformation parameters were performed. Such a structure leads, e.g., for a 4D mesh to 6 distinct 2D projections. The corresponding total energy maps for all even-even nuclei in each of the (Z, N)-sectors and possible projections have been performed and stored. In this way we have constructed a data base facilitating the nuclear geometry analysis in a direct and relatively fast manner.

About Results Selected for Presentation and Selection Criteria

In this PhD document we have presented merely a small fragment of the full information accumulated as the result of our massive calculations. Below we give certain indications about our choice criteria.

- As indicated in the preceding text, we have performed systematic analysis of the nuclear shapes and the corresponding symmetry properties by calculating the potential energy surfaces for several hundreds of even-even nuclei in multidimensional deformation spaces defined using the multipole expansion concept.

- A typical scenario of this type of analysis of the nuclear shape properties found in the literature follows the scheme of an *expansion series*: the lower the expansion multipole (here: quadrupole, octupole, hexadecapole ...) the strongest its presumed importance. It then follows that the first rank symmetry under consideration is the ellipsoidal ('tri-axial') symmetry spanned by $(\alpha_{20}, \alpha_{22})$ shape coordinates.

- Our systematic calculations have shown that important exceptions from such series expansion rules exist in certain zones of the mass table. This happens in particular in the whole region of nuclei in the 'north-east zone of mass table' treating ^{208}Pb as a reference center. Indeed, for $Z \geq 82$ nuclei, an increase in the neutron number leads to a built up of the deformed equilibrium shapes with the lowest multipolarity $\lambda = 3$, i.e., octupole rather than quadrupole shapes and this, often for all the 4 octupole $\alpha_{\lambda=3,\mu=0,1,2,3}$ degrees of freedom.

- It then follows that all the implied shapes break the inversion invariance in the intrinsic reference frames. They correspond to non-ellipsoidal symmetries which in this document are referred to as exotic point-group symmetries – 4 distinct ones. For this reason we have selected this particular zone of the nuclear mass table for a detailed presentation as offering potentially the most promising, new research perspectives.

- These octupole shape effects causing strong shell-gaps are induced by the presence of the 'four-fold' or 'universal' neutron octupole magic number $N = 136$ related to the repulsion between the neutron $2g_{9/2}$ and $1j_{15/2}$ orbitals with the $\Delta\ell = 3$ angular momentum difference, influencing the matrix elements with the potential depending on the $Y_{\lambda=3,\mu}$ multipoles.

- With the help of the point group theory we have shown that the point group symmetries corresponding to pure octupole shapes are

  – C_∞ for $(\alpha_{20} = 0, \alpha_{30} \neq 0)$,
  – C_{2v} for $(\alpha_{20} = 0, \alpha_{31} \neq 0)$,
  – T_d for $(\alpha_{20} = 0, \alpha_{32} \neq 0)$, and,
  – D_{3h} for $(\alpha_{20} = 0, \alpha_{32} \neq 0)$,

  whereas a combination of the non-null quadrupole axial-symmetry deformation with the above octupole ones – repeats 3 among 4 above symmetries except for

  – D_{2d} for $(\alpha_{20} \neq 0, \alpha_{32} \neq 0)$.

- Experimental identification criteria of the exotic symmetries listed above have been formulated using the point-group representation theory and were discussed in detail.

Analysing 4D Nuclear Geometry via 2D Projections: Shortcomings

In this thesis we have performed, as a part of the project, the analysis of the nuclear geometrical properties calculated principally within 4D-type meshes via 2D projections and the 'geographical like ' map illustrations.

Let us consider the functioning of this type of algorithm in more detail. Suppose that the potential energy is calculated in a space of variables (x, y, z, w) and construction of a 2D map with coordinates, say (y, w) corresponds to a minimisation over x and z at each (y, w)-point. This is equivalent to looking for the absolute minimum of the (x, z) surface which changes each time we pass from (y, w)-point to its neighbour, (y', w'). There is no reason for which the evolution of the positions of such absolute minima should develop smoothly (continually) with (y, w) varying, with the result that the (y, w)-map may look smooth but in general will contain unphysical shape-jumps (discontinuities) which will bias the physical interpretation of the results.

- To avoid this type of artificial 'jumps' when analysing the shape evolution, some alternative algorithms should be proposed; such algorithms should consider all the (x, y, z, w)-points with all the coordinates treated at the same time at the same footing.

- In the past, some algorithms of this type were proposed in the literature – based on the one-dimensional trajectories considered in the n-dimensional spaces – the trajectories connecting some potential energy minima of interest for the physicist.
- Such trajectories were sought by minimising the one-dimensional trajectory potential barrier transition probabilities using a one-dimensional Wentzel-Kramers-Brillouin (WKB) quasi-classical approximation.
- To find such trajectories via minimisation of the WKB barrier penetration expressions we have applied the so-called Dijkstra algorithm very well known in the Graph Theory, an important chapter in *Applied Mathematics*. With the help of this technique we were able to obtain an interpretation of the multi-dimensional potential energy calculation results free from the 2D minimisation artefacts which were illustrated in the thesis document.

Static vs. Dynamic Equilibrium Deformations

As it is well known from the collective model of Bohr, the collective motion of the nucleus in a deformation space is described with the help of the corresponding collective Schrödinger equation, whose solutions – wave-functions depending on the deformation parameters – define the shape probability density distributions. Such wave functions can then be used to estimate, e.g., the most probable nuclear deformations, which in general differ significantly from the static ones corresponding to the local potential energy minima.

- We have calculated the dynamical equilibrium deformations and estimated the differences between the static and dynamic ones by solving collective Schrödinger equation in the one-dimensional sections of the potential surfaces.
- At the same time we have studied the collective nuclear energies within zero-phonon and one-phonon approximations. Calculations show that such energies are nearly degenerate, when the potential barriers separating the two octupole minima are higher than the energies in question. It turns out that the implied dynamical equilibrium deformations are comparable.
- Importantly, in the case of flat potential energies, i.e., when the static equilibrium deformations lose their meaning, the dynamical calculations predict significant most probable (dynamical) equilibrium deformations, and thus strengthen our interest in exotic symmetries.

Coexistence Between Octupole Shape Geometrical Symmetries

It follows from our realistic mean-field calculations that the octupole super-magic number $N = 136$ generates strong shell gaps simultaneously in all the 4 $\alpha_{3\mu}$-octupole space directions. As the result, we can expect competing octupole shape coexisting minima and consequently a possible simultaneous manifestation of several exotic symmetries in a single nucleus at the same time.

- Calculations show systematic differences in the 'strength of the octupole effects' measured by the depth of the minima and the heights of the separating barriers. By far the strongest appear the shell effects generated by the tetrahedral symmetry variable α_{32}; next to it appear the pear-shape effects generated by α_{30}, followed by the effects of α_{31} and α_{33}.
- It turns out that in $Z \geq 82$ nuclei, pure octupole effects, $\alpha_{20} = 0$, appear when increasing N as soon as the spherical symmetry is gone; further increase in neutron number leads to combined effects of $\alpha_{20} \neq 0$ simultaneously with $\alpha_{3\mu} \neq 0$.

Effects of Higher Order Deformations: $\lambda \geq 4$

In order to verify the stability of theoretical predictions of the nuclear symmetry properties and their possible dependence on the cut-off choice in terms of λ, we have performed comparative calculations with deformations of increasing multipolarities.

- We have included various combinations of multipole deformations often studied in the literature by other authors, such as α_{40} which was kept most of the time as one of our standard minimisation variables and then the combinations $\{\alpha_{40}, \alpha_{42}\}$, $\{\alpha_{40}, \alpha_{60}\}$ and $\{\alpha_{40}, \alpha_{80}\}$.
- The impact of α_{60} on the ground-state minima is the strongest among other higher order multipolarities in the nuclei in the ranges of $Z \approx 98 - 110$ and $N \approx 144 - 160$. The ground-state energy minima obtained including α_{60} were typically lowered by about 1-2 MeV.

Exotic symmetries in Super-heavy Nuclei

As an illustration of or study of exotic symmetries, we presented the multi-dimensional mesh calculations in super-heavy nuclei with $112 \leq Z \leq 130$ and $166 \leq N \leq 206$.

- The predictive power of our model with the new parametrisation is confirmed in super-heavy nuclei by reproducing the spherical shell closures at $Z = 114$ and $N = 184$ and the comparable results of the properties of the ground-state.

- In the super-heavy nuclei region, the highest fission barriers are found for the tetrahedral deformation ($\alpha_{32} \approx \pm 0.15$) around $N = 196$, which is predicted as the tetrahedral magic number.

- A new exotic symmetry is deduced by combining the oblate-quadrupole deformation with octupole deformation α_{33}. The oblate energy minima obtained including octupole deformation α_{33} are lowered by 1.0-1.5 MeV in the super-heavy nuclei around $118 \leq Z \leq 130$ and $170 \leq N \leq 186$.

Perspectives and Challenges

In our project we have focussed on the effects of all the 4 octupole deformations which turn out to play a very important role in the heavy nuclei with $Z \geq 82$. We confirmed the effects of the tetrahedral symmetry with the strongest effects centred at the doubly magic ${}^{226}_{90}\mathrm{Th}_{136}$ nucleus.

To our knowledge our research is the first suggesting systematic experimental identification criteria of the point group symmetries other that T_d, the latter identified by our group in 2018. Consequently, proceeding with such an identification via systematic investigation of the existing experimental data seems to be the most urgent challenge.

Extending the study of the simultaneous 4-fold octupole effects to medium heavy and lighter nuclei, is another natural challenge.

In recent years the pear-shape octupole effects have been studied by other authors in super-heavy nuclei, cf. e.g. refs. [62, 107, 108] and the strong pear-shape octupole effects were predicted around $N \approx 196$. In the present project, we also extended the calculations to cover the zone of super-heavy nuclei up to $Z_{max} = 130$ and $N_{max} = 206$. Compared to the 4-fold octupole effects around the lead region, similar effects with vanishing quadrupole deformation were found around $Z \approx 110$ and $N \approx 190$.

One of the most interesting observations is that the octuple component $\alpha_{33} \approx 0.2$, accompanied by strong oblate deformation $\alpha_{20} \approx -0.9$ plays an important role in the super-heavy nuclei with $Z > 120$.

Part III

Annex

Chapter 8

ANNEX: Macroscopic-Microscopic Method

An approximate, phenomenological method of calculating total nuclear energies known under the name of the Strutinsky method, or macroscopic-microscopic method, has been introduced by V. Strutinsky, ref. [85]. It is based on the observation that combining certain properties of the nucleon-level densities calculated with the help of the nuclear mean-field approximation (as discussed below) and the classical, macroscopic liquid drop model expression for the nuclear energy offers unprecedented precision in the description of several nuclear structure properties. In particular, nuclear masses, nuclear shape properties such as shape coexistence and competition, fission properties, and many others can be described very successfully and one can find literally thousands of articles employing this method, published by various authors.

The macroscopic-microscopic method has been used in the literature in its various realisations and can be considered a very well established element in nuclear structure physics. In this Annex, we limit ourselves to recalling its principal elements and definitions in the actual realisations used in this project.

8.1 Basic Ideas and Nuclear Energy Expressions

The underlying idea of the macroscopic-microscopic method consists in assuming that the total energy of the nucleus can be expressed as the sum of contributions calculated using classical, macroscopic liquid drop energy expression, below denoted $E_{\rm macro}$, and a contribution usually denoted $E_{\rm micro}$, involving mean-field single-nucleon energies:

$$E_{\rm total.} = E_{\rm macro} + E_{\rm micro}. \tag{8.1.1}$$

Both terms depend on nuclear deformation parameters and on the proton and neutron numbers. The microscopic energy is composed of two contributions called shell and pairing corrections,

$$E_{\text{micro}} = \delta E_{\text{shell}} + \delta E_{\text{pairing}}, \tag{8.1.2}$$

representing the quantum shell effects on top of the deformed liquid drop macroscopic energy leading term.

8.1.1 Macroscopic Energy – Spherical Configuration Variant

The liquid drop model has been constructed to calculate approximately the nuclear energy as a function of deformation and can be used for modelling in particular nuclear binding energies and fission barrier properties in analogy to the drop of a charged liquid. The concept is based on similarities of certain properties of nuclear matter and those of the classical charged and incompressible liquid drop. The corresponding semi-empirical formula used for spherical nuclei reads, cf. ref. [117]:

$$E_{\text{Macro}}(A,Z) = a_{\text{v}}A - a_{\text{sur}}A^{\frac{2}{3}} - a_{\text{C}}\frac{Z^2}{A^{\frac{1}{3}}} - a_{\text{asym}}\frac{(N-Z)^2}{A} + \delta(Z,N), \tag{8.1.3}$$

where Z, N, and A represent the proton, neutron and mass numbers, respectively. The meaning of the introduced symbols is as follows:

1. The volume term, $a_{\text{v}}A$, represents the bulk of the nuclear binding energy produced by A nucleons;
2. The surface term, $a_{\text{sur}}A^{\frac{2}{3}}$, represents an attractive contribution from the surface-tension of the drop;
3. The Coulomb energy term, $a_{\text{C}}\frac{Z^2}{A^{1/3}}$, represents the repulsive electrostatic forces between protons. It increases fast with the number of protons;
4. The so-called asymmetry term, $a_{\text{asym}}\frac{(N-Z)^2}{A}$, describes the variation of stability of the nuclear system with proton-neutron asymmetry, $N-Z$;
5. The phenomenological pairing term, $\delta(Z,N)$, represents the corrections due to the nuclear pairing gaps, for details see below.

It turns out that the selected, systematic features of the nuclear average binding energy can be described successfully according to eq. (8.1.3), with the help of just a few parameters. Notice that the volume and surface terms depend on the nuclear mass number $N+Z$ only, whereas the remaining terms depend on Z and N more explicitly.

In our approach the macroscopic energy is calculated following the prescription referred to as the finite-range liquid drop model (FRLDM), also called Yukawa folded realisation, ref. [109], introducing the deformation of the liquid drop as discussed next.

8.1.2 Nuclear Yukawa Folded Macroscopic Energy Term

Modifications of the historical, spherical-shape formulation of the liquid drop energy expression were introduced by Krappe et al., ref. [118]. The corresponding formulation is very well known in nuclear structure physics and description of any details thereof would bypass the scope of the present project. We limit ourselves to citing the final expression after ref. [109], together with the terminology used in the literature:

$$
\begin{aligned}
E^{\mathrm{FY}}_{\mathrm{Macro}}(Z,N;\alpha) = {} & M_{\mathrm{H}}Z + M_{\mathrm{n}}N && \text{mass excesses}\\
& - a_{\mathrm{vol}}(1-\kappa_{\mathrm{vol}}I^2)A && \text{volume energy}\\
& + a_{\mathrm{surf}}(1-\kappa_{\mathrm{surf}}I^2)B_{\mathrm{surf}}(\alpha) && \text{surface energy}\\
& + \frac{3}{5}\frac{e^2Z^2}{r_0A^{\frac{1}{3}}}B_{\mathrm{Coul}}(\alpha) && \text{Coulomb energy}\\
& - \frac{3}{5}\frac{e^2}{r_0}\left[\frac{5}{4}\left(\frac{3}{2\pi}\right)^{3/2}\frac{Z^{4/3}}{A^{1/3}}\right] && \text{Coulomb exchange correction}\\
& + \frac{Z^2}{A}f(k_Fr_p) && \text{proton form-factor correction}\\
& && \text{to the Coulomb energy}\\
& - a_{\mathrm{asym}}(N-Z) && \text{charge-asymmetry correction}\\
& + W(|I|+d) && \text{Wigner energy}\\
& + a_0A^0 && A^0 \text{ term}\\
& - 1.433\times10^{-5}Z^{2.39} && \text{energy of bound electrons}\\
& + \delta(Z,N) && \text{pairing energy,}
\end{aligned}
\tag{8.1.4}
$$

where the mass number $A = Z + N$ and the relative neutron excess $I = (N - Z)/A$, whereas $\alpha \equiv \{\alpha_{\lambda\mu}\}$ denotes the ensemble of the deformation parameters.

Deformation-Dependent Terms – Surface Energy. In deformed nuclei, increasing deformation usually increases the nuclear surface and the impact of the corresponding energy contribution $B_{\mathrm{surf}}(\alpha)$. The corresponding 6-fold integral expression reads after ref. [118],

$$
B_{\mathrm{surf}}(\alpha) = -\frac{1}{8\pi^2r_0^2a^4}\int_V d\vec{r}\int_{V'}d\vec{r}\,'\left(\frac{|\vec{r}-\vec{r}\,'|}{a}-2\right)\frac{e^{-|\vec{r}-\vec{r}\,'|/a}}{|\vec{r}-\vec{r}\,'|}, \tag{8.1.5}
$$

in which a is the diffuseness range of the Yukawa term and exponential $e^{-|\vec{r}-\vec{r}\,'|/a}$ models the effect of the finite range of the nuclear interaction. With the help of the twofold

application of the Gauss divergence theorem one can transform the above expression into a simplified double surface integral,

$$B_{\rm surf} = \frac{1}{8\pi^2 r_0^2 a^4} \int_\Sigma \int_{\Sigma'} \left\{ 2 - \left[\left(\frac{\sigma}{a}\right)^2 + \frac{2\sigma}{a} + 2 \right] e^{-\sigma/a} \right\} \frac{(\vec{\sigma}\cdot d\vec{S})(\vec{\sigma}\cdot d\vec{S}')}{\sigma^4}, \quad (8.1.6)$$

where $\sigma = |\vec{r} - \vec{r}'|$, $\vec{\sigma} = \vec{r} - \vec{r}'$. The above expression allows to calculate the surface energy employing 4-fold integration which is numerically much faster than the original 6-fold integration. For a spherical nucleus the above expression can be transformed explicitly as in ref. [109],

$$B^0_{\rm surf} = 1 - 3\left(\frac{a}{R_0}\right)^2 + \left(\frac{R_0}{a} + 1\right)\left[2 + 3\frac{a}{R_0} + 3\left(\frac{a}{R_0}\right)^2\right] e^{-2R_0/a}. \quad (8.1.7)$$

Deformation-Dependent Terms – Coulomb Energy. According to ref. [109], Coulomb energy is calculated as

$$B_{\rm Coul}(\alpha) = \frac{15}{32}\frac{A^{-5/3}}{r_0^5} \int_V \int_{V'} \frac{d\vec{r}d\vec{r}'}{|\vec{r} - \vec{r}'|} \left[1 - \left(1 + \frac{1}{2}\frac{|\vec{r} - \vec{r}'|}{a_{\rm den}} \right) e^{-|\vec{r}-\vec{r}'|/a_{\rm den}} \right], \quad (8.1.8)$$

where $a_{\rm den}$ represents the diffusivity constant. For a spherical nucleus, one obtains

$$B^0_{\rm Coul}(\alpha) = 1 - \frac{5}{y_0^2}\left[1 - \frac{15}{8y_0} + \frac{21}{8y_0^3} - \frac{3}{4}\left(1 + \frac{9}{2y_0} + \frac{7}{y_0^2} + \frac{7}{2y_0^3} \right) e^{-2y_0} \right], \quad (8.1.9)$$

where $y_0 = \frac{R_0}{a_{\rm den}}$. The Coulomb corrective factor $f(k_F r_p)$, is given by

$$f(k_F r_p) = -\frac{1}{8}\frac{r_p^2 e^2}{r_0^3}\left[\frac{145}{48} - \frac{327}{2880}x^2 + \frac{1527}{1209600}x^4 \right] \text{ with } x = \left(\frac{9\pi Z}{a_{4A}}\right)\frac{r_p}{r_0}, \quad (8.1.10)$$

in which $r_p = 0.8$ fm and $r_0 = 1.16$ fm represent the proton root-mean-square radius and nuclear radius constant ref. [109], respectively.

The Empirical Corrective Pairing Term. The corresponding paring energy contribution is defined as

$$\delta(Z,N) = \begin{cases} \bar{\Delta}_p + \bar{\Delta}_n - \delta_{np} & \text{for Z and N odd,} \\ \bar{\Delta}_p & \text{for } Z \text{ odd and } N \text{ even,} \\ \bar{\Delta}_n & \text{for } Z \text{ even and } N \text{ odd,} \\ 0 & \text{for } Z \text{ and } N \text{ even,} \end{cases} \quad (8.1.11)$$

where $\bar{\Delta}_p$, $\bar{\Delta}_n$ represent the average proton and neutron pairing gaps and δ_{np} is the average neutron-proton interaction energy, with the corresponding expressions after ref. [109] given by:

$$\bar{\Delta}_p = \frac{r_{\rm mac} B_s(\alpha)}{Z^{\frac{1}{3}}}; \quad \bar{\Delta}_n = \frac{r_{\rm mac} B_s(\alpha)}{N^{\frac{1}{3}}}; \quad \bar{\delta}_{np} = \frac{h}{B_s(\alpha) A^{\frac{2}{3}}}, \quad (8.1.12)$$

where $r_{\rm mac}$ represents the average pairing-gap constant and h, the neutron-proton interaction constant. Above, $B_s(\alpha)$ is defined as the numerical factor representing the ratio of the surface of the deformed nucleus and the surface of the same nucleus at the spherical shape,

$$B_s = \frac{A^{-\frac{2}{3}}}{4\pi r_0} \int_\Sigma dS. \tag{8.1.13}$$

The parameters (constants) used in Eq. (8.1.4) can be found in ref. [109].

8.1.3 Lublin-Strasbourg Drop (LSD) Model

The nuclear liquid-drop model was revisited and extended in ref. [119] within the Lublin-Strasbourg collaboration. The new version is referred to as Lublin-Strasbourg Drop (LSD) Model. The main idea was to add the surface-curvature terms and re-adjusting the parameters to improve the over-all energy description including the fission-barrier heights. The corresponding parameters in the LSD model were adjusted using experimental binding energies of 2766 known nuclei with $Z \geq 8$ and $N \geq 8$.

The final energy expression is given by:

$$\begin{aligned}
E^{\rm LSD}_{\rm Macro}(Z,N,\{\alpha\}) = {} & M_{\rm H}Z + M_n N && \text{mass excesses} \\
& - a_{\rm vol}(1-\kappa_{\rm vol}I^2)A && \text{volume energy} \\
& + a_{\rm surf}(1-\kappa_{\rm surf}I^2)A^{\frac{2}{3}}B_{\rm surf}(\{\alpha\}) && \text{surface energy} \\
& + a_{\rm cur}(1-\kappa_{\rm cur}I^2)A^{\frac{1}{3}}B_{\rm cur}(\{\alpha\}) && \text{curvature energy} \\
& + \frac{3}{5}\frac{e^2Z^2}{r_0^{ch}A^{\frac{1}{3}}}B_{\rm Coul}(\{\alpha\}) && \text{Coulomb energy} \\
& - C_4\frac{Z^2}{A} && \text{proton form-factor correction} \\
& && \text{to the Coulomb energy} \\
& + E_{\rm cong}(N,Z) && \text{congruence energy.}
\end{aligned} \tag{8.1.14}$$

The last term, so-called congruence energy, $E_{\rm cong}(N,Z)$, is defined as in ref. [120]

$$E_{\rm cong}(N,Z) = -10\exp(-42|I|/10). \tag{8.1.15}$$

It is well known that the Coulomb and surface terms depend strongly on deformation. The behaviour of the two discussed macroscopic energy models at small and moderate deformations are rather similar, while at larger deformations they become increasingly different due to the presence of the surface-curvature contributions in the LSD case. These terms are sensitive to the increasing geometrical complexity of the surface since

they involve the geometrical curvature-radii. Taking into account these mechanisms, which may be considered as introducing new degrees of freedom, improves in particular the description of the fission barriers.

8.1.4 Macroscopic Energy Comparison: FYU vs. LSD

In figures (8.1.1)-(8.1.2) we compare differences between the two discussed macroscopic energy models by illustrating the nuclear energies represented as functions of quadrupole, α_{20}, octupole, $\alpha_{3\mu=0,1,2,3}$ and hexadecapole, α_{40} deformations.

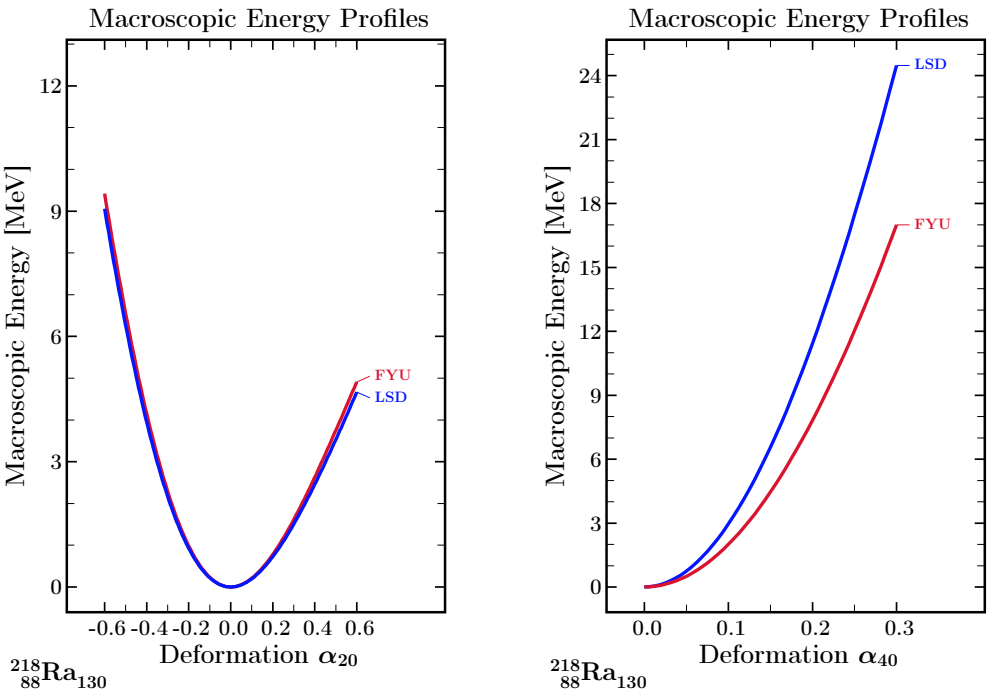

Figure 8.1.1 – *Macroscopic energy comparison between FYU (red curve) and LSD (blue curve) for even $\lambda = 2$ and 4. The energies are comparable at quadrupole deformation $\lambda = 2$ and at small values of the hexadecapole deformation.*

Comparison shows that the deformation dependence on quadrupole deformation α_{20} of the two macroscopic energy expressions are nearly identical. They are relatively close at small values of the hexadecapole deformations α_{40}. We also compare the two macroscopic energies as functions of the octupole deformations $\{\alpha_{30}, \alpha_{31}, \alpha_{32}, \alpha_{33}\}$ in figure (8.1.2). The energy variations are similar, the energies of FYU are always lower than the ones of LSD. It is worth mentioning that the parameters in LSD model have been adjusted to the ground-states and the fission properties of known nuclei. In our present work, we use FYU expression within the macroscopic-microscopic approach.

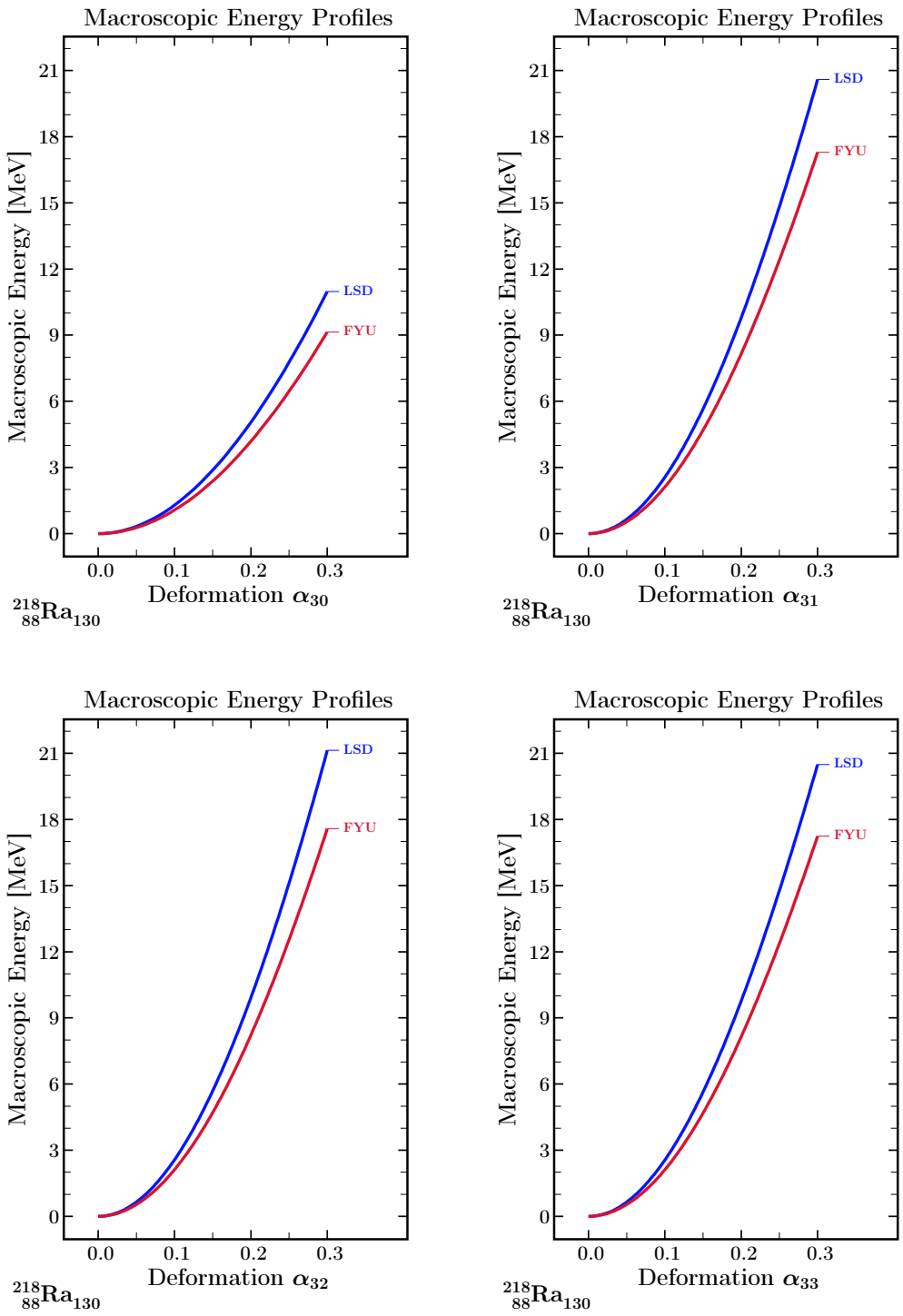

Figure 8.1.2 – *Similar to the preceding one: Comparison of FYU (red curve) and LSD (blue curve) macroscopic energies as functions of octupole deformations* $\{\alpha_{30}, \alpha_{31}, \alpha_{32}, \alpha_{33}\}$. *The energies are comparable at small deformations.*

8.2 Strutinsky Shell Correction Method

The nuclear shell correction energy expression was introduced in 1966 by Strutinsky employing the single-particle energies treated as functions of deformation, cf. refs. [85] and [121]. The basic idea behind the Strutinsky approach is to express the total nuclear energy as the sum of the macroscopic liquid drop energy and the nuclear shell energy.

After Strutinsky the shell correction energy is defined by

$$\delta E_{\text{shell}} = E - \tilde{E}, \tag{8.2.1}$$

where the first term represents the sum of the single-particle energies for particle number n, which are obtained by solving the Schrödinger equation with a mean-field Hamiltonian,

$$E = \sum_n \epsilon_n, \quad (\epsilon_n < \epsilon_{\lambda_F}), \tag{8.2.2}$$

in which λ_F is called Fermi level related to the last occupied particle. The second term in eq. (8.2.1) depends on an auxiliary, so called 'smooth level density function'

$$\tilde{E} = \int_{-\infty}^{\epsilon_{\lambda_F}} \epsilon \tilde{g}(\epsilon) d\epsilon, \tag{8.2.3}$$

where $\tilde{g}(\epsilon)$ denotes the 'Strutinsky-smoothed' single particle level density. The single-particle energy density is defined by

$$g(\epsilon) = \frac{dn}{d\epsilon}. \tag{8.2.4}$$

It represents the number of levels per energy unit. It follows that the particle numbers of the system define the Fermi energies by

$$Z \text{ or } N = \int_{-\infty}^{\epsilon_{\lambda_F}} g(\epsilon) d\epsilon, \tag{8.2.5}$$

whereas the energies are given by

$$E = \int_{-\infty}^{\epsilon_{\lambda_F}} \epsilon g(\epsilon) d\epsilon. \tag{8.2.6}$$

The auxiliary density of single-particle levels, $g(\epsilon)$, is usually represented using the Dirac δ-distribution,

$$g(\epsilon) = \sum_n \delta(\epsilon - \epsilon_n). \tag{8.2.7}$$

Summations/integrations in the above relations extend over the single-particle energies up to the Fermi level.

The formal definition of the density involving Dirac δ-distributions in eq. (8.2.7) can be written down alternatively using an identity expressing the Dirac δ as the infinite series of Hermit polynomials, cf. ref. [40]:

$$\delta(x) = \frac{1}{\sqrt{\pi}} e^{-x^2} \sum_{n=0}^{\infty} c_n H_n(x). \tag{8.2.8}$$

Changing the variable $x \to \epsilon - \epsilon_n$ we find

$$\delta(\epsilon - \epsilon_n) = \frac{1}{\sqrt{\pi}} e^{[-(\epsilon-\epsilon_n)]^2} \sum_{n=0}^{\infty} c_n H_n(\epsilon - \epsilon_n). \tag{8.2.9}$$

With the help of the abbreviation

$$u_n = \frac{(\epsilon - \epsilon_n)}{\gamma}, \tag{8.2.10}$$

we can make the following expressions more compact; the factor γ has the dimension of energy. It follows that

$$g(\epsilon) = \frac{1}{\gamma} \sum_{n=1}^{\infty} \delta(u_n) = \frac{1}{\gamma\sqrt{\pi}} \sum_{n=1}^{\infty} e^{-u_n^2} \sum_{m=0}^{\infty} c_m H_m(u_n), \tag{8.2.11}$$

where c_m are expansion coefficients given by

$$c_m = \begin{cases} \frac{(-1)^{m/2}}{2^m (m/2)!}, & m \text{ even}, \\ 0, & m \text{ odd}, \end{cases} \tag{8.2.12}$$

cf. ref. [40], and it follows that summation over m in eq. (8.2.11) contains only even m.

At this point, we can introduce the 'smoothed level density function $\bar{g}(\epsilon)$' originally introduced by Strutinsky by arbitrarily modifying the infinite summation over m in eq. (8.2.11) in principle extending to ∞, by replacing it by a cut-off parameter p selected as a finite number. It follows that the smoothed energy level density can be written down as:

$$\bar{g}(\epsilon) = \frac{1}{\gamma\sqrt{\pi}} \sum_{n=1}^{\infty} e^{-u_n^2} \sum_{m=0}^{p} c_m H_m(u_n), \tag{8.2.13}$$

where parameters γ and p were introduced in ref. [122] as:

$$\gamma = 1.2\,\hbar\omega \quad \text{with} \quad \hbar\omega \sim 41 A^{-\frac{1}{3}}\text{MeV}, \quad \text{and} \quad p = 6. \tag{8.2.14}$$

8.3 Pairing Effects within Strutinsky Approach

One can include the effect of the nuclear pairing correlations in the total nuclear energy similarly to including the single-particle shell effects of the mean-field by introducing the Strutinsky pairing energy correction. In fact, there are two similar

phenomenological expressions used in the literature to account for the corresponding contributions; they are called 'correction' and 'correlation' energies. They will be discussed next.

• **Pairing Correlation Energy.** We begin with the paring correlation energy. Recall the BCS pairing energy expression for the nuclear superfluid phase with pairing $\Delta \neq 0$. We have

$$E_{\rm BCS} = \sum_{\nu=1}^{N_p} (2\epsilon_\nu v_\nu^2 - G v_\nu^4) - \frac{\Delta^2}{G}, \tag{8.3.1}$$

where v_ν^2, G and Δ represent the probability of occupation of the nucleonic level "ν", pairing constant and pairing gap, respectively. The pairing correlation energy is defined as the difference between the BCS energy of the system with the presence of pairing, $\Delta \neq 0$, and its parter expression without pairing, i.e., $E_{\rm BCS}$ for $\Delta = 0$:

$$\delta E_{\rm correl} = \underbrace{\sum_{\nu=1}^{N_p} (2\epsilon_\nu v_\nu^2 - G v_\nu^4) - \frac{\Delta^2}{G}}_{\Delta\neq 0} - \underbrace{\sum_{\nu=1}^{N_p/2} (2\epsilon_\nu - G)}_{\Delta=0}, \tag{8.3.2}$$

for details cf. Ref. [40]. To provide more details we recall the BCS equations as presented in chapter 4, eqs. (4.2.58-4.2.58):

$$N_p = \sum_{k=1}^{N_p} \left\{ 1 - \frac{\epsilon_k - \lambda}{\sqrt{(\epsilon_k - \lambda)^2 + \Delta^2}} \right\}, \tag{8.3.3}$$

and

$$\frac{2}{G} = \sum_{k=1}^{N_p} \frac{1}{\sqrt{(\epsilon_k - \lambda)^2 + \Delta^2}}, \tag{8.3.4}$$

where N_p is the number of the nucleonic pairs. Once the pairing gap is known, the occupation probability v_k^2 can be calculated form the following standard BCS expression

$$v_k^2 = \frac{1}{2} \left\{ 1 - \frac{\epsilon_k - \lambda}{[(\epsilon_k - \lambda)^2 + \Delta^2]^{1/2}} \right\}, \quad \text{where} \quad k = 1, 2, ..., N_p. \tag{8.3.5}$$

The pairing strength constants G is given in ref. [40] by

$$\frac{1}{G} = \bar{\rho} \ln \left\{ \left[1 + \left(\frac{2\bar{\rho}\bar{\Delta}}{N_p} \right)^2 \right]^{1/2} + \frac{N_p}{2\bar{\rho}\bar{\Delta}} \right\}, \tag{8.3.6}$$

in which the average density of pairs at the Fermi level is

$$\bar{\rho} = \frac{1}{2} \bar{g}(\lambda), \tag{8.3.7}$$

and $\bar{g}(\lambda)$ was introduced in Eq. (8.2.13). The so-called average gap, $\bar{\Delta}$, represents an average empirical trend given by

$$\bar{\Delta} = \frac{\text{const.}}{\sqrt{A}}, \tag{8.3.8}$$

in which the constant, approximately 12 MeV, results from fitting to the experimental data on the odd-even mass differences. However, by using the contemporary experimental data [123], we find that the traditionally used constant '12' is not optimal anymore for all the nuclear mass ranges of interest. In order to represent the experimental data more precisely, we re-write eq. (8.3.8) as follows

$$\bar{\Delta} = \frac{\alpha}{\sqrt{A}}, \tag{8.3.9}$$

The empirical values of the pairing gaps are usually extracted from the odd-even mass (or binding energy) differences. The so-called three-point mass formula was introduced by Satuła and coworkers, ref. [124]. For a given Z one writes

$$\Delta_Z^{(3)} = \tfrac{1}{2}(-1)^N[B(Z,N+1) - 2B(Z,N) + B(Z,N-1)], \tag{8.3.10}$$

similarly for a given N,

$$\Delta_N^{(3)} = \tfrac{1}{2}(-1)^Z[B(Z+1,N) - 2B(Z,N) + B(Z-1,N)], \tag{8.3.11}$$

where B is the (negative) binding energy of the nucleus. In this project the related experimental information was taken from the mass tables of 2016, ref. [123].

By fitting the average behaviour of empirical pairing gaps, we can find the optimal α for different nuclear regions as shown in figures (8.3.1)-(8.3.9). We find correspondingly:

$$\text{Protons}: \quad \begin{cases} \alpha_p = 11.0, & Z \geq 82, \\ \alpha_p = 11.7, & 52 \leq Z \leq 80, \\ \alpha_p = 10.2, & 28 \leq Z \leq 50, \\ \alpha_p = \ 8.2, & 2 \leq Z \leq 28, \end{cases} \tag{8.3.12}$$

and

$$\text{Neutrons}: \quad \begin{cases} \alpha_n = 10.6, & N \geq 126, \\ \alpha_n = 12.0, & 82 \leq N \leq 126, \\ \alpha_n = 11.8, & 52 \leq N \leq \ 80, \\ \alpha_n = 10.0, & 28 \leq N \leq \ 50, \\ \alpha_n = \ 8.2, & 2 \leq N \leq \ 28. \end{cases} \tag{8.3.13}$$

• **Pairing Correction Energy.** In analogy to the Strutinsky shell correction energy we can define the pairing correction energy as the difference between the nuclear energy contribution from the BCS approximation and the corresponding 'average' or 'smoothed' part. With the help of the average density and the pairing strength constants, the uniform distribution of the levels that are treated as the smoothed pairing correlation is given by

$$\bar{E}_{pc} = -\frac{1}{4}\frac{N_p^2}{\bar{\rho}}\left\{\left[1 + \left(\frac{2\bar{\rho}\bar{\Delta}}{N_p}\right)^2\right]^{1/2} - 1\right\} + \frac{1}{2}\bar{\rho}\bar{\Delta}G\tan^{-1}\frac{N_p}{2\bar{\rho}\bar{\Delta}}, \tag{8.3.14}$$

and the pairing correction is calculated as follows

$$\delta E_{\text{correc}} = \delta E_{\text{correl}} - \bar{E}_{pc}. \tag{8.3.15}$$

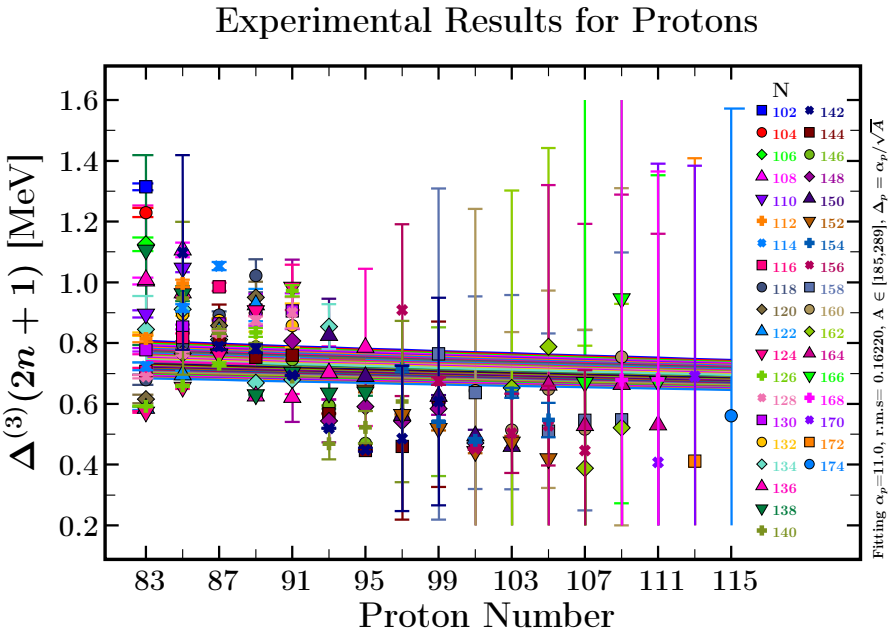

Figure 8.3.1 – *Proton experimental pairing gap energies* $\Delta^{(3)}(2n+1)$ *calculated using eq. (8.3.10) in the nuclei ranges* $Z \geq 82$ *are presented together with the corresponding experimental error bars. Solid lines represent the results of* α*-fitting related to Eq. (8.3.9) with optimal* α *obtained by* χ^2 *minimisation.*

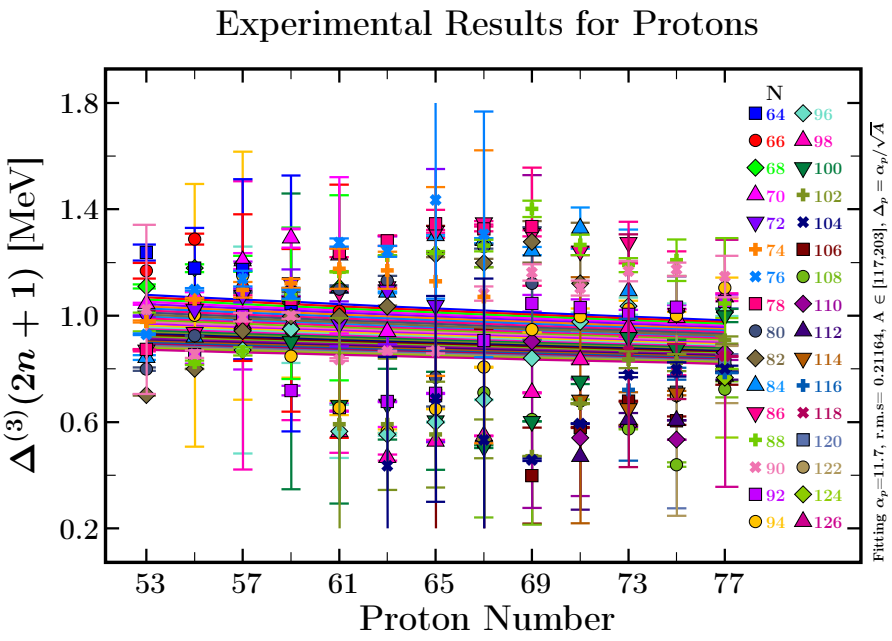

Figure 8.3.2 – *Similar to fig.(8.3.1) for protons in nuclear ranges* $52 \leq Z \leq 80$

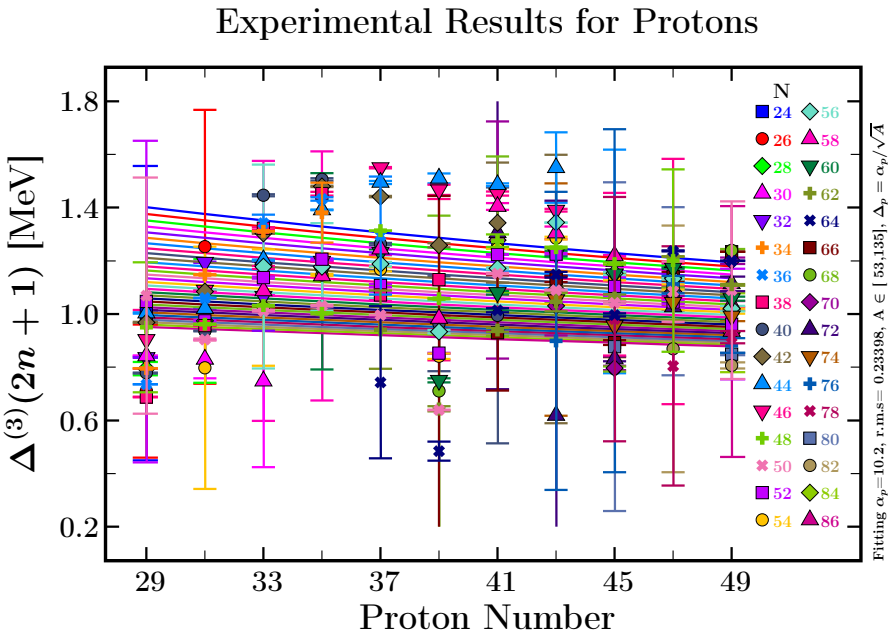

Figure 8.3.3 – *Similar to the preceding one, but for nuclei ranges* $28 \leq Z \leq 50$.

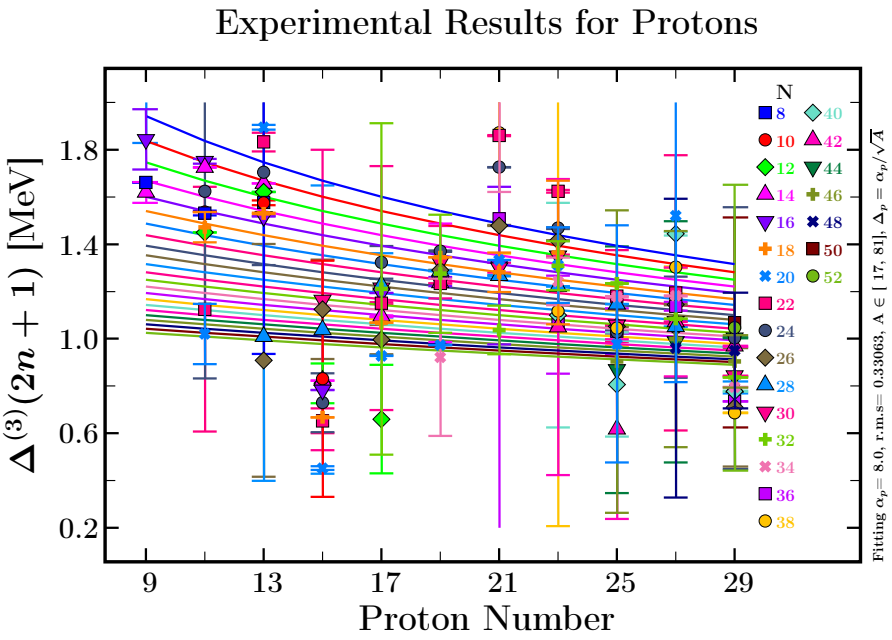

Figure 8.3.4 – *Similar to the preceding one, but for nuclei ranges* $8 \leq Z \leq 28$.

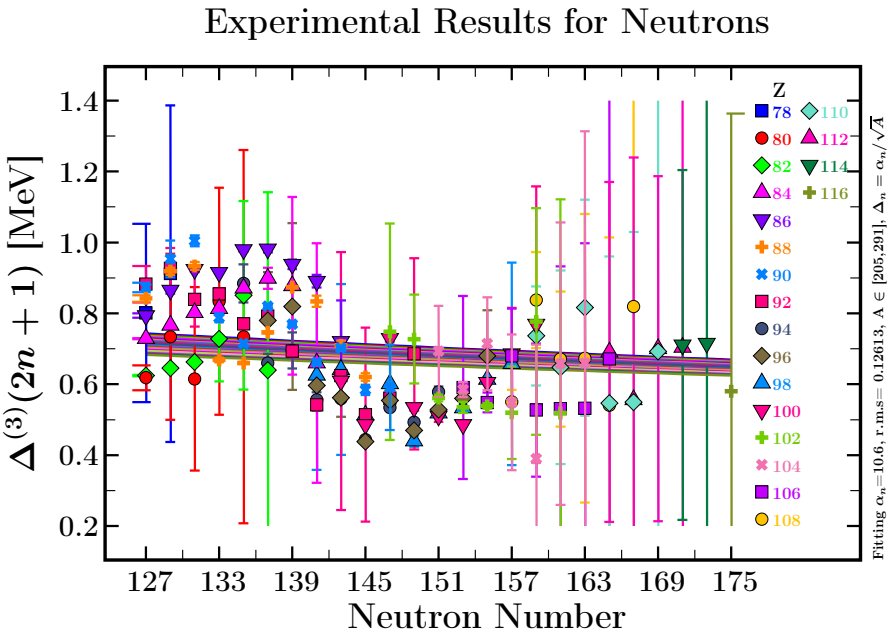

Figure 8.3.5 – *Similar to fig.(8.3.1), but for the results of neutrons in nuclear ranges* $N \geq 126$.

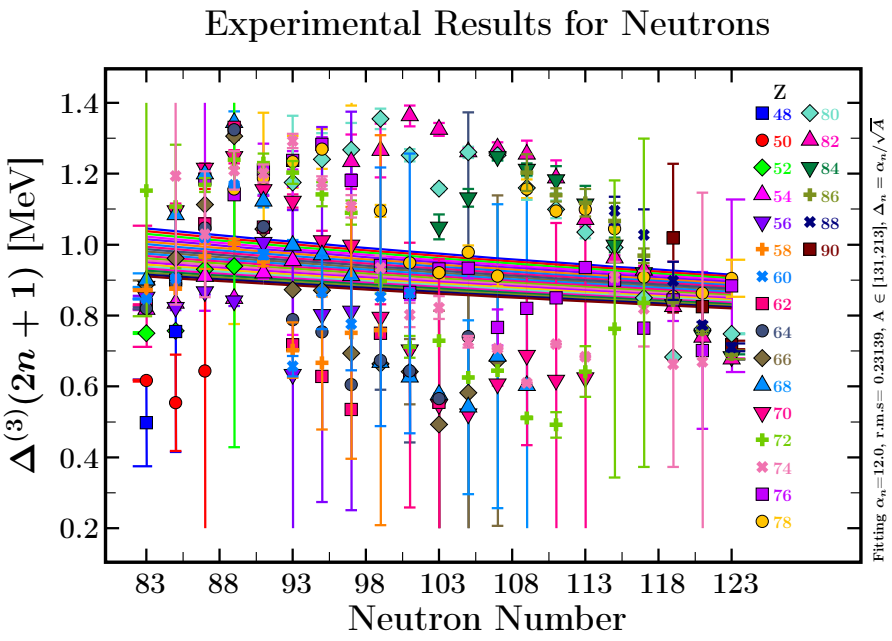

Figure 8.3.6 – *Similar to fig.(8.3.5) for neutrons in nuclear ranges* $82 \leq N \leq 126$.

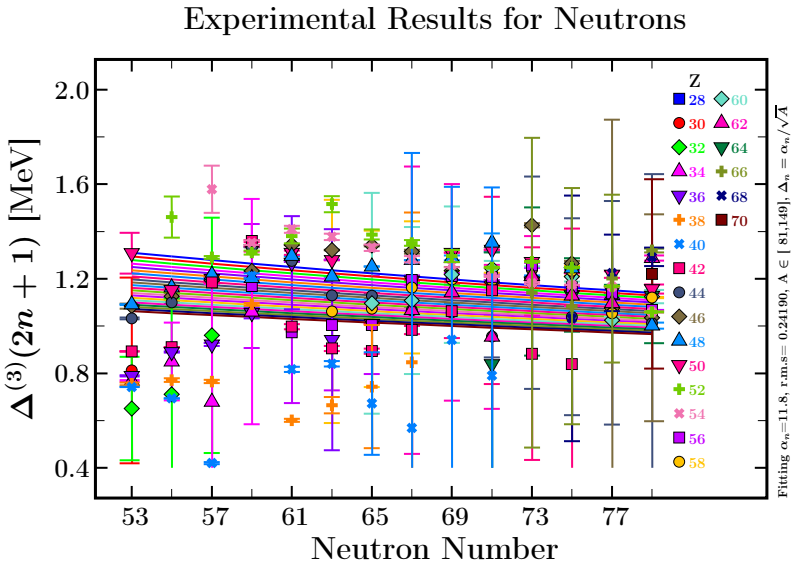

Figure 8.3.7 – *Similar to the preceding one for nuclei ranges* $52 \leq N \leq 80$.

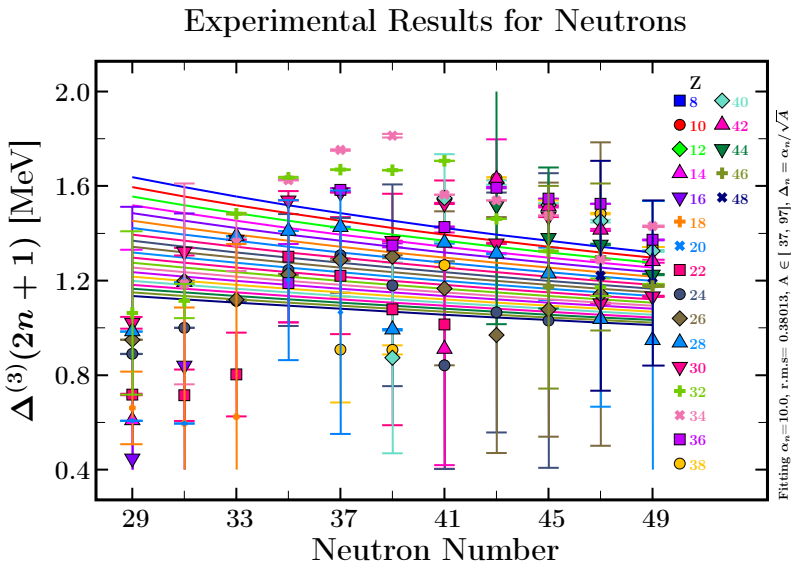

Figure 8.3.8 – *Similar to the preceding one for nuclei ranges* $28 \leq N \leq 50$.

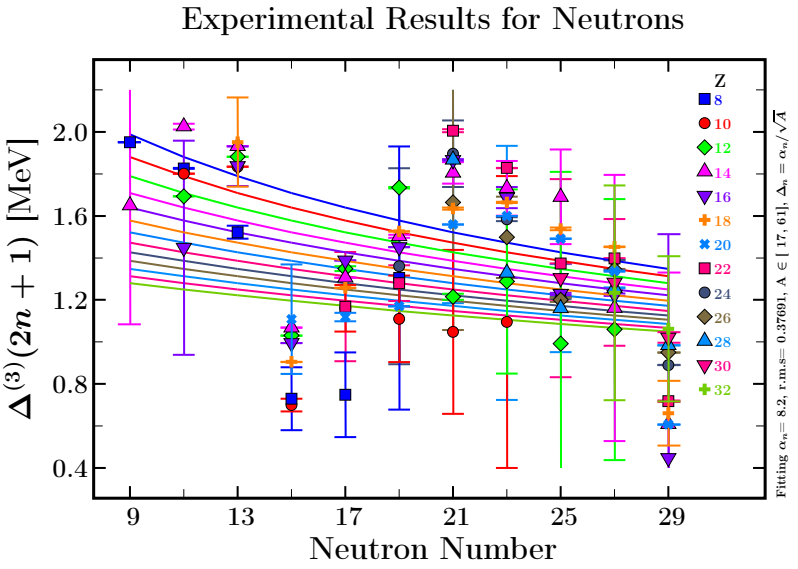

Figure 8.3.9 – *Similar to the preceding one for nuclei ranges* $2 \leq N \leq 28$.

Acknowledgements

First of all I would like to express my sincere gratitude to my supervisor Professor J. Dudek, for his support and guidance in my PhD study and research during the past four years at UMCS. I would like to thank for his patience and passion in teaching me all the new things, new physics concepts and new methods of learning, and new foreign cultures. His motivation and conviction encouraged me the most and provided me with a new picture of what research is. He encouraged me to start thinking and asking questions, no matter how simple the question was, he always gave me hints and guided me to find the way to the right solutions. His enthusiasm also deeply impressed me, being motivated and interested in studying difficult and complex subjects. The fruitful discussions with Professor Dudek inspired my new, various ways of thinking in research and motivated me to keep learning and understanding new things. I really appreciate every opportunity to discuss and study with Professor Dudek.

I would like also to thank one of my most important colleagues, Dr. Irene Dedes, for her patience in teaching me every tiny thing from research to ordinary life. Her proficient programming skills help me a lot and encouraged me to face the difficulties in coding and studying. Her optimistic and cheerful personality also inspires me to open my eyes and try new things. She is the first friend I met in the new country and she made me feel comfortable as one member of our research group. She kept encouraging me in the most difficult moments in the past four years. I really appreciate meeting and to work with her.

Besides that I would like to thank Professor A. Baran for his patient guidance in running computer programs on the LUNAR cluster and thank him for the nice discussions we had. Also I would like to thank Professor H.-L. Wang for his supporting and encouragement in my PhD study.

Studying in Lublin without knowing Polish, our secretary Anna Wielgus helped me a lot, particularly in many everyday aspects of my life, I would like to thank her for all her help.

During these four years, all the PhD students I met at the institute also give me a lot of help. For this I would like to thank Axel, Szczepan, Bartek Baran, and Bartek Kiczek, who shared the office with me. We had nice discussions and talked about everything in the office and they also shared with me their experience in dealing with various problems. In the past years I met two best roommates, Anamaria and Rui Han, I am also very thankful for their support in every aspect after work.

Last but not the least, I would like to thank my friends Yutian Shao, Chen Lu, Wei Lu, HaiYan Meng and Qiong Yang. Although we could not meet in reality in the past two years, our friendship is lasting. At the end, the most important Thank You goes to my parents and my brother for their support, continuous encouragement, and their unconditional love. I thank them for always being there; whenever I needed them they always stayed with me to give me the courage in facing everything.

Bibliography

[1] S. Tagami, Y. R. Shimizu, and J. Dudek, Phys. Rev. C **87**, 054306 (2013).

[2] B. Pritychenko, M. Birch, B. Singh, and M. Horoi, At. Data Nucl. Data Tables **107**, 1 (2016).

[3] J. Dudek, A. Góźdź, K. Mazurek, and H. Molique, J. Phys. G: Nucl. Part. Phys. **37**, 064032 (2010).

[4] P. A. Butler, J. Phys. G: Nucl. Part. Phys. **43**, 073002 (2016).

[5] R. V. Reid Jr, Annals of Physics **50**, 411 (1968).

[6] M. J. A. de Voigt, J. Dudek, and Z. Szymański, Rev. Mod. Phys. **55**, 949 (1983).

[7] D. A. Varshalovich, A. N. Moskalev, and V. K. Khersonskii, *Quantum theory of angular momentum* (World Scientific, 1988).

[8] J. Blomqvist and S. Wahlborn, Ark. Fys. **16**, 543 (1960).

[9] V. A. Chepurnov, Yad. Fiz. **6**, 955 (1967).

[10] E. Rost, Phys. Rev. B **26**, 184 (1968).

[11] J. Dudek, A. Majhofer, J. Skalski, T. Werner, S. Cwiok, and W. Nazarewicz, J. Phys. G **5**, 1359 (1979).

[12] A. Gaamouci, I. Dedes, J. Dudek, A. Baran, N. Benhamouda, D. Curien, H. L. Wang, and J. Yang, Phys. Rev. C **103**, 054311 (2021).

[13] A. Bohr and B. R. Mottelson, *Nuclear Structure:(In 2 Volumes) Volume I: Single-Particle MotionVolume II: Nuclear Deformations* (World Scientific, 1998).

[14] J. Dudek, B. Szpak, B. Fornal, and A. Dromard, Phys. Scr. **154**, 4002 (2013).

[15] I. Dedes and J. Dudek, Acta Physica Polonica B, Proceedings Supplement **10**, 51 (2017).

[16] A. Tarantola, B. Valette, et al., Journal of geophysics **50**, 159 (1982).

[17] I. Dedes, Approche stochastique du probléme du pouvoir prédictif dans la modélisation du champ moyen (PhD Thesis, Université Louis Paster de Strasbourg, Strasbourg, France, 2017). (2017).

[18] N. Schunck, Ph.D. thesis, Université Louis Pasteur-Strasbourg I (2001).

[19] L. D. Landau and E. M. Lifshitz, *Quantum mechanics: non-relativistic theory*, vol. 3 (Elsevier, 2013).

[20] M. Abramowitz and I. A. Stegun, US Department of Commerce; National Bureau of Standards Applied Mathematics Series **55** (1965).

[21] S. A. Teukolsky, B. P. Flannery, W. Press, and W. Vetterling, SMR **693**, 59 (1992).

[22] J. Dobaczewski and J. Dudek, Comp. Phys. Comm. **102**, 166 (1997).

[23] J. Bardeen, L. N. Cooper, and J. R. Schrieffer, Phys. Rev. **108**, 1175 (1957).

[24] A. Bohr, B. R. Mottelson, and D. Pines, Phys. Rev. **110**, 936 (1958).

[25] D. R. Inglis, Phys. Rev. **96**, 1059 (1954).

[26] J. Dudek, A. Goźdź, N. Schunck, and M. Miśkiewicz, Phys. Rev. Lett. **88**, 252502 (2002).

[27] M. Hamermesh, *Group Theory and Its Application to Physical Problems* (Addison-Wesley, 1964).

[28] J. F. Cornwell, *Group theory in physics: An introduction* (Academic press, 1997).

[29] J. Dudek, D. Curien, I. Dedes, K. Mazurek, S. Tagami, Y. R. Shimizu, and T. Bhattacharjee, Phys. Rev. C **97**, 021302 (2018).

[30] J. Dudek, J. Dobaczewski, N. Dubray, A. Góźdź, V. Pangon, and N. Schunck, International Journal of Modern Physics E **16**, 516 (2007).

[31] J. Dudek, A. Goźdź, and N. Schunck, Acta. Phys. Pol. B. **34**, 2491 (2003).

[32] J. Dudek, D. Curien, N. Dubray, J. Dobaczewski, V. Pangon, P. Olbratowski, and N. Schunck, Phys. Rev. Lett. **97**, 072501 (2006).

[33] J. Dudek, A. Góźdź, and D.Rosły, Acta Phys. Pol. **32**, 2625 (2001).

[34] J. Yang, J. Dudek, I. Dedes, A. Baran, D. Curien, A. Gaamouci, A. Góźdź, A. Pedrak, D. Rouvel, H. Wang, et al., Phys. Rev. C **105**, 034348 (2022).

[35] A. Góźdź, M. Miśkiewicz, and J. Dudek, International Journal of Modern Physics E **17**, 272 (2008).

[36] K. T. Hecht, Journal of Molecular Spectroscopy **5**, 355 (1961).

[37] W. G. Harter and D. E. Weeks, The Journal of chemical physics **90**, 4727 (1989).

[38] G. Herzberg, *Molecular Spectra and molecular structure-Vol I*, vol. 1 (Read Books Ltd, 2013).

[39] K. Pomorski, Phys. Rev. C **70**, 044306 (2004).

[40] M. Bolsterli, E. O. Fiset, J. R. Nix, and J. L. Norton, Phys. Rev. C **5**, 1050 (1972).

[41] P. A. Butler and W. Nazarewicz, Rev. Mod. Phys. **68**, 349 (1996).

[42] I. Hamamoto, B. Mottelson, H. Xie, and X. Zhang, Zeitschrift für Physik D Atoms, Molecules and Clusters **21**, 163 (1991).

[43] M. Martin, Nuclear Data Sheets **108**, 1583 (2007).

[44] P. Bonche, S. J. Krieger, M. S. Weiss, J. Dobaczewski, H. Flocard, and P.-H. Heenen, Phys. Rev. Lett. **66**, 876 (1991).

[45] J. Skalski, Phys. Lett. B **274:1** (1992).

[46] J. Skalski, P. H. Heenen, P. Bonche, H. Flocard, and J. Meyer, Nucl. Phys. A **551**, 109 (1993).

[47] I. Ahmad and P. A. Butler, Annu. Rev. Nucl. Part. Sci. **43**, 71 (1993).

[48] L. M. Robledo and G. F. Bertsch, Phys. Rev. C **84**, 054302 (2011).

[49] L. P. Gaffney, P. A. Butler, M. Scheck, A. B. Hayes, F. Wenander, M. Albers, B. Bastin, C. Bauer, A. Blazhev, S. Bönig, et al., Nature(London) **497**, 199 (2013).

[50] P. A. Butler, L. P. Gaffney, P. Spagnoletti, K. Abrahams, M. Bowry, J. Cederkäll, G. de Angelis, H. De Witte, P. E. Garrett, A. Goldkuhle, et al., Phys. Rev. Lett. **124**, 042503 (2020).

[51] K. Nomura, R. Rodríguez-Guzmán, Y. M. Humadi, L. M. Robledo, and J. E. García-Ramos, Phys. Rev. C **102**, 064326 (2020).

[52] K. Nomura, R. Rodríguez-Guzmán, L. M. Robledo, and J. E. García-Ramos, Phys. Rev. C **103**, 044311 (2021).

[53] W. Greiner and J. Reinhardt, *Field quantization* (Springer Science & Business Media, 2013).

[54] E. W. Dijkstra et al., Numerische mathematik **1**, 269 (1959).

[55] K. W. Robert Sedgewick, *Algorithms Fourth Edition* (Princeton University, 2011).

[56] A. Baran, K. Pomorski, A. Lukasiak, and A. Sobiczewski, Nuclear Physics A **361**, 83 (1981).

[57] D. Rouvel and J. Dudek, Phys. Rev. C **99**, 041303 (2019).

[58] M. M. R. Chishti, D. O. Donnell, G. Battaglia, M. Bowry, D. A. Jaroszynski, B. S. N. Singh, M. Scheck, P. Spagnoletti, and J. F. Smith, Nat.Phys. **16**, 853 (2020).

[59] W. Nazarewicz, P. Olanders, I. Ragnarsson, J. Dudek, G. Leander, P. Möller, and E. Ruchowsa, Nucl. Phys. A **429**, 269 (1984).

[60] L. M. Robledo and P. A. Butler, Phys. Rev. C **88**, 051302 (2013).

[61] L. M. Robledo, J. Phys. G: Nucl. Part. Phys. **42**, 055109 (2015).

[62] S. E. Agbemava, A. V. Afanasjev, and P. Ring, Phys. Rev. C **93**, 044304 (2016).

[63] Z. Xu and Z.-P. Li, Chin. Phys. C **41**, 124107 (2017).

[64] D. Bonatsos, D. Lenis, N. Minkov, D. Petrellis, and P. Yotov, Phys. Rev. C **71**, 064309 (2005).

[65] P. G. Bizzeti and A. M. Bizzeti-Sona, Phys. Rev. C **88**, 011305 (2013).

[66] Z. Patyk and A. Sobiczewski, Nucl. Phys. A **533**, 132 (1991).

[67] Z. Patyk and A. Sobiczewski, Phys. Lett. B **256**, 307 (1991).

[68] D. L. Hill and J. A. Wheeler, Phys. Rev. **89**, 1102 (1953).

[69] S. Raman, C. Nestor, and P. Tikkanen, Atomic Data and Nuclear Data Tables **78**, 1 (2001).

[70] Y. Oganessian, Journal of Physics G: Nuclear and Particle Physics **34**, R165 (2007).

[71] J. Wheeler, W. Pauli, ed p. 163 (1955).

[72] F. G. Werner and J. A. Wheeler, Physical Review **109**, 126 (1958).

[73] J. Wheeler, in *Proceedings of the 'International Conference on the Peaceful Uses of Atomic Energy', Geneva* (1955), vol. 2, pp. 155–163.

[74] S. Hofmann and G. Münzenberg, Reviews of Modern Physics **72**, 733 (2000).

[75] K. Morita, K. Morimoto, D. Kaji, T. Akiyama, S.-i. Goto, H. Haba, E. Ideguchi, R. Kanungo, K. Katori, H. Koura, et al., J. Phys. Soc. Japan **73**, 2593 (2004).

[76] L. Stavsetra, K. Gregorich, J. Dvorak, P. Ellison, I. Dragojević, M. Garcia, and H. Nitsche, Phys. Rev. Lett. **103**, 132502 (2009).

[77] C. E. Düllmann, M. Schädel, A. Yakushev, A. Türler, K. Eberhardt, J. Kratz, D. Ackermann, L.-L. Andersson, M. Block, W. Brüchle, et al., Phys. Rev. Lett. **104**, 252701 (2010).

[78] Y. T. Oganessian, F. S. Abdullin, P. Bailey, D. Benker, M. Bennett, S. Dmitriev, J. G. Ezold, J. Hamilton, R. A. Henderson, M. Itkis, et al., Phys. Rev. Lett. **104**, 142502 (2010).

[79] Y. T. Oganessian, F. S. Abdullin, S. Dmitriev, J. Gostic, J. Hamilton, R. Henderson, M. Itkis, K. Moody, A. Polyakov, A. Ramayya, et al., Phys. Rev. Lett. **108**, 022502 (2012).

[80] Y. T. Oganessian, V. Utyonkov, Y. V. Lobanov, F. S. Abdullin, A. Polyakov, R. Sagaidak, I. Shirokovsky, Y. S. Tsyganov, A. Voinov, A. Mezentsev, et al., Phys. Rev. C **79**, 024603 (2009).

[81] V. Zagrebaev and W. Greiner, Phys. Rev, C **78**, 034610 (2008).

[82] V. Zagrebaev and W. Greiner, Phys. Rev. C **83**, 044618 (2011).

[83] M. G. Mayer, Physical Review **74**, 235 (1948).

[84] A. Sobiczewski, F. Gareev, and B. Kalinkin, Physics Letters **22**, 500 (1966).

[85] V. Strutinsky, Nucl. Phys. A **95**, 420 (1967).

[86] S. Polikanov, V. Druin, V. Karnaukhov, V. Mikheev, A. Pleve, N. Skobelev, V. Subbotin, G. Terakopyan, and V. Fomichev, Sov. Phys. JETP **15**, 1016 (1962).

[87] D. Vautherin and D. t. Brink, Phys. Rev. C **5**, 626 (1972).

[88] S. Ćwiok, W. Nazarewicz, and P.-H. Heenen, Phys. Rev. Lett. **83**, 1108 (1999).

[89] K. Rutz, M. Bender, T. Bürvenich, T. Schilling, P.-G. Reinhard, J. A. Maruhn, and W. Greiner, Phys. Rev. C **56**, 238 (1997).

[90] R. K. Gupta, S. Patra, and W. Greiner, Mod. Phys. Lett. A **12**, 1727 (1997).

[91] S. Patra, W. Greiner, and R. K. Gupta, J. Phys. G: Nucl. Part. Phys **26**, L65 (2000).

[92] M. Bender, W. Nazarewicz, and P.-G. Reinhard, Physics Letters B **515**, 42 (2001).

[93] A. Afanasjev, S. Agbemava, and A. Gyawali, Phys. Lett. B **782**, 533 (2018).

[94] P. Indelicato, J. Bieroń, and P. Jönsson, Theoretical Chemistry Accounts **129**, 495 (2011).

[95] A. Sobiczewski and K. Pomorski, Progress in Particle and Nuclear Physics **58**, 292 (2007).

[96] Y. T. Oganessian and V. Utyonkov, Reports on Progress in Physics **78**, 036301 (2015).

[97] S. Hofmann, S. Heinz, R. Mann, J. Maurer, G. Münzenberg, S. Antalic, W. Barth, H. Burkhard, L. Dahl, K. Eberhardt, et al., Eur. Phys. J. A **52**, 1 (2016).

[98] S. Hofmann, in *EPJ Web of Conferences* (EDP Sciences, 2018), vol. 182, p. 02054.

[99] L. Malov, G. Adamian, N. Antonenko, and H. Lenske, Phys. Rev. C **104**, 064303 (2021).

[100] P. J. Siemens and H. Bethe, Phys. Rev. Lett. **18**, 704 (1967).

[101] C. Wong, Ann. of Phys. **77**, 279 (1973).

[102] C.-Y. Wong, Phys. Rev. C **17**, 331 (1978).

[103] K. Dietrich and K. Pomorski, Phys. Rev. Lett. **80**, 37 (1998).

[104] J. Dechargé, J.-F. Berger, K. Dietrich, and M. Weiss, Phys. Lett. B **451**, 275 (1999).

[105] S. Agbemava and A. Afanasjev, Physical Review C **103**, 034323 (2021).

[106] Y. Cao, S. E. Agbemava, A. V. Afanasjev, W. Nazarewicz, E. Olsen, et al., Physical Review C **102**, 024311 (2020).

[107] S. Agbemava and A. Afanasjev, Phys. Rev. C **96**, 024301 (2017).

[108] A. Afanasjev, H. Abusara, and S. Agbemava, Phys. Scr. **93**, 034002 (2018).

[109] P. Moller, J. Nix, W. Myers, and W. Swiatecki, Atom. Data and Nucl. Data Tables **59**, 185 (1995).

[110] M. Warda and J. L. Egido, Physical Review C **86**, 014322 (2012).

[111] P. Jachimowicz, M. Kowal, and J. Skalski, Physical Review C **95**, 034329 (2017).

[112] P. Jachimowicz, M. Kowal, and J. Skalski, Atomic Data and Nuclear Data Tables **138**, 101393 (2021).

[113] S. Ćwiok, J. Dobaczewski, P.-H. Heenen, P. Magierski, and W. Nazarewicz, Nucl. Phys. A **611**, 211 (1996).

[114] P. Jachimowicz, M. Kowal, and J. Skalski, Physical Review C **83**, 054302 (2011).

[115] L. Prochniak and A. Staszczak, Acta Phys. Pol. B **44**, 287 (2013).

[116] P. Jachimowicz, M. Kowal, and J. Skalski, Int. J. Mod. Phys. E **19**, 508 (2010).

[117] H. A. Bethe and R. F. Bacher, Rev. Mod. Phys. **8**, 82 (1936).

[118] H. J. Krappe, J. R. Nix, and A. J. Sierk, Phys. Rev. C **20**, 992 (1979).

[119] K. Pomorski and J. Dudek, Phys. Rev. C **67**, 044316 (2003).

[120] W. D. Myers and W. J. Swiatecki, Nucl. Phys. A **601**, 141 (1996).

[121] V. Strutinsky, Nucl. Phys. A **122**, 1 (1968).

[122] T. Werner and J. Dudek, Atom. Data and Nucl. Data Tables **50**, 179 (1992).

[123] M. Wang, G. Audi, F. G. Kondev, W. J. Huang, S. Naimi, and X. Xu, Chin. Phys. C **41**, 03000 (2017).

[124] W. Satuła, J. Dobaczewski, and W. Nazarewicz, Phys. Rev. Lett. **81**, 3599 (1998).

[125] D. Rouvel, PhD. thesis, University of Strasbourg, France, 2014. (2014).

[126] K. Davies and J. Nix, Phys. Rev. C **14**, 1977 (1976).

[127] E. B. Wilson Jr, The Journal of Chemical Physics **3**, 276 (1935).

[128] Z. Patyk, A. Sobiczewski, P. Armbruster, and K.-H. Schmidt, Nucl. Phys. A **491**, 267 (1989).

[129] N. N. D. C. N. database, Brookhaven National Laboratory (2021).

[130] N. Minkov and P. Walker, Eur. Phys. J. A **48**, 80 (2012).

[131] N. Minkov and P. Walker, Phys. Scr. **89**, 054021 (2014).

[132] L. Bonneau, N. Minkov, D. D. Duc, P. Quentin, and J. Bartel, Phys. Rev. C **91**, 054307 (2015).

[133] S. C. Pancholi, Modern Physics Letters A **36**, 2130013 (2021).

[134] M. Kowal, P. Jachimowicz, and A. Sobiczewski, Physical Review C **82**, 014303 (2010).

[135] J. Hamilton, S. Hofmann, and Y. T. Oganessian, Annual Review of Nuclear and Particle Science **63**, 383 (2013).

[136] N. V. Zamfir and D. Kusnezov, Phys. Rev. C **63**, 054306 (2001).